UNIVERSIDAD DE CANTABRIA
DEPARTAMENTO DE INGENIERÍA DE COMUNICACIONES

TESIS DOCTORAL

Wideband Microwave Circuits for Radioastronomy Applications

Circuitos de Microondas de Banda Ancha para Aplicaciones de Radioastronomía

Autor: Enrique Villa Benito

Directores: Beatriz Aja Abelán - Mª Luisa de la Fuente Rodríguez

Tesis Doctoral para la obtención del título de Doctor por la Universidad de Cantabria en Tecnologías de la Información y Comunicaciones en Redes Móviles

Santander, Noviembre de 2014

To all my family

and people from my setting.

Acknowledgments

Once this long period of time has arrived to its end, it is time to acknowledge and thank the invaluable help, advice and support I have received along this work.

First and foremost, I would like to thank Eduardo Artal for giving me the opportunity to work within the research group that he leads. I hope I have successfully covered the expectations he put on me and the work I have been in charge of.

I would like to express my sincerest gratitude to my advisors Beatriz Aja and Luisa de la Fuente. They have given me invaluable help, advices, experience, optimism and support along this time, and, which is more important, their patience. This work would not have been feasible without them.

I also have to acknowledge the rest of the researching group for their support and patience. The useful and stimulating conversations with Juan Luis Cano, Jaime Cagigas, Ana R. Pérez and David Ortiz are the basis to the development of some of the circuits designed for radio astronomy receivers.

I am also grateful to my colleagues in the Department of 'Ingeniería de Comunicaciones' at University of Cantabria. Among them I would like to acknowledge

to the Technology Laboratory for the support in the fabrication and assembly of the circuits.

Last but not least, my warmest thanks to my family and close friends.

This work was financially supported by the Spanish Ministry for Economy and Competitiveness, Plan Nacional de I+D+i, Space national program project ESP2004-07067-C03-02, Astronomy and Astrophysics program projects AYA2007-68058-C03-03 and AYA2010–21766-C03–03, and the CONSOLIDER-INGENIO 2010 programme under Reference No. CSD2010–00064.

Abstract

The design of sensitive receivers is a significant issue especially when the application area is the radio astronomy. The receivers designed for these purposes operate in a wideband frequency range and will receive a tiny incoming signal. Hence, the need of being sensitive receivers. Some receivers for radio astronomy are focused on the analysis of the origin of the Universe, so the very low power level input signal is the 'first light'. The remnant of that signal is the radiation of the Cosmic Microwave Background (CMB), which can be measured from the whole sky. With a detailed analysis of the CMB, the QUIJOTE project will provide information about the polarization of that radiation in the frequency range from 10 to 47 GHz. Besides, the low power level of the incoming signal cause that the receiver combines the room temperature operation with the cryogenic one.

The QUIJOTE radiometers, as the receivers for radio astronomy applications are named, are composed of wideband microwave circuits on hybrid technology, as 180º and 90º phase switches and detectors. This work is focused on the design of these circuits for any physical temperature of operation that the receiver could show, and it must cover to the following issues: the phase switches must show a flat low-error phase difference with low amplitude imbalance between states in the whole frequency range, while the detectors must provide a flat sensitivity with significant return loss in the frequency band. Their designs involve the knowledge of discrete devices which leads the models performed in this work. Two characterization methods are described to perform these models at both

room and cryogenic temperatures. These methods enable the analysis of the behaviour of discrete devices by the effect of the physical temperature, when it is changed from room to cryogenic temperature.

Finally, a representative QUIJOTE radiometer is assembled and characterised. The receiver is implemented using the circuits described and designed during this thesis among others. The functionality test carried out to the radiometer supports the theory involved in its development.

Resumen

El Universo se originó a partir de una gran explosión, a partir de la cual se establece el instante en el que todo se creó de la nada. El nombre que recibe dicha explosión es Big Bang. Hasta aquel momento, la materia era un punto de densidad infinita que, de manera repentina, explosionó y se expandió en todas direcciones, creando un medio homogéneo isótropo de alta densidad y temperatura que estaba en continua expansión. A medida que dicho medio se expandía, también se reducía su temperatura, y se producían colisiones entre las partículas que lo componían transformando su masa en energía. Estas partículas iniciales eran electrones, protones y neutrones. Dichas partículas se fueron combinando, generando núcleos atómicos, y una vez que se alcanzó una temperatura lo suficientemente baja, se combinaron los electrones y los núcleos formados. Esta combinación generó una radiación que viajaba a través del Universo y es conocida como Radiación de Fondo Cósmico de Microondas (CMB por su nombre en lengua inglesa).

Esta radiación es la luz más antigua del Universo y evidencia fundamental de la teoría del Big Bang. Se trata de una emisión uniforme del tipo cuerpo negro[1] que proviene de todas partes del cielo. Su existencia fue postulada por G. Gamow, R. Alpher y R. Herman en los años 1940, pero no fue hasta 1964 cuando fue accidentalmente descubierta. A. Penzias y R. Wilson estaban realizando una campaña de medidas en los laboratorios Bell, cuando la antena del receptor que estaban utilizando recibía una señal muy débil la

[1] Un cuerpo negro es un objeto ideal que absorbe toda la radiación electromagnética que le llega y que emite un espectro de luz dependiente de su temperatura.

cual no se podía eliminar independientemente de la dirección a la que apuntase dicha antena.

Desde entonces la comunidad científica ha estado muy interesada en la caracterización de dicha señal como principal evidencia del Big Bang. Para ello se han desarrollado diversos instrumentos científicos, basados en receptores en la banda de ondas milimétricas de muy alta sensibilidad. Dichos receptores se llaman radiómetros, y pueden estar desarrollados tanto para misiones espaciales como terrestres. La primera misión espacial dedicada a la medida del CMB fue el Cosmic Background Explorer – COBE en los años 1980, mientras que a principios de los años 2000 sus resultados fueron mejorados por el proyecto Wilkinson Microwave Anisotropy Probe – WMAP. Más recientemente, en el año 2009, la misión PLANCK fue enviada al espacio obteniendo resultados mejorados de las misiones anteriores, generando mapas celestes como el que se muestra en la Fig. 1.

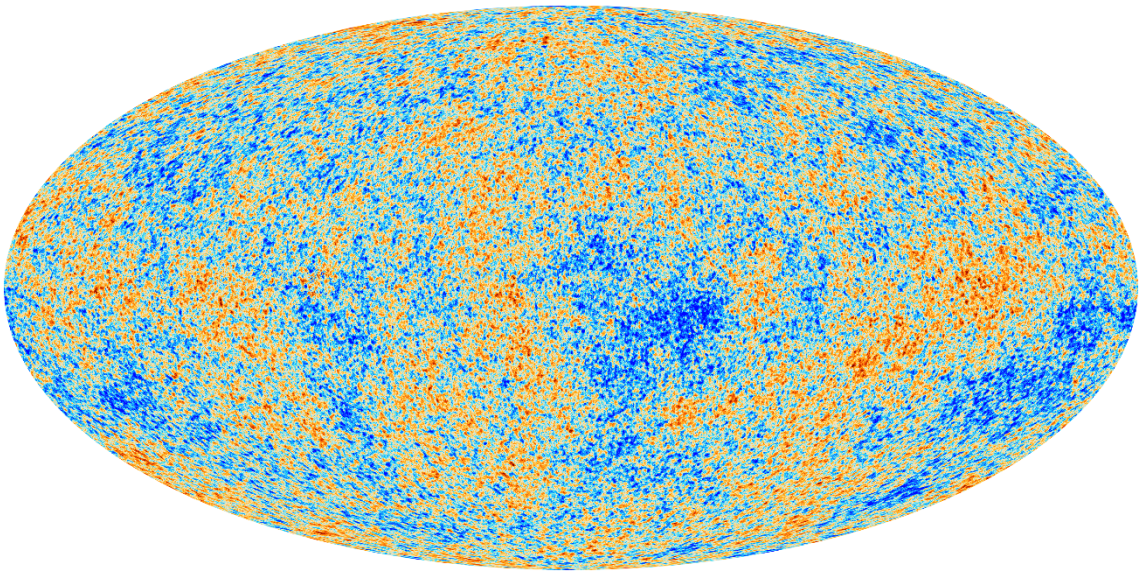

Fig. 1. Imagen del mapa celeste obtenido por el satélite PLANCK después de 15.5 meses de observación. [1.13]

De manera paralela, misiones terrestres se han ido desarrollando para complementar los datos obtenidos por las misiones espaciales. Entre los proyectos de estación terrena desarrollados destacan QUIET y FARADAY.

Dentro de este contexto, el Departamento de Ingeniería de Comunicaciones (DICOM) de la Universidad de Cantabria ha estado involucrado en el desarrollo de este tipo de receptores, colaborando de manera esencial en el diseño, desarrollo e integración de los módulos posteriores del satélite PLANCK en las bandas de 30 y 44 GHz. Durante

los últimos años, y como continuación del trabajo desarrollado, se viene trabajando en un nuevo proyecto basado en estación terrena llamado QUIJOTE. En este proyecto se está caracterizando la polarización del CMB y otras emisiones galácticas y extragalácticas en el rango de frecuencias de 10 a 47 GHz, y complementará a los datos del satélite PLANCK. El DICOM es responsable del desarrollo, caracterización e integración de los receptores en las bandas de 26 a 36 GHz y de 35 a 47 GHz. El esquema que sigue el receptor de la banda de 26 a 36 GHz es el que se muestra en la Fig. 2. Estos receptores combinan la operación a temperatura ambiente (300 K) con partes enfriadas a temperaturas criogénicas (alrededor de 20 K). El motivo de trabajar a temperaturas criogénicas es reducir la temperatura de ruido del sistema permitiendo así alcanzar los niveles de sensibilidad requeridos para ser capaces de medir las señales tan débiles que se espera recibir.

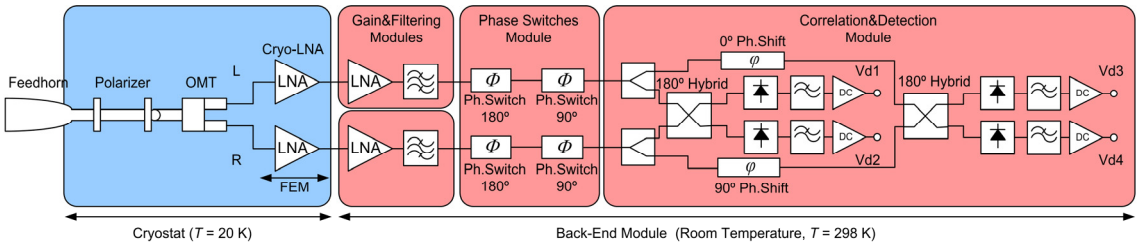

Fig. 2. Esquema del receptor de QUIJOTE que opera en la banda de 26 a 36 GHz.

En este sentido, y dentro del desarrollo de esta tesis, se aborda el diseño e integración del receptor de la banda de 26 a 36 GHz. Inicialmente no estaba definida la temperatura de operación de cada subsistema en el receptor, con lo que el diseño de los circuitos debía cumplir que operase tanto a temperatura ambiente como a temperatura criogénica.

Para el desarrollo del receptor es necesario el diseño de circuitos de microondas de banda ancha, como son conmutadores de fase de 180º y de 90º, así como los detectores. Los circuitos conmutadores deben proporcionar una diferencia de fase plana, de 180º o de 90º respectivamente, en el rango de frecuencias del receptor, a la vez que el desequilibrio de amplitud que presenten entre sus estados conmutados sea lo menor posible. En el caso de los detectores, deben proporcionar la conversión de la potencia de la señal de microondas a niveles de tensión a su salida, para lo que utilizan diodos Schottky.

El diseño de los circuitos descritos anteriormente conlleva el conocimiento de dispositivos discretos para su utilización en los mismos en ambas temperaturas de

funcionamiento posibles. En su caso, los diseños realizados utilizan diodos, bien basados en uniones tipo Schottky o bien en uniones tipo PIN, para conseguir bien la conmutación de fase o bien la detección. Tres tipos de diodos se presentarán en este trabajo: un diodo Schottky de barrera alta MA4E2037, un diodo Schottky 'zero-bias' HSCH-9161 y un diodo PIN HPND-4005. Por lo tanto, la necesidad de conocer dichos dispositivos de manera precisa para la realización de los diseños, deriva en el desarrollo de modelos precisos de los diodos para predecir su funcionamiento tanto en corriente continua como en parámetros de Scattering pequeña señal.

Para el desarrollo de los modelos de los diodos se han implementado dos técnicas de medida TRL ('thru-reflect-line') que permiten caracterizar los dispositivos tanto a temperatura ambiente como a criogénica. La solución que se presenta en la Fig. 3, basada en transiciones de línea coplanar con pasos a masa (CPWG) a microstrip, es la que se ha utilizado para el desarrollo de los modelos, ya que la utilización de los pasos a masa habilita el modelado desde baja frecuencia. La otra opción que se presenta en el Capítulo II de esta tesis está basada en el uso de transición de CPW a microstrip utilizando 'stubs' radiales en los contactos coplanares, que introduce una limitación en frecuencia debido a su banda de operación.

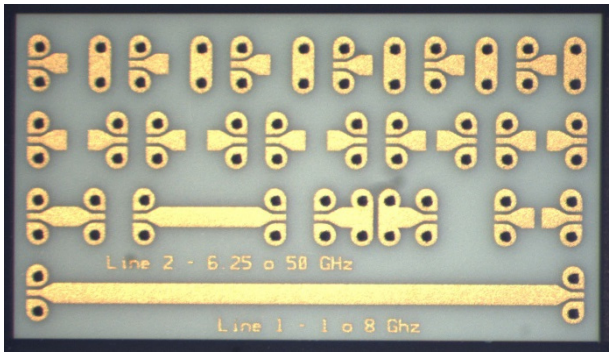

Fig. 3. Kit de calibración CPW-microstrip con pasos a masa desarrollado en sustrato de alúmina de 254-μm de grosor.

A su vez se ha evaluado el impacto que tiene el cambio drástico de la temperatura de operación en los materiales dieléctricos. De esta manera, se han estimado los cambios que se producen en varios substratos utilizados en el diseño de circuitos mediante la técnica del resonador, obteniendo mejoras en las pérdidas que presentan los mismos por trabajar a temperatura criogénica.

Considerando los modelos implementados para los diodos, se han desarrollado los diseños de los conmutadores de fase de 180º y de 90º utilizando tanto diodos PIN HPND-

4005 como diodos Schottky MA4E2037. Se ha desarrollado un análisis pormenorizado de las estructuras utilizadas en ambos circuitos, con el objeto de conseguir la respuesta óptima en sus resultados en diferencia de fase y desequilibrio de amplitud. Ambos circuitos están diseñados para permitir trabajar a temperatura ambiente como a criogénica. Unas fotografías de los circuitos implementados para los conmutadores de fase de 180º y de 90º se muestran en las Fig. 4 y Fig. 5 respectivamente.

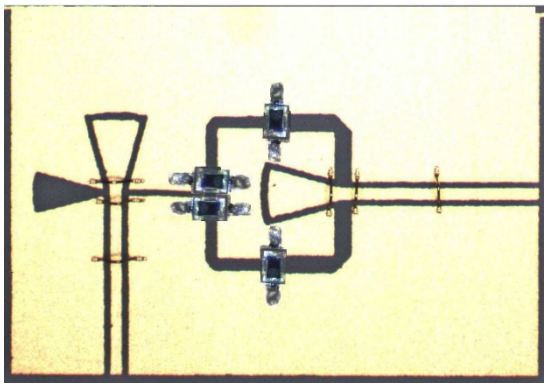

Fig. 4. Conmutador de fase de 180º con diodos PIN HPND-4005 fabricado en sustrato de alúmina de 254-μm de grosor.

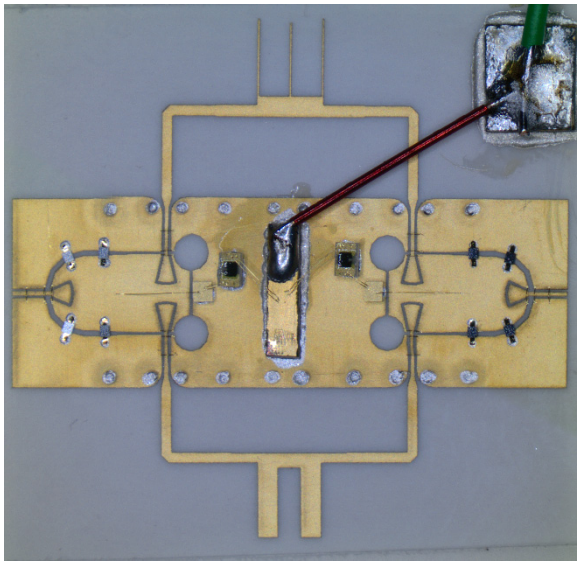

Fig. 5. Conmutador de fase de 90º con diodos Schottky MA4E20374 fabricado en sustrato de alúmina de 254-μm de grosor.

Los resultados de la medida del circuito conmutador de fase de 180º nos proporciona a temperatura ambiente para el caso de diodos PIN una diferencia de fase de 179.2º, con un error aproximado de 1º, con unas pérdidas de inserción aproximadas de 2.1 dB, con un desequilibrio de amplitud de 0.36 dB con pérdidas de retorno mejores de 12 dB en la banda de 26 to 36 GHz con un consumo total de corriente de 40 mA. Por el contrario, cuando se utilizan diodos Schottky se obtiene una diferencia de fase media en

la misma banda de 181.2º, con un error de fase menor de 2º, pérdidas de inserción aproximadas de 1.8 dB, pérdidas de retorno mejores de 9 dB con el mismo consumo de corriente de 40 mA. Cuando se enfría el circuito a 15 K, la medida del circuito con diodos Schottky proporciona una diferencia de fase aproximada de 176º para distintos puntos de polarización del diodo. Cuando se polariza el circuito a 5 mA por diodo, se han medido unas pérdidas de inserción medias de 1.2 dB en la banda de 26 a 36 GHz, lo que supone una reducción de unos 0.6 dB respecto a las pérdidas del circuito a temperatura ambiente con 20 mA por diodo. En el caso de la medida en criogenia del circuito con diodos PIN se ha visto que el comportamiento de este tipo de diodos en criogenia no es apropiado, ya que necesitan una corriente extremadamente alta para trabajar a estas temperaturas y que supondría que la disipación de calor calentaría el sistema criogénico, con lo que no se podría llegar a temperaturas tan bajas.

La medida del circuito conmutador de fase de 90º a temperatura ambiente ha proporcionado para el caso de diodos PIN una diferencia de fase de 87.1º con un error menor de 4.5º en la banda de 26 a 36 GHz con un consumo total de corriente de 80 mA. Por el contrario, cuando se utilizan diodos Schottky se obtiene una diferencia de fase media en la misma banda de 91º, con un error de fase menor de 5º para un consumo total de 80 mA. Tras la experiencia con el circuito conmutador de fase de 180º, la medida en criogenia sólo se ha llevado a cabo con los diodos Schottky, proporcionando una diferencia de fase media en la banda de 26 a 36 GHz de alrededor de 88º, con una mejora en las pérdidas de inserción del circuito por trabajar a 15 K de alrededor de 1.2 dB con una reducción del 80% del consumo de potencia.

En esta tesis también se ha llevado a cabo el diseño y caracterización de un detector a diodo Schottky para su integración en el receptor del instrumento QUIJOTE en la banda de 30 GHz. La solución implementada para el detector está basada en la realización de una red de adaptación para el diodo que cumpla dos funciones: ecualizar la sensibilidad y presentar un nivel mínimo para las pérdidas de retorno en la banda de operación (26 – 36 GHz). Se ha desarrollado el estudio y diseño de una red con líneas de transmisión con pérdidas, implementando como resistencias distribuidas en tecnología 'thin-film'. El circuito finalmente implementado se muestra en la Fig. 6. Con esta solución se consigue una sensibilidad media alrededor de 1066 mV/mW con pérdidas de retorno mejores de 12 dB en su funcionamiento a temperatura ambiente. Cuando el detector es enfriado a una temperatura de 15 K, es necesario polarizar el diodo ya que se ha desplazado la tensión de codo del dispositivo hacia valores superiores, con lo que el funcionamiento en

condiciones de ausencia de polarización no es posible. Para distintos valores de corriente a través del diodo se obtiene un valor de sensibilidad que disminuye a medida que se polariza el diodo a un valor de corriente mayor, así como un incremento en el punto de compresión 1-dB que se mide para el detector.

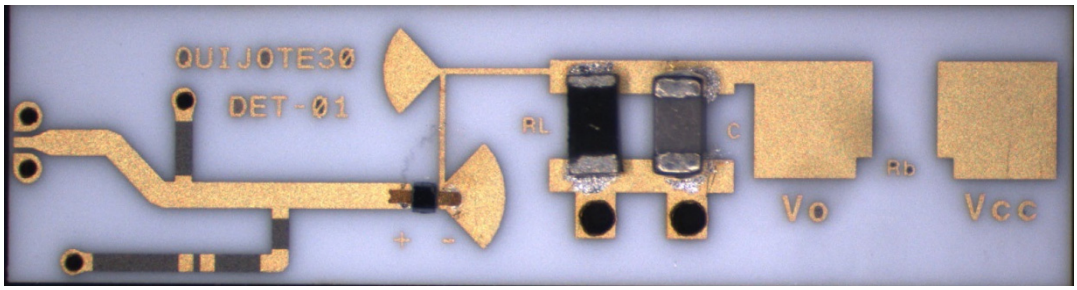

Fig. 6. Detector a diodo Schottky HSCH-9161 fabricado en sustrato de alúmina de 254-μm de grosor.

Como se ha descrito anteriormente, los diferentes circuitos diseñados van a ser empleados en el receptor del instrumento QUIJOTE, cuyo esquema se ha mostrado en la Fig. 2. Se ha realizado el estudio del funcionamiento del sistema, mostrando los diferentes subsistemas diseñados tanto en el grupo de investigación como los desarrollados para esta tesis. Los conmutadores de fase de 180º y de 90º se han montado en un único módulo para su integración en el receptor, como se muestra en la Fig. 7. La integración de los distintos módulos que componen el receptor ha permitido la realización de pruebas de funcionalidad del mismo, que han concluido que el sistema opera de manera apropiada tal como el desarrollo teórico define.

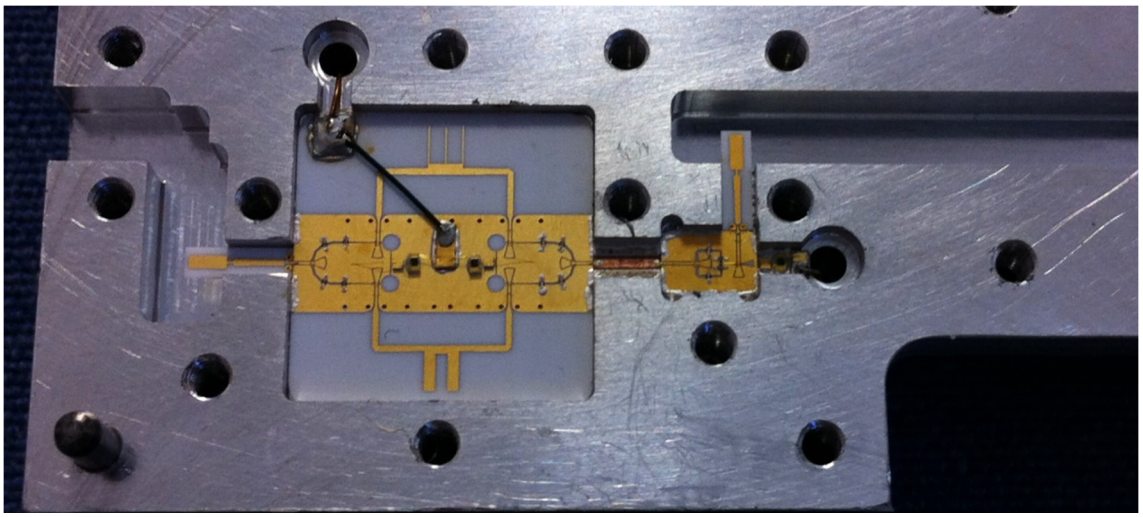

Fig. 7. Conmutadores de fase integrados en un único módulo para su uso en el receptor de QUIJOTE.

Acronyms

ADS: Advanced Design System

GaAs: Gallium Arsenide

BEM: Back-End Module

BPF: Band Pass Filter

cm: Centimetre

CMB: Cosmic Microwave Background

COBE: Cosmic Microwave Background Explorer

CPW: Coplanar Waveguide

CPWG: Grounded Coplanar Waveguide

DAS: Data Acquisition System

dB: Decibel

dBm: Decibel referenced to the power of 1 milliwatt

DC: Direct Current

DUT: Device under test

ENR: Excess Noise Ratio

FEM: Front End Module

GHz: Gigahertz

GSG: Ground Signal Ground

HFI: High Frequency Instrument

Hz: Hertz

IAF: Fraunhofer-Institut für Angewandte Festkörperphysik

K: Kelvin

kHz: kilohertz

LFI: Low Frequency Instrument

LHCP: Left Hand Circular Polarization

LNA: Low Noise Amplifier

LPF: Low Pass Filter

LRM: Line Reflect Match

LRRM: Line Reflect Reflect Match

mA: Milliamp

mHEMT: Metamorphic High Electron Mobility Transistor

MHz: Megahertz

MIC: Microwave Integrated Circuit

mm: Millimetre

MMIC: Monolithic Microwave Integrated Circuit

NF: Noise Figure

Np: Neper

OMT: OrthoMode Transducer

PCB: Printed Circuit Board

pHEMT: Pseudomorphic High Electron Mobility Transistor

QUIET: Q/U Imaging ExperimenT

QUIJOTE: Q-U-I JOint TEnerife

RF: Radiofrequency

RHCP: Right Hand Circular Polarization

SMA: SubMiniature version A

SOLT: Short Open Load Thru

SOLR: Short Open Load Reciprocal Thru

TE: Transverse Electric

TEM: Transverse Electromagnetic

TRL: Thru Reflect Line

WMAP: Wilkinson Microwave Anisotropy Probe

μK: MicroKelvin

μm: Micrometre

Contents

Chapter I

Introduction

1.1. Introduction

The origin of the Universe started with a great explosion, which establishes the moment when everything was created from the nothing. That explosion is called the Big Bang [1.1]-[1.3]. Up to that moment, the matter was an infinite density point, which suddenly exploded and expanded to everywhere creating a homogenous isotropic high-density high-temperature mean, which was continuously in expansion and cooling down. That mean was composed of elementary particles, which were colliding with each other transforming their mass into energy.

The Universe continued its expansion and cooling process, appearing, initially, the electrons and, time after, protons and neutrons. The combination of these particles formed basic atoms nuclei, as helium and hydrogen. Time later, the temperature was low enough that enabled the combination of electrons and nuclei, which caused a radiation, dominated by photons, travelling through the Universe. This radiation is known as the Cosmic Microwave Background (CMB). A timeline of the Universe expansion according this theory is shown in Fig. 1. 1.

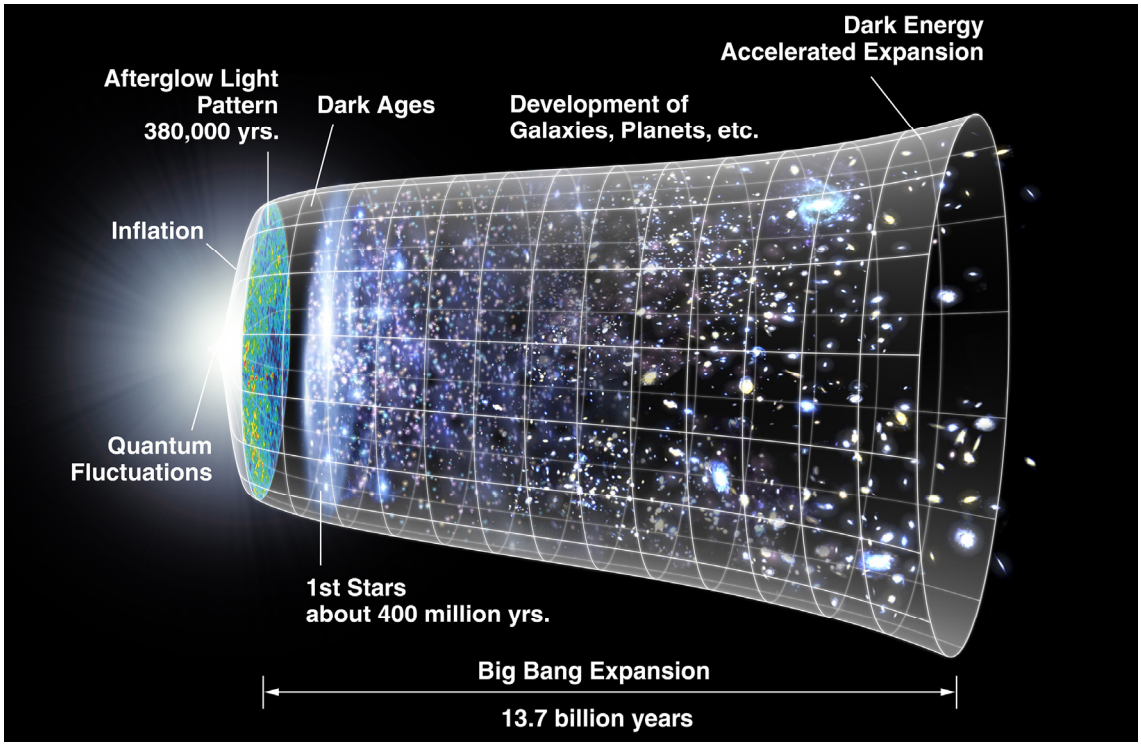

Fig. 1. 1. Timeline of the Universe according to Big Bang Theory [1.3].

The CMB, therefore, is the oldest light in the Universe and crucial for fundamental cosmology as evidence of the Big Bang [1.4]. The CMB radiation is an emission of uniform black body thermal energy coming from all parts of the sky. It is isotropic to roughly one part in 10^5, with variations of only few μK [1.5]. The existence of the CMB radiation was postulated by G. Gamow, R. Alpher and R. Herman in the late 1940s when they were investigating the nucleosynthesis of light elements [1.6]. However, it was first detected in 1964, when A. Penzias and R. Wilson accidentally measured an excess of noise-like signal which could not be removed [1.7]. Since then, the scientific community has been deeply interested in the characterization of the CMB as the main proof of the Big Bang theory through the use of sensitive radio astronomy receivers. Hence, a first space mission dedicated to the analysis of the CMB was the Cosmic Background Explorer (COBE) [1.8] in the late 1980s, which measured the CMB anisotropies and whose results were improved by the Wilkinson Microwave Anisotropy Probe (WMAP) [1.8] in the early 2000s. More recently, the PLANCK mission [1.9] was launched with a wider frequency range and more sensitive receivers than the previous experiments, aimed for imaging temperature and polarization anisotropies of the CMB. Additionally, ground-based missions are being developed and they are intended to complement the data obtained from the satellites and to measure

other CMB parameters. Among ground-based projects, QUIET [1.10] and FARADAY [1.11] have developed sensitive radiometers based on the schemes of previous receivers performing high-quality sky maps.

The observation of WMAP satellite [1.12] returned the sky-map shown in Fig. 1. 2, in which after 9 years of observation the view of the primordial Universe is created. The signal which corresponds to the Milky Way has been subtracted from the data, using the Multi-Frequency Instrument data. As comparison, a view of the Universe seen by PLANCK [1.13] is shown in Fig. 1. 3, with more sensitive receivers than in WMAP.

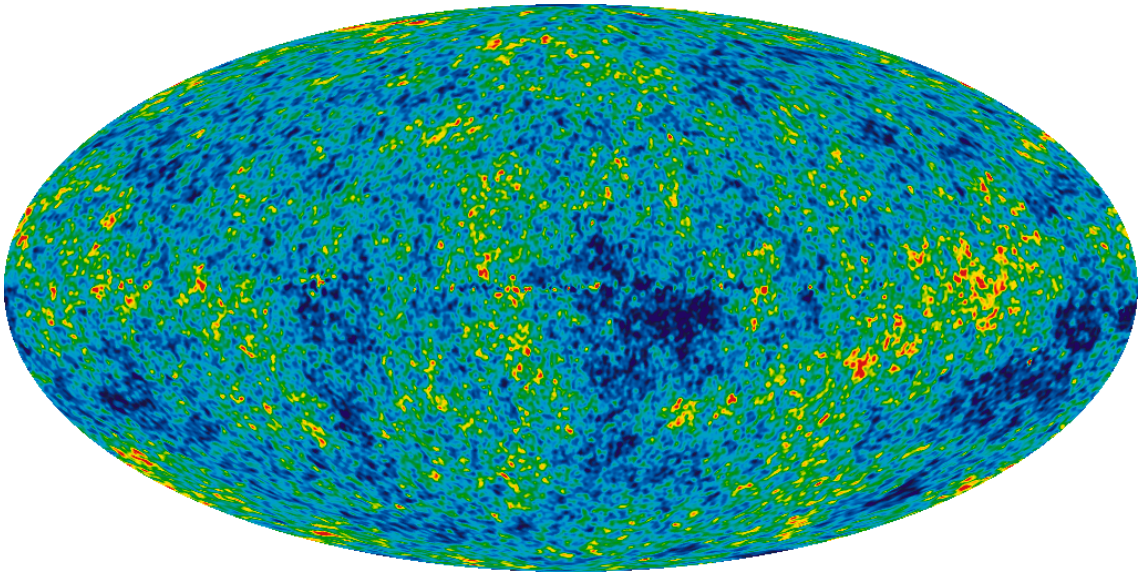

Fig. 1. 2. All-sky picture of the primordial Universe created from nine years of WMAP data [1.12].

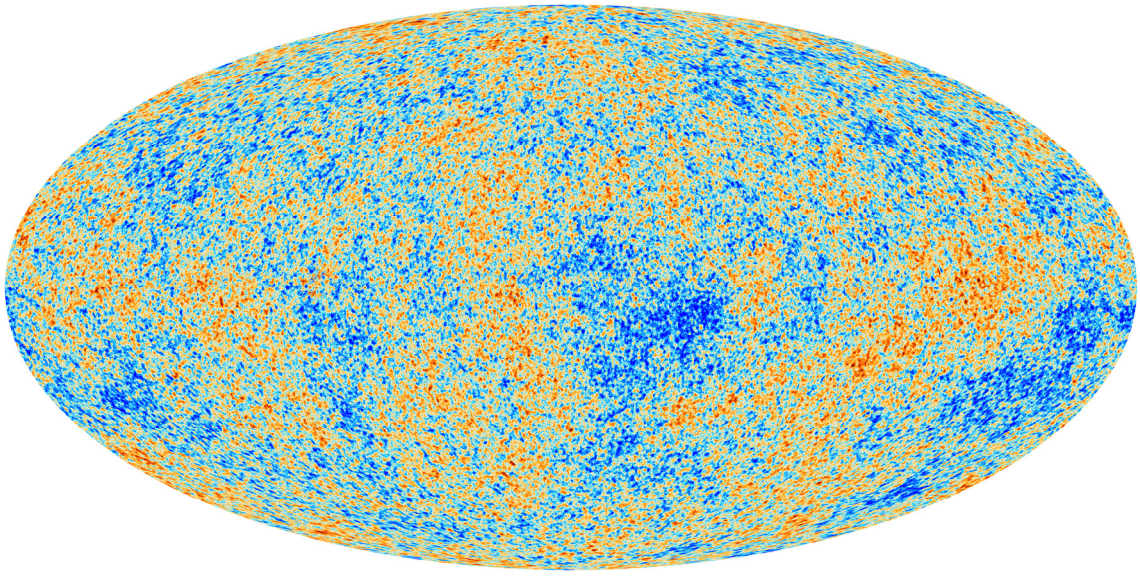

Fig. 1. 3. All-sky picture of the Universe from 15.5 months of PLANCK data [1.13].

1.2. Thesis Motivation

Since the beginning of the PLANCK project [1.13], the Department of 'Ingeniería de Comunicaciones' (DICOM) at University of Cantabria (UC) has been involved in the development of low-noise receivers for radio astronomy applications. In that project, the group was in charge of the design and integration of the Back-End Modules (BEM) of the 30 and 44 GHz receivers for the Low Frequency Instrument (LFI). The PLANCK satellite was launched in 2009 and interesting results are being obtained from its sky scanning.

During the last years, a new radio astronomy project, called QUIJOTE, is being developed which is intended for characterizing the polarization of the CMB and other galactic and extragalactic emissions. Additionally, its observations will complement the data of PLANCK in the frequency range from 10 to 47 GHz. In this new project, the DICOM group is responsible of the design and the integration of the 26 to 36 GHz receiver, from the antenna to the output detected signals.

Typical receiver configurations use part of the subsystems cooled down to cryogenic temperatures, since their effective contributions to the equivalent noise temperature of the receiver are greatly reduced. Therefore, the knowledge of discrete devices and circuits performances under cryogenic conditions is primordial in order to obtain the best performance receiver when different physical temperatures are expected in it.

Besides, the need of minimizing the systematic errors and 1/f noise entails the electrical switching of the signals in the receiver. This is overcome using a multi-state architecture radiometer with the combination of 180º- and 90º-phase switches. Their performance is crucial for the receiver since high phase or amplitude imbalances degrade the full receiver and the engineering and scientific goals would be at risk.

Finally, the extremely low-power level of the incoming signals to a radio astronomy receiver involves the use of high sensitivity detectors able to transform that low-power signals to affordable output signals.

This thesis focuses on the design of broadband circuits to be used in the 26 to 36 GHz QUIJOTE receiver, especially in the phase switches and the detector. Moreover, special attention is paid to the cryogenic behaviour of discrete devices and materials, obtaining small signal models as main source to proceed with successful circuit designs.

1.3. Thesis Structure

This thesis is divided into different chapters dealing with different circuits and subsystems aimed for the development of a radio astronomy receiver. At the beginning of document, in Chapter I, an introduction to the main application field of the circuits described in the following chapters is included.

In Chapter II, the use of dedicated measurement kits is described with the goal of performing the characterization of devices and circuits at quite different physical temperatures (300 K and 12 K). Then, two different kits based on the TRL measurement technique are presented to characterize the behaviour of devices. Besides, a method based on microstrip straight resonators is analysed to estimate the modification that substrates suffer under cryogenic temperatures. The extremely variation in the temperature makes the features of the materials change. Therefore, the knowledge of how they change over temperature is significant to the design of circuits which can operate at both room and cryogenic temperatures.

The previous measurement techniques developed in Chapter II results in the capability of performing the modelling of devices to be used in an accurate design of microwave circuits. Chapter III is focused on the modelling of diodes as a common device in microwave circuitry, especially the Schottky and the PIN diodes. This chapter includes the current-voltage features and small signal models obtained for three different diodes and studies the modifications caused by the effect of extremely low temperatures operation.

Chapter IV shows the design of a new 180º phase switch in the Ka-band based on hybrid technology using the diodes modelled in the previous chapter. A coplanar-waveguide and slotline topologies are used to obtain an out-of-phase signal depending on the bias point of the diodes, which act as selectors of the transmission path. The complete analysis of the phase switch and the characterization of the circuit at room and cryogenic temperatures are described.

The design and characterization of a hybrid technology Ka-band 90º phase switch is presented in Chapter V. The circuit also uses the diodes analysed in Chapter III to perform the phase difference and it is based on a new single-pole double-throw switch configured in coplanar-waveguide and slotline transmission lines. The circuit is thoroughly analysed for two different substrates, based on wideband band-pass filters,

considering π–networks as basic cells. Finally, several circuits are manufactured and tested at both 300 K and 12 K.

Chapter VI is devoted to a Schottky diode square-law detector implemented in microstrip technology. The diode model used in this circuit was described in Chapter III. The circuit uses a new matching network technique based on lossy transmission lines to achieve outstanding results in the Ka-band and to improve available results in the literature. The analysis at cryogenic temperature is also described.

A full radio astronomy receiver working in the Ka-band is presented in the Chapter VII as the final application of the subsystems described in previous chapters. Other subsystems used in the receiver are also detailed. This chapter starts with a short introduction to radio astronomy receiver configurations and, then, the design and characterization of the QUIJOTE polarimeter are shown.

Finally, Chapter VIII exposes the general conclusions obtained along the thesis and it gives the future actions which will be interesting in order to continue with this work.

Chapter II

Measurement Techniques and Substrate Characterization

2.1. Introduction

The design of any circuit implies the knowledge of the individual devices or components which are involved in its development. Normally, circuit design starts with the extraction of the required models, which are obtained from measurements such as Scattering parameters (S-parameters) or DC performance.

Besides, the use of hybrid technologies involves the insertion of devices in any configuration in the circuit, which implies additional interconnections and these are initially not considered. All the effects introduced by these connections are worthy of consideration within the frequency band in which the designs are performed, especially in high frequency bands.

In addition, circuits working under cryogenic conditions makes more challenging the knowledge of devices or material characteristics. The dispersion of material features with the working physical temperature could modify the whole behaviour of the circuit designed giving unexpected results.

This chapter describes S-parameters measurement techniques to characterize circuits or devices in millimetre-wave frequencies, focused on thru-reflect-line calibration technique. Two procedures are described based on the use of groundless and grounded coplanar waveguide-to-microstrip transitions. The chapter concludes with the characterization of three different substrates, used in the circuits designed in later chapters, and their features at room and cryogenic temperatures using the series-gap-coupled straight resonator method.

2.2. Description of the Measurement Technique

To model a single device a set of measurements has to be performed in order to obtain its features under different conditions. In the particular case of S-parameters characterization, all the interconnections and items, which compose the measurement set-up, must be well-known and properly deducted. Therefore, prior to measure the device, a suitable calibration is performed according to the measurement technique.

2.2.1 Overview of Calibration Techniques

The initial approach in order to perform an accurate measurement is the calibration process. The calibration removes the systematic errors of the measurement set-up by the characterization of precise and well-known devices, called *standards*, using a vector network analyzer. This procedure gives back a set of parameters which describes and corrects the set-up features and defines the reference plane in which the device under test (DUT) is characterized through the deembedding of the set-up imperfections [2.1]-[2.3].

The above errors due to the hardware involved in the radiofrequency test system (cables, connectors…) define the time invariant systematic errors. Therefore, the calibration technique is able to correct them. Additionally, random time variant errors are also present in any circuit characterization, which cannot be removed. Finally, drift errors could appear during the tests in case the performance of the subsystems suffers from variations. They can be corrected with a new calibration process.

The available calibration methods are defined by a set of standards. The most common calibration techniques specifying the required standards in each case are summarized in Table 2. 1. These standards are needed to be precisely known in terms of magnitude and phase over the desired frequency range, and are modelled with a defined

factors for their use in the network analyzer in order to correct frequency-dependence effects.

Table 2. 1. Common calibration techniques.

Method	*Standards*
SOLT	Short, Open, Load, Thru
SOLR	Short, Open, Load, Reciprocal Thru
TRL	Thru, Reflect, Line
LRM	Line, Reflect, Match
LRRM	Line, Reflect, Reflect, Match

The SOLT technique [2.1] relies on the definition of the standard features in the same reference plane. This technique brings a better calibration while the standards radiofrequency features are better known. Indeed, this fact can be seen as the main drawback for this method because it needs an accurate model of each element, especially when increasing the operating frequency. Therefore, small deviations in the definition of the standards can cause large errors in the measurement. The physical standards in microstrip technology for this method are depicted in Fig. 2. 1(a). The reference plane is defined by the red dashed line.

The SOLR method [2.1] can be explained as a particular case of the previous one technique, in which an imperfect thru is required, such as a 90º connection. This leads to the need of knowing the offset delay of the thru and it must ensure reciprocal behaviour (S_{21}=S_{12}). Detailed microstrip standards are shown in Fig. 2. 1(b).

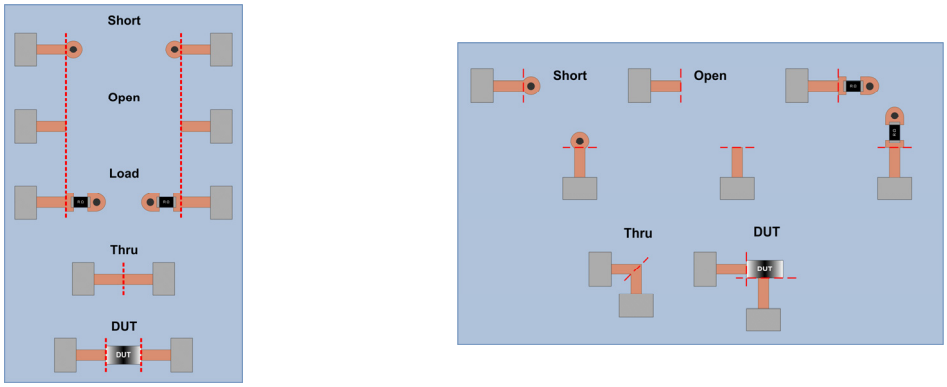

(a) (b)

Fig. 2. 1. SOL-based standards in microstrip technology. (a) SOLT. (b) SOLR.

The TRL method [2.1], [2.4] is a method based on transmission lines standards. This technique sets the reference plane at the thru's midpoint when no offset delay is defined. The DUT must be led by the same length lines of the thru. The reflect standard

can be defined using an open or a short standard, but the sign of its reflection coefficient must be known. The best-defined standard in this technique is the line, as its characteristic impedance sets the reference impedance for the measurement set-up. The use of line standards limits the operation bandwidth of the method. A single line TRL kit works properly over an octave bandwidth, so multi-line kits must be designed in order to cover higher frequency bands. The length of the line standard is a quarter-wavelength larger than the thru, calculated at the centre frequency of the bandwidth. The optimum frequency range covered by a line is defined by the lower and upper limit in which the phase delay between it and the thru is from 20º up to 160º [2.5]. A multi-line TRL kit in microstrip technology and based on two quarter-wavelength lines is shown in Fig. 2. 2. Several variations to the original TRL method have been developed, based on two transmission lines as LRL (line-reflect-line), on the substitution of an attenuator for the line as in TRA (thru-reflect-attenuate) technique, or the TSD (thru-short-delay) method.

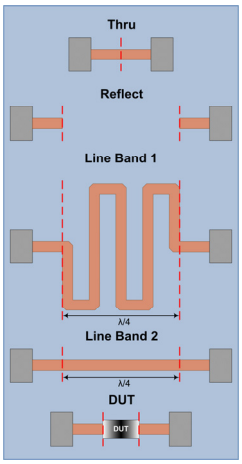

Fig. 2. 2. Multi-line TRL standards.

The LRM method [2.1], [2.6] is a similar method to TRL, but substituting the line for a precision load, which defines the characteristic impedance. The reflect can be defined as either a short or an open. Its definition, in terms of their model as an inductance or a capacitance, respectively, is not needed to be known, because of the use of a well-known load [2.6]. This is an advantage faced to SOLT technique. At the same time, the use and knowledge of the load are their main drawbacks. Additionally, the use of long lines to lead the load can corrupt the match with a parasitic inductance, reducing the accuracy of this method. This method combines the performance of the SOLT at low frequencies and the TRL at high ones, improving their accuracy when well-known

load LRM is performed. A typical LRM kit in microstrip technology is depicted in Fig. 2. 3.

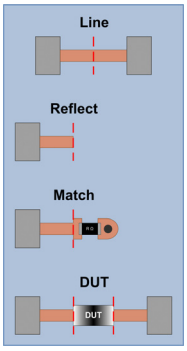

Fig. 2. 3. LRM standards.

The LRRM [2.1] is an improved LRM technique, in which the undesired inductive effect of the match standard in LRM is minimized by using an additional reflect standard. This technique shows the advantage that the reflect standards do not need to be as detailed as in SOLT. The correction of the inductive effect in the match standard is achieved by focusing on the conductance of the open standard, adjusting the calibration coefficients until the open's conductance equals zero. An example of LRRM kit in microstrip technology is shown in Fig. 2. 4.

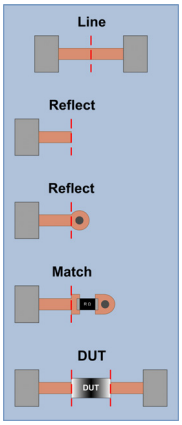

Fig. 2. 4. LRRM standards.

Summarizing, the selection of a proper calibration method is often based on the available or feasible fabrication process. Additionally, the accuracy of each method depends on the frequency band in which the calibration kit is designed. At high frequencies, the TRL technique is preferred when a good line standard definition is possible. Besides, when reliable high quality reflect standards are available, the SOLT technique is preferred at high frequencies.

2.2.2 Measurement Procedure

The characterization of devices can be achieved under different techniques depending on their required parameters. The performance of the circuit to be designed establishes the features of the device to be known, including S-parameters, DC performance or noise figure among others. In particular, the extraction of accurate S-parameters is quite significant while the operating frequency increases, since non predicted effects are not modelled or frequency-dependent anomalous behaviours could appear.

In order to obtain measurements of devices, a coplanar probe station is used [2.7]. So an accurate method in coplanar technology should be developed. Commonly, devices are assembled in microstrip technology due to the ease of its series or shunt insertion in a circuit. Therefore, a coplanar waveguide (CPW) to microstrip solution is implemented in order to characterize the devices in the coplanar probe station at room temperature. Besides, this technique is also useful when a cryogenic probe station is available, but size restrictions should be taken into account.

A brief summary of the calibration techniques described in previous section is listed in Table 2. 2.

Table 2. 2. Calibration techniques summary.

Method	*Advantages*	*Disadvantages*
SOLT	Simple, not-band limited	Very well-defined standards, lower accuracy at high frequencies
SOLR	Not well-defined thru	Accuracy degradation and slightly less definition than SOLT
TRL	Highest accuracy, minimal standard definition	Very good transmission lines, band limited
LRM/LRRM	High accuracy, not band limited	Load definition

According to the above information, the TRL technique is selected because of its ease in the implementation and the well described way to define and design a calibration kit [2.8]. Besides, it provides the highest accuracy. TRL kit solutions are implemented and described in the following sections in order to fulfil with probe station measurements.

2.3. Coplanar Waveguide to Microstrip Calibration Kit

The initial approach is based on the design of conductor backed CPW-to-microstrip transitions, in which via holes are not implemented. The design of this type of transition provides an easier and low-cost fabrication process in a well-defined bandwidth using a compact structure. Besides, the measurement of devices, which do not require any ground connection in their accesses and are implemented in microstrip technology, is simplified for its characterization in a coplanar probe station using this type of transitions.

The conductor backed CPW-to-microstrip kit is designed on a 254-μm thick alumina substrate (ε_r=9.9), with a 3-μm electroplated gold and a dielectric loss tangent tan δ= 1e-4 [2.9]. It is intended to cover the band from 20 to 40 GHz, with special interest in the 26 to 36 GHz.

2.3.1 Conductor Backed Coplanar Waveguide to Microstrip Transition

The development of a calibration kit using two different transmission lines starts with the design of a transition from one type of transmission line (CPW) to the other one (microstrip). Several approaches, [2.10]-[2.15], from CPW to microstrip transitions consider a section of CPW line which is connected to the microstrip line and the backside metallization is partially removed in the CPW section; other designs modify the impedance of the CPW line by changing widths and gaps between CPW side metallizations, which enables the impedance to be matched to the one of the microstrip line.

The design implemented in this work is developed using conductor backed CPW and is based on the use of modified radial stub structures for the side metallizations of the CPW line and a tapered line from CPW to microstrip lines which gradually adapts their impedances. The stub radial structure is shown in Fig. 2. 5. The use of radial stubs in the side metallizations of the CPW line provides a virtual short-circuit in the surface near the centre CPW line and enables the measurement in the coplanar probe station with ground-signal-ground (GSG) type probes. The modification in the typical radial stub shape is caused by the minimization of two factors: the etched material and, furthermore, the distance in order to land the probes. The modified stub radial structure is shown in Fig. 2. 5(b). One of the sloping sides and the upper curve in the radial stub

are converted into straight sides. These modifications do not imply any modification in its electrical behaviour and enable a size minimization of the structure.

(a) (b)

Fig. 2. 5. Stub radial. a) Typical shape. b) Modified structure for the transition.

The new stub is designed with the goal of having a short-circuit at 30 GHz. The frequency band which is covered by the stub depends on its opening angle and its length. An angle of 60º is selected as the initial parameter in order to cover in a more accurate way the band from 20 to 40 GHz. The width of the input line is selected as 185 µm. This value is selected equal to the length of the straight section of CPW line in via-holes commercial adapter substrates [2.16]. The analysis of the stub dimensions is performed with ADS in order to achieve the best length of the stub to tune the frequency band. As preliminary value, in order to start the sweep, the theoretical value of a quarter-wavelength is selected. This value is slightly different due to the electromagnetic simulations and, finally, the length for the stub is fixed to 675 µm. The electromagnetic simulation is performed with Momentum ADS from Agilent and it is shown in Fig. 2. 6. The input reflection coefficient of the modified structure (circle blue line) shows almost the same electrical behaviour than the original radial stub (square red line).

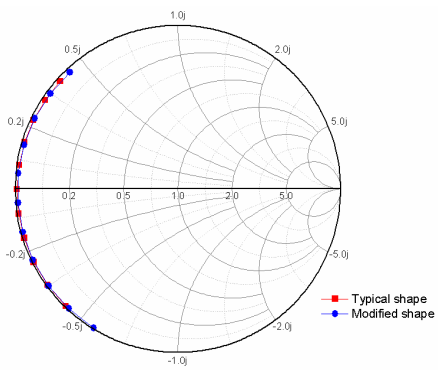

Fig. 2. 6. Input reflection coefficient.

A basic conductor backed CPW line with its design parameters is shown in Fig. 2. 7. The width of centre conductor (W_C) and the gap (g) between it and the side

metallizations are the parameters to fix in order to get a 50 Ω transmission line. Using the tool LineCalc of ADS, these values are easily obtained. An additional consideration must be taken into account about the measurement procedure in order to calculate these parameters. The measurement in a probe station is performed with a well-known pitch probes. The pitch fixes the maximum distance between the midpoint of the CPW centre conductor and the place in which the ground contact of the probe is landed.

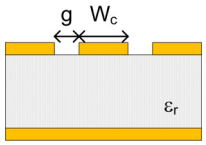

Fig. 2. 7. Conductor backed CPW line.

The GSG probes available to perform the test have a pitch of 150 μm and enable frequency tests up to 67 GHz to be performed. Therefore, a 50 Ω conductor backed CPW line on 0.254-μm alumina substrate is obtained with W_C = 104 μm and g = 60 μm.

Finally, the transition ends with a 50 Ω microstrip line (254 μm width). Hence, a modal match between CPW and microstrip is expected. A gradually solution could be implemented by performing steps in the impedance of CPW sections until fully convert it to a microstrip line [2.12], [2.14]. A tapered solution is used in which the side planes of CPW line are gradually removed and the centre CPW conductor width is also gradually modified with a moderate change in its width. The final design is depicted in Fig. 2. 8. The electrical response, in terms of input and output return loss and insertion loss, of the CPW-to-microstrip transition is depicted in Fig. 2. 9. The simulation is performed using Momentum from ADS, and different simulation ports are used. In the microstrip access, a typical 50 Ω single excitation port is used, while for the CPW access an internal port with two additional 'ground reference' ports referred to the internal one are used in order to emulate the CPW mode.

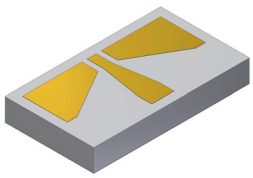

Fig. 2. 8. CPW-to-microstrip transition. Dimensions: 1x1.774x0.254 mm^3.

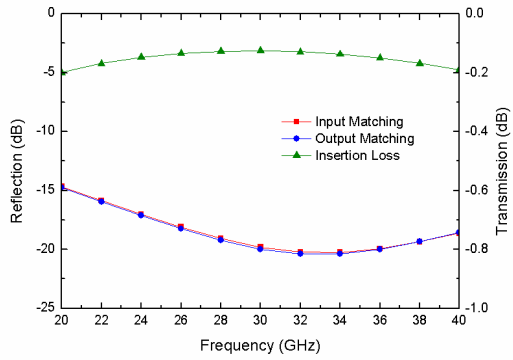

Fig. 2. 9. CPW-to-microstrip transition simulation with Momentum.

2.3.2 Calibration Kit

Once the transition is designed, the calibration kit is defined considering the TRL technique [2.8]. The thru standard is simply based on joining together two of the transitions designed. The operating frequency band of the calibration kit fixes the number of line standards to be used. As the objective band goes from 20 to 40 GHz, an only line kit is designed due to the functionality of a single thru-line pair is useable in a 8:1 bandwidth. The line standard follows the same basis than the thru, but it has an additionally 50 Ω quarter-wavelength microstrip line between both transitions. This extra line is calculated at the centre frequency of the desired band for the kit (30 GHz) and its equivalent delay is 8.36 ps (physical length equal to 0.943 mm) on the alumina substrate. Artistic views of both standards are shown in Fig. 2. 10.

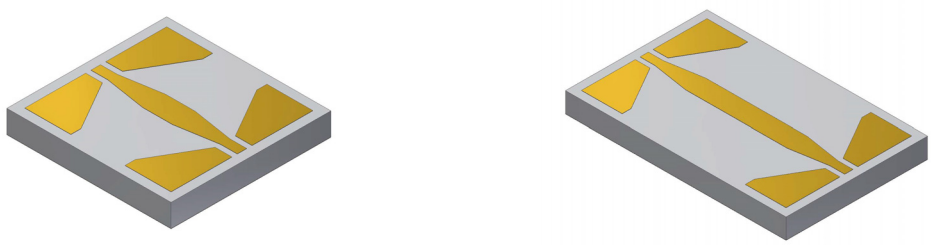

(a) (b)

Fig. 2. 10. Standards of the kit. (a) Thru (Dimensions: 1.823x1.774x0.254 mm^3). (b) Line (Dimensions: 2.766x1.774x0.254 mm^3).

The reflect standard is selected as an open, and it is achieved by directly use the CPW-to-microstrip transition without any transmission load in the microstrip access. In order to perform an open standard for both coplanar probe contacts, two transitions are faced by its microstrip accesses, but with a quarter-wavelength (at 30 GHz) separated between them.

The electromagnetic simulations of the different standards are shown in Fig. 2. 11 and Fig. 2. 12. The return loss and insertion loss of the thru and line standards are analyzed in the whole frequency band, while the open is analyzed by its reflection coefficient and the coupling factor between accesses. The coupling factor between open standards is considered due to the possible radiated signal from one to the other access, which is minimized increasing the distance between them.

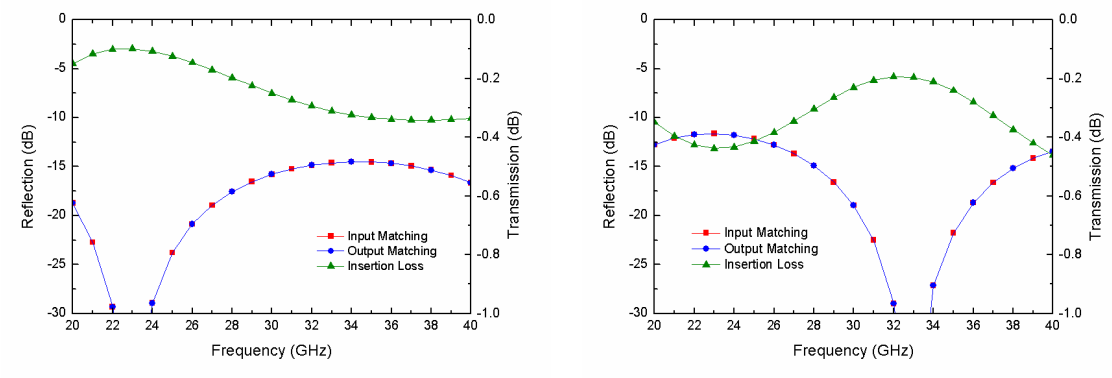

(a) (b)

Fig. 2. 11. Calibration kit standards simulation responses. (a) Thru. (b) Line.

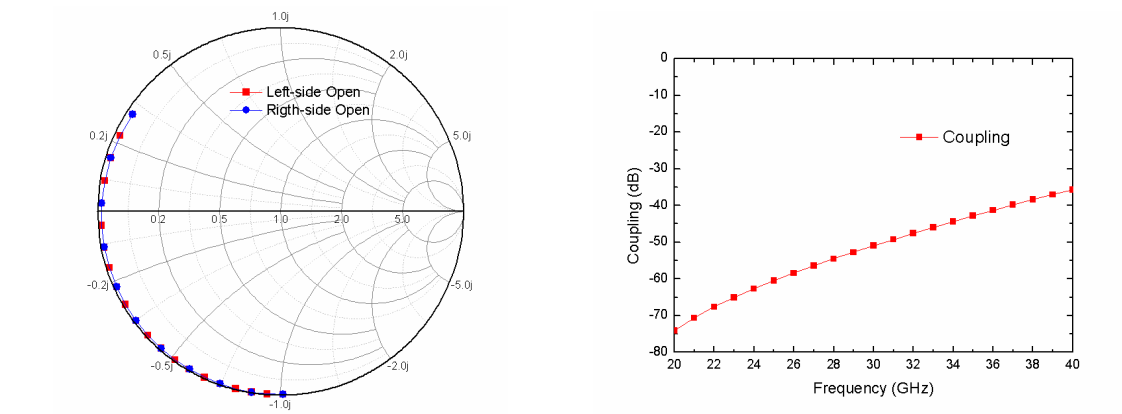

(a) (b)

Fig. 2. 12. Simulation of calibration kit open standard. (a) Reflection coefficient. (b) Coupling.

Fig. 2. 12(a) shows the simulation of open standards for both accesses: the blue curve corresponds to the transition on the left side of the substrate, while the red one to the transition on the right side. Fig. 2. 13 shows the complete calibration kit on alumina substrate, in which looking at standards called R1 or R2, for example, the left- and right-side standards are easily identified.

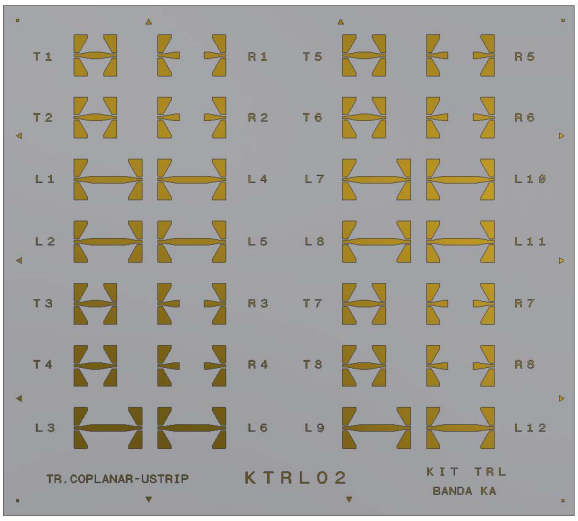

Fig. 2. 13. Artistic view of the CPW-to-microstrip calibration kit. Dimensions: 21.586x19.3x0.254 mm^3.

2.3.3 Device Characterization

The characterization of devices starts with a proper calibration to correct errors in the measurement set-up. Prior to perform a TRL calibration using the kit designed, the characterization of the different standards is done. The measurement set-up includes a vector network analyzer E8364A from Agilent Technologies, a pair of coplanar probes model 67A-GSG-150-C from PicoProbe by GGB Industries and 2.4-mm phase-stable flexible coaxial cables. The calibration for the characterization of the standards is performed with the CS-5 calibration substrate from PicoProbe by GGB Industries.

A calibration substrate with multiple standards is manufactured and is shown in Fig. 2. 14. The results obtained from the S-parameter measurement of the different standards are shown in Fig. 2. 15. These results are representative of the different replicas in the calibration substrate and fit the simulation results, validating the simulation technique.

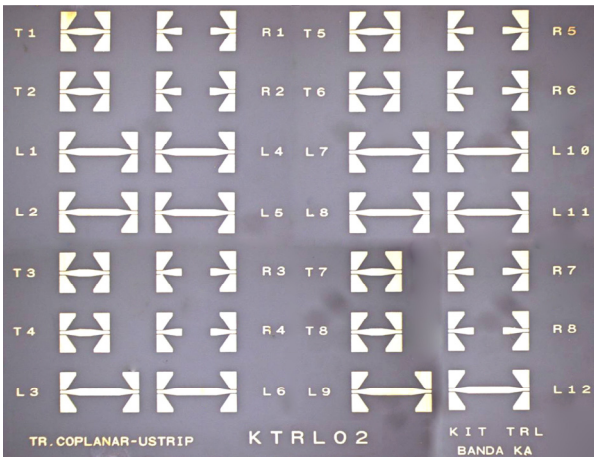

Fig. 2. 14. CPW-to-microstrip calibration kit on alumina substrate.

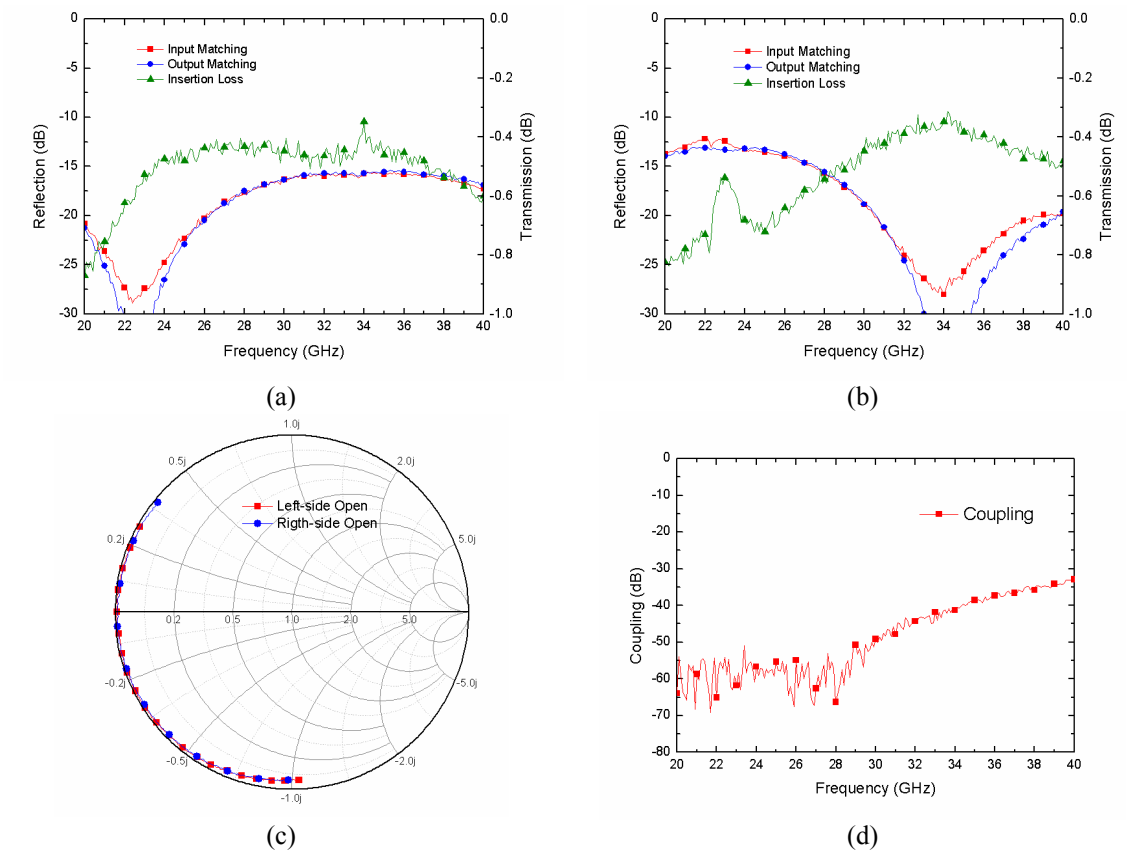

Fig. 2. 15. Measurement of the calibration kit standards. (a) Thru. (b) Line. (c) Open reflection coefficient. (d) Coupling between opens.

The calibration kit is validated using different devices or circuits, which are assembled or implemented with the transition designed. A Schottky diode HSCH-9161, in its obsolete manufacturer version [2.17], is assembled with the transition in short-circuit configuration using a virtual short-circuit tuned in the frequency band with a radial stub. Fig. 2. 16 shows the assembly of the diode with the transitions; additionally, it shows the assembly with commercial CPWG-to-microstrip transitions in series configuration in order of compare the results. The characterization is performed with an input power of -30 dBm in both measurements and the comparison between them is shown in Fig. 2. 17. The green curve is obtained modifying the measurement of the diode in series configuration with commercial transitions. A virtual ground is added in the cathode of the diode. It is performed by the electromagnetic simulation of the radial stub designed for the measurement in Fig. 2. 16(a).

(a) (b)

Fig. 2. 16. Schottky diode HSCH-9161 assembled with transitions. (a) With designed transitions in short-circuit configuration. (b) With commercial transition in series configuration.

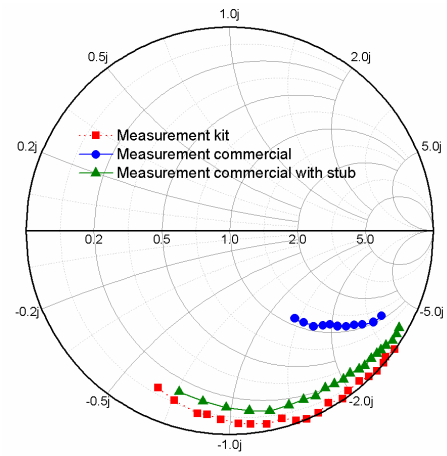

Fig. 2. 17. Schottky diode HSCH-9161 input reflection coefficient characterization for an input power of -30 dBm.

As a second device to be characterized using the transitions, a thin film resistor [2.18]-[2.19] is designed. The alumina substrate available in our facilities has a resistive layer based on nickel-chromium alloy with a resistivity of 20 Ω/square [2.9]. The transitions are positioned at a distance of 393 µm and the width of the resistor is 254 µm. Therefore, the equivalent resistor value is around 30 Ω. Fig. 2. 18 shows the resistor etched on the alumina, and the measurement results compared to the electromagnetic simulations are depicted in Fig. 2. 19.

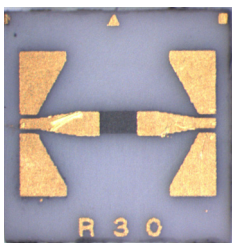

Fig. 2. 18. 30 Ω thin film series resistor.

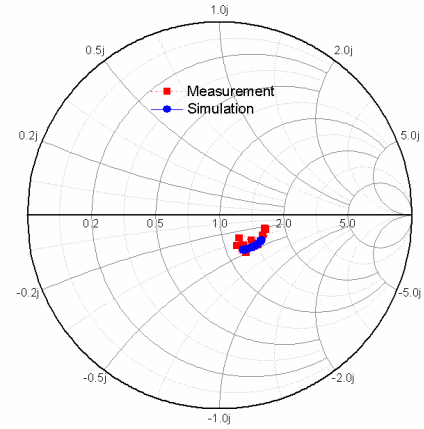

(a)

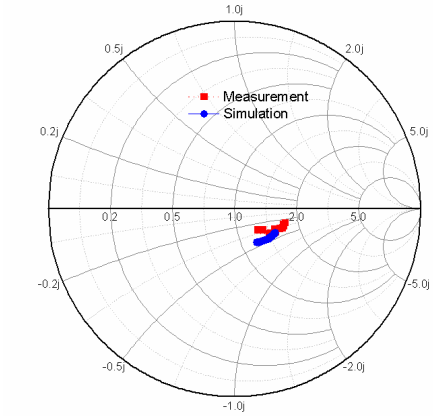

(b)

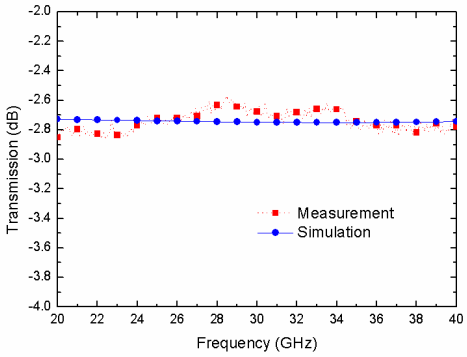

(c)

Fig. 2. 19. Thin film resistor S-parameters characterization and simulation comparison. (a) Input reflection coefficient. (b) Output reflection coefficient. (c) Transmission loss.

Two band-pass filters are designed in order to be integrated in the QUIJOTE receiver. Two prototypes are designed and implemented together the transitions. Working frequency band from 26 to 36 GHz, return loss greater than 10 dB and good out-of-band rejection are their electrical specifications. Once the measurement set-up is calibrated using the kit, the characterization results and the electromagnetic simulations with Momentum are compared in Fig. 2. 22. The measurement results are depicted in dotted line, while the simulation in solid one.

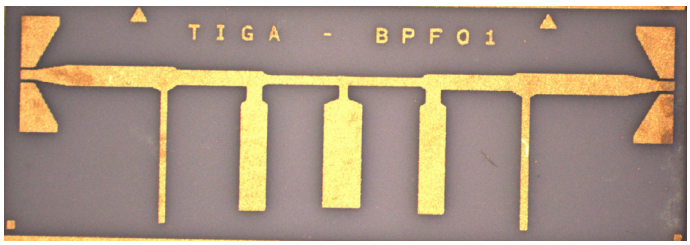

Fig. 2. 20. Band-pass filter BPF01.

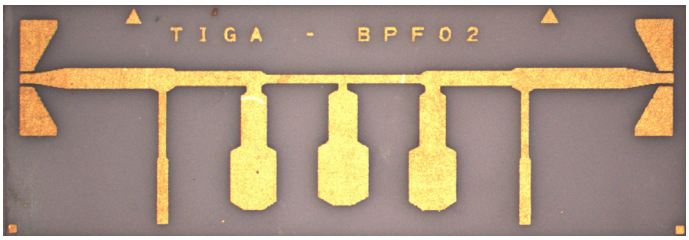

Fig. 2. 21. Band-pass filter BPF02.

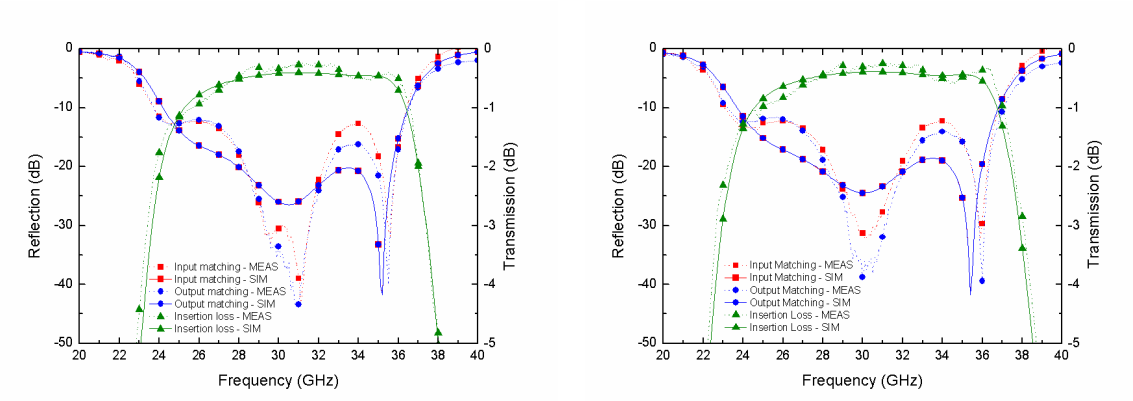

(a) (b)

Fig. 2. 22. Band-pass filter S-parameters measurement and simulation comparison. (a) BPF01. (b) BPF02.

The different solutions implemented on alumina substrate fit the simulation once the calibration is performed with the designed kit. Therefore, the measurement technique using this transition is validated.

2.4. Coplanar Waveguide to Microstrip with Via-holes Calibration Kit

A second approach is used in the characterization of devices in the coplanar probe station, and it is based on the design of CPW-to-microstrip transitions with via-holes. This type of transition increases fabrication tasks and costs due to the need of perforating the substrate. Besides, the fabrication in the same ceramic substrate (alumina) than the other choice implies the use of more specific tools in order to make the holes, such as laser machines.

The CPW-to microstrip with via-holes kit is intended to cover the band from 1 to 50 GHz, so a multiline TRL kit is developed.

2.4.1 Coplanar Waveguide to Microstrip with Via-holes Transition

The previous design in section 2.3 based on transitions without via-holes interconnection shows limitations in the frequency band which is able to cover. Therefore, the characterization of devices under that technique is focused on a well-defined frequency band. On the other hand, when a more general and full-band characterization is desired, the use of a wider frequency band calibration tool is needed.

Thereupon, a transition based on commercial adaptors [2.16], [2.20] is designed. This transition using CPW and microstrip transmission lines with via-holes enables the test of devices or circuits from low to high frequency bands with minor frequency dependence such as the previous transition. The frequency dependence lies on the desired characterization band and the definition of the TRL kit, which implies a multi-line kit to be designed.

The characterization with this choice is performed under room and cryogenics temperatures. Therefore, the parameters of the input CPW line in the transition takes into account both options. The room temperature measurement set-up is composed of the same detailed in previous sections. The cryogenic test bench is based on the use of a cryogenic probe station with 100-µm pitch GSG coplanar probes. Assuming this fact, the 50 Ω CPW line has the width of centre line W_C = 77.5 µm and the gap g = 44 µm (considering the same parameters shown in Fig. 2. 7), while the 50 Ω microstrip width is 254 µm. The side metallizations of the CPW line are designed with round shapes with 150-µm diameter via-holes inside them. Consequently, these side planes of the CPW line are electrically connected to the back metallization of the substrate. Besides, the connection of the CPW and microstrip lines is also performed by a tapered line, in order to match in a gradual mode the electrical fields from the CPW line to the microstrip one. The transition designed is shown in Fig. 2. 23.

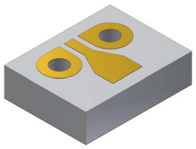

Fig. 2. 23. CPW-to-microstrip with via-holes transition. Dimensions: 0.728x0.945x0.254 mm³.

The transition is simulated using Momentum from ADS. The stimulus in each access, in the CPW line or in microstrip one, are defined as in section 2.3.1. The S-parameters of the simulation are shown in Fig. 2. 24.

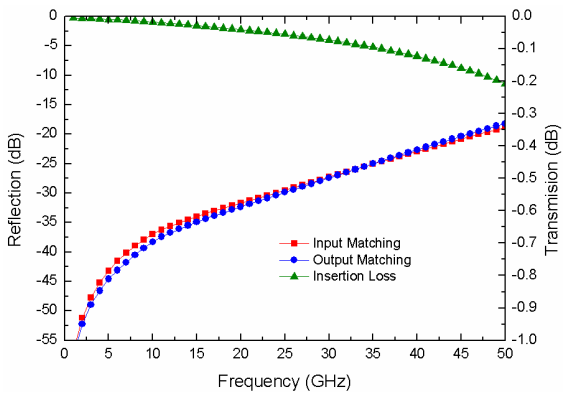

Fig. 2. 24. CPW-to-microstrip with via-holes transition S-parameter response.

2.4.2 Calibration Kit

The lack of available commercial transitions from CPWG-to-microstrip with the appropriate pitch of the coplanar probes used in the cryogenic probe station makes the transitions designed useful for device characterization. Therefore, although commercial calibration kits are feasible to be used inside the cryogenic probe station, a dedicated calibration kit using the transition with via-holes is defined in a TRL technique with the purpose of performing cryogenic characterization.

Besides, the high frequency band which is intended to be covered (from 1 to 50 GHz) makes that the kit needs more than one line standard. As mentioned before, each thru-line covers a maximum 8:1 bandwidth, so two lines are required.

The thru standard is defined as the union of two transitions by their microstrip accesses. The line standard is defined with two different elements: the first one covers the band from 1 to 8 GHz, whereas the second one works from 6.25 up to 50 GHz. The 50 Ω quarter-wavelength extra line is calculated at the centre frequency for each frequency section (4.5 and 28.125 GHz each one), which corresponds to a 55.56 ps delay, 6.375 mm line length in the lower frequency band section (called Line 1 from now on) and 8.9 ps delay, 0.9925 mm line length in the higher one (named Line 2 from now on). The short standard is defined with an additional metallization at the end of the transition in which via-holes are implemented. Artistic views of the standards are shown in Fig. 2. 25. The standards are simulated aided with electromagnetic simulator and their results are depicted in Fig. 2. 26. Their electrical behaviour is analyzed in the whole frequency range from 1 to 50 GHz, although the line standards Line 1 and Line 2 are defined in the calibration kit in a shorter bandwidth. The input and output return loss and insertion loss of the thru and line standards are depicted, while the input reflection coefficient for the short.

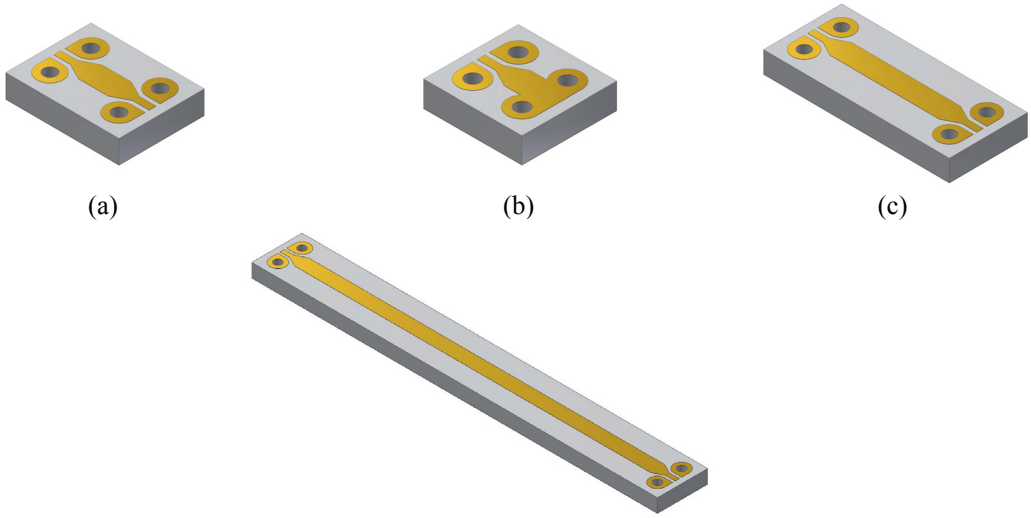

Fig. 2. 25. Standards designed for the CPW-to-microstrip with via-holes calibration kit. (a) Thru (Dimensions: 1.255x0.945x0.254 mm³). (b) Short (Dimensions: 0.981x0.945x0.254 mm³). (c) Line 2 (Dimensions: 2.248x0.945x0.254 mm³). (d) Line 1 (Dimensions: 7.63x0.945x0.254 mm³).

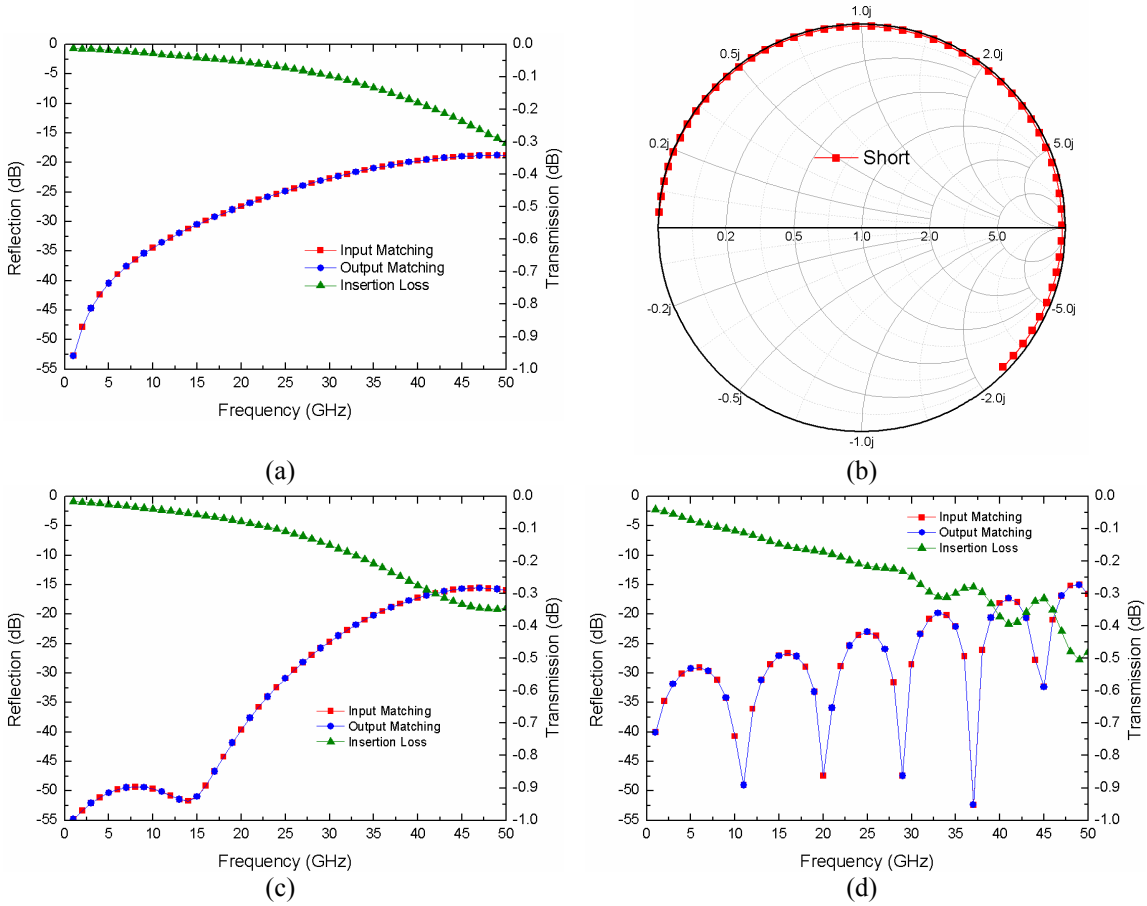

Fig. 2. 26. Electromagnetic simulation response of the different standards of theCPW-to-microstrip kit with via-holes. (a) Thru. (b) Short. (c) Line 2. (d) Line 1.

The complete calibration kit on alumina substrate and different transitions ready for device integration is shown in Fig. 2. 27.

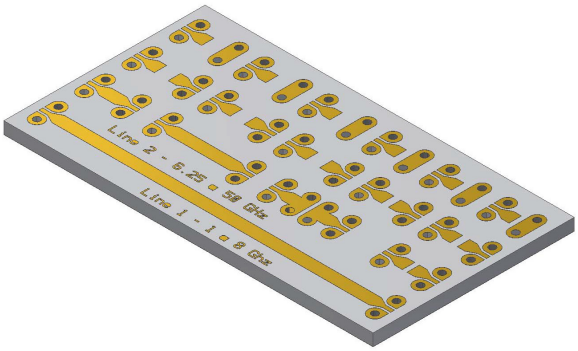

Fig. 2. 27. Artistic view of the CPW-to-microstrip with via-holes calibration kit. Dimensions: 7.8x4.25x0.254 mm³.

2.4.3 Device Characterization

The characterization of devices perform using the transition with via-holes is widely described in Chapter 3, in which different microwave diodes, Schottky and PIN devices, are measured at room and cryogenic temperatures. These measurements enable the devices to be modelled in the band of interest in a wide range of temperature, from room temperature down to cryogenic ones, since the transition is designed with the proper sizes to be used inside a cryogenic probe station.

The characterization of the different standards at room temperature is performed using the same set-up than in section 2.3.3, while the cryogenic measurement is developed in a cryogenic probe station at Fraunhofer-Institut für Angewandte Festkörperphysik (IAF) facilities, in which a pair of 100-µm pitch coplanar probes are used. The calibration substrate is shown in Fig. 2. 28. The substrate contains several transitions prepared to characterize one-port or two-port devices.

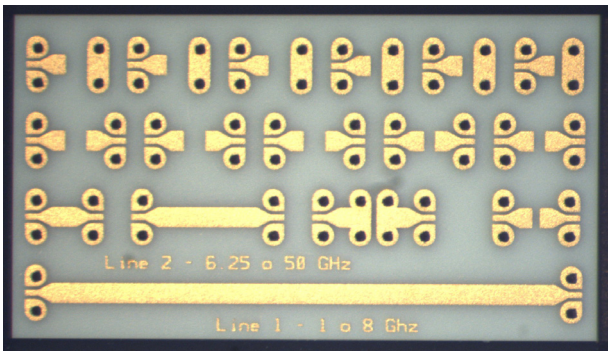

Fig. 2. 28. CPW-to-microstrip with via-holes calibration kit on 254-µm alumina substrate. Row #1 contains transitions for one-port devices; Row #2 transitions for two-port devices; Rows #3 and #4 calibration standards.

The results obtained from the measurement of the different standards at room and cryogenic temperatures are shown in Fig. 2. 29. The cryogenic measurements are performed at a physical temperature of 15 K. The glitches in the cryogenic results are due to difficulty in a correct landing of the coplanar probes in the substrate. As expected, the insertion loss of the different transmission lines is lower under cryogenic conditions than at room temperature, because of the increase in the electrical conductivity of the gold layer in the substrate [2.21]-[2.22] and the reduction of the losses in the substrate [2.23].

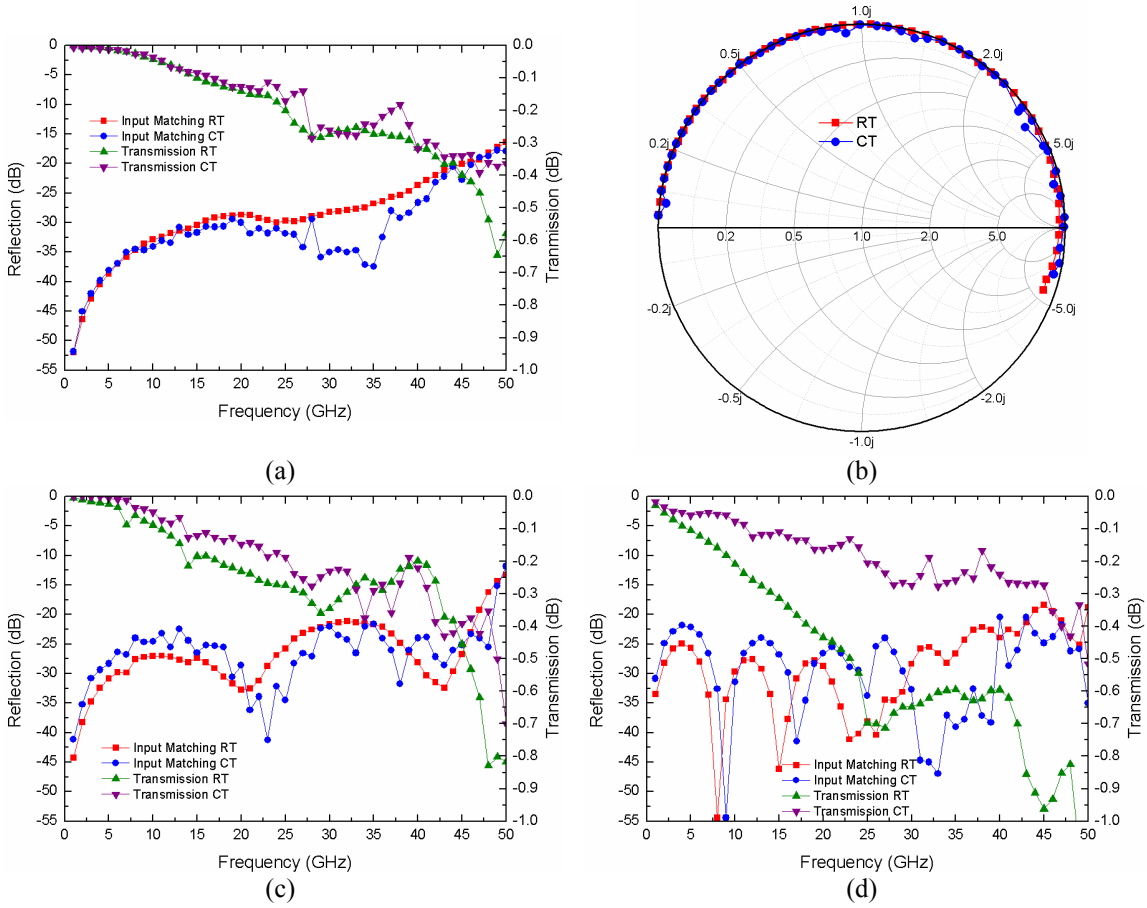

Fig. 2. 29. Characterization of the different standards of the CPW-to-microstrip with via-holes calibration kit at room (RT) and cryogenic temperatures (CT). (a) Thru. (b) Short. (c) Line 2. (d) Line 1.

2.5. Substrate Characterization

A significant issue in order to perform the design of microwave circuits is the knowledge about materials you are going to use. This topic becomes more important when the physical working temperature is under cryogenic conditions [2.24]. Substrate features are usually not specified at cryogenic temperatures, so how the dielectric relative permittivity (ε_r) or losses, among others, change is unknown. In the same way,

the metallization layers over the substrate are modified by the effect of the temperature, achieving electrical conductivity variations for example. Therefore, the performance of a circuit could be significantly different when the physical temperature significantly changes (from 300 K to 15 K).

2.5.1 Measurement Techniques

The experimental characterization of materials is based on indirect measurements of specific parameters of a dielectric substrate, in which a material sample is tested in order to obtain its electrical response. The techniques can be classified into different groups attending a combined classification of the kind of used device and the measured parameters [2.25]: techniques using the reflection and transmission coefficients in a waveguide or transmission line; techniques using the reflection and transmission coefficients in free space; techniques based on impedance bridges; and, finally, techniques based on resonators.

The materials to be characterized in this work are low-loss substrates, such as 254-μm alumina [2.9] or Teflon-based substrates [2.26] in 127-μm and 254-μm thick versions. The substrates are intended to be characterized at room temperature and under cryogenic conditions (15 K). From previous experience with different designs, they show small variations in their features by the fact of working at very low temperatures.

The technique based on resonators is the most appropriate when low-loss materials are under test because it is the most sensitive. Besides, it is the easiest one compared to the use of a cavity or waveguide in the other techniques or the use of large samples. The resonator technique enables the measurement at only one frequency or its resonance modes, but it could be performed in any frequency band. Moreover, it is the most suitable technique for cryogenic characterization, since it makes easier the measurement procedure inside a cryostat than other techniques.

2.5.2 Microstrip Resonator Technique

As the chosen technique for material characterization is based on the design of a resonator, a technology in which the resonator is performed must be defined. In case of a stripline technology, information about the relative dielectric permittivity is directly obtained from resonant frequency; when CPW or microstrip lines are used, the effective dielectric permittivity is measured. Nevertheless, the easiness of design and test procedure in these both last cases makes more suitable for the extraction of an

estimation of the material features. Moreover, microstrip technology is implemented and, afterwards, assembled in a chassis in an easier way than CPW. Therefore, microstrip technology is chosen for the resonator designs.

The use of microstrip resonator has been widely analyzed [2.27]-[2.29], in different configurations, such as ring resonator, straight one with unique gap or with double gap coupling. The resonator is composed of a half-wavelength, or an integer multiple of it, transmission line, as expressed by

$$L = n \cdot \frac{\lambda_g}{2} \tag{2.1}$$

where L is the physical length of the resonator, n is the multiple factor and λ_g is the wavelength at the resonant frequency.

Analyzing the microstrip resonator, its electrical features can be extracted. Its main characteristic parameters are the resonant frequency f_r and the quality factor Q. The wavelength at the resonant frequency is calculated as

$$\lambda_g = \frac{c}{f_r \cdot \sqrt{\varepsilon_{eff}}} \tag{2.2}$$

where ε_{eff} is the effective dielectric constant and c is the speed of light in vacuum. Thus, the ε_{eff} is calculated as

$$\varepsilon_{eff} = \left(\frac{n \cdot c}{2 \cdot f_r \cdot L} \right)^2 \tag{2.3}$$

The quality factor gives an estimation of the losses in the full structure, so the attenuation constant α can be obtained. The quality factor is expressed as a three-term equation, which depends on the losses of the conductor strip Q_c, the losses of the dielectric material Q_d and radiation losses Q_r.

$$Q = \left(\frac{1}{Q_c} + \frac{1}{Q_d} + \frac{1}{Q_r} \right)^{-1} \tag{2.4}$$

When low-loss transmission lines are analyzed, the quality factor can be expressed as

$$Q = \frac{\pi}{2 \cdot \alpha \cdot L} \tag{2.5}$$

where α, mentioned above, is the attenuation constant, expressed in Np/m. Converting it into dB/m, the attenuation constant is calculated from Q value as

$$\alpha = 8.686 \cdot \frac{\pi \cdot f_r \cdot \sqrt{\varepsilon_{eff}}}{n \cdot Q \cdot c} \quad (dB / m) \tag{2.6}$$

Using this technique, an estimation of the effective dielectric constant and the losses in the material are achieved, but it is not able to obtain in a precise way the losses of the different material parts.

2.5.3 Microstrip Resonator Design and Characterization

This section describes the resonators designed for the different substrates. In order to ease the characterization, a low-frequency resonant frequency is selected. The stability of the substrate parameters [2.9] while increasing frequency (from 1 MHz to 10 GHz) enables to make this approach. Therefore, the resonant frequency is 4 GHz for all cases. The designs are aided with electromagnetic simulators.

The details of each resonator are explained in the following sections, in which information about the physical configuration for each substrate is given. The straight resonators are designed using 50 Ω half-wavelength microstrip line ending in an open-circuit at both accesses. The resonance effect is coupled by microstrip gaps, whose widths are fixed in order to have a loose coupling. The gap width is a significant parameter, since if its value is too wide the coupling is not noticeable so the resonant behaviour will be not observed. On the other hand, if its value is too narrow, the coupling effect is too high, and the resonator is degraded by the effect of the external loads. Therefore, a maximum value in the transmission S-parameter at the resonant frequency lower than -20 dB is aimed as a design rule. An electromagnetic model of the gap is used for the design, aided with Momentum simulator.

A specific aluminium chassis involving all the resonators is designed, providing SMA connectors as radiofrequency interface. A view of the chassis and the lid is shown in Fig. 2. 30. The chassis includes several threaded holes in order to assure a good thermal link for the cooling down. Its mechanical drawings are included in Annex I. The length of the chassis is fixed by the greater length of the microstrip resonators in the different substrates.

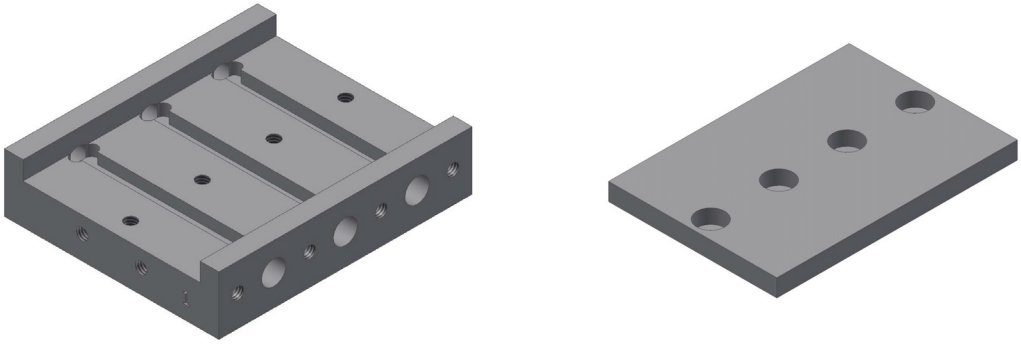

Fig. 2. 30. Artistic view of the chassis designed for the resonators. Dimensions are 42.9x36.34x10 mm^3.

The assembly inside the chassis is shown in Fig. 2. 31, in which the upper circuit is the 254-µm alumina one, the resonator in the middle is on 254-µm thick CLTE-XT and the lower is the 127-µm thick CLTE-XT substrate. The chassis is prepared to have only a pair of connectors at the same time to reduce the physical dimensions of the body. SMA connectors are from Radiall, composed of the receptacle [2.30], a Teflon insulator [2.31] and the pin [2.32].

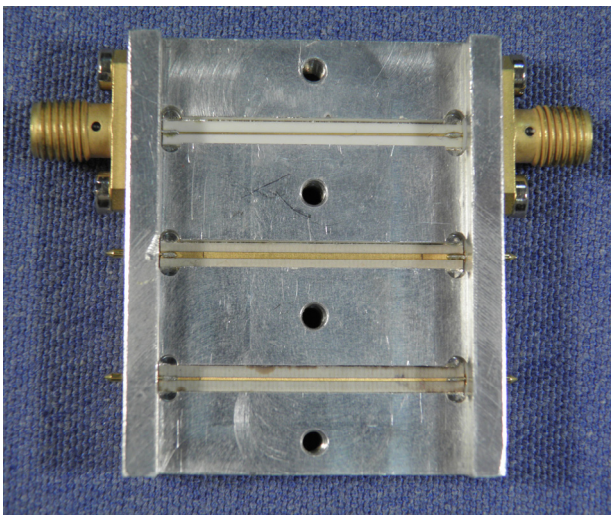

Fig. 2. 31. Assembly of the three resonators inside the chassis.

The characterization is performed in two stages both inside the cryostat: first, the measurement at ambient temperature, and, finally, the cryogenic test. A vector network analyzer E8364A is used for both tests. The assembly inside the cryostat requires some interconnections between the cold base and the device under test in order to reach the lowest temperature. In case the thermal links are not appropriately anchored to the cold base, the thermal gradient between the cold base and the device will be high. This implies that the physical temperature of the device will be quite different from the minimum reachable. Besides, the assembly is composed of semi-rigid and flexible K-

connector cables to connect the chassis with the outside of the cryostat. A view of the assembly inside the cryostat is shown in Fig. 2. 32.

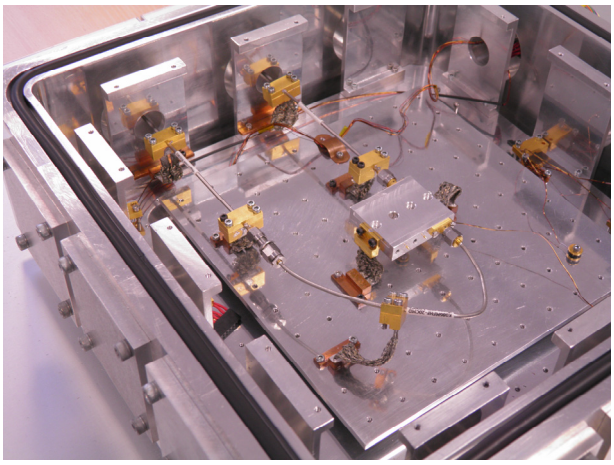

Fig. 2. 32. Assembly of the chassis inside the cryostat.

A 254-μm thick Alumina Substrate

The initial approach for the resonator is the calculus of the half-wavelength at 4 GHz for this substrate with a 50 Ω microstrip line in alumina substrate (width of 250 μm). The information provided by the manufacturer (ε_r= 9.9) is used, and then, adjusted with Momentum in order to have the proper resonant frequency. The gaps are tuned to obtain at room temperature a peak in the transmission Scattering parameter lower than -20 dB at the resonant frequency.

Once adjusted, the parameters for the resonator are the following:

- L_R = 14.3 mm
- gap = 0.03 mm

A limitation in the gap width is observed, since smaller distances of the above mentioned are quite difficult to be manufactured with high resolution in internal facilities. Additional 50 Ω transmission lines are put at the outputs of the resonator in order to fulfil size requirements. A view of the resonator is shown in Fig. 2. 33.

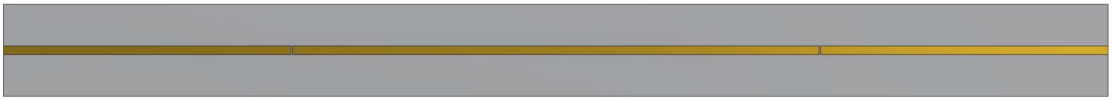

Fig. 2. 33. Artistic view of the 254-μm thick alumina resonator.

The characterization inside the cryostat at room and cryogenic temperature is performed. The thermal cycle reach a temperature of 12 K in the resonator chassis,

measured with a high precision thermal sensor. The measurements of both temperature responses are shown in Fig. 2. 34.

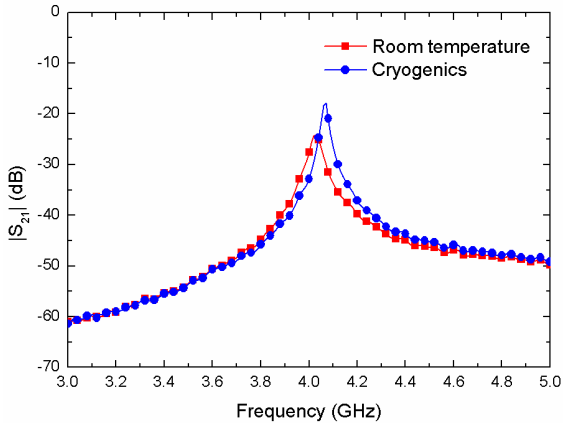

Fig. 2. 34. Measurement of transmission parameter of the alumina microstrip resonator at room (red curve) and cryogenic temperature (blue one).

From the measurements, the calculus of the effective dielectric constant ε_{eff} is done. An approximation to calculate the relative dielectric constant ε_r from ε_{eff} is used [2.33]. The quality factor is calculated from the measurement of the resonant frequency and the 3-dB bandwidth (Δf_{3dB}) in which the power has dropped to the half of the value in the resonant frequency. Both expressions are given by

$$\varepsilon_r = \frac{2\cdot\varepsilon_{eff} - 1 + \dfrac{1}{\sqrt{1+12\cdot\dfrac{h}{W}}}}{1 + \dfrac{1}{\sqrt{1+12\cdot\dfrac{h}{W}}}} \tag{2.7}$$

$$Q = \frac{f_r}{\Delta f_{3dB}} \tag{2.8}$$

where h is the height of the substrate (m) and W the width of the microstrip line (m).

For the cryogenic temperature calculations, the thermal coefficient of expansion α_C is taken into account [2.34]-[2.35]. The material shrinks while the temperature decreases, so the physical length at room temperature is not the same as the length at cryogenic one. The length under cryogenics L_{CT} [2.35] is estimated as given by

$$L_{CT} = L_R + (1+\Delta L) = L_R\cdot(1+\alpha_C\cdot(T_C - T_0)) \tag{2.9}$$

where α_C is the thermal coefficient of expansion (K^{-1}), T_C the cryogenic temperature (K), T_0 the room temperature (K) and L_R the physical length of the resonator at room temperature (mm).

The alumina substrate is composed of gold metallizations as conductive layers. The thermal coefficient of expansion of gold is $\alpha_C = 14.2\text{x}10^{-6}\ K^{-1}$. Therefore, the equivalent length for the 254-µm thick alumina resonator at 12 K is 14.24 mm.

Measured and calculated results for both temperatures are listed in Table 2. 3. The attenuation α at room temperature is 1.796 times higher than the attenuation estimated at cryogenic temperature, so the reduction in losses is significant for the alumina substrate. The dielectric constant modifies its value around 1% of the value estimated at room temperature, considering the figure of merit $\Delta\varepsilon_{eff}$ defined as

$$\Delta\varepsilon_{eff}(\%) = \frac{\left|\varepsilon_{eff\_RT} - \varepsilon_{eff\_CT}\right|}{\varepsilon_{eff\_RT}} \cdot 100 \tag{2.10}$$

Table 2. 3. Estimated electrical features for 254-µm thick alumina substrate at room temperature (300 K) and cryogenic temperature (12 K).

Temperature (K)	*fr* (GHz)	$\lvert S_{21}\rvert$ (dB)	ε_{eff}	ε_r	Δf_{3dB} (GHz)	Q	α (dB/m)
300	4.03	-24.119	6.775	10.056	0.05	80.6	11.838
12	4.07	-17.899	6.696	9.933	0.028	145.357	6.591

B 254-µm thick CLTE-XT Substrate

The initial approach for this resonator follows the same steps than the previous one. The manufacturer provides a dielectric constant ε_r= 2.89. For this substrate, a 50 Ω microstrip line width is 630 µm. Once adjusted with the Momentum tool, the parameters for the resonator are the following:

- L_R = 24.2 mm
- gap = 0.05 mm

A view of the resonator is shown in Fig. 2. 35, with the additional 50 Ω transmission lines in both accesses, and the characterization inside the cryostat at room and cryogenic temperature is shown in Fig. 2. 36.

Fig. 2. 35. Artistic view of the 254-µm thick CLTE-XT resonator.

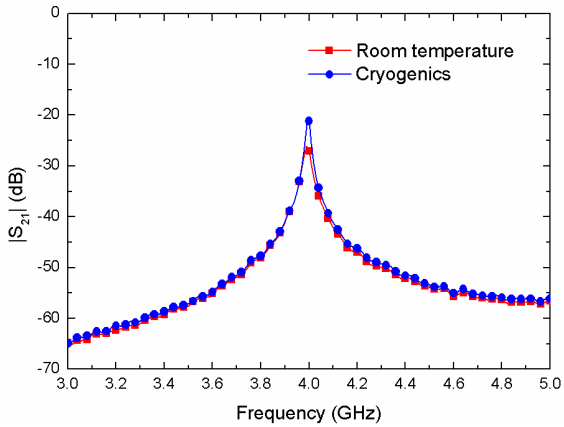

Fig. 2. 36. Measurement of transmission parameter of 254-µm thick CLTE-XT microstrip resonator at room (red curve) and cryogenic temperature (blue one).

From the measured results, the calculations of the different parameters are performed taking into account the equations from (2.7) to (2.10). The CLTE-XT substrate is composed of copper metallizations in both sides of the substrate. The thermal coefficient of expansion of copper is $\alpha_C = 16.6\text{x}10^{-6}\ \text{K}^{-1}$. Therefore, the equivalent length for the 254-µm thick CLTE-XT resonator at 12 K is 24.086 mm.

Measured and calculated results for both temperatures are listed in Table 2. 4. The attenuation α at room temperature is 1.475 times higher than the attenuation estimated at cryogenic temperature, so the reduction in losses is lower than the case in alumina substrate. The dielectric constant modifies its value around 0.5% of the value estimated at room temperature.

Table 2. 4. Estimated electrical features for 254-µm CLTE-XT substrate at room temperature (300 K) and cryogenic temperature (12 K).

Temperature (K)	*fr* (GHz)	$\|S_{21}\|$ (dB)	ε_{eff}	ε_r	Δf_{3dB} (GHz)	Q	α (dB/m)
300	3.99	-26.043	2.413	2.999	0.034	117.353	4.804
12	4	-21.181	2.424	3.014	0.023	173.913	3.257

C 127-µm thick CLTE-XT Substrate

The initial approach for this resonator follows the same steps than the previous one, with a dielectric constant $\varepsilon_r = 2.79$ from manufacturer and 300 µm for a 50 Ω microstrip line. Once adjusted with the Momentum tool, the parameters for the resonator are the following:

- $L_R = 24.2$ mm
- gap = 0.05 mm

An artistic view of the resonator is shown in Fig. 2. 37 and the results of the measurements in Fig. 2. 38.

Fig. 2. 37. Artistic view of the 127-µm thick CLTE-XT resonator.

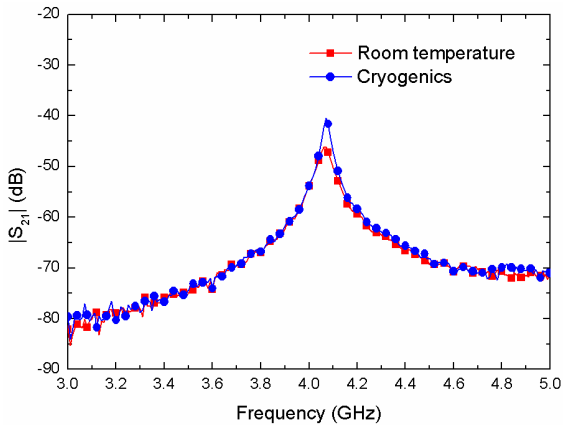

Fig. 2. 38. Measurement of transmission parameter of 127-µm thick CLTE-XT microstrip resonator at room (red curve) and cryogenic temperature (blue one).

Applying the thermal coefficient of expansion of copper, the equivalent length for the 127-µm thick substrate at 12 K is 24.086 mm.

Measured and calculated results for both temperatures are listed in Table 2. 5. The attenuation α at room temperature is 1.797 times higher than the attenuation estimated at cryogenic temperature, so there is a significant reduction in losses. The dielectric constant modifies its value around 1% of the value estimated at room temperature.

Table 2. 5. Estimated electrical features for 127-μm CLTE-XT substrate at room temperature (300 K) and cryogenic temperature (12 K).

Temperature (K)	*fr* (GHz)	$\|S_{21}\|$ (dB)	ε_{eff}	ε_r	Δf_{3dB} (GHz)	Q	α (dB/m)
300	4.07	-46.121	2.319	2.877	0.056	117.353	7.757
12	4.07	-40.431	2.341	2.909	0.031	173.913	4.315

2.6. Conclusions

This chapter has described two measurement techniques based on the development of a TRL calibration kit to perform tests in a coplanar probe station. Additionally, the characterization of dielectric substrates under different physical temperatures has been fulfilled using the straight resonator technique.

A home-made calibration kit has been designed based on the use of CPW-to-microstrip transition without via-holes. The characterization of devices or circuits using this transition has been successfully demonstrated, since the effect of the transitions is properly defined and discounted in the calibration process. Moreover, the characterization of devices using this kit has been validated when a low-cost and easy implementation solution is needed at room temperature, although the kit is also useful at cryogenic temperatures.

The limitation in the covered frequency band of the via-holes-less transitions due to the use of virtual grounds makes that a new transition and kit have been developed. A transition from CPWG-to-microstrip transition with via-holes and a multi-line calibration kit have been designed. The extension in the frequency band covered by this new kit was obtained by the use of an additional line standard. This approach was not feasible with the other kit. Besides, the development of the kit has been also motivated due to the specific cryogenic measurement set-up not fully compatible with commercial available solutions. This transition and kit has been measured at room temperature and under cryogenic temperature in order to characterize their behaviour. A reduction in losses at cryogenic temperatures has been obtained in the different tests, as it is expected when the working temperature is radically reduced up to a few Kelvins. The characterization of the standards of the kit with via-holes at different physical temperatures has been presented. At last, this kit has been performed for a low-

frequency to high-frequency bands analysis is aimed and, specially, under cryogenic temperatures in a concrete measurement set-up.

Finally, the characterization of substrate features using the straight resonator technique has been described. Three different substrates have been analyzed at room and cryogenic temperatures. The results obtained from the tests only depict an estimation of what happens when the working physical temperature has been radically modified. It has been proved that the three substrates have slight variations in the relative dielectric constant which confirms the temperature stability of the material. Besides, a significant reduction in the total losses has been obtained. The 254-μm alumina substrate and the 127-μm CLTE-XT substrate have reduced their losses at cryogenic temperature almost to the half value to the measured at room temperature, while the reduction in the 254-μm CLTE-XT substrate is lower than the two previous substrates, but with lower nominal losses.

Chapter III

Diode Modelling over Temperature

3.1. Introduction

The microwave circuits which are going to be described in the following chapters use diodes as main discrete devices in order to achieve the desired performance. Therefore, their behaviour, in terms of radiofrequency and DC responses, under quite different conditions or in extreme physical temperatures, such as working at around 15 K, must be known or predicted as a reliable source in order to foresee the response. Furthermore, the feasibility of working at a different physical temperature makes more challenging the knowledge of their behaviour when cryogenic conditions are achieved. Therefore, the proper design of circuits in a wide temperature range partially depends on the knowledge of the device when such extreme temperature conditions are involved, since the behaviour of the devices can severely change.

Under this arrangement, the behaviour of diodes changes with the physical temperature, and the information provided by manufacturers is not complete enough, especially under cryogenic conditions. Thus, the performance of a circuit under design could not be confident predicted when cooled down measurements are expected.

Therefore, this chapter describes the modelling of microwave diodes in order to have an accurate model to design microwave circuits. The modelling is performed at room (300 K) and cryogenic (15 K) temperatures. The cryogenic behaviour of devices is modelled when a physical temperature of 15 K is reached. Three types of diodes are presented and modelled: a Schottky diode model MA4E2037 from MACOM [3.1], a zero-bias Schottky diode model HSCH-9161 from Avago technologies [3.2] and a PIN diode model HPND-4005 from Agilent Technologies [3.3].

3.2. Diode Basics

The diodes under analysis are Schottky and PIN structures. In this section, a brief basic description of the different diode structures is described, in terms of the type of elements that are joined in each device.

3.2.1 Schottky Diode

The physical contact of materials with different band structures results on a hetero-junction. In the specific case of a metal-semiconductor contact, two types of junctions can be originated depending on the semiconductor doping level: ohmic contacts or Schottky junction [3.4]-[3.6].

The Schottky junction is based on a metal-semiconductor contact in which a rectification mechanism is formed. Fig. 3. 1 shows the basic structure of a metal-semiconductor contact. In the late thirties of the 20th century, Walter Schottky suggested that this rectifying phenomenon comes from the existence of a potential barrier because of a stable space charge in the semiconductor.

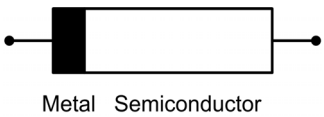

Fig. 3. 1. Structure of a metal-semiconductor junction.

Its working principle is quite similar to the one of a p-n semiconductors junction: a current flow appears due to the difference in the metal and semiconductor charge concentrations. The use of a metal-semiconductor junction instead of a semiconductor-semiconductor one implies that the charge accumulation problems of a p-n junction are avoided and the potential barrier is lower.

Typical metals used for the junction are molybdenum, platinum, chromium, tungsten and some silicon compounds, such as palladium or platinum silicides, while the most featured semiconductors are silicon or gallium arsenide.

Rectification, frequency mixers or square-law detectors are usual applications for Schottky diodes. Their use as varactors is limited by the smaller capacitance range they can provide facing the p-n junctions.

3.2.2 PIN Diode

The PIN diode structure is defined by the connection of a P-doped semiconductor, an N-doped semiconductor and, between them, an intrinsic layer [3.6]-[3.8]. In fact, this layer is slightly doped by P or N impurities, so an ideal intrinsic layer is unachievable. The intrinsic layer modifies the expected behaviour of a p-n junction, since the high amount of stored charge in it. This layer behaves as a variable resistor depending on the bias. The basic layer structure of a PIN junction is shown in Fig. 3. 2.

Fig. 3. 2. Layer structure of a PIN diode.

The PIN structure works as follows: charge carriers from P and N regions flow into the intrinsic layer and the diode conducts current when an equilibrium level between charges is reached (same number of electrons and holes). When an external forward bias is applied, this mechanism is sped up.

The typical semiconductors used for PIN diodes are silicon or gallium arsenide. The PIN diodes are focused in applications such as attenuators, switches, high power handling devices and systems with variable resistance requirements.

3.3. Schottky Diode Modelling

Two Schottky barrier diodes are presented and modelled in this section. A high-barrier level Schottky diode model MA4E2037 from MACOM Technology Solutions [3.1] and a zero-bias low-barrier Schottky diode model HSCH-9161 (new version) from Agilent Technologies [3.2]. Both devices are beam lead gallium arsenide diodes.

The modelling is performed both at room and cryogenic temperatures. The measurements are made using the TRL kit with via-holes described in the previous chapter. The room temperature tests are done in the facilities of the Engineering

Communication Department (DICOM), while the cryogenic ones in the cryogenic probe station at Fraunhofer-Institut für Angewandte Festkörperphysik (IAF) facilities. The radiofrequency measurements are performed using a vector network analyzer PNA E8364A from Agilent Technologies and a HP8510C at room and cryogenic temperatures respectively using coplanar probe stations. The DC features are tested using a semiconductor device parameter analyzer B1500A from Agilent Technologies at DICOM and a semiconductor parameter analyzer model 4155A from Agilent technologies at IAF for cryogenic tests.

3.3.1 MA4E2037

As stated before, one of the Schottky diodes under analysis is a commercial model from MACOM Technologies. The selection of this device meets design requirements of having a low series resistance and low junction capacitance in forward and reverse bias. These requirements are set by the condition of behaving as a good short-circuit or a good open-circuit in millimetre-wave frequencies when forward or reverse bias is applied to the device respectively. Therefore, the application intended for this diode is a microwave switch.

The features obtained from the manufacturer datasheet are listed in Table 3. 1. No information about temperature behaviour, below or above the maximum ratings in the datasheet, is provided, so the cryogenic response of the diode is not known, but a reduction in the equivalent resistance under forward bias is expected. Hence, the need of modelling the device at such extreme temperature conditions in order to predict its performance. Two photographs of the diode are shown in Fig. 3. 3: the top view shows the diode body, while the bottom view shows a detail through a microscope image of the Schottky contact.

Table 3. 1. Datasheet features for the diode MA4E2037 at room temperature.

Parameter	*Typical Values (300 K)*
C_j – Junction Capacitance	0.02 pF
R_s – Series Resistance	4 Ω
V_f – Forward Voltage	0.7 V
V_{br} – Reverse Breakdown Voltage	7 V

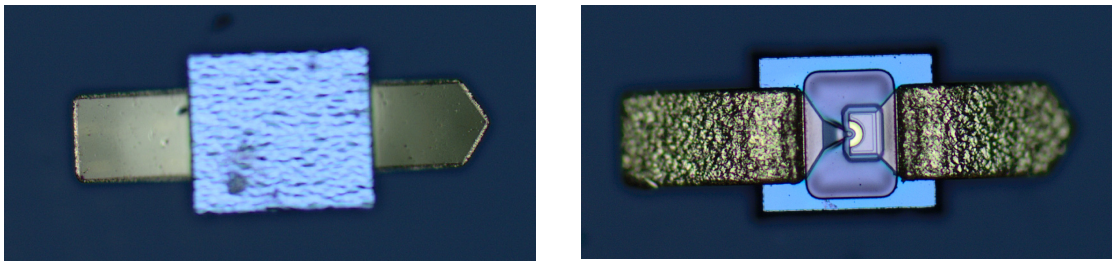

(a) (b)

Fig. 3. 3. Photograph of the Schottky diode MA4E2037. (a) Top view. (b) Bottom view.

A Model extraction procedure

Schottky diodes have been widely analyzed in order to be modelled [3.9]-[3.22], based on different approaches and techniques. The model presented here comprises of DC and radiofrequency behaviours to adjust the response in a more accurate way. Besides, the model is performed under cryogenic conditions, which is a challenging issue due to the complexity of understanding how a device modifies its behaviour. The literature describes some cryogenic approaches for the current-voltage (I-V) feature, such as considering a semi-analytical model [3.9] or based on capacitance-voltage (C-V) measurements [3.10]. Other techniques use models based on Norde's function [3-11], which calculates the series resistance and barrier height.

The modelling of the diode is performed following different steps. This procedure is used for both physical temperatures. First of all, the diode is characterized, performing DC I-V feature and radiofrequency tests. After that, an initial fitting of the I-V curve is done in order to obtain basic parameters of the diode through the use of the Schottky diode law [3.23]. This equation can be expressed in terms of the voltage in the diode junction if the series equivalent resistance R_S of the diode is considered and introduced on it, and is given by

$$I = I_S \cdot \left(e^{\left(\frac{q \cdot (V_C - I \cdot R_S)}{n \cdot k \cdot T} \right)} - 1 \right) \tag{3.1}$$

where I_S is the saturation current (A), V_C is the applied voltage in the diode (V), n the ideality factor, R_S is the series resistance of the diode (Ω), k the Boltzmann constant ($1.38 \cdot 10^{-23}$ J/K), q the electron charge ($1.6 \cdot 10^{-19}$ C) and T the physical absolute temperature (K).

Using equation (3.1), the I-V fitting returns n, R_S and I_S parameters of the diode. In order to obtain the values of n and I_S, a linear section of the curve is chosen and fitted by a first order linear polynomial, taking logarithmic scales in the values. The linear

region of the curve is observed when small forward bias is applied, so the exponential value in equation (3.1) is very large compared to the subtracted '1', which can be omitted. Therefore, the approximation is given by

$$\log(I) = a \cdot V + b \tag{3.2}$$

where $a = q/(n \cdot k \cdot T)$ and $b = \log(I_S)$. The series resistance Rs is negligible in the linear region, and it is adjusted in the non-linear region of the I-V curve. As initial approach, R_S is considered as a constant value.

Afterwards, radiofrequency performance in terms of small signal Scattering parameters is modelled in a frequency range using the three parameters (n, I_S and R_S) obtained in the I-V fitting for the Schottky diode. Besides, the Schottky junction is modelled as a shunt circuit composed of a capacitance and a resistance. The electrical sketch used for the model is shown in Fig. 3. 4. The model includes parasitic elements (L_{S1} and C_P) in order to take into account the effects of the contacts of the device.

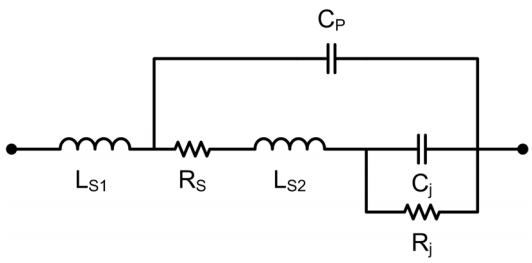

Fig. 3. 4. Small signal model for MA4E2037 Schottky diode.

The model of the Schottky junction, as stated before, is performed with a shunt circuit composed of a capacitance C_j, which models the junction capacitance, and a resistance R_j, which models the junction resistance. The preliminary value of the C_j is obtained from the datasheet, while the value of the R_j [3.24] is given by

$$R_j = \frac{n \cdot k \cdot T}{q} \cdot \frac{1}{(I_{bias} + I_S)} \tag{3.3}$$

since a small signal behaviour is modelled because there is not rectification current in the diode due to the application to radio astronomy receivers, in which a very low-power incoming signal is expected, so rectification process in the diode is not achieved.

Using this electrical circuit, the reverse and forward radiofrequency response of the diode can be modelled and fitted, so the values of the different elements are obtained. While the Scattering parameters are trying to be fitted, a new issue arises. The

assumption of having a constant R_S in the whole circuit response cannot be assumed, since under low-bias conditions the Scattering parameters do not fit in an accurate way.

The first approximation in order to solve this issue is to consider a value of the series resistance (R_{S1}) which depends on the bias point. A differential technique depending on voltage and current values is considered [3.19]. This method uses an I-V point (V_{min} and I_{min}) in order to have differential values; these points V_{min} and I_{min} are any I-V coordinate of the linear section in the I-V curve. The expression for the non-constant series resistance is given by

$$R_{S1} = \frac{0.001 \cdot V_{\min}}{I_{bias} + 10^{-30}} - \\ - \frac{1}{I_{bias} + 10^{-30}} \cdot \left[\left(V_d - V_{\min}\right) - \frac{n \cdot k \cdot T}{q} \cdot \left(\ln\left(I_{bias} + 10^{-30}\right) - \ln\left(I_{\min}\right) \right) \right] \quad (3.4)$$

where voltage values are considered in V while currents in A.

Assuming this approximation, the forward bias behaviour of the diode is modelled in a correct way, but when reverse bias is applied a further consideration must be taken. If R_{S1} is the equivalent series resistance of the diode, the equivalent impedance of the diode is not predicted when reverse bias is applied. Therefore, another bias-dependant resistance is considered, given by

$$R_{S2} = R_{SC} \cdot \left(1 + 10^{6} \cdot I_{bias}\right) \quad (3.5)$$

where R_{SC} is the initial constant value (R_S) obtained in the first I-V fitting of the diode. Assuming this equation, when high forward bias is applied to the diode a high value for R_{S2} is obtained, while for reverse bias, with almost negligible current consumption, the value of R_{S2} is close to the R_{SC}. In this equation the value of I_{bias} is in A.

These resistances R_{S1} and R_{S2} are in shunt configuration in order to model the forward and reverse bias conditions, since R_{S1} plays an active role for forward bias, while R_{S2} for reverse conditions. Therefore, the small signal model shown in Fig. 3. 4 is modified and the new considered model is depicted in Fig. 3. 5.

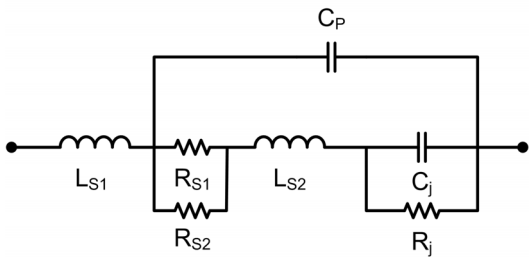

Fig. 3. 5. Modified small signal model for MA4E2037 Schottky diode.

Taking into account this, the fitting of the I-V curve is performed assuming the fact of having a non-constant series resistance.

Therefore, as a summary of the model extraction, it is obtained in two steps:

· First, the I-V curve is fitted. The parameters n and I_S are obtained from the linear region of the curve. The value of the series resistance is obtained assuming a non-constant value with a shunt pair of resistances ($R_{S1}//R_{S2}$) depending on the fitting of the non-linear region of the I-V curve.

· The radiofrequency performance is fitted assuming the values from I-V fitting. Therefore, the I-V fitting defines the small signal model which is used (Fig. 3. 5).

This model is valid at room and cryogenic temperatures, because of the initial approach of calculating the diode parameters (n, I_S and R_S) through the I-V curve and the dependence on the temperature (T) of the diode equation.

B MA4E2037 Model

The measurements are performed both at room and at cryogenic temperatures. A cryogenic temperature sensor is used for the cryogenic test in order to know the physical temperature the device reaches. The physical temperature measured of the diode is 15 K. The measurements are done using the kit presented in the previous chapter based on CPW-to-microstrip transitions with via holes.

The first tests performed are the I-V features. The results obtained for both physical temperatures are shown in Fig. 3. 6. The results show the increase in the knee voltage by the effect of the temperature, due to the increase of the energy bandgap (E_g) while lowering the temperature [3.4], [3.9].

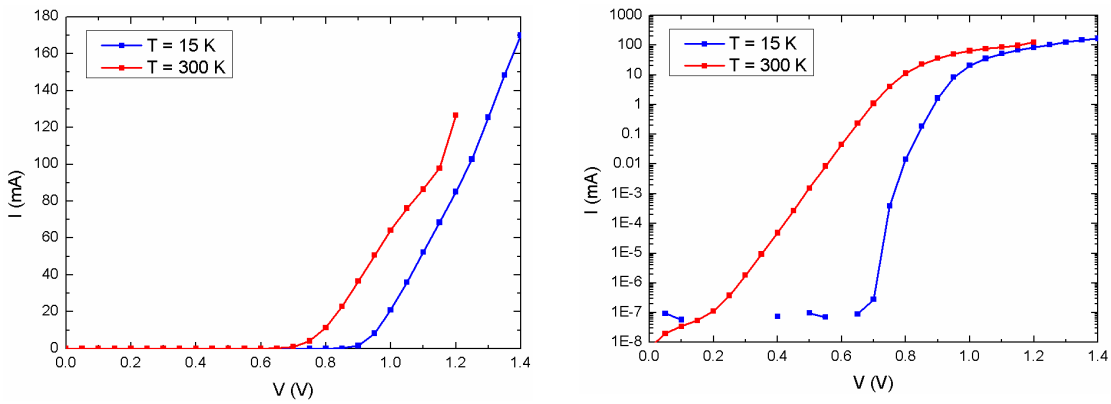

Fig. 3. 6. Measured I-V characteristic at room temperature (red) and at cryogenics (blue). (a) Linear scale. (b) Logarithmic scale.

From these curves, the fitting of the I-V curve is performed using a variable series resistance, composed of a shunt pair R_{S1} and R_{S2}. The results for room and cryogenic temperatures are shown in Fig. 3. 7, where an accurate agreement between the measurement and the model simulation is demonstrated. The values of the resistances R_{S1} and R_{S2} assuming equations (3.4) and (3.5), respectively, and versus the diode voltage are shown in Fig. 3. 8. In the R_{S1} curve, the current measured for low applied voltage to the diode is almost negligible, with values around 10^{-12} A, and the inaccuracy of the measurement set-up makes that some values cannot be calculated.

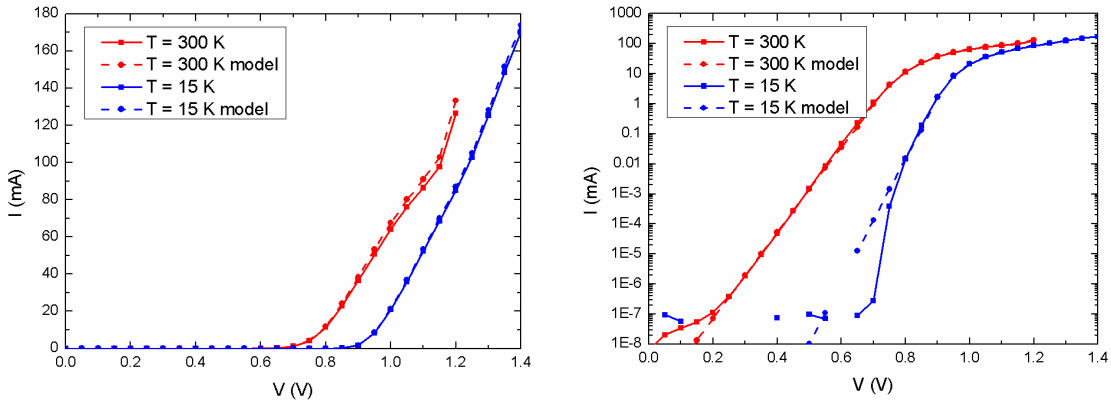

(a) (b)

Fig. 3. 7. Fitting of the I-V characteristic at room temperature (red) and at cryogenics (blue) in dashed lines considering shunt R_{S1}-R_{S2} resistance. (a) Linear scale. (b) Logarithmic scale.

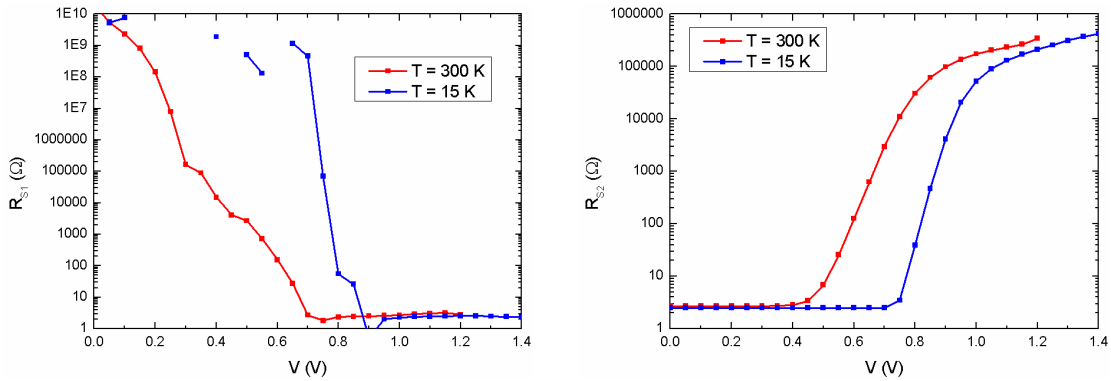

(a) (b)

Fig. 3. 8. Adjusted values of each resistance of the shunt pair R_{S1} and R_{S2} at room (red) and cryogenic (blue) temperatures in logarithmic scales. (a) R_{S1}. (b) R_{S2}.

The values for n and I_S are extracted from the fitting of the linear part of the I-V curve. The values of R_{SC}, equation (3.5), are used to fit the non-linear region of the I-V characteristic and obtain the R_{S2} resistance. These values are listed in Table 3. 2 for physical temperatures of 300 K and 15 K.

Table 3. 2. Parameters extracted from the I-V curve model at room and cryogenic temperatures.

Parameter	*Room Temperature (300 K)*	*Cryogenic Temperature (15 K)*
n – Ideality Factor	1.17	16.34
I_S – Saturation Current (A)	$9.55 \cdot 10^{-14}$	$5.35 \cdot 10^{-22}$
R_{SC} – Constant Parameter (Ω)	2.7	2.5

From the results listed above, a huge increase in the ideality factor of the diode at cryogenic temperatures is obtained. This is due to the conduction in the diode is highly influenced by tunnel effect when the temperature is reduced [3.25].

Once the I-V parameters are obtained, the small signal Scattering parameters are fitted in order to obtain the small signal model of the diode. The frequency range in which the model is fitted goes from 1 GHz to 40 GHz and an input power of -30 dBm is applied. The model shown in Fig. 3. 5 is used in order to fit the Scattering parameters and is implemented in ADS. The response at room temperature is depicted in Fig. 3. 9 and compared to the measured Scattering parameters. From the results, when the model based on a variable bias-dependant series resistance is used, it agrees the test in an accurate way. The values of n, I_S and R_S listed in Table 3. 2 are used for the calculus of the resistances of the model (R_{S2} and R_j). The values for V_{min} and I_{min} used for the calculus are 0.3 V and $1.82 \cdot 10^{-9}$ A, obtained from the I-V curve at room temperature (300 K). Updating the values for those valid at cryogenics temperatures (15 K), the model is extracted in the same way at this physical temperature. The values from the I-V curve for V_{min} and I_{min} used for the calculus at 15 K are 0.8 V and $1.45 \cdot 10^{-5}$ A respectively. The electrical responses at cryogenic temperature for different bias points are shown in Fig. 3. 10. The model of the diode fits the measurements in the whole frequency range under analysis.

In order to obtain the fitting of the Scattering parameters depending on the bias point, the model has additional elements (L_{s1}, L_{s2}, C_P and C_j) as shown in Fig. 3. 5. These parameters model parasitic effects and the junction capacitance of the diode. The values achieved for each element are listed in Table 3. 3. From reverse bias conditions applied to the diode it is obtained the parasitic elements of the model show constant values with the temperature. Besides, the value of the junction capacitance is also modelled as a constant value at room and cryogenic temperatures.

Table 3. 3. Parameters extracted from the fitting of the Scattering parameters at both physical temperatures.

Parameter	*Value*
L_{S1}	100 pH
L_{S2}	230 pH
C_P	0.02 pF
C_j	0.036 pF

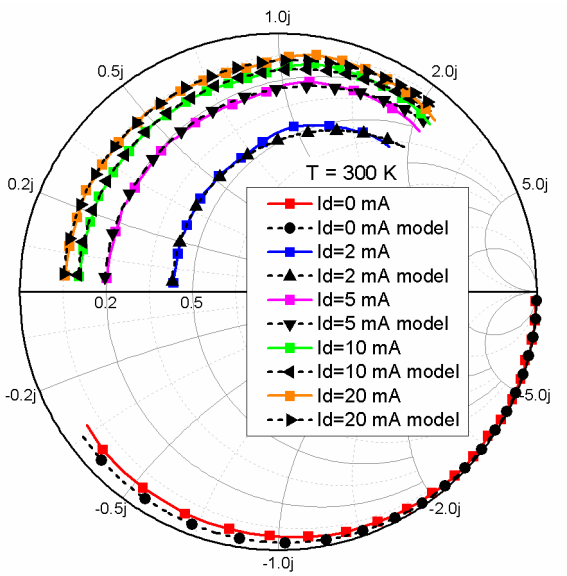

Fig. 3. 9. Small signal Scattering parameters fitting using variable R_S (freq=1 to 40 GHz) at room temperature (300 K). Model responses in dashed black line.

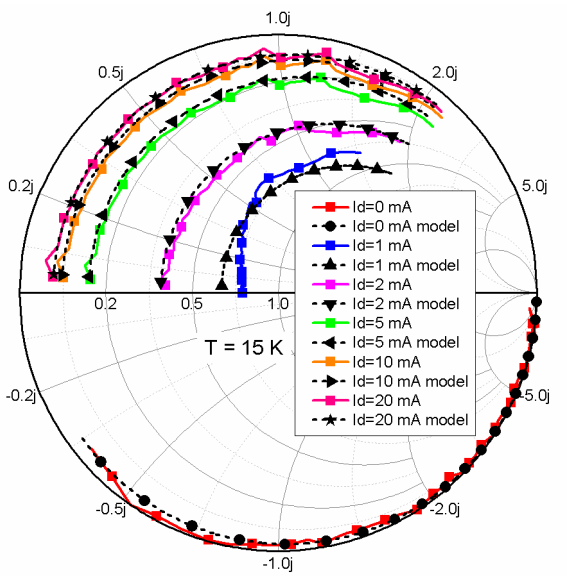

Fig. 3. 10. Small signal Scattering parameters fitting using variable R_S (freq=1 to 40 GHz) at cryogenic temperature (15 K). Model responses in dashed black line.

3.3.2 HSCH-9161

The second Schottky diode under analysis is another commercial device from Agilent Technologies. The choice of this component meets the design requirement of having a zero-bias diode in order to be used as a microwave square-law detector. The fact of being a low-barrier device makes easier the design of the final detector, since the use of a bias network for the diode is avoided. The knowledge in an accurate way of the diode impedance over a bandwidth is crucial in the design of a detector, since the need of performing a matching network for the diode in order to maximize the delivery power to the diode to perform the conversion. Moreover, its voltage sensitivity is also needed to be modelled in order to know the conversion rate from radiofrequency power to detected voltage at its output.

The features obtained from the manufacturer datasheet are listed in Table 3. 4. As in the previous device, there is no information about its temperature behaviour, below or above the maximum ratings (operating temperature from -65 to 150 ºC), so the cryogenic response of the diode is unknown. Two photographs of the diode are shown in Fig. 3. 11: the top view shows its body, while the bottom view shows a detailed image of the Schottky contact.

Table 3. 4. Datasheet features for the diode HSCH-9161 at room temperature.

Parameter	*Typical Values (300 K)*
C_j – Junction Capacitance	0.035 pF
R_s – Series Resistance	20 Ω
V_f – Forward Voltage	0.1 V
γ – Voltage Sensitivity (minimum value)	500 mV/mW

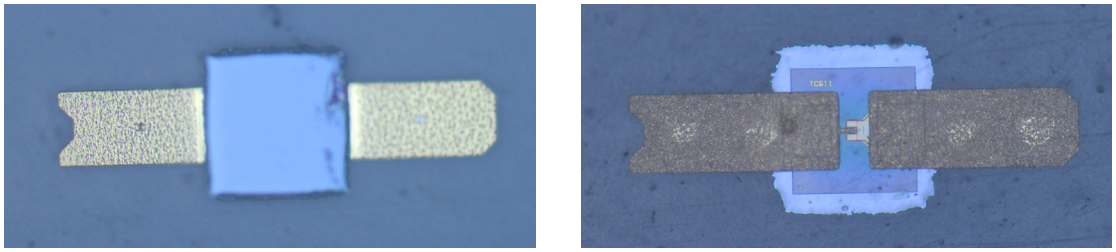

(a) (b)

Fig. 3. 11. Photograph of the Schottky diode HSCH-9161. (a) Top view. (b) Bottom view.

A Model extraction procedure

The extraction of a useful model of the HSCH-9161 is similar to the procedure for the MA4E2037. The main difference is when the diode is working at room temperature, since the low-barrier behaviour of the Schottky junction makes easier the model extraction. Moreover, not only the small signal model is performed, but also the large signal behaviour since the diode rectifies the incoming microwave power into output voltage. The model developed in this work fits the DC, radiofrequency and radiofrequency-to-DC conversion behaviours at room and cryogenic temperatures.

Initially, the diode is characterized at room and cryogenic temperatures, performing DC current-voltage (I-V) feature and radiofrequency tests. As a zero-bias diode is under modelling, the procedure for room and cryogenic temperature is slightly different. The approach for room temperature is based on constant series resistance for the diode, since only zero-bias condition is analyzed in its radiofrequency response. When the diode is working under cryogenic conditions, it is needed to be biased because the knee voltage increases [3.4], [3.9], and a bias dependence of the series resistance is considered.

At room temperature, the fitting of the I-V curve is done using equation (3.1), returning n, R_S and I_S parameters of the diode, assuming constant series resistance and performing the fitting of a linear section of the curve using (3.2).

Next, radiofrequency performance in terms of small signal Scattering parameters is modelled in a frequency range using those three parameters for the Schottky diode response, needed for the calculus of R_j using (3.3). The electrical sketch used for the model is shown in Fig. 3. 12. The model includes parasitic elements (L_S and C_P) in order to take into account the effects of the contacts of the device. This model is used for the room temperature behaviour, since the fitting is accurate using the constant series resistance approach.

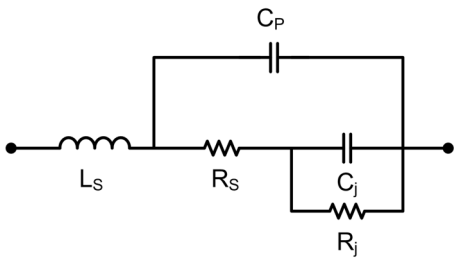

Fig. 3. 12. Small signal model for HSCH-9161 Schottky diode at room temperature.

When working at cryogenic temperatures, the behaviour of the small signal Scattering parameters is not well fitted using the previous room temperature approach. The same issue than in the MA4E2037 Schottky diode is used, with a variable series resistance depending on the bias point applied to the diode. So the I-V fitting is done using a pair of shunt resistances and, then, the small signal model is fitted. Consequently, the electrical model at cryogenic temperature is shown in Fig. 3. 13, in which the series resistance is a shunt pair composed of R_{S1} and R_{S2}, which obeys equations (3.4) and (3.5) respectively. The value of R_{SC} for R_{S2} is a constant value obtained in the I-V characteristic fitting.

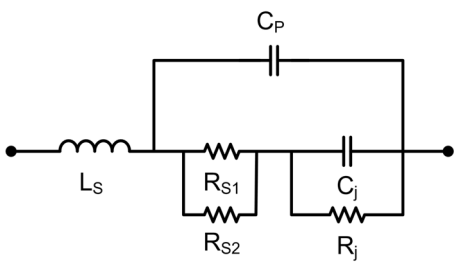

Fig. 3. 13. Small signal model for HSCH-9161 Schottky diode at cryogenic temperature.

In order to finish the model at both temperatures, a non-linear model is needed to be achieved since the diode is going to be used as part of a detector. Therefore, the model is modified in order to have a non-linear device with the same physical characteristics obtained from the DC and small signal models. The electrical circuit for the non-linear model is shown in Fig. 3. 14, in which an electrical model of a diode junction from ADS is used [3.26] and shown in Fig. 3. 15. This model is temperature dependant and all the current and conductances are calculated from input parameters, such as saturation current, ideality factor, junction capacitance and so on. The model is used at both temperatures, using the corresponding parameters.

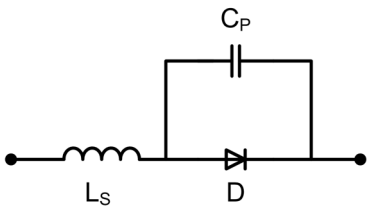

Fig. 3. 14. Non-linear model for HSCH-9161 Schottky diode.

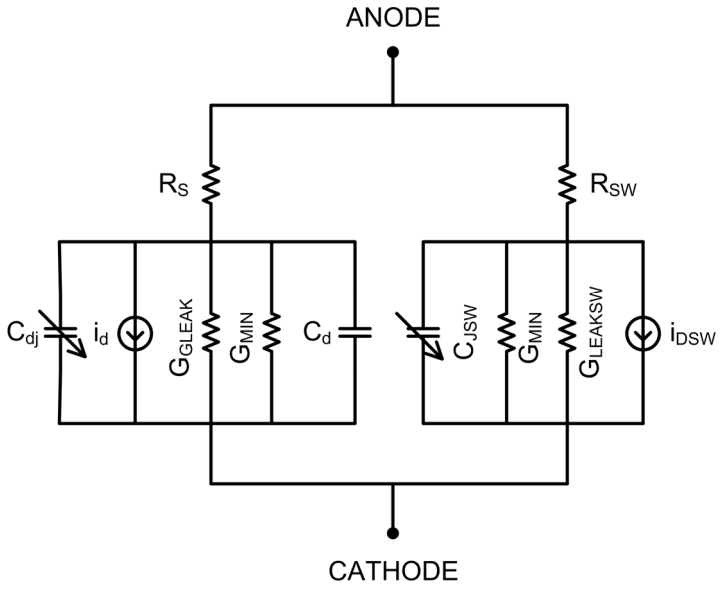

Fig. 3. 15. Non-linear electrical model for diode junction (label 'D') used in ADS simulator.

This model enables the analysis of the non-linear conversion from radiofrequency power to DC voltage based on harmonic balance. In case of the room temperature behaviour, the radiofrequency-to-DC conversion is easily achieved in the simulator by its zero-bias condition. However, when cryogenic behaviour is being modelled, the non-constant resistance with the bias point must be provided since the simplicity of the equivalent Schottky diode modelled with the element labelled 'D' does not enable to change its resistance. Therefore, the model is provided of a data component in order to seek the bias point of the diode and to read the equivalent series resistance in that point.

B HSCH-9161 Model

The measurements are performed both at room temperature and at cryogenic one. The cryogenic test reached a temperature of 15 K. The measurements are also done using the kit presented in the previous chapter based on CPW-to-microstrip transitions with via holes. The results obtained for the I-V features at both physical temperatures are shown in Fig. 3. 16. An increase in the knee voltage by the effect of decreasing temperature is measured as expected [3.4], [3.9].

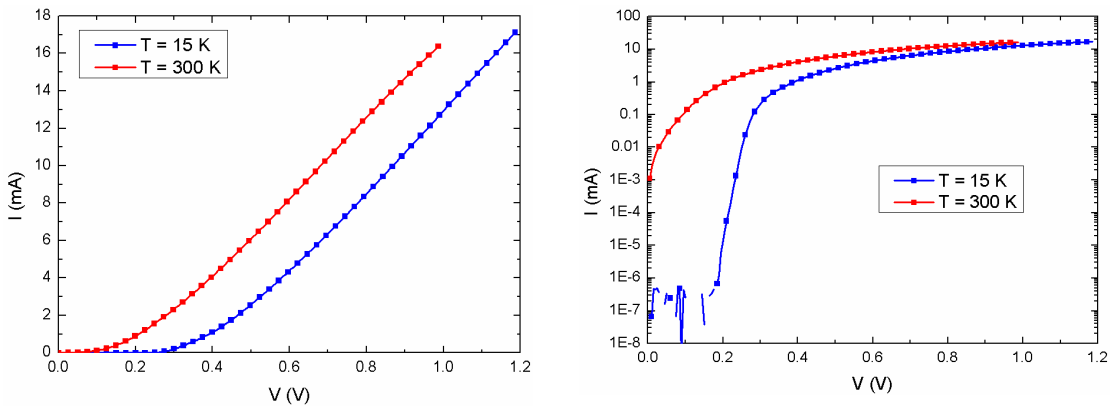

(a) (b)

Fig. 3. 16. Measured I-V characteristic at room temperature (red) and at cryogenics (blue). (a)Linear scale. (b) Logarithmic scale.

The I-V characteristics of the diode at both temperatures are fitted and the results obtained are shown in Fig. 3. 17. The linear section of the curve provides the value of n and I_S, while the non-linear region R_S. The values of these parameters are listed in Table 3. 5 for both physical temperatures (300 K and 15 K). The results at room temperature are well fitted with the single series resistance R_S, while the cryogenic fitting is accurate using the shunt pair of resistances (R_{S1} and R_{S2}). The value of R_{SC} in equation (3.5) for the calculus of R_{S2} is adjusted in the non-linear region of the I-V feature. Its value is R_{SC}=20 Ω. The values of both resistances versus the diode voltage are shown in Fig. 3. 18. From these results, an increase in the ideality factor of the diode at cryogenic temperatures is obtained [3.25].

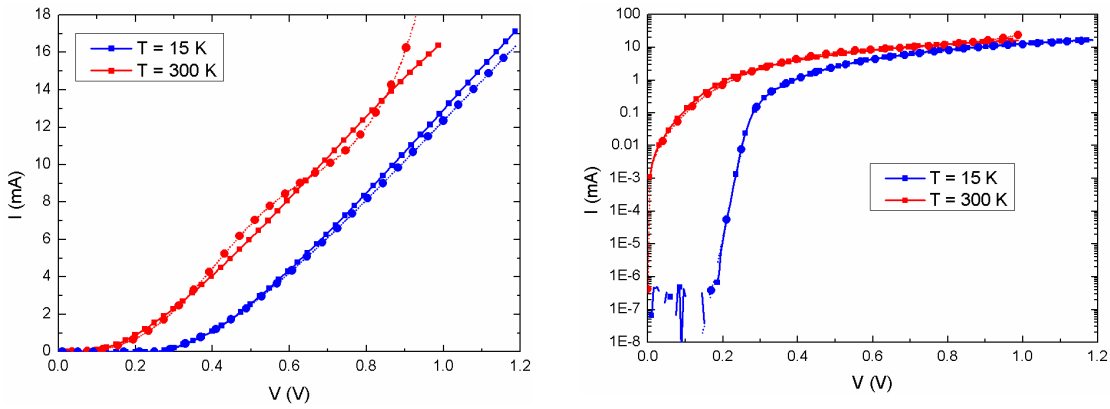

(a) (b)

Fig. 3. 17. Fitting of the I-V characteristic at room temperature (red) with single R_S and at cryogenics (blue) in dashed lines considering shunt R_{S1}-R_{S2} resistances at cryogenics. (a) Linear scale. (b) Logarithmic scale.

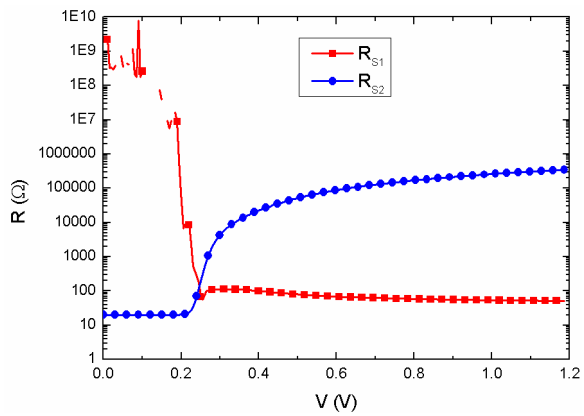

Fig. 3. 18. Adjusted values of each resistance of the shunt pair R_{S1} and R_{S2} at cryogenic temperature in logarithmic scale.

Table 3. 5. Parameters extracted from the I-V curve model at room and cryogenic temperatures.

Parameter	*Room Temperature (300 K)*	*Cryogenic Temperature (15 K)*
n – Ideality Factor	1.32	6.21
I_S – Saturation Current (A)	$6.33 \cdot 10^{-6}$	$2.34 \cdot 10^{-19}$
R_S – Series Resistance (Ω)	43.2	-

The Scattering parameters are fitted in order to obtain the small signal model of the diode. The frequency range in which the model is fitted goes from 1 to 40 GHz. The measurements are made with an input power of -30 dBm. The fitting at room temperature is performed and the comparison of the model and the measured results are shown in Fig. 3. 19. Under cryogenic operation, the model is based on variable series resistance, and the comparison of the model and the measurements at 15 K is depicted in Fig. 3. 20. The values of n and I_S listed in Table 3. 5 and R_{SC} are used for the calculus of the resistances of the cryogenic model (R_{S2} and R_j). The values for V_{min} and I_{min} obtained from the I-V curve which are used for the calculus of the resistances are 0.205 V and $3.07 \cdot 10^{-8}$ A respectively. When working at cryogenic temperatures, the diode modifies its behaviour from a zero-bias device to a higher potential barrier diode since the knee voltage increases. Therefore, an external bias point is applied to the diode in order to test its behaviour and analyze its impedance for its use as a part of a detector, in which a bias point is needed to convert the radiofrequency signal into DC voltages.

The values in the fitting of the parasitic elements and the junction capacitance, which are considered constant with the temperature, are listed in Table 3. 6.

Table 3. 6. Parameters used for the fitting of the small signal model at both physical temperatures.

Parameter	*Value*
L_S	155 pH
C_P	0.035 pF
C_j	0.018 pF

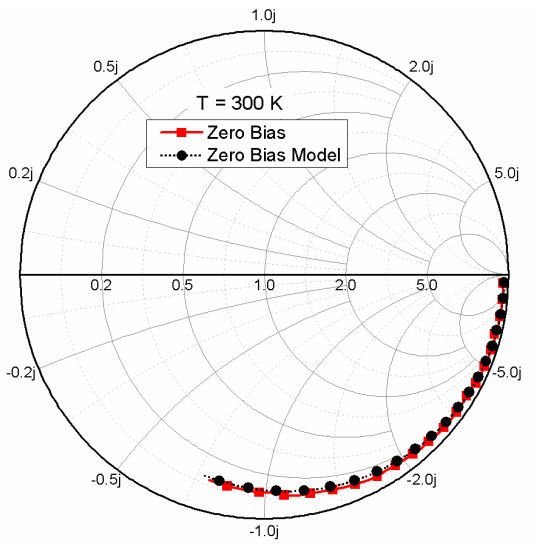

Fig. 3. 19. Small signal Scattering parameters fitting using constant Rs (freq=1 to 40 GHz) at room temperature (300 K). Model response in dashed black line.

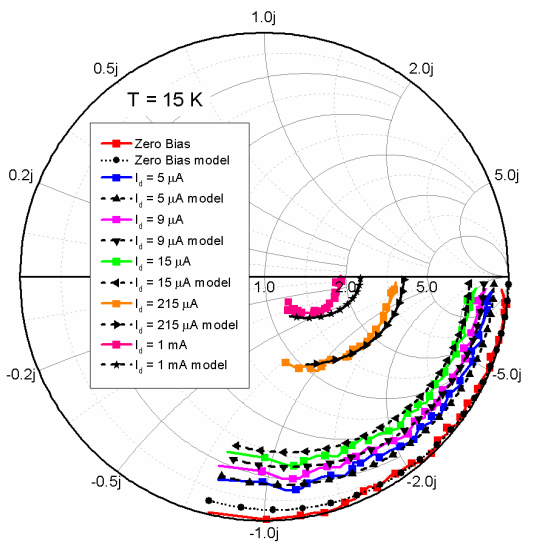

Fig. 3. 20. Small signal Scattering parameters fitting using variable Rs (freq=1 to 40 GHz) at cryogenic temperature (15 K). Model response in dashed black line.

The last step of the modelling is to fit the non-linear behaviour of the diode. This is a significant issue in order to perform the radiofrequency-to-DC response working as a detector diode. The model is performed using the model tool included in ADS for a P-

N junction. This diode model is defined as shown in the Fig. 3. 14 using the parameters listed in Table 3. 5 and Table 3. 6. As this diode is going to be used in a microwave detector, the voltage sensitivity parameter is essential. Then, S_{DIODE} is defined as the conversion ratio between the DC voltage in the output of the device and the available input radiofrequency signal to the device, given by

$$S_{DIODE} = \frac{V_{DC}}{P_{RF}} \tag{3.6}$$

where V_{DC} is the DC output voltage (V) and P_{RF} (W) is the available power at the input.

In order to perform a sensitivity analysis, the input power P_{RF} is swept from very low to high values at a fixed frequency. A radiofrequency ground is added in the diode cathode (node V_{DC}) in order to perform the analysis. The results obtained from this analysis are useful in order to design the detector (further described in chapter VI), and then they are compared to real measurements, since individual tests of the radiofrequency-to-DC conversion of the diode is not performed.

First of all, the non-linear model is simulated in order to calculate its I-V characteristic. The simulation is compared to the measurements at room temperature and at cryogenic temperature. These results are shown in Fig. 3. 21 and an accurate prediction of the I-V characteristic is achieved using this non-linear model.

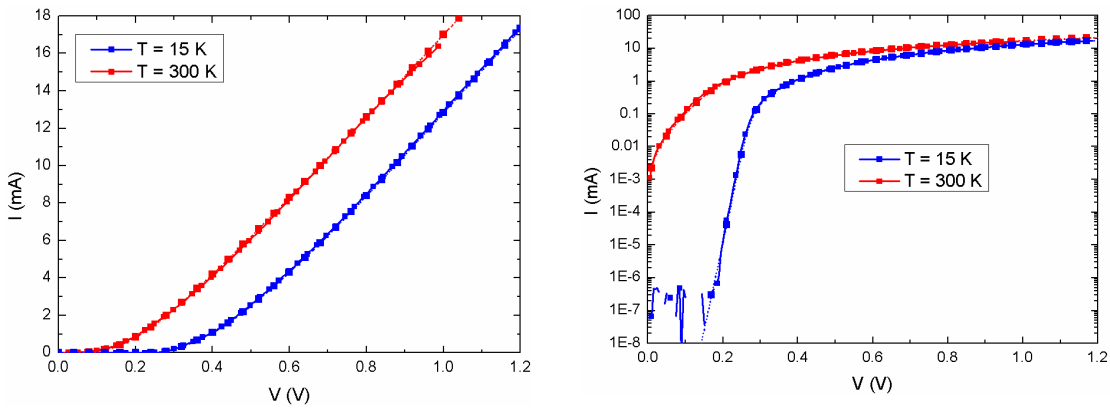

Fig. 3. 21. Fitting of the I-V characteristic at room temperature (red) and at cryogenics (blue) in dashed lines using non-linear model. (a) Linear scale. (b) Logarithmic scale.

The simulation of the model is performed analyzing two cases: modifying the power level and modifying the frequency of the input signal. The analysis at room temperature is made under zero-bias conditions. The results are shown in Fig. 3. 22; when the power level of the input signal at a fixed frequency of 30 GHz is swept, since the detector is going to be used in the band from 26 to 36 GHz, a sensitivity S_{DIODE} of

around $3.2 \cdot 10^3$ mV/mW is obtained. As the available input power increases (values higher than P_{RF} = -24 dBm), a compression in the diode is predicted, but the diode is expected to be excited with a lower input power. When the frequency of the input signal, with a fixed available input power of P_{RF} = -30 dBm, is swept, the model returns a non-constant sensitivity S_{DIODE} with the frequency.

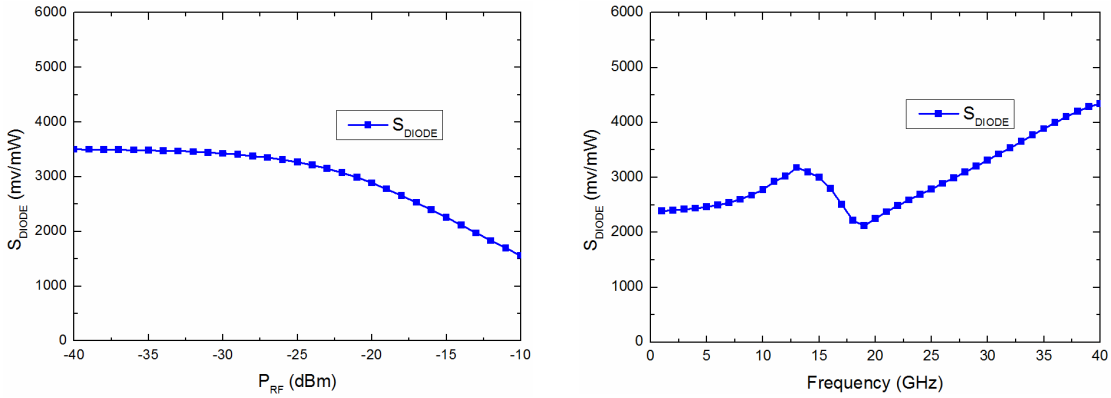

(a) (b)

Fig. 3. 22. Sensitivity of the diode at room temperature (300 K). (a) Variable power level of the input signal at freq = 30 GHz. (b) Frequency sweep of the input signal with available power P_{RF} = -30 dBm.

The model under cryogenic temperatures is simulated with the same set-up than at room temperature. The difference is the need of providing a bias network for the diode. The diode shows variable voltage sensitivity depending on the bias point of the diode. The simulation results for S_{DIODE} are shown in Fig. 3. 23 for two bias point. Higher sensitivity is predicted for low current bias point than high current cases in the diode. Besides, the compression of the diode also depends on the bias current, handling a higher input power with linear characteristic in cases of higher currents biasing the diode.

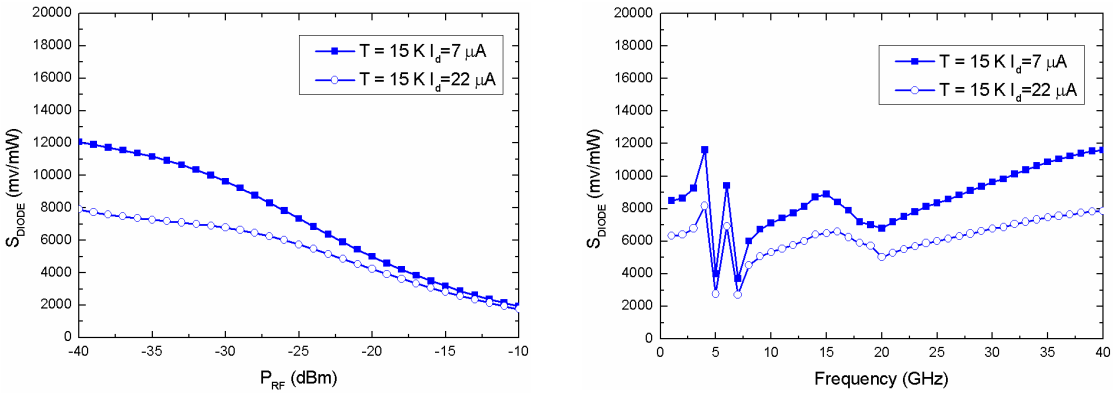

(a) (b)

Fig. 3. 23. Sensitivity of the diode at cryogenic temperature (15 K) for two different bias points. (a) Power sweep of the input signal at freq = 30 GHz. (b) Frequency sweep of the input signal with available power P_{RF} = -30 dBm.

3.4. HPND-4005 PIN Diode Modelling

Another kind of diode under analysis is a PIN device from Avago Technologies. PIN diodes are usually used as radiofrequency switches due to their fast impedance change from forward to reverse bias when a high rate modulated signal is applied to them. Besides, PIN devices with low resistance in forward bias are suitable for acting as a good short-circuit. Additionally, these low capacitance diodes under reverse bias conditions are useful for high isolation applications.

The HPND-4005 diode is intended a good short-circuit or a good open-circuit in millimetre-wave frequencies when forward or reverse bias is applied to the device, in order to act as a microwave switch in the circuits designed.

The features obtained from the manufacturer datasheet are listed in Table 3. 7. Its temperature behaviour, below or above the maximum ratings, is not provided, so its cryogenic response is unknown. Two photographs of the diode are shown in Fig. 3. 24: the top view shows the diode body, while the bottom view shows a detail of the PIN structure through a microscope images.

Table 3. 7. Datasheet features for the diode HPND-4005.

Parameter	*Typical Values*
C_j – Junction Capacitance	0.017 pF
R_s – Series Resistance	4.7 Ω
V_f – Maximum Forward Voltage	1 V
V_{br} – Reverse Breakdown Voltage	120 V

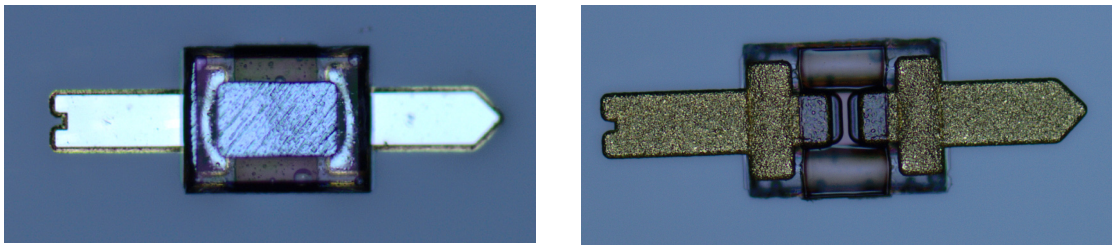

(a) (b)

Fig. 3. 24. Photograph of the PIN diode HPND-4005. (a) Top view. (b) Bottom view

A Model extraction procedure

The extraction of a model for the HPND-4005 is similar to the procedure for the Schottky diodes. Initially, the diode is characterized at room and cryogenics temperatures, performing DC I-V feature and radiofrequency tests.

At both physical temperatures, the fitting of the I-V characteristic is done using equation (3.1), since when low-frequency signals are applied to PIN diodes, they behave as P-N junctions due to the period of the signal is longer than the intrinsic layer carrier lifetime [3.27]. From this fitting, the n and I_S parameters of the diode are returned, and the R_S is estimated from the fitting of the non-linear region of the curve.

In the particular case of radiofrequency performance, the small signal Scattering parameters are modelled in a frequency range using n, I_S and R_S parameters obtained from the I-V fitting. But the assumption of having a constant R_S cannot be approached. The fact of having an excitation signal whose period is similar or above than the intrinsic carrier lifetime makes that the intrinsic layer acts as a conductive surface for that incoming signal. Therefore, a PIN diode behaves as a current controlled resistance when a high frequency signal excites it [3.27].

The electrical sketch used for the PIN diode model is shown in Fig. 3. 25. The model includes parasitic elements (L_{S1}, L_{S2} and C_P) in order to take into account the effects of the contacts of the device. This model is used for both physical temperatures (300 K and 15 K).

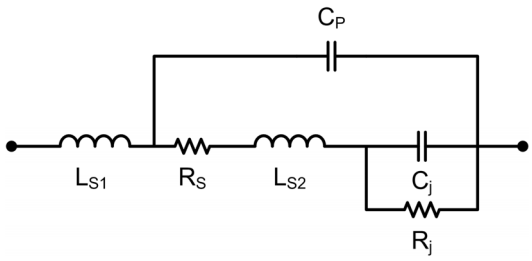

Fig. 3. 25. Small signal model for HPND-4005 PIN diode.

The above model shows an only series resistance, but it is composed of two resistances: one is the R_S obtained from the I-V fitting and the other is bias point dependant resistance. The approximation for the variable resistance is fitted using an inversely proportional equation [3.28]. Therefore, the bias-dependant resistance for the PIN diode model is given by

$$R_S = R_{SI-V} + R_{SVAR} = R_{SI-V} + \frac{A}{\left(I_{bias} + 1 \cdot 10^{-14}\right)^K} \tag{3.7}$$

where R_{SI-V} is the series resistance obtained from the I-V fitting (Ω), A and K are constants and I_{bias} the current through the diode (A).

B HPND-4005 Model

The measurements are performed both at room and cryogenic temperatures. The cryogenic test reached a temperature of 15 K. The measurements are also done using the kit presented in the previous chapter based on CPW-to-microstrip transitions with via holes.

The modelling of PIN diodes has been widely described in the literature describing time-domain response or physics-based models, such as [3.29]-[3.34] among others. The electrical model described in this work for the PIN diode HPND-4005 fits the I-V feature and the small signal S-parameters in order to aid the circuit design.

The measurement of the PIN diode I-V feature is performed in the same way as in the previous diodes using the semiconductor network analyzer. A new issue arises from this technique for HPND-4005 diode: hysteresis loops appear in the characteristic when the physical temperature decreases. Traditional way of extracting the I-V characteristic of a device is based on static measurements in which the voltage is increased from zero to a maximum value. This way to proceed returns a hysteresis phenomenon in the I-V characteristic at cryogenic temperatures, as shown in Fig. 3. 26. The hysteresis is due to the impact ionization phenomenon [3.35], which can derive in avalanche multiplication at high field applied to the device [3.36]. Moreover, this hysteresis effect is also increased due to the self-heating of the diode by the use of static I-V measurement [3.37]. Besides, an increase in the knee voltage by the effect of decreasing temperature is measured due to the increase in the potential barrier height by the reduction of the intrinsic carrier concentration at cryogenic temperatures [3.38]. Therefore, in order to avoid the I-V characteristics with hysteresis, pulsed I-V measurements are performed since self-heating and trapping effects do not have enough time to occur [3.37]. The results in Fig. 3. 26 show the hysteresis loop at 15 K when the applied voltage is swept in forward (from 0 to 1.2 V) and reverse (from 1.2 to 0 V) cycles for positive voltages. In the forward cycle, the I-V feature follows the blue trace with a sudden current jump from very few amps to a limited value in the analyzer; the I-V feature in the reverse cycle follows the red trace, providing a different current value for the same voltage.

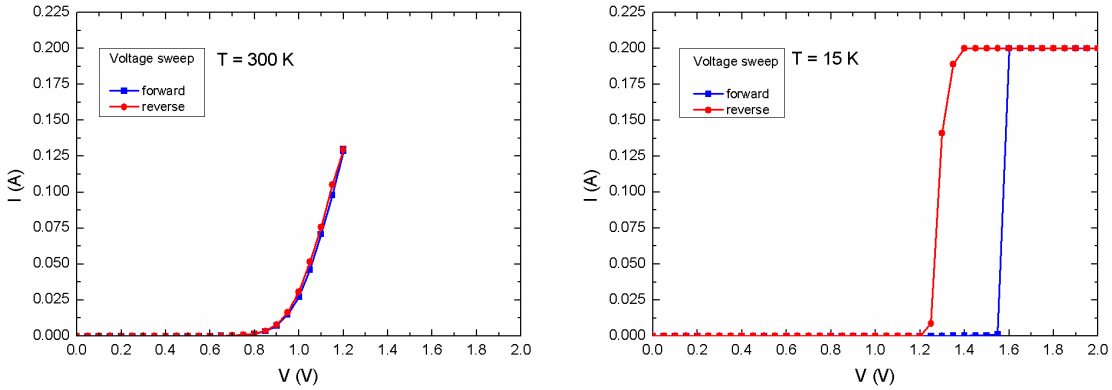

(a) (b)

Fig. 3. 26. Measured static I-V characteristic in forward and reverse bias cycle. (a) Room temperature (300 K). (b) Cryogenic temperature (15 K).

The pulsed I-V characteristic is configured with a signal defined with a pulse length of t = 500 µs and a pulse separation of t = 500 ms. The measurements at room and cryogenic temperatures shown in Fig. 3. 27 are obtained. A trace without hysteresis is measured and the forward and reverse cycles agree in the current value corresponding for the same applied voltage. The I-V feature at 15 K is limited to a maximum current value, hence the last point in the figure for the highest applied voltage. The pulsed signal uses a short pulse in order to assure the lack of above phenomena.

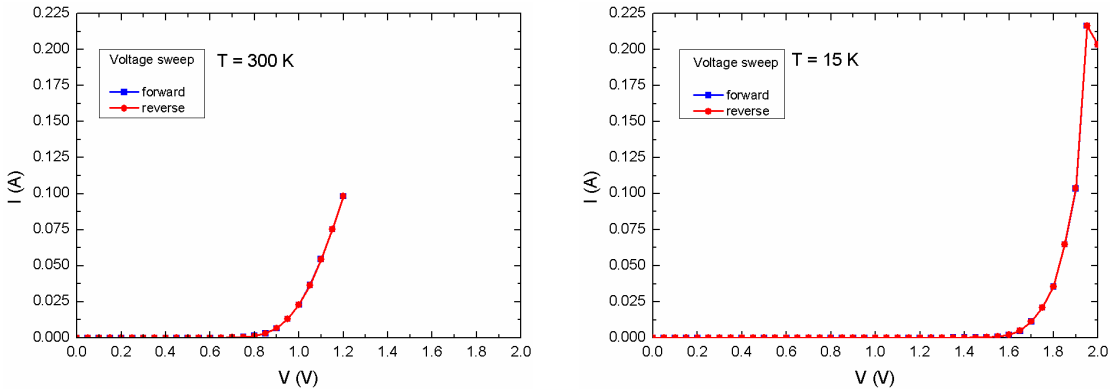

(a) (b)

Fig. 3. 27. Measured pulsed I-V characteristic in forward and reverse bias cycle. (a) Room temperature (300 K). (b) Cryogenic temperature (15 K).

Therefore, the I-V characteristics of the PIN diode at both temperatures are fitted using the pulsed measurement. The results obtained are shown in Fig. 3. 28. The linear section of the curve provides the value of n and I_S, while R_S is obtained from the non-linear region. The values of these parameters are listed in Table 3. 8 for both physical temperatures, 300 K and 15 K. An increase in the ideality factor of the diode is obtained at cryogenic temperatures.

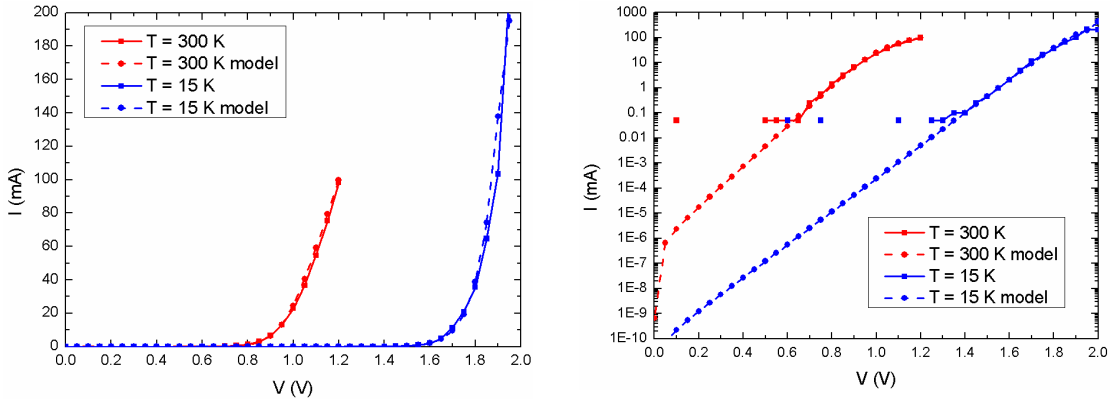

(a) (b)

Fig. 3. 28. Fitting of the pulsed I-V characteristic at room temperature (red) and at cryogenics (blue) in dashed lines. (a) Linear scale. (b) Logarithmic scale.

Table 3. 8. Parameters extracted from the I-V curve model at room and cryogenic temperatures.

Parameter	*Room Temperature (300 K)*	*Cryogenic Temperature (15 K)*
n – Ideality Factor	2.08	51.08
I_S – Saturation Current (A)	$4.37 \cdot 10^{-10}$	$6.34 \cdot 10^{-14}$
$R_{SI\text{-}V}$ – Series Resistance (Ω)	0.85	0.24

The small signal S-parameters are fitted in order to obtain the small signal model of the diode. The frequency range in which the model is fitted goes from 1 to 40 GHz. The tests are performed with an input power of -30 dBm. A variable series resistance model is used at both physical temperatures using the model shown in Fig. 3. 25 and the equation (3.7). The values of the R_{SVAR} at room and cryogenic temperatures are shown in Fig. 3. 29, in which the value for negligible currents in the diode is too high. The fitting at room temperature is performed and the comparison of the model and the measured results are shown in Fig. 3. 30. The model fits in an accurate way the measurements, with smaller impedance for higher current in the diode. The fitting at cryogenic temperatures (15 K) is shown in Fig. 3. 31, in which the comparison to the cryogenic tests is done. The cryogenic measurement could be only performed in high bias point, since the polarization system, used in the cryogenic probe station for the S-parameter tests, does not enable a pulsed measurement. For that reason, the bias points included in the figure key are higher than 140 mA. Although the impedance values of the PIN diode depending on the bias point are quite similar, a slight reduction in its value is observed for higher forward current.

The values of the parasitic elements and the junction capacitance, which are considered constant with the temperature, used in the fitting are listed in Table 3. 9. Besides, the constant values used in equation (3.7) in order to fit the variable series resistance are listed in Table 3. 10 for both physical temperatures.

Table 3. 9. Parameters used for the fitting of the small signal model at both physical temperatures.

Parameter	*Value*
L_{S1}	130 pH
L_{S2}	165 pH
C_P	0.035 pF
C_j	0.024 pF

Table 3. 10. Values for the variables used in the series resistance at both physical temperatures.

Parameter	*Value (300 K)*	*Value (15 K)*
A	0.25	0.65
K	0.307	0.3

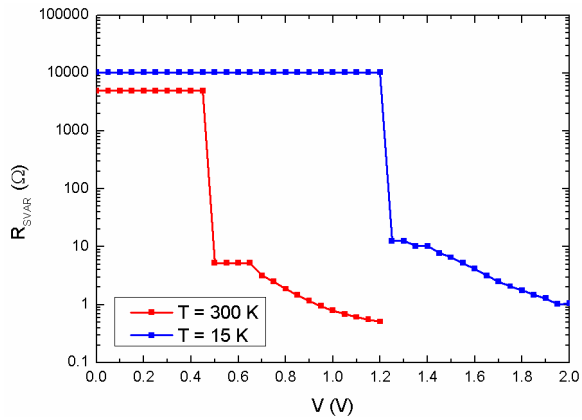

Fig. 3. 29. Adjusted values of variable resistance of the PIN diode model at room (300 K) and cryogenic (15 K) temperature in logarithmic scale.

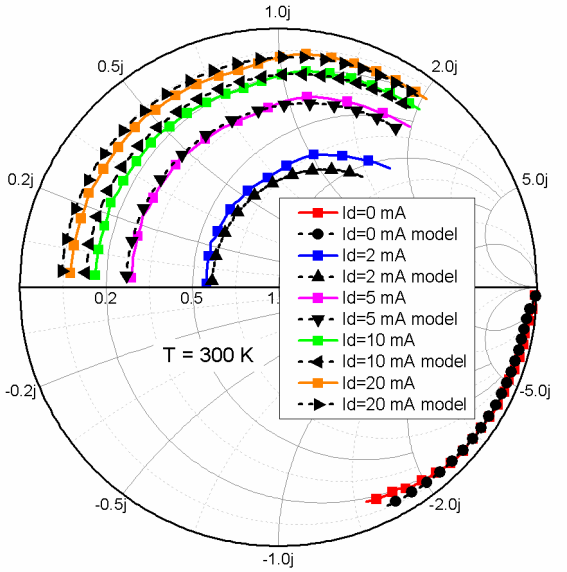

Fig. 3. 30. Small signal Scattering parameters fitting (freq=1 to 40 GHz) at room temperature (300 K). Model response in dashed black line.

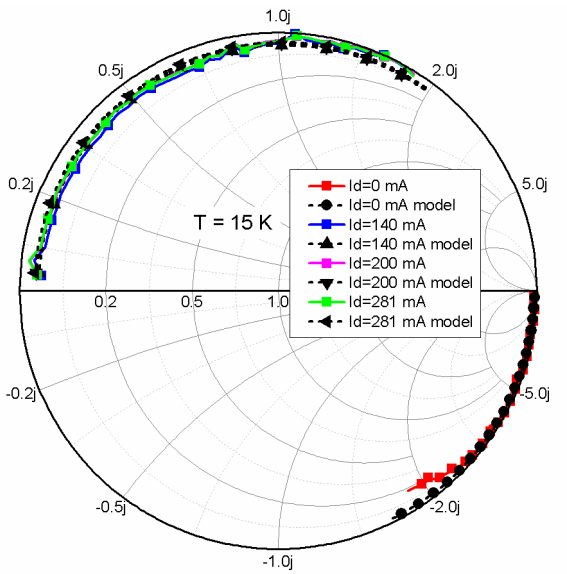

Fig. 3. 31. Small signal Scattering parameters fitting (freq=1 to 40 GHz) at cryogenic temperature (15 K). Model response in dashed black line.

3.5. Conclusions

This chapter has described the modelling of three diodes in order to obtain an equivalent electrical scheme useful for the design of microwave circuits. The use of the measurement kit described in chapter II based on CPWG-to-microstrip transitions with via-holes has enabled the characterization in probe stations in order to get the I-V characteristic and the Scattering parameters of the diodes.

Three different diodes have been analyzed: two Schottky devices and a PIN diode. The two Schottky diodes have different features, since one of them is a high-barrier

Schottky diode model MA4E2037 from MACOM Technology Solutions and the other one is a zero-bias Schottky diode model HSCH-9161 from Avago Technologies. The PIN diode is the model HPND-4005 from Agilent Technologies.

The characterization of the set of diodes has been performed at room temperature (300 K) and at cryogenic temperature (15 K). The characterization under cryogenic conditions is a challenging issue, since the difficulty on the prediction of the behaviour of devices developed in commercial technologies. The measurement and modelling of the three diodes at a physical temperature of 15 K have been successfully performed and described in this chapter.

The modelling of the Schottky diode MA4E2037 has demonstrated accurate fitting according the measurements in terms of I-V characteristic and Scattering parameters. A variable series resistance depending on the bias point has been used in the model. An increase of the knee voltage and the ideality factor and a reduction of the saturation current of the diode at cryogenic temperatures have been obtained.

In case of the modelling of the zero-bias Schottky diode HSCH-9161, the model has also fitted the measurements at both physical temperatures. A constant series resistance has been used in the room temperature model, while a variable series resistance at cryogenic temperature. Besides, a non-linear model has been developed in order to analyze the radiofrequency-to-DC response acting as a detector. An increase of the knee voltage and the ideality factor and a reduction of the saturation current of the diode at cryogenic temperatures have been also obtained. Moreover, the diode model has predicted a variable voltage sensitivity and a different compression point at cryogenic temperature depending on the bias point of the diode.

Finally, the PIN diode has been modelled using a variable series resistance in order to fit the radiofrequency response. Nevertheless, a constant resistance model is implemented for the I-V characteristic fitting. A pulsed measurement has been implemented for the I-V characterization due to hysteresis loops that appear in the response depending on the physical temperature. An increase of the knee voltage and the ideality factor and a reduction of the saturation current of the diode at cryogenic temperatures have been measured.

Chapter IV

Design of a 180º Phase Switch Using Uniplanar Hybrid Technology

4.1. Introduction

180º phase switches are common circuits used in communication systems in order to excite a subsystem with an out-of-phase signal. The precision in the change of the phase signal will define the quality of the full transmitter or receiver, so a low phase error is desired. Additionally, accurate amplitude balance is required for its use in a radio astronomy receiver in which the amplitude in each receiver state must be similar. Different technologies have been implemented in order to achieve the 180º phase shift, such as MMIC technology [4.1]-[4.5], MEMS-based designs [4.6]-[4.7], using baluns [4.8], reflection-type circuits [4.9] or substrate integrated waveguide (SIW) [4.10]-[4.11]. Some of the available solutions in the literature do not include the switching device, only performing the phase shifter in a wideband range.

This chapter shows the design and characterization of a 180º phase switch in one-sided hybrid technology. The use of uniplanar technology, such as ground-less coplanar waveguide (CPW) and slotline, enables an easy connection of series or shunt devices

and a high level of integration with other circuits or subsystems; besides, the use of via holes for ground connection is avoided. The previously mentioned advantages over microstrip technology make this choice a competitive solution in order to achieve flat wideband phase shift response. Furthermore, the use of hybrid technology faced to monolithic one shows advantages in terms of cost, total production-to-characterization consuming time and post-production circuit tuning. The phase shift is achieved by the proper switching of slotline transmission path in which the radiofrequency signal flows and excites a CPW line by either one or the other feasible slot in this kind of transmission line

4.2. 180º Phase Switch Electrical Design

The design of the 180º phase switch is aimed for its use in the QUIJOTE phase II radiometer working in the Ka-band. The initial design specifications are detailed in Table 4. 1. The circuit is intended to be fully designed in hybrid technology using uniplanar transmission lines. Therefore, discrete devices such as microwave diodes are used to control the circuit state which modulates its phase. They are assembled in the circuit, taking the advantage of the easy connection over slotline transmission lines.

Table 4. 1. Design specifications for the 180º phase switch.

Frequency range	26-36 GHz
Input/Output Return Loss	>10 dB
Average Phase Shift	180º
Maximum Phase Error	5º
Maximum Amplitude Imbalance	0.5 dB

4.2.1 Principle of Operation

The proposed 180º phase switch is based on the use of CPW and slotline as transmission lines and the existence of identical dual transmission paths in slotline technology, choosing between them by the appropriate combination of switching elements. Thus, the microwave signal travels by one of these different but symmetrical paths and feeds an output CPW line by one of its slots. Depending on the excited slot of the CPW line, a 180º phase difference in the signal at the output of the circuit is provided.

The block diagram of the proposed phase switch is shown in Fig. 4. 1. The phase switch circuit can be divided into three different parts in order to understand its operation: the input in which a transition from CPW to slotline transmission lines is performed, the slotline paths and the output transition from slotline to CPW transmission line. The approach of getting a 180º phase difference is achieved by the combination of the two last parts in order to excite the CPW output line with the selected transmission path in slotline.

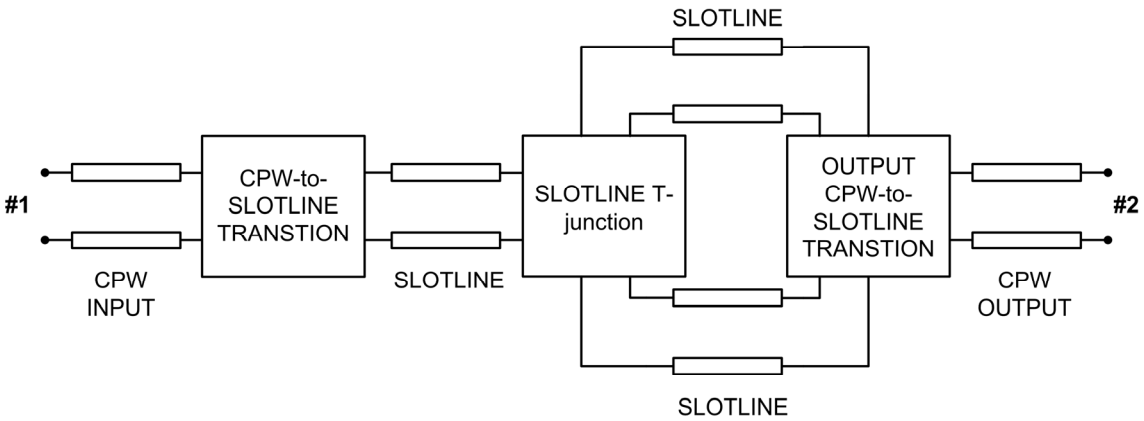

Fig. 4. 1. Schematic of the proposed 180º phase switch.

As described above, the proposed topology is defined using CPW and slotlines as transmission lines. Both lines are developed without backside metallization and their common characteristics are detailed in [4.12]-[4.13]. The basic configuration for both transmission lines are shown in Fig. 4. 2, consisting of a dielectric material with two slots or a single one etched for CPW or slotline respectively in the metallization.

Fig. 4. 2. Conventional transmission lines. (a) CPW. (b) Slotline.

The CPW transmission line as a three conductor transmission line can propagate two fundamental modes: the even-mode and the odd-mode. The CPW even-mode shows the same potential in the side metallizations, while in the odd-mode these metallic contacts have opposite sign potentials. The 180º phase switch approach considers the only propagation of the CPW even-mode, so the odd-mode should be suitably removed by equipotential bridges placed at an electrical distance equal to a

quarter-wavelength between them. The slotline is a two conductor transmission line in which the energy flows between conductors. The electrical field distribution in a cross-section for both transmission lines considered in the design are shown in Fig. 4. 3.

Fig. 4. 3. Electric field distribution. (a) CPW even-mode. (b) Slotline mode.

As a multi-technology transmission line circuit, transitions from one to the other lines are defined in order to properly accommodate CPW mode to slotline one and vice versa. A basic sketch of a transition is shown in Fig. 4. 4. The circuit has CPW input and it is transitioned to slotline, in which an easy interface for the connection of shunt device is performed.

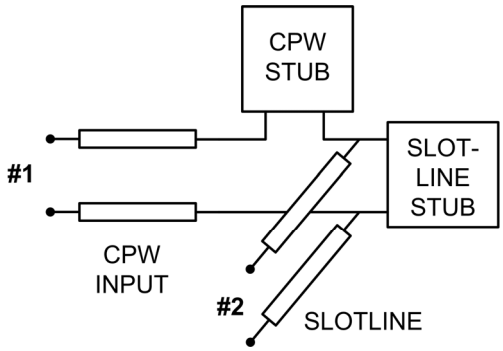

Fig. 4. 4. Basic schematic of a CPW-to-slotline transition.

Once the slotline mode is the propagating one, a slotline T-junction is designed in order to have dual transmission paths. At the outputs of the T-junction, switching devices are placed in order to select the transmission path that will excite the slotline-to-CPW transition at the output. The switching devices are microwave diodes and they have to show a low series resistance in their forward polarization state, while a low junction capacitance in the reverse one.

The output of the circuit is performed in CPW line, so a new transition from slotline-to-CPW is designed. The output transition is a key section for the proper phase behaviour of the circuit. The dual slotline paths feed each one of the slots in the output CPW line. As the switching devices select the propagation path, only one of these slots is excited with the microwave signal and a CPW even-mode is propagated in the line.

When the path is switched, the feeding slot is the opposite one in the CPW line, and an out-of-phase CPW even-mode is transmitted. A detailed drawing containing the electric field components in the different stages is depicted in Fig. 4. 5, in which a simplified layout of a CPW-to-slotline transition is shown. The black patch in the figures symbolizes a short-circuit, implemented by a microwave diode, between slotline metallizations. Besides, these effects are located at specific places and, together with the non-transmitting slotline path, are part of the output transition.

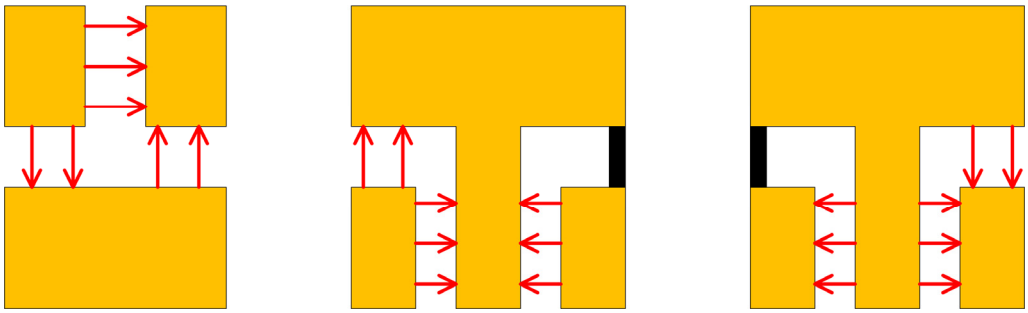

Fig. 4. 5. Electric field lines. (a) Slotline T-junction. (b) Slotline-to-CPW transition excited by left-side slot. (c) Slotline-to-CPW transition excited by right-side slot.

The Fig. 4. 5(a) shows the electric field lines in the slotline T-junction. As initial approach, one of the slotline output lines is removed by the effect of the short-circuit. Therefore, as shown in Fig. 4. 5(b) and Fig. 4. 5(c), the electric field components in the CPW output lines correspond to out-of-phase even-modes, in which air bridges at CPW junctions are used in order to odd-mode suppression.

4.2.2 Input CPW-to-Slotline Transition

As previously stated, the input of the circuit is performed in CPW line and dual slotline paths with switching devices are required to feed the output CPW line. Therefore, a transition from CPW to slotline transmission lines is designed to fulfil these requirements.

This type of transition has been widely reported [4.14]-[4.27], analysing the best combination of elements to improve the behaviour of the transition. The proper combination of the stubs in CPW and slotline technologies, sketched in Fig. 4. 4, provides wide operating bandwidths; moreover, the frequency band is tuned with these stubs. Typically, the input and output transmission lines of a transition are set to an impedance value equal to 50 Ω, and a mode conversion is only performed.

The design of any circuit must consider multiple requirements, such as fabrication issues, measurement procedure and capability of integration between others. The circuits are going to be characterized in a coplanar probe station and are going to be integrated into other subsystems in the receiver. The design of the circuit in CPW technology as access transmission lines makes it fully compatible with coplanar tests and valid for being cascaded to other circuits. The fabrication process restrictions fix a limitation in the smallest dimension of an etched metallization, either width in CPW or gap in slotline. Hence, widths or slots greater than 50 μm are set since smaller dimensions are not ensured to be properly etched. Additionally, the 50 Ω impedances for the CPW and slotline transmission lines are calculated, for an alumina substrate [2.9], taking into account the measurement procedure with 150-μm pitch probes. Hence, the widths or gaps of the characteristics parameters in each line (see Fig. 4. 2) are obtained and listed in Table 4. 2. The election of the slotline impedance is fixed by the minimum feasible gap, which provides the nearest impedance value to the ideal 50 Ω. The selected equivalent impedance of the slotline transmission line for a 50 μm gap is Z ≈ 70 Ω.

Table 4. 2. Dimensions of the CPW and slotline lines.

Variable	Value
g	50 μm
W_C	104 μm
s	11 μm

The transition is designed using radial stubs in both CPW and slotline transmission lines as a solution that provides a wider frequency band response [4.20]. A layout of the input transition is shown in Fig. 4. 6.

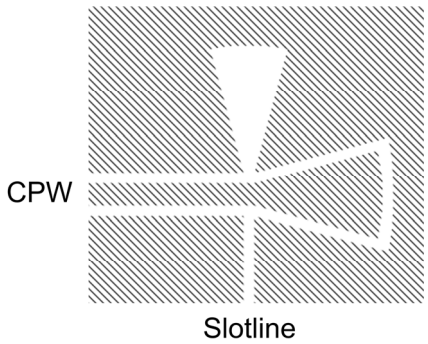

Fig. 4. 6. Layout of the input CPW-to-slotline transition.

4.2.3 Output Slotline-to-CPW Transition

The output transition from slotline to CPW transmission lines is performed using the slotline paths which directly go out from the slotline T-junction and a new CPW line. A layout of the output transition is shown in Fig. 4. 7, in which the diodes as switching devices are placed. The output transition is composed of a straight stub in slotline, defined with a switching element (D3-D4), and a radial stub in CPW line. The theoretical length of the stubs is a quarter-wavelength at the centre frequency of the working bandwidth, which defines the minimum length of the slotline paths before the output CPW. Since the size of the radial stub is similar to the straight stub and it is enclosed by the slotline paths, the length of the dual symmetrical slotline paths is set to half-wavelength. Hence, two switching elements are placed in each slotline at a quarter-wavelength distance in order to choose the transmission path. Therefore, the second diode (D3 or D4) in the path composes the straight stub of the transition to CPW line and, additionally, increases the isolation of the non-transmitting path.

The set of diodes is assembled in anti-parallel configuration for each path. Then, if a negative voltage is applied to the circuit, the diodes D1 and D3 are equivalent short-circuits, so diodes D2-D4 are in open-circuit condition, and the microwave signal is transmitted by the right path in the figure (D2-D4 diodes path). When the applied bias is reversed, the set of diodes behaves in the opposite state and the signal goes by the left path (D1-D3 path).

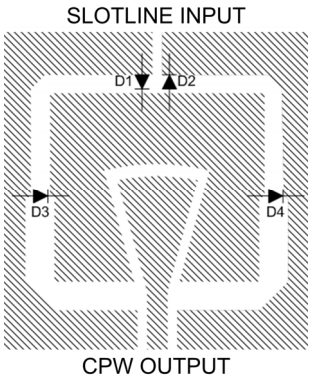

Fig. 4. 7. Layout of the output CPW-to-slotline transition.

The CPW line has the same dimensions than the input line, listed in Table 4. 2. The dimensions of the slotline paths are optimized in order to overcome mismatching effects. Therefore, the impedances of the two quarter-wavelength sections in slotline are set to different values greater than the fabrication restriction.

4.2.4 Phase Switch Design

Once the input and output transitions from CPW to slotline are described, the full phase switch circuit consists of the interconnection of the individual elements. The layout of the circuit is shown in Fig. 4. 8, in which the air bridges in the CPW lines, symbolised by black lines, and the diodes are included.

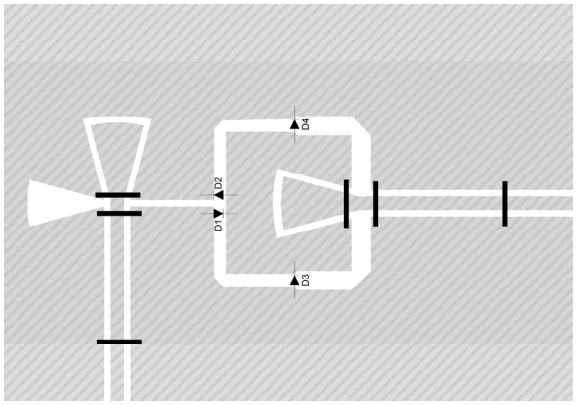

Fig. 4. 8. Phase switch circuit with the diodes and equipotential bridges assembled.

This section describes the analysis and performance of the circuit. The different subcircuits are cascaded and the effect of their interconnection is considered in order to achieve the best result. The circuit is analysed using the HPND-4005 PIN diode.

A Phase Switch Analysis

As previously described, the 180º phase switch circuit is composed of two transitions from CPW to slotline transmission lines and a slotline T-junction to have two possible transmission paths. The different impedances and electrical lengths of each section must be considered, specially taking into account the use of impedance values different from 50 Ω. In order to facilitate the analysis, the circuit shown in Fig. 4. 9 is used, assuming straight stubs, to achieve initial values for the impedances and electrical lengths described in the figure. Only one transmitting branch is considered, since it is symmetrical in the other circuit state. The straight stubs are used since their available well-known models [4.13] make easier the analysis. Once these initial values are obtained, they are replaced with radial stubs in order to guarantee the wideband operation in the 26 to 36 GHz frequency band.

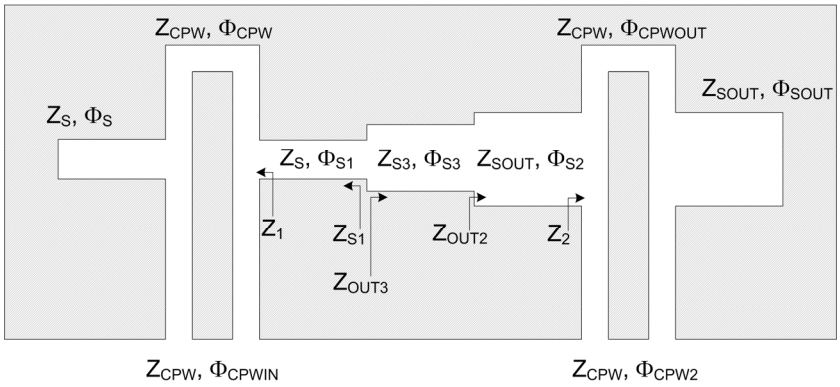

Fig. 4. 9. Phase switch dimensions for the circuit analysis.

The circuit analysis is aimed for obtaining outstanding return loss at both accesses while a flat phase shift response is achieved, so the mismatching between the input and output transitions is intended to be minimized with the condition given by

$$Z_{S1} = Z_{OUT3}^{*} \tag{4.1}$$

Therefore, in order to achieve the above condition and perform circuit analysis, an equivalent transmission line model of the CPW-to-slotline transition is assumed. The end-effects in each transmission line, either CPW or slotline, are considered as equivalent reactances. The equivalent circuit is shown in Fig. 4. 10. Besides, the end-effects can be redefined in terms of series reactances X_{CPW} and X_S and a resistance R, after modal transformation. The modal transformation ratio between CPW and slotline in this analysis is considered to be equal to 1.

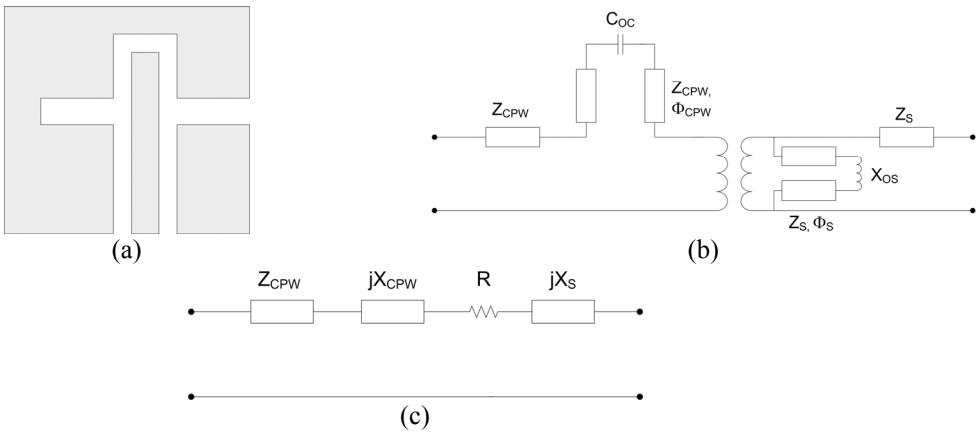

Fig. 4. 10. CPW-to-slotline transition with straight stubs. (a) Basic layout. (b) Transmission line equivalent circuit. (c) Transformed equivalent circuit.

The basic transmission line equation for the impedance calculus is applied, so the reactance values for the equivalent open-circuit in CPW line and short-circuit in slotline can be obtained as

$$jX_{CPW} = Z_{CPW} \cdot \frac{\frac{1}{jwC_{OC}} + jZ_{CPW}\tan(\Phi_{CPW})}{Z_{CPW} + \frac{\tan(\Phi_{CPW})}{wC_{OC}}} \tag{4.2}$$

$$jX_{OS} = Z_S \cdot \frac{jX_{OS} + jZ_S\tan(\Phi_S)}{Z_S - X_{OS}\tan(\Phi_S)} \tag{4.3}$$

and, after the transformation from one to the other transmission line type, an equivalent slotline impedance given by

$$R = \frac{Z_S \cdot X_{OS}^2}{Z_S^2 + X_{OS}^2} \tag{4.4}$$

$$X_S = \frac{Z_S^2 \cdot X_{OS}}{Z_S^2 + X_{OS}^2} \tag{4.5}$$

The open end-effect C_{OC} in the CPW line and the short end-effect X_{OS} in a slotline, both used in above expressions, are thoroughly analysed in [4.28] and [4.29] respectively.

In order to obtain the condition described in (4.1), the impedances in different slotline sections shown in Fig. 4. 9 are calculated. Using the previous equations (4.2)-(4.5), the impedances Z_1 and Z_2, in Fig. 4. 9, are given by

$$Z_1 = Z_{CPW} + jX_{CPW} + R + jX_S \tag{4.6}$$

$$Z_2 = Z_{CPW} + jX_{CPWOUT} + R_{OUT} + jX_{SOUT} \tag{4.7}$$

which correspond to the impedances at the transition edges in the input and output CPW-to-slotline transitions. By adding the slotline sections, the impedances Z_{S1}, Z_{OUT2} and Z_{OUT3} are expressed as

$$Z_{S1} = Z_S \frac{Z_1 + j \cdot Z_S\tan(\Phi_{S1})}{Z_S + j \cdot Z_1\tan(\Phi_{S1})} \tag{4.8}$$

$$Z_{OUT2} = Z_{SOUT} \frac{Z_2 + j \cdot Z_{SOUT}\tan(\Phi_{S2})}{Z_{SOUT} + j \cdot Z_2\tan(\Phi_{S1})} \tag{4.9}$$

$$Z_{OUT3} = Z_{S3} \frac{Z_{OUT2} + j \cdot Z_{S3}\tan(\Phi_{S3})}{Z_{S3} + j \cdot Z_{OUT2}\tan(\Phi_{S3})} \tag{4.10}$$

Once the impedances, at the point in which the slotline T-junction is located, are known, the analysis in order to fulfil the condition expressed in (4.1) is performed. Each slotline path in Fig. 4. 9 is defined by its impedance value and its electrical length and combinations between their values are performed to obtain minimum error in (4.1). The

real and imaginary part of the equation are compared trying to reach the following conditions

$$\min\left(real(Z_{S1}) - real\left(Z_{OUT3}{}^{*}\right)\right) \tag{4.11}$$

$$\min\left(imag(Z_{S1}) - imag\left(Z_{OUT3}{}^{*}\right)\right) \tag{4.12}$$

When minimum values are obtained in above expressions, the input and the output transitions are adequately matched and optimum performance is expected in terms of return loss.

The analysis is performed at 26, 31 and 36 GHz, as the lower, centre and upper frequencies of the operation band. When the sweep of the impedances and electrical lengths of the slotline paths is performed, a set of possible values for them is obtained for a threshold value of a defined figure of merit Z_{dif} (4.15). The figure of merit Z_{dif} is defined as the square root of the weighted average of the squared real part, Z_{difr}, and imaginary part, Z_{difi}, of the differential impedance between Z_{S1} and the complex conjugate of Z_{OUT3}, and they are expressed as

$$Z_{difr} = real(Z_{S1}) - real\left(Z_{OUT3}{}^{*}\right) \tag{4.13}$$

$$Z_{difi} = imag(Z_{S1}) - imag\left(Z_{OUT3}{}^{*}\right) \tag{4.14}$$

$$Z_{dif} = \sqrt{\frac{\left|Z_{difr}\right|^2 + \left|Z_{difi}\right|^2}{2}} \tag{4.15}$$

From above expressions, a minimum value of Z_{dif} is desired in order to have complex conjugate impedances in the junction of the input and output transitions. As initial considerations in the analysis, some of the impedances and electrical lengths are fixed to minimize the number of variables under swept. Therefore, the impedance Z_{CPW} of the CPW input and output lines are set to 50 Ω, with the dimensions listed in Table 4. 2, and their electrical lengths Φ_{CPWIN} and Φ_{CPW2} are set to 180º, a distance which enables the assembly of air bridges from side to side of the CPW input and output lines in order to ensure equal potentials on the side planes. The electrical length of the CPW open-circuits Φ_{CPW} and Φ_{CPWOUT}, of the intermediate slotline path Φ_{S3} and of the input slotline short-circuit Φ_{S} are set to 90º, as the typical quarter-wavelength electrical length stubs. The electrical length of the slotline short-circuit Φ_{SOUT} is equal to Φ_{S2} since they are defined by the position of the diodes. The impedance Z_{S} of the slotline path at the input transition is set to 70 Ω, which corresponds to the minimum feasible etched width

(50 μm) in the fabrication process. Hence, three variables are swept in order to achieve the condition (4.1): Z_{SOUT}, Φ_{S1} and Φ_{S2}. The slotline impedance Z_{S3} is given by

$$Z_{S3} = \sqrt{Z_{SOUT} \cdot Z_S} \tag{4.16}$$

as in a microstrip-technology quarter-wavelength transformer.

The electrical lengths Φ_{S1} and Φ_{S2} are swept in the range between 45º and 180º, while the impedance value Z_{SOUT} takes values in the margin from 85 to 110 Ω. Then, the weighted impedance difference Z_{dif} is calculated in the lower, centre and upper frequencies of the operating bandwidth (26, 31 and 36 GHz) for the different combinations, obtaining a set of values after a threshold value is fixed for (4.15) at the centre frequency of 31 GHz. The threshold condition for the weighted impedance difference is given by

$$Z_{dif} \leq 3 \tag{4.17}$$

as a trade-off between having many and none solutions for higher and lower threshold respectively.

Once the set of variables is analysed, the initial values selected for the electrical lengths Φ_{S1} and Φ_{S2} and the impedance Z_{SOUT} are listed in Table 4. 3. This solution implies that Z_{dif}=1.295 at 31 GHz, Z_{dif}=12.859 at 26 GHz and Z_{dif}=39.167 at 36 GHz.

Table 4. 3. Selected values for the swept variables.

Variable	Value
Z_{CPW}	50 Ω
Φ_{S1}	78.75º
Φ_{S2}	56.25º
Z_{SOUT}	110 Ω

Considering the values obtained for Z_{dif} at the side frequencies of the band, in order to improve the circuit performance, the straight stubs are replaced with radial ones in the input CPW-to-slotline transition (Z_S, Φ_S, Z_{CPW}, Φ_{CPW}) and in the output CPW line (Z_{CPW}, Φ_{CPWOUT}). Then, the operation bandwidth is broadened by the minimization of the weighted difference impedance in the side frequencies. The radial stubs are designed with a subtended angle of 30º in both CPW and slotline technologies.

B Phase Switch Performance

The optimization process is aided with electromagnetic simulator such as Momentum from ADS, in which a quasi-3D analysis is performed. The use of CPW and slotlines transmission lines defines that the substrate does not have backside metallization. Additionally, for slotline, a metallic material is not expected underneath the substrate in order to support the circuit since the slotline mode could not work properly and the circuit could degenerate into a bad performance. A trench or cavity with a depth of around 2 times the height of the substrate is determined from simulation results as the minimum height with no observable changes in the response.

The electromagnetic simulation of the full circuit takes into account these effects and, moreover, the measurement procedure which is intended. The circuit is going to be characterized in a coplanar probe station, so an additional structure must be used in order to avoid the contact with the probe station base. Hence, a foam-based low dielectric constant substrate [4.30] is used, with a ε_r=1.18 and a 2.59-mm thickness. The optimization is intended to obtain return loss better than 10 dB in the operation band, a flat 180º phase difference and a low amplitude imbalance between states.

The final layout of the circuit is the one shown in Fig. 4. 8. The equipotential bridges, which are gold bonding wires in the real circuit, are modelled by straight gold lines in an additional layer in the substrate structure with via holes which interconnect to the circuit surface. The equivalent substrate structure implemented in the simulator is shown in Fig. 4. 11. This solution enables the optimization of the circuit.

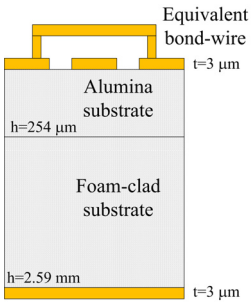

Fig. 4. 11. Substrate structure for the electromagnetic simulation (the figures are not drawn to scale).

After initial results are obtained with the equivalent bond-wires in the circuit, an additional simulation is performed in order to include the effect of the switching devices, implemented with HPND-4005 PIN diodes [3.3]. A layout of the phase switch circuit for the electromagnetic simulation, including the simulation ports, is shown in Fig. 4. 12. The electromagnetic simulator does not enable the insertion of the diode

elements, so this simulation includes internal ports (D1 to D4 in the figure) in the location in which the diodes will be assembled. The input and output of the circuit, labelled with the ports P1 and P2 in the figure, show two GND ports related to their centre ports respectively, which emulate the even CPW mode. Once the simulation is performed, the 9-port dataset is loaded with the ON-OFF diode impedances obtaining the S-parameters of the phase switch circuit. The diodes are implemented with the electrical model described in the chapter 3.4 for the HPND-4005 PIN diode.

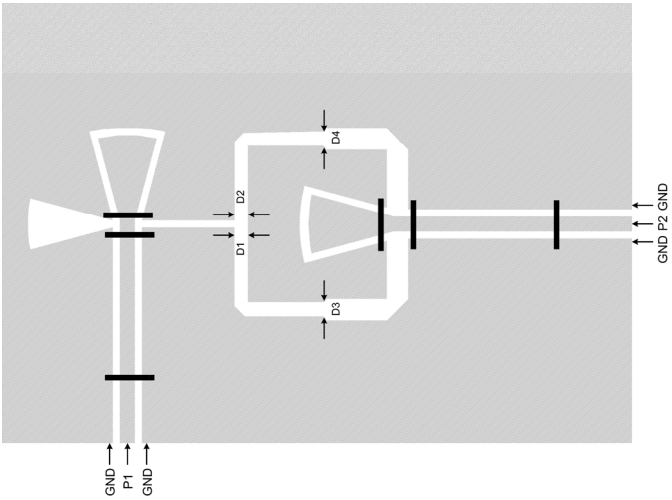

Fig. 4. 12. Layout of the phase switch for the electromagnetic simulation including the internal ports.

Once the circuit is optimized, the final dimensions are listed in Table 4. 4 (the electrical lengths are considered at the centre frequency of the operation band, 31 GHz). Three new variables are listed which correspond to the radius of the radial stubs implemented instead of the straight stubs.

Table 4. 4. Final dimensions after the optimization of the circuit (at centre frequency f=31 GHz).

Variable	Value	Variable	Value
Z_{CPW}	50 Ω	Φ_{S3}	82.1º
Z_S	68.8 Ω	Φ_{S2}	65º
Z_{S3}	88.9 Ω	Φ_{CPW2}	133º
Z_{SOUT}	105.2 Ω	r_{Φ_S}	600 µm
Φ_{CPWIN}	128º	r_{Φ_CPW}	600 µm
Φ_{S1}	51.2º	r_{Φ_CPWOUT}	600 µm

The circuit is analysed in both possible states and the electromagnetic simulations with the model of the diode are shown in Fig. 4. 13, in terms of the input and output return loss, insertion loss, phase difference and amplitude imbalance between states. From the model of the diode described in chapter 3.4, the diodes are biased with a

current I_d=20 mA to obtain a low equivalent series resistance. The simulations show input return loss better than 13 dB and insertion loss of about 2 dB in the frequency band from 26 to 36 GHz, and an average phase difference of 178.9º ± 1º with an average amplitude imbalance of 0.18 dB in the band.

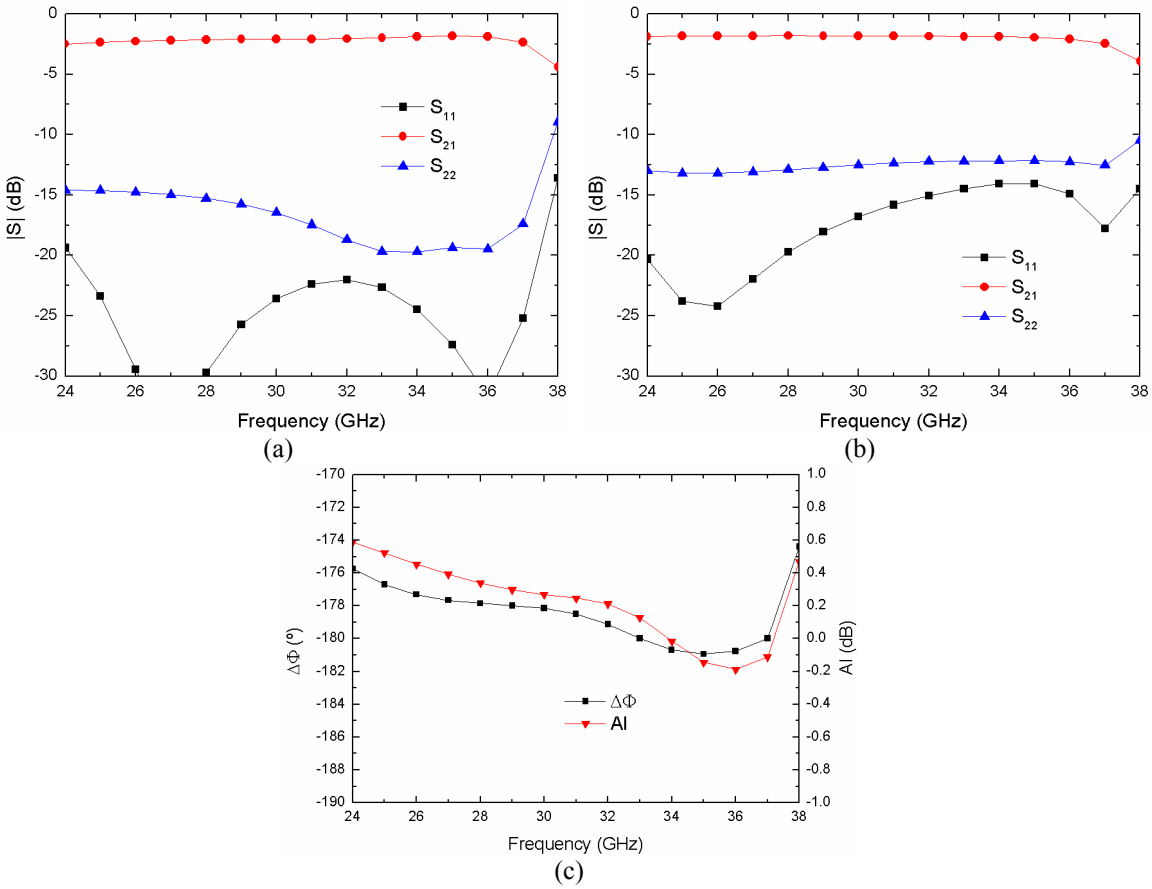

Fig. 4. 13. 180º Phase Switch S-parameters simulation results. (a) State #1. (b) State #2. (c) Phase Difference and Amplitude Imbalance.

4.3. Phase Switch Characterization

The characterization of the 180º phase switch is performed at room temperature in the coplanar probe station and, then, in a chassis at cryogenic temperature inside the cryostat. A vector network analyzer E8364A is used for both tests. At room temperature, the measurement set-up is composed of a pair of coplanar probes model 67A-GSG-150-C from PicoProbe by GGB Industries and 2.4-mm phase-stable flexible coaxial cables. A LRM calibration is performed with the CS-5 calibration substrate from PicoProbe by GGB Industries. For the cryogenic test, the circuit is assembled in a chassis and the measurement set-up is composed of 2.4-mm feedthroughs to connect the chassis with the outside of the cryostat.

The measurement of the circuit is performed using two different switching devices: the HPND-4005 PIN diode and the MA4E2037 Schottky diode. The behaviour of the PIN diode described in chapter 3 makes it unsuitable for cryogenic operation (15 K); hence, the Schottky diode is selected at that physical temperature since its power consumption is much lower than the case of the PIN diode and, then, the heating up of the cryostat is avoided.

4.3.1 Room Temperature Measurements

The 180º phase switch in 254-µm alumina substrate is characterized at room temperature in the coplanar probe station. As described before, the alumina substrate is placed over a low dielectric constant foam-clad substrate to avoid the direct connection of the bottom surface of the substrate and the base of the probe station.

The circuit in alumina substrate with the PIN diodes assembled is shown in Fig. 4. 14. In the photograph, the DC bias network of the diodes is not included, which is composed of a quarter-wavelength bond wire at the centre frequency (31 GHz), a capacitor to ground C = 0.5 pF, and a series resistor R = 10 Ω. The results of the phase switch measurement using the HPND-4005 diodes are shown in Fig. 4. 15, obtaining an average phase difference of 179.2º, a phase error lower than 1º, insertion loss of about 2 dB (similar to the predicted ones using the diode model), amplitude imbalance of about 0.3 dB and return loss better than 13 dB from 26 to 36 GHz. The results with PIN diodes are performed for a total DC current consumption of 40 mA/state.

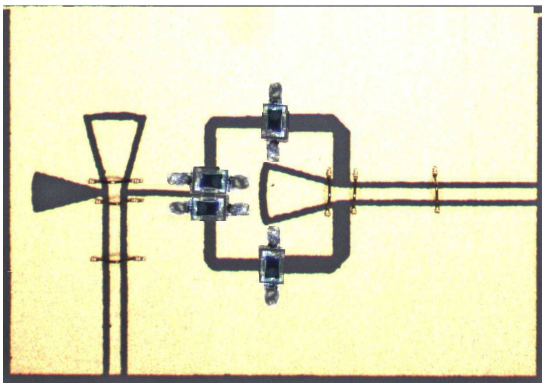

Fig. 4. 14. Photograph of the 180º phase switch on alumina substrate with four PIN diodes as switching devices. Dimensions are 3.08x4.432 mm^2.

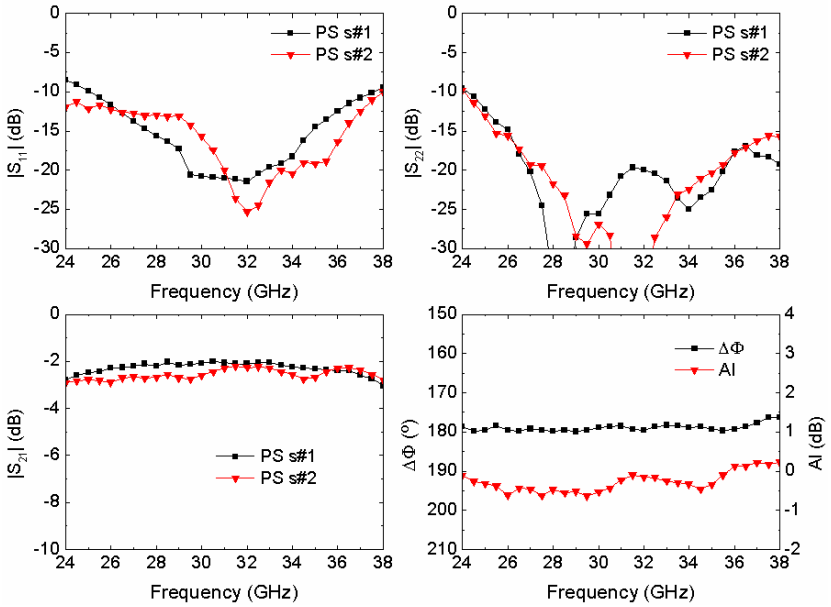

Fig. 4. 15. Alumina phase switch circuit measurements with PIN diodes: S-parameters for both states, phase difference (ΔΦ) and amplitude imbalance (AI).

Additionally, in order to compare the performances of the circuit using different switching devices, the phase switch has been also characterized using MA4E2037 Schottky diodes [3.1]. The assembly is shown in Fig. 4. 14, which includes the DC bias network. The results of the measurement of the circuit in the two possible states are shown in Fig. 4. 17, obtaining an average phase difference of 181.2º, a phase error lower than 2º and insertion loss lower than 2 dB from 26 to 36 GHz. The results with Schottky diodes are performed for a total DC current consumption of 40 mA/state. Comparing these results with the ones obtained using the HPND-4005 PIN diode, the frequency band is slightly shifted to lower frequencies. This effect is due to the effect of the equivalent capacitance of the Schottky diode under reverse bias, which is not flat versus frequency as in the case of the PIN diode.

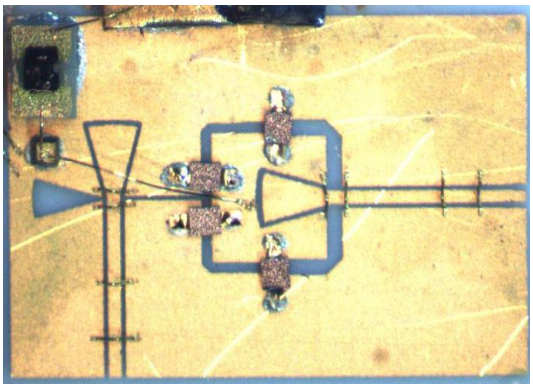

Fig. 4. 16. Photograph of the 180º phase switch on alumina substrate with Schottky diodes as switching devices and the bias network.

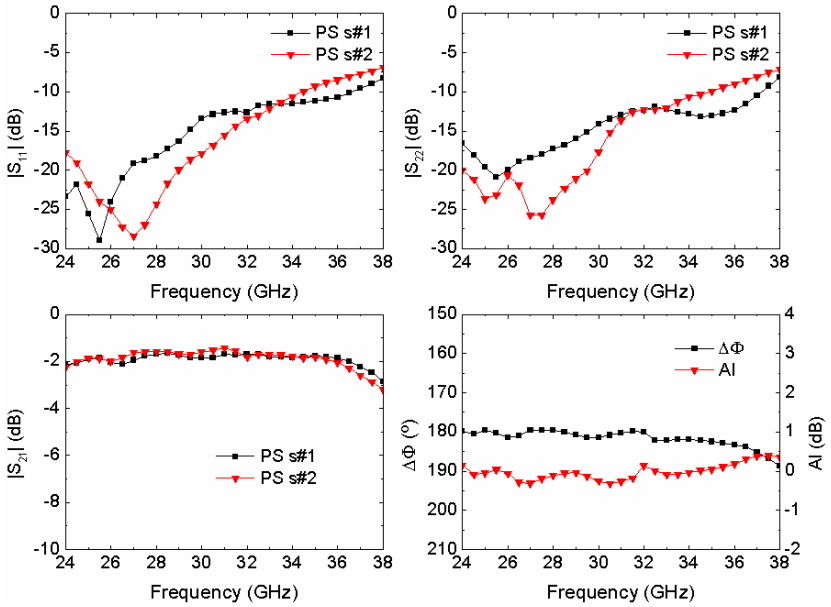

Fig. 4. 17. Alumina phase switch circuit measurements with Schottky diodes: S-parameters for both states, phase difference (ΔΦ) and amplitude imbalance (AI).

A summary of the results measured for both circuits using the two different diodes are listed in Table 4. 5, in terms of the mean values in the 26 to 36 GHz frequency band.

Table 4. 5. Comparison of the results measured of the 180º phase switch in 254-µm alumina substrate in the frequency band from 26 to 36 GHz (IL=Insertion loss; RL=Return loss).

Phase Switch	ΔΦ (º)	IL (dB)	AI (dB)	RL (dB)	I_d/state (mA)
PIN Diodes	179.2±1º	2.1	0.36	12	40
Schottky Diodes	181.2º±2º	1.8	0.01	9	40

4.3.2 Cryogenic Temperature Measurements

The 180º phase switch is also characterized at cryogenic temperatures (15 K). As in the case of the room temperature measurements, the circuit is assembled with both PIN and Schottky diodes, despite the high power consumption of PIN diodes, from previous results as individual device, makes it inadvisable for cryogenic operation. However, to compare performances, two circuits with HPND-4005 and MA4E2037 diodes as switching devices are respectively assembled and characterized.

A Phase Switch Simulation at Cryogenic Temperatures

In order to estimate the circuit performance at 15 K, the electromagnetic simulation of the circuit, considering the cryogenic features (ε_r and attenuation improvement factor) of the 254-µm alumina substrate described in chapter 2, is done. As consideration, the improvement factor in the attenuation is only applied to the conductor losses, since they are much greater than the dielectric losses. The small signal model of the MA4E2037 Schottky diode in chapter 3 is used. The simulation is performed in the same way than described for the Fig. 4. 12, using internal ports in the location where the diodes will be assembled.

The circuit is analysed in both possible states and the electromagnetic simulations with the cryogenic model of the diode are shown in Fig. 4. 18, in terms of the input and output return loss, insertion loss, phase difference and amplitude imbalance between states. From the measurements of the circuit, a current consumption of $I_d = 5$ mA is applied to the cryogenic diode model. The simulations show insertion loss of about 1.3 dB in the frequency band from 26 to 36 GHz, and an average phase difference of 181.77º ± 3º with an average amplitude imbalance of 0.18 dB in the band.

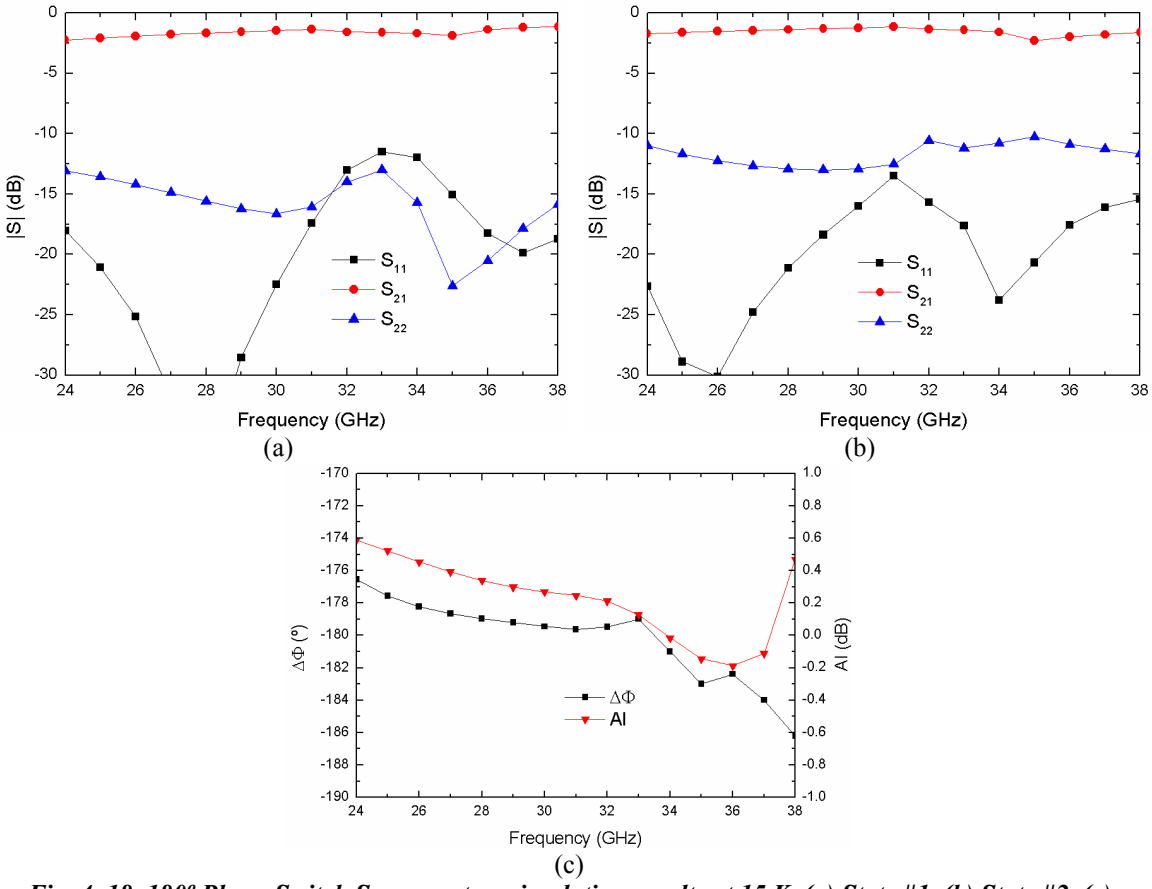

Fig. 4. 18. 180º Phase Switch S-parameters simulation results at 15 K. (a) State #1. (b) State #2. (c) Phase Difference and Amplitude Imbalance between state #1 and state #2.

B Phase Switch Mechanical Design

A mechanical chassis is designed to assemble the 180º phase switch circuit inside it and to perform the characterization at cryogenic temperatures (15 K). A view of the chassis and the lid is shown in Fig. 4. 19. The chassis includes threaded holes in order to assure a good thermal link for the cooling down. Besides, the phase switch circuit is assembled over an empty cavity (2.59-mm depth) in order to avoid the mismatching of the slotline mode (view in Fig. 4. 19(c)). Its mechanical drawings are included in Annex II.

The chassis is manufactured in brass and provides 2.4-mm coaxial connectors as radiofrequency interfaces. The 2.4-mm connectors [4.31] are from Southwest Microwave using 50 Ω seals [4.32]. Additionally, in order to assure good electrical contact during the cool down, the assembly of the CPW transmission line to coaxial transition is provided with sliding contacts [4.33]. Since the thickness of the straight contact of the sliding contact is around 150 μm, greater than the centre conductor of the CPW line (104 μm listed in Table 4. 2), the accesses of the circuits are tapered to a different 50 Ω line configuration. Extra CPW lines are connected at the input and output of the 180º phase switch circuit and the dimensions of these new lines are listed in Table 4. 6. A view of the modified circuit is shown in Fig. 4. 20.

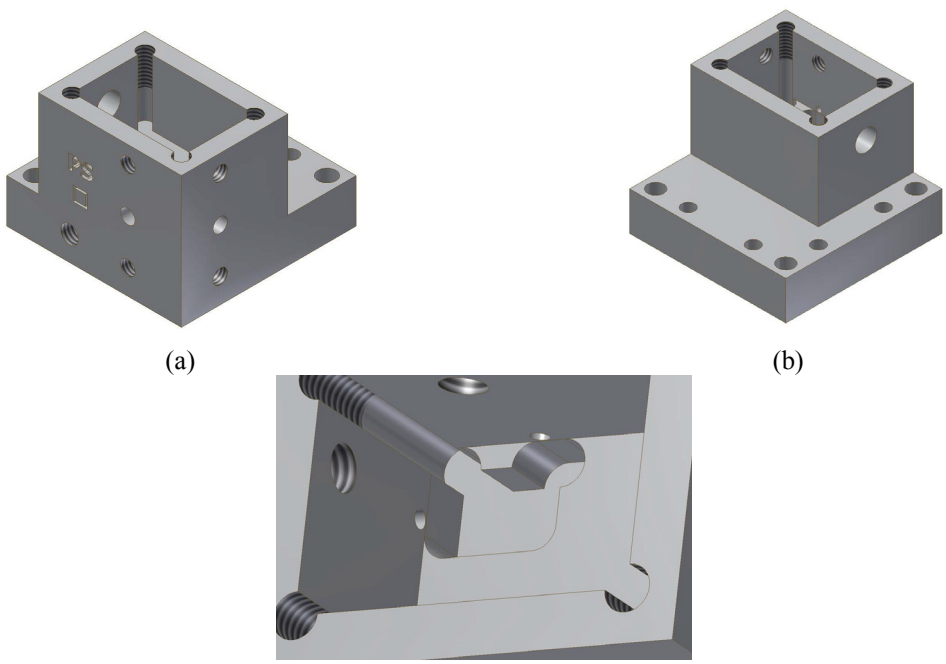

Fig. 4. 19. Artistic views of the chassis designed for the 180º phase switch in the cryogenic tests. Dimensions are 24x24x18 mm³.

Table 4. 6. Dimensions of the modified CPW lines.

Variable	Value
g'	100 µm
Wc'	247 µm

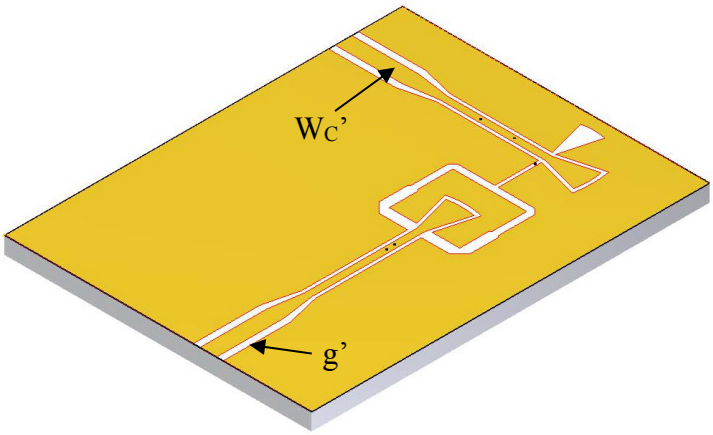

Fig. 4. 20. Layout of the modified phase switch for the cryogenic measurements.

C Characterization

The chassis inside the cryostat is thermally anchored to the cold base of the cryostat to be cooled down. Detailed views of the phase switch assembly inside the cryostat and the chassis are shown in Fig. 4. 21.

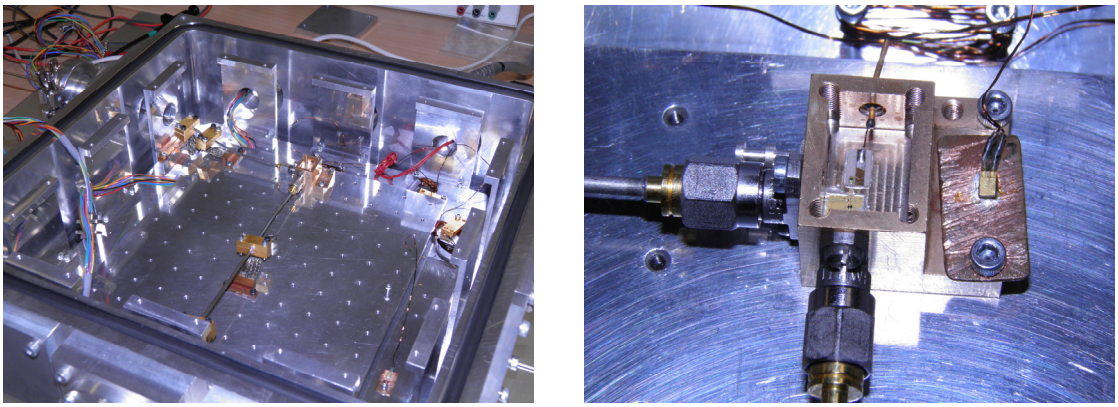

(a) (b)

Fig. 4. 21. Photograph of the cryogenic measurement set-up. (a) Assembly of the chassis inside the cryostat. (b) Detailed view of the circuit inside the chassis.

The characterization is performed using 2.4-mm coaxial feedthroughs which connect the outside of the cryostat to the chassis inside it. They are thermally attached, using heat sinks, to the different cold stages of the cryostat. The coaxial cables are model PN052140 from ARS and use a sliding mechanism which enable the introduction of a variable length of cable inside the cryostat without affecting the vacuum inside.

This measurement set-up defines the calibration reference plane outside the cryostat. Therefore, a preliminary measurement of the cables connected in 90º configuration through a 2.4-mm coaxial bend is done at cryogenic temperature in order to correct the phase switch measurement. Then, the phase switches chassis are assembled, cooled down and characterized for both switch states and the different diodes.

The measurement of the 2.4-mm cables is performed at a physical temperature of 15 K. The connection between input and output cables is done with a short coaxial bend, which losses at cryogenic temperatures are negligible compared to the ones of the cables. Hence, the transmission loss of the two cables is approached by

$$L_{2.4\_CONN}(dB) = 7.525^{-6} \cdot freq(Hz)^{0.5705} \tag{4.18}$$

Using (4.18), the losses of the 2.4-mm feedthroughs are deducted from the S-parameter measurement and the insertion loss of the phase switch circuit assembled in the mechanical chassis is obtained.

Initially, the 180º phase switch including HPND-4005 PIN diodes is assembled and measured at cryogenic temperatures. From the results provided in chapter 3, a high current bias point is needed for the HPND-4005 diode in order to provide a low series equivalent resistance.

The measurement results at 15 K of the circuit for different bias points (from 10 to 50 mA per diode) are shown in Fig. 4. 22. Mean values of the phase difference and insertion loss in the frequency band from 26 to 36 GHz are listed in Table 4. 7. From these results, the phase switch circuit using HPND-4005 diodes has not reduced its insertion loss at cryogenic operation compared to the results at room temperature. Besides, the low bias point for the diodes increases the losses in the circuit since the diode has a high series resistance in the ON state. Thus, high power consumption is required for the PIN diodes at cryogenic conditions in order to improve its cryogenic performance with respect to the room temperature circuit characteristic in terms of insertion loss. This solution is not acceptable working at cryogenics since it causes the heating up of the cryostat, increasing the physical temperatures several Kelvin. Therefore, the solution based on Schottky diodes can improve the performance of the phase switch, since for low bias conditions a low series equivalent resistance for the diode is expected, based on the results of the MA4E2037 diode measured as a single device at cryogenic temperature.

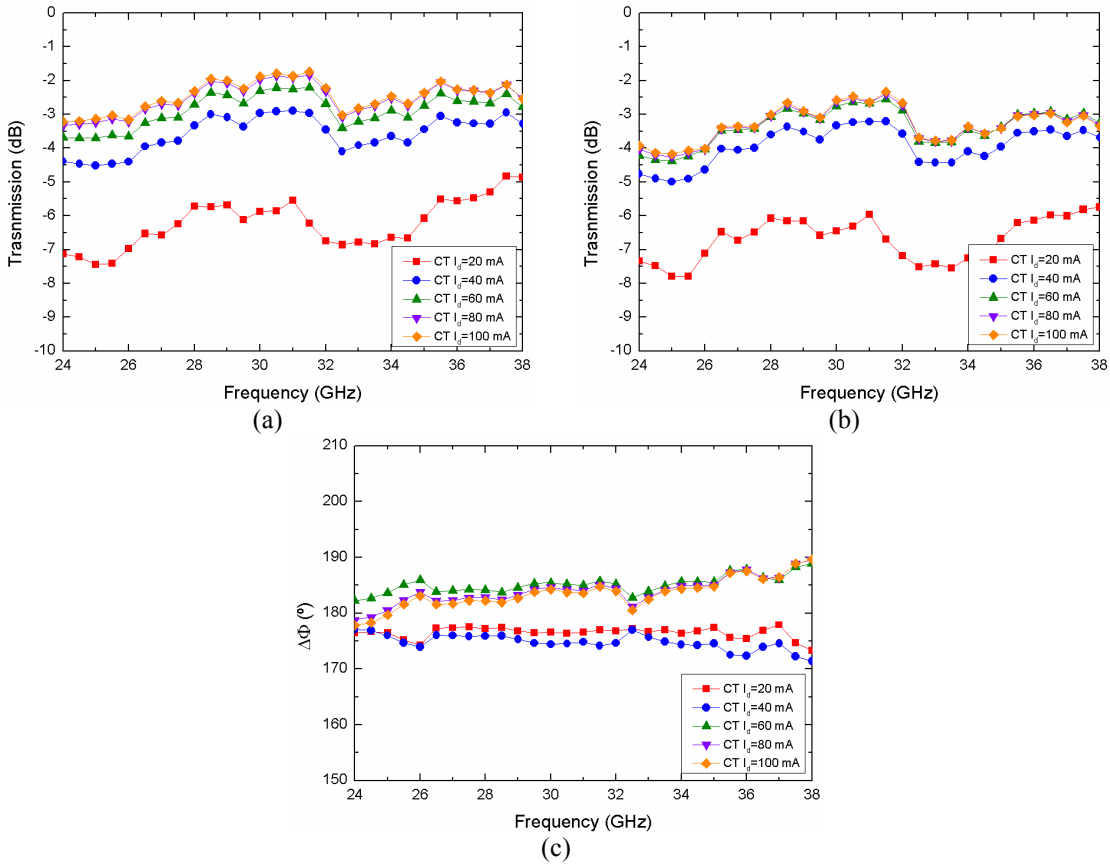

Fig. 4. 22. Results of the cryogenic measurements (CT = Cryogenic temperature) with PIN diodes. (a) Transmission losses in state #1. (b) Transmission losses in state #2. (c) Phase difference between sate #1 and state #2 for each bias point.

Table 4. 7. Mean values of the results measured of the 180º phase switch with PIN diodes in the frequency band from 26 to 36 GHz at cryogenic temperature (CT=15 K).

Conditions	ΔΦ (º)	State #1 IL (dB)	State #2 IL (dB)
CT I_d=20 mA	176.8º±3º	6.3	6.6
CT I_d=40 mA	174.9º±3º	3.5	3.8
CT I_d=60 mA	184.9º±3º	2.8	3.2
CT I_d=80 mA	183.9º±3º	2.5	3.1
CT I_d=100 mA	183.4º±3º	2.5	3.1

Thus, the 180º phase switch is assembled using MA4E2037 Schottky diodes and its characterization is done. The measurement results at 15 K of the circuit for different bias points (from 1 to 20 mA per diode) are shown in Fig. 4. 23. Mean values of the phase difference and insertion loss in the frequency band from 26 to 36 GHz are listed in Table 4. 8.

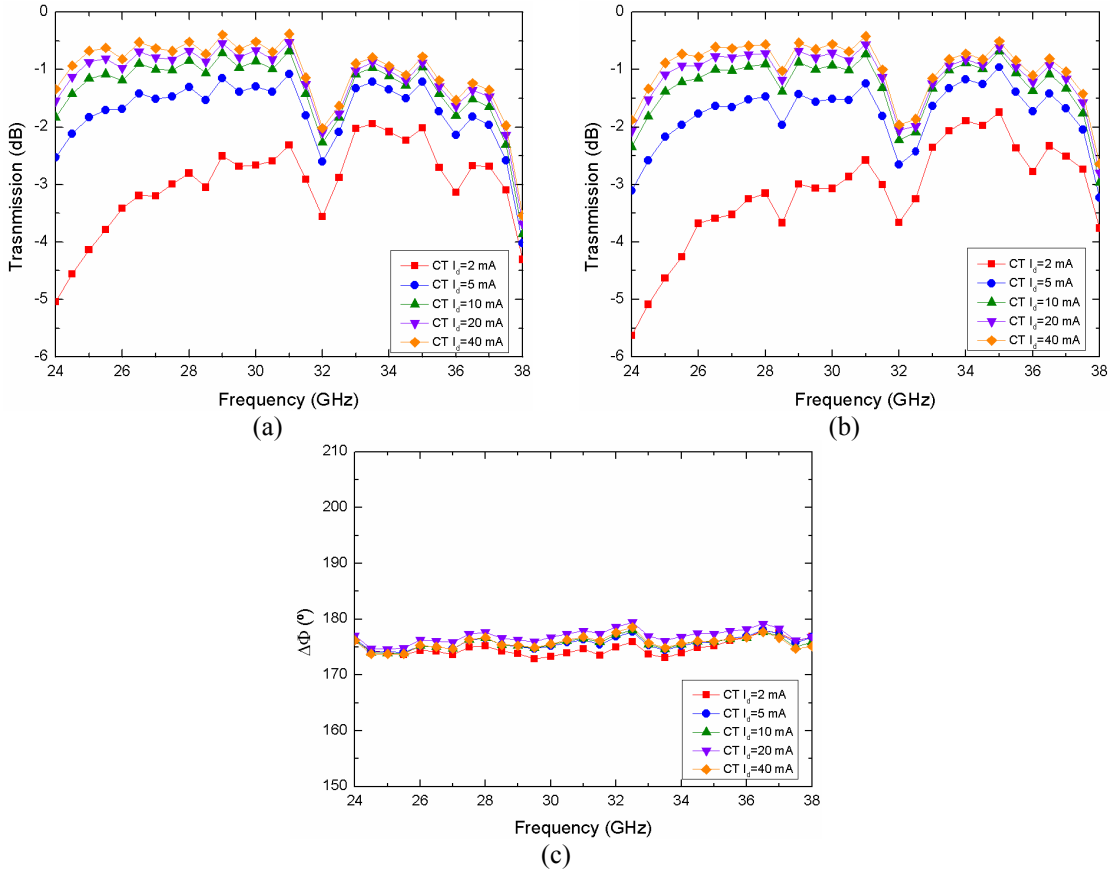

Fig. 4. 23. Results of the cryogenic measurements (CT = Cryogenic temperature) with Schottky diodes. (a) Transmission losses in state #1. (b) Transmission losses in state #2. (c) Phase difference between state #1 and state #2 for each bias point.

Table 4. 8. Mean values of the results measured of the 180º phase switch with Schottky diodes in the frequency band from 26 to 36 GHz at cryogenic temperature (CT=15 K).

Conditions	ΔΦ (º)	State #1 IL (dB)	State #2 IL (dB)
CT I_d=2 mA	174.5º±2º	2.7	2.8
CT I_d=5 mA	175.7º±2º	1.5	1.6
CT I_d=10 mA	175.9º±2º	1.2	1.2
CT I_d=20 mA	177.2º±2º	1	1
CT I_d=40 mA	176.1º±2º	0.9	0.9

At cryogenic temperature, a reduction in the insertion loss of the circuit is obtained using the MA4E2037 Schottky diode, which depends on the bias current of the diodes. From these results, a suitable bias point for the circuit is 10 mA, which correspond to 5 mA per diode at 15 K, providing an insertion loss improvement of around 0.6 dB with respect to 300 K ambient temperature results (see Table 4. 5).

4.4. Conclusions

This chapter has described the design and characterization of a 180º phase switch circuit at both room and cryogenic temperatures for operating in the 26 to 36 GHz frequency band, using CPW and slotline topologies with different diodes as switching devices.

A new 180º phase switch circuit in alumina substrate has been described, based on the existence of dual symmetrical paths which excite an output CPW line for its different gaps in which the transmission path is selected by the actuation of a set of diodes. The design of the proposed circuit has been analysed, obtaining equivalent electrical schematics as starting point. The analysis of wideband CPW-to-slotline transitions in order to obtain the best suitable solution for their electrical lengths and impedances has been described. A new slotline-to-CPW transition has been designed and analysed, based on double symmetrical paths which are connected to slotline T-junction.

Two possible solutions depending on the type of diodes used in the circuit have been presented for room temperature (300 K) and under extreme cryogenic conditions (15 K). The two diode choices are the HPND-4005 PIN diode and the MA4E2037 Schottky diode.

The design of the 180º phase switch has been aided with electromagnetic simulators and the models of the PIN and Schottky diodes described in chapter 3 have been used in order to estimate circuit performance.

The characterization of the phase switch at room temperature has been performed with both diodes in a coplanar probe station. The circuit based on PIN diode has shown an average phase difference of 179.2º, a phase error of around 1º, insertion loss of about 2.1 dB, amplitude imbalance of about 0.36 dB and return loss better than 12 dB from 26 to 36 GHz with a total current consumption of 40 mA. On the other hand, the circuit using Schottky diodes have provided an average phase shift of 181.2º, a phase error lower than 2º, insertion loss of about 1.8 dB, an almost negligible amplitude imbalance and return loss better than 9 dB, in the same frequency band, for a total current consumption of 40 mA.

The characterization of the 180º phase switch at cryogenic temperature (15 K) has been also performed with both diodes. In the particular case of the circuit with PIN diodes, the measurement has been made for different bias points. The results have not

improved the performance of the circuit at room temperature, obtaining adequate phase difference but similar or even higher insertion losses in addition to a very high power consumption, which for a cryogenic environment is not desired. This high DC bias point makes the warming up of the cryostat, therefore the use of the HPND-4005 PIN diode at cryogenic temperatures is not recommendable. When the circuit has been tested with MA4E2037 Schottky diodes, at cryogenic temperature, a phase difference of around 176º has been obtained for the different bias points applied to the diodes, and a reduction in the insertion loss of the circuit has been measured. For a current consumption of 5 mA per diode at 15 K, average insertion loss of 1.2 dB from 26 to 36 GHz have been obtained, which reduces about 0.6 dB the insertion loss at room temperature with 20 mA per diode. Therefore, the use of Schottky diodes is adequate at cryogenic temperatures since it enables a low power consumption and the performance of the phase switch is also outstanding.

Chapter V

Design of 90º Phase Switches Using Hybrid Technology

5.1. Introduction

The design of an accurate broadband 90º phase switch in hybrid technology is a significant issue in order to develop quite different subsystems for radio communications receivers. Since Schiffman proposed the approach based on coupled-strip transmission lines relative to a straight transmission line and obtained wideband behaviour with low error in phase difference [5.1], several designs have been performed in order to achieve 90º phase shifters using quite different hybrid topologies [5.2]-[5.18]. Most of reported works do not implement in the designs the use of switching devices in order to translate the phase shifter into a phase switch. Therefore, the analysis of the effect of combining the shifting branches, using switches, in the phase response by increasing the relative in-band error or mismatching issues between subsystems, is not considered. Moreover, depending on the phase switch application, the combination of the branches must fulfil a minimum amplitude imbalance between branches.

This chapter presents the development of 90º phase switches in hybrid technology using two different substrates. The combination between shifting branches is performed using different solutions. First, commercial single pole double throw (SPDT) microwave monolithic integrated circuit (MMIC) switches are used. Besides, new hybrid SPDT based on modified transitions from coplanar waveguide (CPW) to slotline transmission lines are designed with diodes as switching devices in order to select the transmission path.

5.2. 90º Phase Switch Electrical Design

The 90º phase switch is designed to be part of the QUIJOTE phase II radiometer, operating in the frequency band from 26 to 36 GHz. Some design considerations are listed in Table 5. 1. In order to accomplish phase and amplitude requirements, the analysis of the interaction between phase shifting branches and the SPDT is crucial because of the mismatching between them affects phase and amplitude errors, adding ripple in the responses.

Table 5. 1. Design specifications for the 90º phase switch.

Frequency range	26-36 GHz
Input/Output Return Loss	>10 dB
Average Phase Shift	90º
Maximum Phase Error	10º
Maximum Amplitude Imbalance	1 dB

5.2.1 Principle of Operation

The 90º phase switches are based on the combination of two broadband networks, whose insertion phases differ in 90º, using two wideband SPDT in order to convert the four accesses phase shifter network into a two accesses network. A schematic view of the proposed topology is shown in Fig. 5. 1.

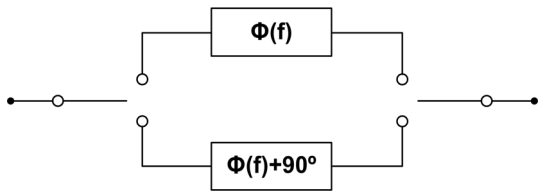

Fig. 5. 1. 90º phase switch schematic.

The broadband shifting networks are defined as Ka-band band pass filters. Using this configuration, the phase shifter branches are expected to show high return loss and low insertion loss. Furthermore, the filters contribute in the definition of the system effective bandwidth, a key aspect in a radio astronomy receiver since all the extra noise signal which enters it is mixed with the information signal and makes more difficult the detection of the real data in acquisition systems due to the very low input power signal from the observation to the receiver. The band pass filters are considered as π-networks in which the phase shift is the difference achieved between the insertion phases of each filter. Two different solutions are implemented using short-circuited or open-circuited shunt stub configurations for each one.

The SPDT must ensure in-phase symmetrical response from its input to the outputs when the signal is being transmitted by each one, as well as high isolation between outputs and between input and non-transmitting output. Besides, the impact of the interconnection of the SPDT and the filters is analyzed in order to fix minimum values of isolation and return loss of the SPDTs.

5.2.2 Band Pass Filter Design on Teflon-based Substrate

The first combination of band pass filters is designed in a π-network configuration using short-circuited shunt stubs. Therefore, a soft 127-μm Teflon-based substrate [2.26] is used in order to facilitate the fabrication process of prototypes.

The analysis of the phase shifting networks behaviour is discussed in the following sections, starting from the single analysis of short-circuited shunt stub π-network.

A Single Short-circuited Shunt Stub π-network Analysis

The π-network topology which is analyzed as basic cell of the filters is shown in Fig. 5. 2 (a), considering symmetrical π-topologies. The equivalent admittance matrix, depicted in Fig. 5. 2 (b), of a single π-network can be easily derived from circuit analysis, and, at a single frequency, it is given by

$$[Y] = j\cdot\begin{bmatrix} -\left(Y_P\cdot\cot(\theta_{si})+Y_S\cdot\cot(\theta_i)\right) & Y_S\cdot\csc(\theta_i) \\ Y_S\cdot\csc(\theta_i) & -\left(Y_P\cdot\cot(\theta_{si})+Y_S\cdot\cot(\theta_i)\right) \end{bmatrix} \tag{5.1}$$

where $Y_P = 1/Z_P$ and $Y_S = 1/Z_S$ are the admittances of the transmission lines and θ_i their electrical lengths.

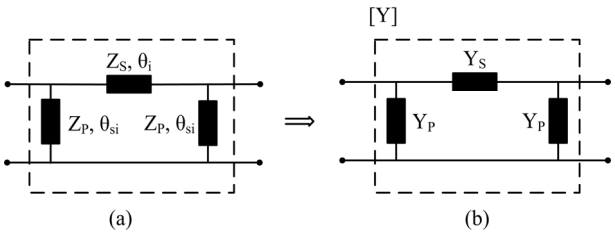

Fig. 5. 2. π-network topology. (a) Single network. (b) Equivalent Y-matrix.

Since the analyzed π-network is symmetrical, using (5.1), the transmission phase can be expressed, at a single frequency, as

$$\Phi_{\pi}(f_0) = \cos^{-1}\left(-\frac{Y_{11}}{Y_{12}}\right) = \cos^{-1}\left(\frac{Y_P \cdot \cot(\theta_{si}) + Y_S \cdot \cot(\theta_i)}{Y_s \cdot \csc(\theta_i)}\right) \tag{5.2}$$

The above expression can be solved only when the following condition is satisfied

$$|Y_{11}| \leq |Y_{12}| \tag{5.3}$$

A particular case when the series and shunt impedances are identical enables expression (5.2) to be rewritten as

$$\Phi_{\pi}(f_0) = \cos^{-1}\left(\frac{\sin(\theta_{si} + \theta_i)}{\sin(\theta_{si})}\right) \tag{5.4}$$

B 90º Phase Shifter Design Considerations

The 90º phase switch is based on a phase shifter based on two band pass filters designed using π-networks. The schematic topology of both filters is shown in Fig. 5. 3, in which the phase shifters are called respectively BPF #1 and BPF #2.

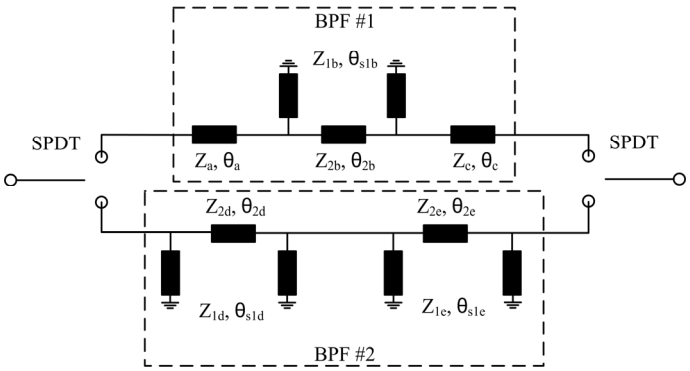

Fig. 5. 3. Band Pass Filter schematics of the proposed 90º phase switch.

The filter BPF #1 is composed of a π-network with a pair of series transmission lines in its accesses. On the other hand, BPF #2 uses two cascaded π-networks.

Considering the impedance and electrical length of each transmission line and substituting them into (5.1), the admittance matrix of each filter can be obtained. Besides, the series transmission lines as a reciprocal network can be represented by an equivalent π-network [5.19] and its admittance matrix is given by

$$[Y]_L = j\cdot\begin{bmatrix} \dfrac{1}{Z_L\cdot\tan(\theta_L)} & \dfrac{-1}{Z_L\cdot\sin(\theta_L)} \\ \dfrac{-1}{Z_L\cdot\sin(\theta_L)} & \dfrac{1}{Z_L\cdot\tan(\theta_L)} \end{bmatrix} \tag{5.5}$$

and the equivalent matrix is shown in Fig. 5. 4.

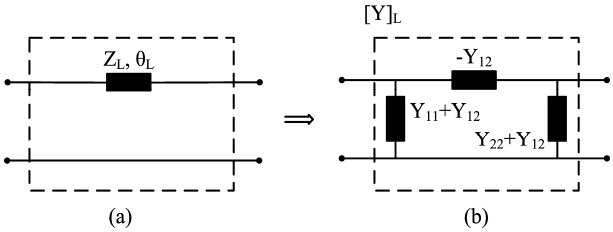

Fig. 5. 4. Equivalent π-network of a series transmission line. (a) Series line. (b) Equivalent Y-matrix.

Therefore, using the expression (5.2) for calculating the phase of a π-network, the frequency-dependant transmission phase of each filter can be expressed as

$$\Phi_{BPF\,\#1}(\eta) = \eta\cdot(\theta_a + \theta_c) + \cos^{-1}\left(\frac{Y_{1b}\cdot\cot(\eta\cdot\theta_{s1b}) + Y_{2b}\cdot\cot(\eta\cdot\theta_{2b})}{Y_{2b}\cdot\csc(\eta\cdot\theta_{2b})}\right) \tag{5.6}$$

$$\begin{aligned}\Phi_{BPF\,\#2}(\eta) = {} & \cos^{-1}\left(\frac{Y_{1d}\cdot\cot(\eta\cdot\theta_{s1d}) + Y_{2d}\cdot\cot(\eta\cdot\theta_{2d})}{Y_{2d}\cdot\csc(\eta\cdot\theta_{2d})}\right) \\ & + \cos^{-1}\left(\frac{Y_{1e}\cdot\cot(\eta\cdot\theta_{s1e}) + Y_{2e}\cdot\cot(\eta\cdot\theta_{2e})}{Y_{2e}\cdot\csc(\eta\cdot\theta_{2e})}\right)\end{aligned} \tag{5.7}$$

where $\eta = f/f_0$ is the normalized frequency, $Y_i = 1/Z_i$ is the admittance and θ_i the electrical length of each transmission line. In order to obtain the phase difference of the phase shifter, (5.6) and (5.7) are deducted.

Once the expression of the phase difference is achieved, the analysis of impedance and electrical length values for each transmission line must be performed in order to achieve 90º phase shift with minimum in-band phase error. As initial approach the electrical length of the transmission lines is considered as a quarter-wavelength. Moreover, the π-networks in BPF #2 are defined identical, so $Z_{1d} = Z_{1e}$ and $Z_{2d} = Z_{2e}$. Hence, the phase difference between band pass filters under these conditions is expressed as

$$\Delta\Phi(\eta) = \eta\cdot\pi + \cos^{-1}\left(\left(\frac{Y_{1b}}{Y_{2b}}+1\right)\cdot\cos\left(\eta\frac{\pi}{2}\right)\right) - 2\cdot\cos^{-1}\left(\left(\frac{Y_{1d}}{Y_{2d}}+1\right)\cdot\cos\left(\eta\frac{\pi}{2}\right)\right) \tag{5.8}$$

This analysis consists of impedance value sweeps in order to achieve 90º phase shift between branches. The phase error PE is defined as a figure of merit as

$$PE(^\circ) = \left|90^\circ - \left|\Delta\Phi(^\circ)\right|\right| \tag{5.9}$$

The analysis provides optimum value for the impedances by calculating the maximum value of the phase error over the frequency band from 26 to 36 GHz. A range of impedances between $Z_0/\sqrt{2}$ and $\sqrt{2}\cdot Z_0$ is considered (assuming $Z_0 = 50\ \Omega$), and a combination of values is taken for the ratios Y_{1b}/Y_{2b} and Y_{1d}/Y_{2d} in (5.8). For each ratio of impedances in BPF #1, the ratio of impedances in BPF #2 is swept. Fig. 5. 5 shows the maximum error over the band. The minimum in-band PE is obtained when the ratios Y_{1b}/Y_{2b} and Y_{1d}/Y_{2d} are around 1, whereas the maximum PE is achieved for the ratios $Y_{1b}/Y_{2b} = 1/\sqrt{2}$ and $Y_{1d}/Y_{2d} = \sqrt{2}$.

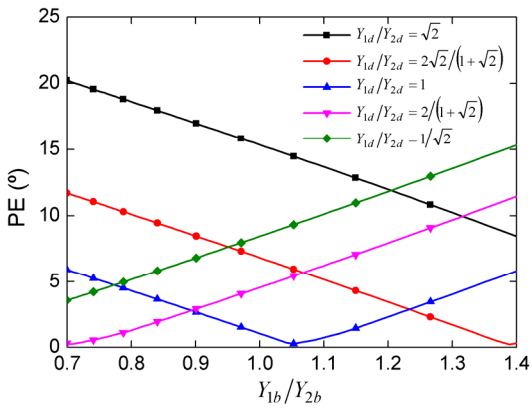

Fig. 5. 5. Maximum phase error versus admittance ratios of BPF #1 in the frequency band from 26 to 36 GHz for different admittance ratios of BPF #2.

The phase difference for both cases are, respectively, given by

$$\Delta\Phi_{\min}(\eta) = \eta\cdot\pi - \cos^{-1}\left(2\cdot\cos\left(\eta\frac{\pi}{2}\right)\right) \tag{5.10}$$

$$\Delta\Phi_{\max}(\eta) = \eta\cdot\pi + \cos^{-1}\left(\left(\frac{1}{\sqrt{2}}+1\right)\cdot\cos\left(\eta\frac{\pi}{2}\right)\right) - 2\cdot\cos^{-1}\left(\left(\sqrt{2}+1\right)\cos\left(\eta\frac{\pi}{2}\right)\right) \tag{5.11}$$

The above analysis provides a value of impedance ratio aiming for minimum PE, but additional considerations must be taken into account in order to fulfil design

requirements to define the characteristic impedances of the transmission lines, since PE is only dependent on the ratio between them. Therefore, assuming the ratio of impedances in each branch is equal to 1, a range of values for the impedances is defined in order to calculate the S-parameters of each band pass filter.

The analysis of S-parameters defines two extra design considerations: the amplitude imbalance and the return loss. The amplitude imbalance, AI, is defined as

$$AI\left(dB\right) = 10 \cdot \log 10 \left| S_{21\,BPF\,\#1} \,/\, S_{21\,BPF\,\#2} \right|^2 \tag{5.12}$$

A minimum value over the band 26-36 GHz is desired in (5.12) and, simultaneously, optimum return loss, so impedance value sweeps are performed for both filters. The selected values of impedances, in a range from low to high figures, are between $Z_0/\sqrt{2}$ and $\sqrt{2}\cdot Z_0$. The impedances of the input Z_a and output Z_c transmission lines in BPF #1 are assumed to be the same values as the impedances of the π-network in its branch $Z_{1b} = Z_{2b}$. The maximum value of the amplitude imbalance in the 26-36 GHz frequency range versus normalized admittance of BPF #1 ($\overline{Y_{1b}} = Y_{1b}/Y_0$) is shown in Fig. 5. 6. Since the selected admittance ratio is 1, the admittances of the BPF #2 are swept maintaining this ratio for all of them ($Y_{1d} = Y_{2d} = Y_{1e} = Y_{2e}$). As shown in Fig. 5. 6, the optimum value for AI is achieved when the normalized admittance for both filters is equal to 1.

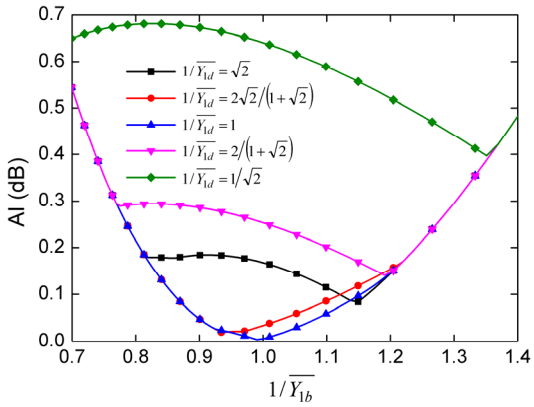

Fig. 5. 6. Maximum amplitude imbalance versus normalized admittance of BPF #1 in the frequency band from 26 to 36 GHz for different normalized admittances of BPF #2.

Moreover, the return loss in each branch is analyzed for the same admittance, since optimum return loss and minimum AI are not always achieved for the same conditions. The maximum return loss over the frequency range from 26 to 36 GHz versus normalized admittance is depicted in Fig. 5. 7. The values of the normalized

admittances $\overline{Y_i}$, where i represents each labelled impedance in Fig. 5. 3, are the admittances for filters BPF #1 and BPF #2. Considering $\overline{Y_i} = 1$, both filters show a return loss level better than 20 dB in the band of interest; in the case of an admittance ratio that is not 1, unbalanced input return loss is obtained.

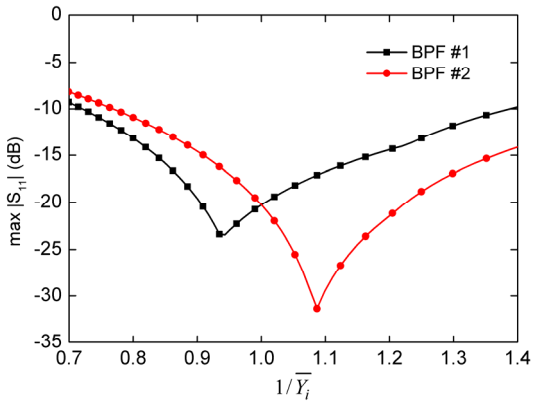

Fig. 5. 7. Maximum input return loss versus normalized admittance of BPF #1 and BPF #2 in the frequency band from 26 to 36 GHz.

The analysis of AI and return loss, shown in Fig. 5. 6 and Fig. 5. 7, are based on the use of S-parameters. In this particular case, the expressions of input return loss and insertion loss are analyzed when quarter-wavelength transmission lines are used, the admittance ratios are fixed at 1 ($Y_{1b}/Y_{2b} = 1$, $Y_{1d}/Y_{2d} = 1$, and $Y_{1e}/Y_{2e} = 1$) and the impedances of the input and output series transmission lines in BPF #1 have the same value as the impedances of the π-network in BPF #1 ($Z_a = Z_b = Z_{1b}$). The input return loss and insertion loss of each branch, considering $\overline{Y_i} = 1$, are given by

$$S_{11(BPF\#1)} = \frac{-j\cdot 6\cdot(\cos(\eta\pi)+1)}{2\cdot\sin(\eta\pi)+9\cdot\sin(2\eta\pi)+j\cdot[1+2\cdot\cos(\eta\pi)+9\cdot\cos(2\eta\pi)]} \tag{5.13}$$

$$S_{11(BPF\#2)} = \frac{-j\cdot 3\cdot\left(3\cdot\cos\left(\eta\frac{\pi}{2}\right)+3\cdot\cos\left(3\eta\frac{\pi}{2}\right)\right)}{2\cdot\sin\left(\eta\frac{\pi}{2}\right)+4\cdot\sin\left(3\eta\frac{\pi}{2}\right)+j\cdot\left[7\cdot\cos\left(\eta\frac{\pi}{2}\right)+5\cdot\cos\left(3\eta\frac{\pi}{2}\right)\right]} \tag{5.14}$$

$$S_{21(BPF\#1)} = \frac{8\cdot\sin\left(\eta\frac{\pi}{2}\right)}{2\cdot\sin(\eta\pi)+9\cdot\sin(2\eta\pi)+j\cdot[1+2\cdot\cos(\eta\pi)+9\cdot\cos(2\eta\pi)]} \tag{5.17}$$

$$S_{21(BPF\#2)} = \frac{2\cdot\sin\left(\eta\frac{\pi}{2}\right)}{2\cdot\sin\left(\eta\frac{\pi}{2}\right)+4\cdot\sin\left(3\eta\frac{\pi}{2}\right)+j\cdot\left[7\cdot\cos\left(\eta\frac{\pi}{2}\right)+5\cdot\cos\left(3\eta\frac{\pi}{2}\right)\right]} \tag{5.16}$$

As conclusion, the proposed 90º phase switch enables minimum phase error and amplitude imbalance to be achieved, as well as remarkable return loss in the band of interest. The circuit analysis shows that a design using quarter-wavelength transmission lines at the centre frequency f_0 with characteristic impedance of $Z_0 = 50\ \Omega$ satisfies the requirements of error, imbalance and matching. Furthermore, this transmission line impedance makes the implementation of the circuit easier. The performances in terms of input return loss, insertion loss, phase difference and amplitude imbalance from 24 to 38 GHz of the ideal phase shifter for both filters are depicted in Fig. 5. 8.

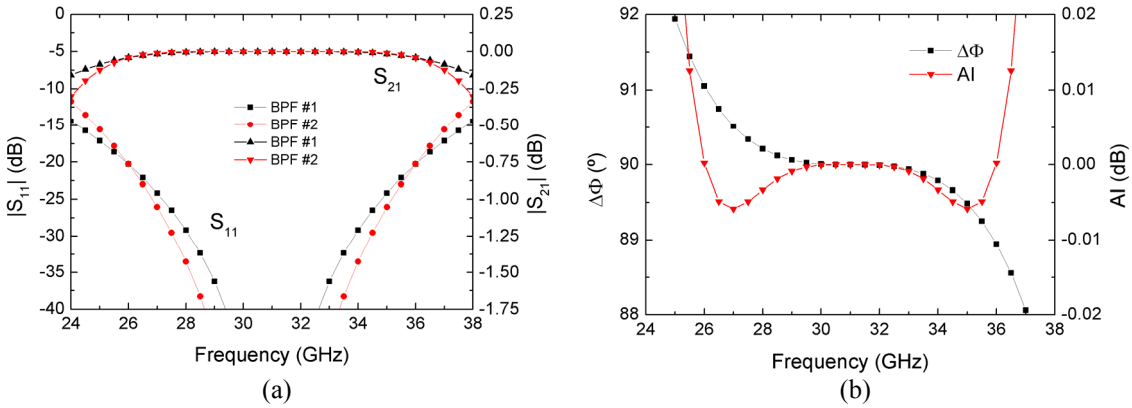

Fig. 5. 8. Ideal response of short-circuited stubs filters. (a) Return loss and insertion loss. (b) Phase difference and amplitude imbalance.

C 90º Phase Shifter Design

The previous analysis determines the ideal initial design parameters for the short-circuited stub microstrip band pass filters, which are set to 50 Ω impedance quarter-wavelength transmission lines. The design is done on CLTE-XT Arlon substrate, with 127-µm thickness, $\varepsilon_r = 2.79$ and $\tan\delta = 0.0012$. The design is aided with 3D electromagnetic simulators and, considering the microstrip approach for optimization purpose, hereafter the interconnections (T-junctions) between transmission lines are added and taken into account due to their relevant effect in millimeter-wave frequencies. Therefore, design parameters are optimized in order to fulfill PE, AI and return loss requirements. Besides, the BPF #2 is divided into two cascaded π-networks as shown in Fig. 5. 3. Thus, the shunt stubs of each network, connected to the same electrical point and with the same impedances ($Z_{1d} = Z_{1e}$), are simplified to an equivalent shunt stub with the same impedance value and an equivalent electrical length given by

$$\theta_{seq} = \cot^{-1}\left(\cot\left(\theta_{s1d}\right) + \cot\left(\theta_{s1e}\right)\right) \tag{5.17}$$

Once the optimization is performed, the schematic of both filters with the equivalent shunt stub in BPF #2 is depicted in Fig. 5. 9(a). Moreover, it shows the dimensions of the different transmission lines, in terms of widths and physical lengths. The layouts of the final filters are shown in Fig. 5. 9(b).

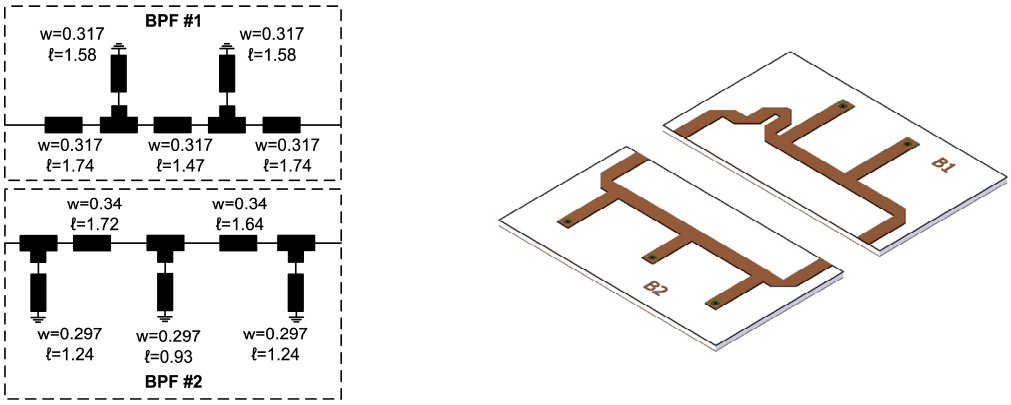

(a) (b)

Fig. 5. 9. CLTE-XT filters. (a) Schematics of the filters with dimensions (in mm) of the microstrip lines. (b) Layout of both filters.

The results of the electromagnetic simulation are shown in Fig. 5. 10. Fig. 5. 10(a) depicts the insertion loss and the return loss of both filters, while Fig. 5. 10(b) shows the phase difference and the amplitude imbalance between them.

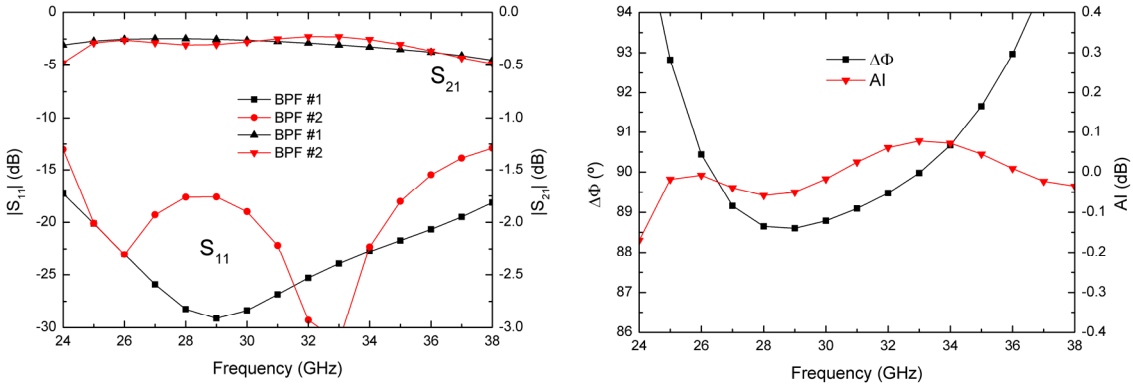

(a) (b)

Fig. 5. 10. Electromagnetic simulation of the CLTE-XT filters. (a) Return loss and insertion loss. (b) Phase difference and amplitude imbalance.

The simulation results show input return loss better than 15 dB and insertion loss of about 0.3 dB in the frequency band from 26 to 36 GHz. Phase difference result shows an average value of 91.39º ± 4º and an average amplitude imbalance of 0.05 dB from 24 to 38 GHz. Therefore, a relative bandwidth of 45 % is achieved. Considering the bandwidth of the radiometer (from 26 to 36 GHz), a phase difference of 89.9º ± 2.5º is obtained.

5.2.3 Band Pass Filter Design on Alumina Substrate

A second choice is selected using a 254-μm alumina substrate [2.9] and based on the combination of band pass filters designed in a π-network configuration using open-circuited shunt stubs.

The same analysis as in previous section with the phase shifter is performed, starting with the analysis of a single π-network with open-circuited shunt stubs as basis of the filters.

A Single Open-circuited Shunt Stub π-network Analysis

The basic π-network topology used in the design of the filters is shown in Fig. 5. 11(a). The equivalent admittance matrix, depicted in Fig. 5. 11(b), of a single π-network can be easily obtained at a single frequency and it is given by

$$[Y] = j \cdot \begin{bmatrix} Y_P \cdot \tan(\theta_{si}) - Y_S \cdot \cot(\theta_i) & Y_S \cdot \csc(\theta_i) \\ Y_S \cdot \csc(\theta_i) & Y_P \cdot \tan(\theta_{si}) - Y_S \cdot \cot(\theta_i) \end{bmatrix} \tag{5.18}$$

where $Y_P = 1/Z_P$ and $Y_S = 1/Z_S$ are the admittances of the transmission lines and θ_i their electrical lengths.

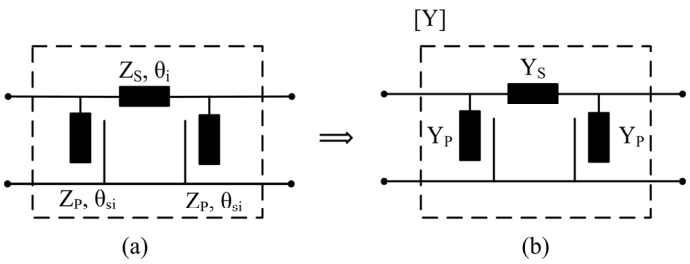

Fig. 5. 11. π-network topology. (a) Single network. (b) Equivalent Y-matrix.

Using (5.19) and considering a symmetrical π-network, the transmission phase of the network can be expressed, at a single frequency, as

$$\Phi_\pi(f_0) = \cos^{-1}\left(-\frac{Y_{11}}{Y_{12}}\right) = \cos^{-1}\left(\frac{-Y_P \cdot \tan(\theta_{si}) + Y_S \cdot \cot(\theta_i)}{Y_s \cdot \csc(\theta_i)}\right) \tag{5.19}$$

which can be only solved when the expression (5.3) is satisfied.

The particular case of identical impedance value in series and shunt transmission lines enables to simplify the phase expression as

$$\Phi_\pi(f_0) = \cos^{-1}\left(\frac{\cos(\theta_{si} + \theta_i)}{\cos(\theta_{si})}\right) \tag{5.20}$$

B 90º Phase Shifter Design Considerations

The schematic topology is analogous as the previous design using short-circuited shunt stubs, but swapping them with open-circuited ones. It is shown in Fig. 5. 12, in which the phase shifters are called respectively BPF #1 and BPF #2.

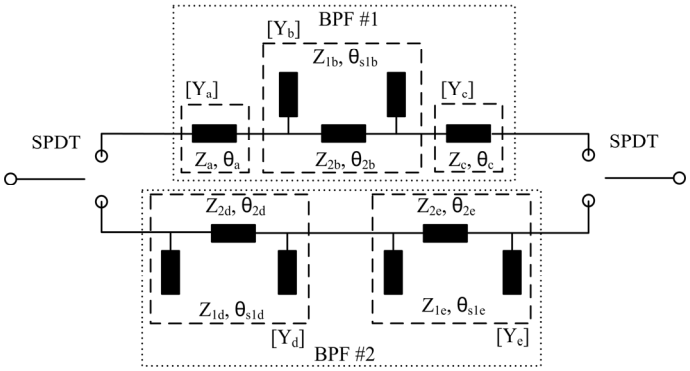

Fig. 5. 12. Schematics of the proposed filters for the 90º phase switch.

If the impedance and electrical length of each transmission line is substituted into (5.18), the admittance matrix of each π-network in the filters can be obtained. Moreover, using (5.5) for the series transmission lines, the full matrix of the BPF #1 can be achieved.

The frequency-dependant phase of each filter is calculated using the expression (5.19) and it is given by

$$\Phi_{BPF\,\#1}(\eta) = \cos^{-1}\left(\frac{-Y_{1b}\cdot\tan(\eta\cdot\theta_{s1b}) + Y_{2b}\cdot\cot(\eta\cdot\theta_{2b})}{Y_{2b}\cdot\csc(\eta\cdot\theta_{2b})}\right) + \eta\cdot(\theta_a + \theta_c) \tag{5.21}$$

$$\Phi_{BPF\,\#2}(\eta) = \cos^{-1}\left(\frac{-Y_{1d}\cdot\tan(\eta\cdot\theta_{s1d}) + Y_{2d}\cdot\cot(\eta\cdot\theta_{2d})}{Y_{2d}\cdot\csc(\eta\cdot\theta_{2d})}\right) + \cos^{-1}\left(\frac{-Y_{1e}\cdot\tan(\eta\cdot\theta_{s1e}) + Y_{2e}\cdot\cot(\eta\cdot\theta_{2e})}{Y_{2e}\cdot\csc(\eta\cdot\theta_{2e})}\right) \tag{5.22}$$

where $\eta = f/f_0$ is the normalized frequency, $Y_i = 1/Z_i$ is the admittance and θ_i the electrical length of each transmission line. The difference between both expressions provides the phase difference of the phase shifter.

The analysis of impedance and electrical length values for each transmission line must provide minimum in-band phase error. As initial approach for this case, the electrical length of the series transmission lines is considered as a quarter-wavelength, while the shunt ones are set to half-wavelength at centre frequency. Moreover, the π-networks in BPF #2 are defined identical, so $Z_{1d} = Z_{1e}$ and $Z_{2d} = Z_{2e}$, while $Z_a = Z_b = Z_{2b}$

is considered in BPF #1. Under these conditions, the phase difference of the phase shifter is expressed as

$$\Delta\Phi(\eta) = \eta\cdot\pi + \cos^{-1}\left(\frac{-Y_{1b}}{Y_{2b}}\cdot\tan(\eta\pi)\cdot\sin\left(\eta\frac{\pi}{2}\right) + \cos\left(\eta\frac{\pi}{2}\right)\right) - 2\cdot\cos^{-1}\left(\frac{-Y_{1d}}{Y_{2d}}\cdot\tan(\eta\pi)\cdot\sin\left(\eta\frac{\pi}{2}\right) + \cos\left(\eta\frac{\pi}{2}\right)\right) \quad (5.23)$$

Defining the figure of merit (5.9) for this case, the impedance value sweeps are performed in order to achieve the minimum phase error from the set of maximum values for impedance combinations in the band from 26 to 36 GHz. A range of impedances between $Z_0/\sqrt{2}$ and $\sqrt{2}\cdot Z_0$ is considered, with $Z_0 = 50\ \Omega$, for the ratios Y_{1b}/Y_{2b} and Y_{1d}/Y_{2d} in (5.23), and the ratio of impedances in BPF #2 is swept for each ratio of impedances in BPF #1. Fig. 5. 13 shows the maximum phase error over the band. Since several minima are obtained for close values of ratio Y_{2d}/Y_{1d}, a threshold value for PE is set in order to obtain the best choice. Considering a PE lower than 0.5º, three minimum in-band values are obtained when the ratios (Y_{2b}/Y_{1b}, Y_{2d}/Y_{1d}) are set to [(1, 1.35), $(1+\sqrt{2})/2$, 1.55), ($\sqrt{2}$, 1.72)]. The selected value will arise from the analysis of the S-parameters, in terms of the return loss, and the amplitude imbalance. Minimum value AI and optimum return loss are desired.

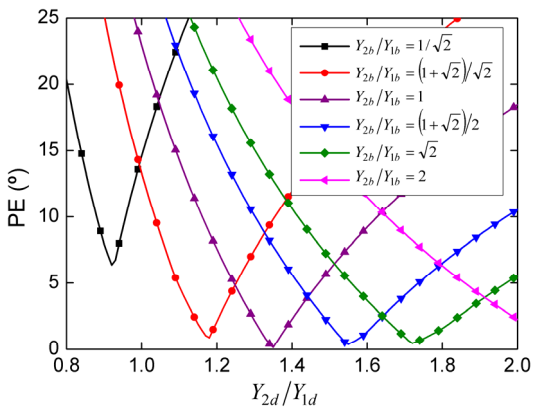

Fig. 5. 13. Maximum phase error versus admittance ratios of BPF #1 in the frequency band from 26 to 36 GHz for different admittance ratios of BPF #2.

Considering the ratios of admittances (Y_{2b}/Y_{1b}, Y_{2d}/Y_{1d}) in each branch for minimum PE, the admittances Y_{2b} and Y_{2d} are swept in a range between $1/\sqrt{2}\cdot Y_0$ and $\sqrt{2}/Y_0$ (Y_0=1/50) and the AI are analyzed. The maximum value of the amplitude imbalance for each sweep is calculated in the 26-36 GHz frequency range and they are shown in Fig. 5. 14(a), (b) and (c) for the three ratios.

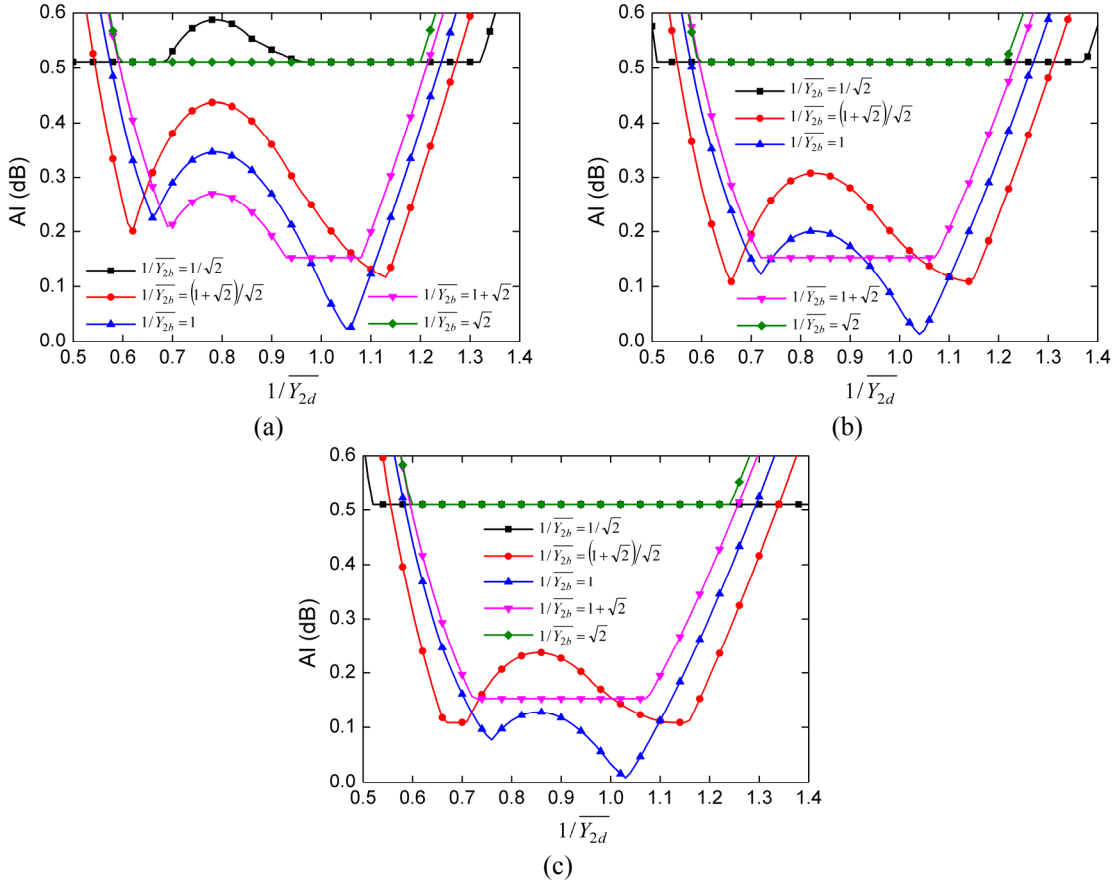

Fig. 5. 14. Maximum amplitude imbalance versus normalized admittance of BPF #2 in the band from 26 to 36 GHz for different ratios of admittances (Y2b/Y1b, Y2d/Y1d) in each branch. (a) Ratio (1, 1.35). (b) Ratio ((1+$\sqrt{2}$)/2, 1.55). (c) Ratio ($\sqrt{2}$, 1.72).

From the above figures, the three sweeps that provide the smallest value of AI are shown together in Fig. 5. 15 versus $1/\overline{Y_{2d}}$, since the $1/\overline{Y_{2b}}$ sweep provides an optimum value equal to 1. An optimum value for AI is achieved when the normalized admittances for both filters are equal to $1/\overline{Y_{2d}}=1.03$, $\overline{Y_{1d}}=\overline{Y_{2d}}/1.72$, $\overline{Y_{2b}}=1$ and $\overline{Y_{1b}}=\overline{Y_{2b}}/\sqrt{2}$.

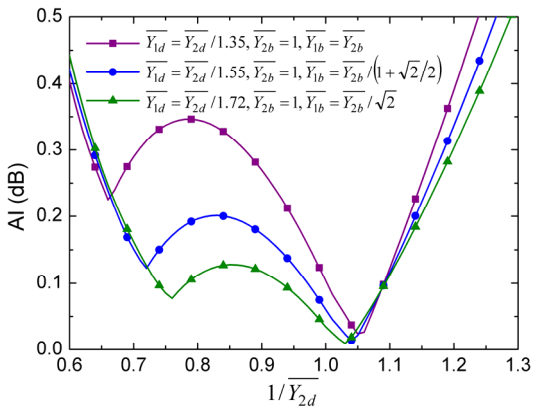

Fig. 5. 15. Maximum amplitude imbalance versus normalized series admittance, $\overline{Y_{2d}}$, in the frequency band from 26 to 36 GHz for different admittance ratios.

Moreover, the return loss in each branch is analyzed for the minimum AI sweeps. The maximum return loss over the frequency range from 26 to 36 GHz versus normalized series admittance is depicted in Fig. 5. 16 for both filters and the three ratios. The optimum values are achieved when $1/\overline{Y_{2b}} = 1.13$ for BPF #1 and $1/\overline{Y_{2d}} = 0.89$ for BPF #2. When the lowest AI value is considered, the maximum return loss is better than 15 dB for both filters.

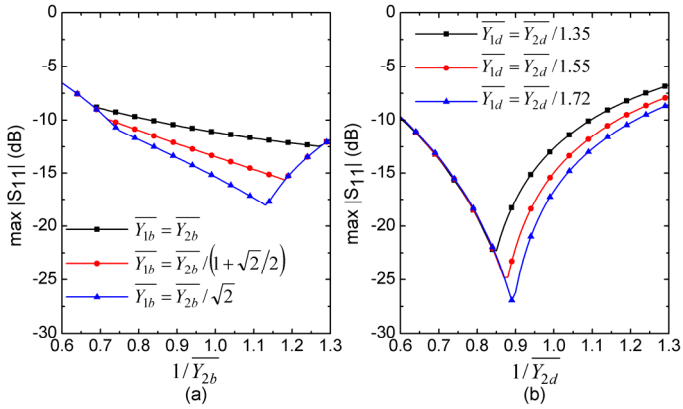

Fig. 5. 16. Maximum input return loss versus normalized series admittances in the frequency band from 26 to 36 GHz. (a) BPF #1. (b) BPF #2.

This analysis shows optimum AI and return loss for different values of the swept normalized series admittance, but close to 1. Therefore, as a trade-off between AI and return loss, the normalized series admittances $\overline{Y_{2d}}$ and $\overline{Y_{2b}}$ are fixed to 1 as initial approach and the admittance ratios of $(Y_{2b}/Y_{1b}, Y_{2d}/Y_{1d}) = (\sqrt{2}, 1.72)$ are selected. Under these conditions, the phase difference of the phase shifter is given by

$$\Delta\Phi(\eta) = \eta\cdot\pi + \cos^{-1}\left(\frac{-1}{\sqrt{2}}\cdot\tan(\eta\pi)\cdot\sin\left(\eta\frac{\pi}{2}\right) + \cos\left(\eta\frac{\pi}{2}\right)\right) - 2\cdot\cos^{-1}\left(\frac{-1}{1.72}\cdot\tan(\eta\pi)\cdot\sin\left(\eta\frac{\pi}{2}\right) + \cos\left(\eta\frac{\pi}{2}\right)\right) \tag{5.24}$$

The input return loss and insertion loss of each filter are calculated by matrix transformation using the cascaded admittance matrixes of each subnetwork and series transmission lines (Z_a and Z_c), which are given by

$$[Y_a] = [Y_c] = j\cdot\begin{bmatrix} \frac{1}{50}\cdot\cot\left(\eta\frac{\pi}{2}\right) & \frac{1}{50}\cdot\csc\left(\eta\frac{\pi}{2}\right) \\ \frac{1}{50}\cdot\csc\left(\eta\frac{\pi}{2}\right) & \frac{1}{50}\cdot\cot\left(\eta\frac{\pi}{2}\right) \end{bmatrix} \tag{5.25}$$

$$[Y_b] = j\cdot\begin{bmatrix} \frac{1}{70.7}\cdot\tan(\eta\pi) - \frac{1}{50}\cdot\cot\left(\eta\frac{\pi}{2}\right) & \frac{1}{50}\cdot\csc\left(\eta\frac{\pi}{2}\right) \\ \frac{1}{50}\cdot\csc\left(\eta\frac{\pi}{2}\right) & \frac{1}{70.7}\cdot\tan(\eta\pi) - \frac{1}{50}\cdot\cot\left(\eta\frac{\pi}{2}\right) \end{bmatrix} \quad (5.26)$$

$$[Y_d] = [Y_e] = j\cdot\begin{bmatrix} \frac{1}{86}\cdot\tan(\eta\pi) - \frac{1}{50}\cdot\cot\left(\eta\frac{\pi}{2}\right) & \frac{1}{50}\cdot\csc\left(\eta\frac{\pi}{2}\right) \\ \frac{1}{50}\cdot\csc\left(\eta\frac{\pi}{2}\right) & \frac{1}{86}\cdot\tan(\eta\pi) - \frac{1}{50}\cdot\cot\left(\eta\frac{\pi}{2}\right) \end{bmatrix} \quad (5.27)$$

The ideal performance in terms of input return loss, insertion loss, phase difference and amplitude imbalance from 24 to 38 GHz of the filters is depicted in Fig. 5. 17. The proposed 90º phase shifter enables minimum phase error and amplitude imbalance to be achieved with remarkable return loss in the band of interest, using a design composed of quarter- and half-wavelength for series and shunt transmission lines respectively at the centre frequency f_0, with a ratio of admittances defined by $(Y_{2b}/Y_{1b}, Y_{2d}/Y_{1d}) = (\sqrt{2}, 1.72)$ considering $Y_{1b}=Y_{1d}=1/Z_0$.

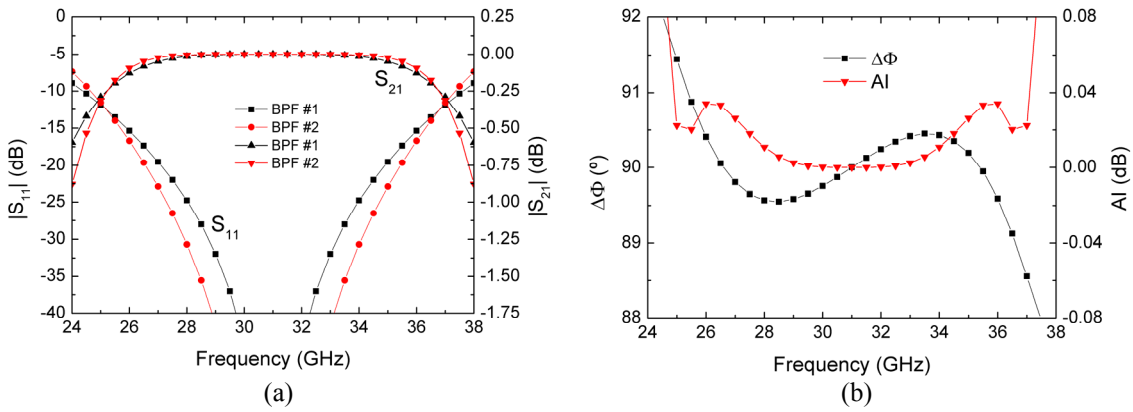

Fig. 5. 17. Ideal response of open-circuited stubs filters. (a) Return loss and insertion loss. (b) Phase difference and amplitude imbalance.

C 90º Phase Shifter Design

The design is implemented on alumina substrate, with 254-µm thickness, $\varepsilon_r = 9.9$ and tan δ = 0.0001, and the initial parameters are the defined in the above analysis.

The design is also optimized using 3D electromagnetic simulators in order to fulfill PE, AI and return loss requirements, taking into account the same considerations as in section 5.2.2.C for the interconnections of transmission lines. Moreover, the shunt stubs in BPF #2 of each network, connected to the same electrical point and with the same impedances ($Z_{1d} = Z_{1e}$), are analogous simplified using (5.17) as in the Teflon-based substrate.

The equivalent schematic of both filters is depicted in Fig. 5. 18(a), in which the dimensions, in terms of widths and physical lengths, are defined. The layouts of both filters are shown in Fig. 5. 18(b).

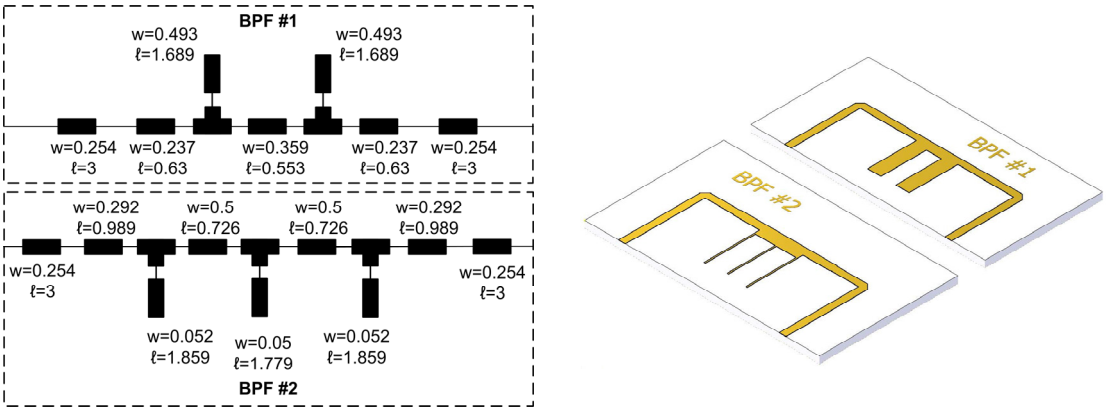

(a) (b)

Fig. 5. 18. Alumina filters. (a) Schematics of both filters with dimensions (in mm) of the microstrip lines. (b) Layout of each filter.

The results of the electromagnetic simulation are shown in Fig. 5. 19, in terms of return loss, insertion loss, phase difference and amplitude imbalance between filters. The simulation shows input return loss better than 17 dB and insertion loss of about 0.5 dB in the frequency band from 26 to 36 GHz. Phase difference result shows an average value of 88.97º ± 5º and an average amplitude imbalance of 0.18 dB from 24 to 37 GHz. Therefore, a relative bandwidth of 42 % is achieved. Considering the bandwidth of the radiometer (from 26 to 36 GHz), a phase difference of 88.8º ± 0.9º is obtained.

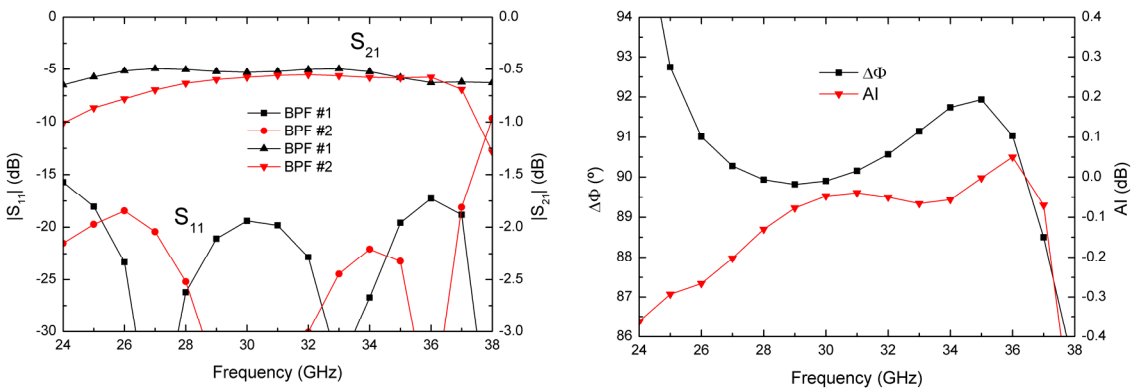

(a) (b)

Fig. 5. 19. Electromagnetic simulation of alumina filters. (a) Return loss and insertion loss. (b) Phase difference and amplitude imbalance.

5.2.4 Phase Switch Hybrid Design Using MMIC SPDT

The initial approach is based on the integration of the filters together with available commercial SPDT MMICs. High return loss and high isolation between outputs as well as between input and isolated output are requirements for the SPDT choice.

Two commercial devices are selected as SPDT: the model HMC975 [5.20] from Hittite and the model AMMC-2008 [5.21] from Avago Technologies. Both SPDTs are shown in Fig. 5. 20. The HMC975 device is based on the use of PIN diodes in series-shunt topology and shows isolation level better than 40 dB while return loss better than 10 dB up to 50 GHz. The AMMC-2008 model is based on the use of pseudomorphic high electron mobility transistors (pHEMT) with isolation better than 20 dB and return loss better than 15 dB up to 50 GHz.

(a) (b)

Fig. 5. 20. Commercial SPDT MMICs. (a) HMC975 based on PIN diodes (1.76x1.1 mm^2); (b) AMMC-2008 based on pHEMT transistors (0.93x0.63 mm^2).

Both devices are assembled with the 127-µm CLTE-XT filters in order to be part of the 90º phase switch. Therefore, gold bond wires are implemented to interconnect the SPDTs and the filters, which have an impact on the phase performace.

5.2.5 Phase Switch Hybrid Design Using CPW-to-Slotline SPDT

The previous solution shows the issue of the interconnection between the SPDTs and the shifting branches. This is performed by gold bond wires, which add a new error source to the phase switch response. The difficulty of performing identical wires makes that the phase error increases, since a minor difference in length between wires causes a significant relative electrical length because of the frequency band. Besides, mismatching effects appear by their insertion between SPDT and filters increasing the ripple in the S-parameter responses.

In order to overcome and minimize these effects, a SPDT switch is designed using hybrid technology. The SPDT is based on the combination of CPW and slotline

transmission lines and discrete PIN diodes as switching devices assembled in the slotline, acting either as a short-circuit or an open-circuit. Thus, a solution based on alumina substrate is implemented using PIN diodes. The design is aided with electromagnetic simulators.

A SPDT Switch on Alumina Substrate

The SPDT switch solution is designed in hybrid technology combining CPW and slotline, in which a switching device can be easily integrated. The SPDT is based on a modified transition from CPW line to slotline, with double possible slotline outputs. A sketch and a layout of the SPDT switch are shown in Fig. 5. 21. This transition has double and symmetric output ways in which the short-circuited quarter-wavelength slotline stub is performed by a diode, which is easily assembled in slotlines. In order to improve isolation results, two switching elements are used in each slotline branch, so the equivalent electrical length of each slotline way is three quarter-wavelength. The devices are placed at a quarter-wavelength electrical distance from the input and output CPW-to-slotline transitions and between them. Besides, a transition from CPW-to-microstrip line is implemented in order to connect the filters with the SPDT.

The CPW and slotline circuits are designed with no bottom metallization, whereas for the microstrip it is provided. Therefore, the etching of back metallization is added in the CPW-to-microstrip transition, implementing 0.2 mm radius via holes to improve the response (see Fig. 5. 21(b)). The design is implemented in 254-μm alumina substrate ($\varepsilon_r = 9.9$). The side CPW contacts are gradually tapered. In order to bias the switching devices, a narrow gap is introduced between slotline round stubs. This gap creates an isolated area where a DC bias point could be provided.

The odd mode in the CPW line is removed with equipotential bridges located at CPW and slotline junctions. Ideally, the switching device is performed by a gold bond wire for simulation purposes.

Besides, with the purpose of measuring the circuit in the coplanar probe station, restrictions in the physical dimensions are fixed. Taking this into account, a 50 Ω CPW line is feasible to be etched. Therefore, the impedance of the input and output CPW lines are 50 Ω. Besides, the thick of metallization (3 μm) over the substrate makes that the etching of the dimensions for the CPW lines is feasible, which enables the use of 150-mm pitch probes in the characterization.

The physical dimensions, after optimization process, of the SPDT are listed in Table 5. 2. The length of the input CPW line is 0.81 mm, while for the outputs are 0.886 mm.

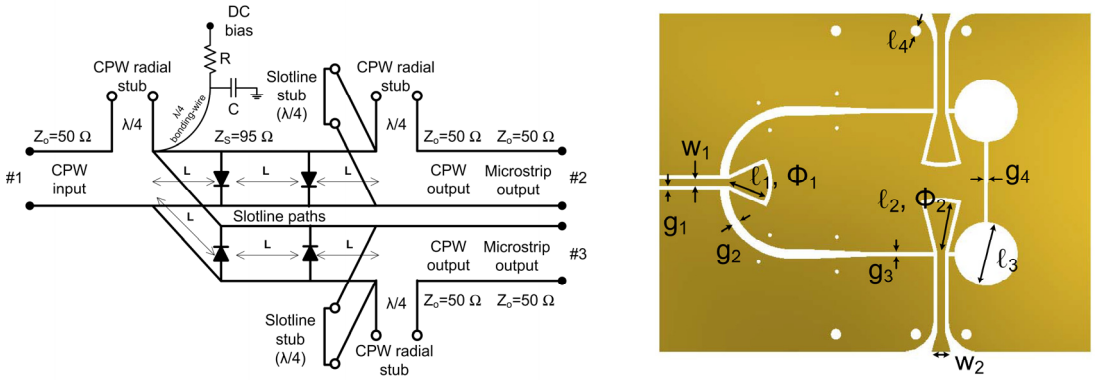

(a) (b)

Fig. 5. 21. CPW-slotline-microstrip SPDT in 254-μm alumina substrate (Dimensions: 5.778x4.55x0.254 mm³). (a) Schematic diagram (L=λ/4 at centre frequency). (b) Layout showing the circuit dimensions.

Table 5. 2. Physical dimensions of the alumina SPDT.

Variable	Value	Variable	Value
g_1, g_3, g_4	0.05 mm	ℓ_2	0.66 mm
g_2	0.121 mm	ℓ_3	0.85 mm
w_1	0.104 mm	ℓ_4	0.2 mm
w_2	0.25 mm	Φ_1	45º
ℓ_1	0.51 mm	Φ_2	27º

5.2.6 SPDT Non-idealities Impact

The phase switch is considered as the block diagram shown in Fig. 5. 22, composed of the SPDTs and the filters designed. The minimization of the mismatching between them is a design goal in order to show the minimum error in phase difference and amplitude imbalance. Therefore, the reflection coefficients between subnetworks are defined and enable the mismatching effects, at reference planes R_1 and R_2, to be analyzed in terms of error in phase difference ($E\Phi$) and amplitude imbalance (EAI). Besides, the effect of the isolated branch is also considered.

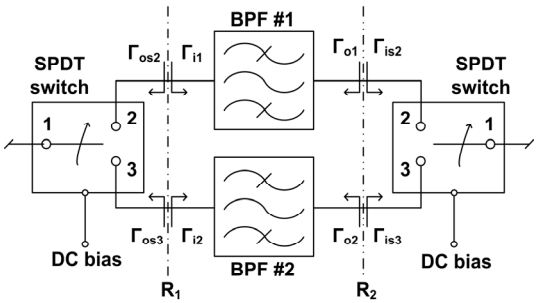

Fig. 5. 22. Schematic of the proposed topology with reflection coefficient between subsystems at reference planes R_1 and R_2.

The analysis considers reciprocal and identical SPDTs and is fulfilled when the transmission is performed by BPF #1. The analysis for the switched state transmitting by BPF #2 ($S_{21BPF\#2\_C}$) is analogous. The S-matrix of the whole circuit is obtained, defining SPDTs and BPFs by their S-matrixes composed of terms S_{ijS} (i, j=1, 2, 3) for the SPDT and $S_{ijBPF\#k}$ (i, j= 1, 2) for the BPFs and k=1, 2 indicates the filter. The transmission parameter in this state is given by

$$S_{21BPF\#1\_C} = \frac{1}{1-F-B+B\cdot F-C\cdot E}\cdot\left[\frac{S_{21S}\cdot S_{21BPF\#1}\cdot(D+E\cdot A-B\cdot D)}{(1-S_{22BPF\#1}\cdot\Gamma_{is2})} + \frac{S_{31S}\cdot S_{21BPF\#2}\cdot(D+E\cdot A-B\cdot D)}{(1-S_{22BPF\#2}\cdot S_{33S})}\right] \tag{5.28}$$

where

$$\Gamma_{is2} = S_{22S} + \frac{S_{32S}^2\cdot\Gamma_{o2}}{1-S_{33S}\cdot\Gamma_{o2}} \tag{5.29}$$

$$\Gamma_{o2} = S_{22BPF\#2} + \frac{S_{21BPF\#2}^2\cdot S_{33S}}{1-S_{11BPF\#1}\cdot S_{33S}} \tag{5.30}$$

$$\Gamma_{i1} = S_{11BPF\#1} + \frac{S_{21BPF\#1}^2\cdot\Gamma_{is2}}{1-S_{22BPF\#1}\cdot\Gamma_{is2}} \tag{5.31}$$

$$\Gamma_{i2} = S_{11BPF\#2} + \frac{S_{21BPF\#2}^2\cdot S_{33S}}{1-S_{22BPF\#2}\cdot S_{33S}} \tag{5.32}$$

and $A=S_{21S}$, $B=S_{22S}\cdot\Gamma_{i1}$, $C=S_{32S}\cdot\Gamma_{i2}$, $D=S_{31S}$, $E=S_{32S}\cdot\Gamma_{i1}$ and $F=S_{33S}\cdot\Gamma_{i2}$.

Both transmission parameters for each circuit state are obtained using the alumina filters as shifting branches, which enables the errors in phase difference and amplitude imbalance to be calculated by subtracting the calculated phase difference and amplitude imbalance of the phase switch to the values of the ideal BPFs (*AI* and ΔΦ in section 5.2.3), shown in Fig. 5. 19. These errors are defined by

$$EAI = 10 \cdot \log 10 \left| S_{21BPF\#1\_C} / S_{21BPF\#2\_C} \right|^2 - AI \tag{5.33}$$

$$E\Phi = \angle \left(S_{21BPF\#1\_C} / S_{21BPF\#2\_C} \right) - \Delta\Phi \tag{5.34}$$

The above expressions take into account the non-idealities of each subsystem and the interaction between them. SPDTs isolation (S_{31S}) and output return loss (S_{22S}) are swept over the operating frequency range. High isolation between output ports of the SPDTs (S_{32S}) is considered, so its impact is negligible. The Fig. 5. 23(a) and (b) depict the errors in phase and amplitude for different isolation values (S_{31S}) and perfect matching at transmitting output. Isolation greater than 16 dB provides phase errors and amplitude errors lower than 5º and 0.6 dB in the band from 26 to 36 GHz. In Fig. 5. 23(c) and (d), a 16 dB isolation is considered and the SPDTs output return loss (S_{22S}) are swept. Therefore, mismatching errors in SPDT interconnections are analyzed. When output return loss is better than 14 dB, phase errors and amplitude errors lower than 6º and 0.6 dB in the band from 26 to 36 GHz are obtained for the 254-µm alumina filters.

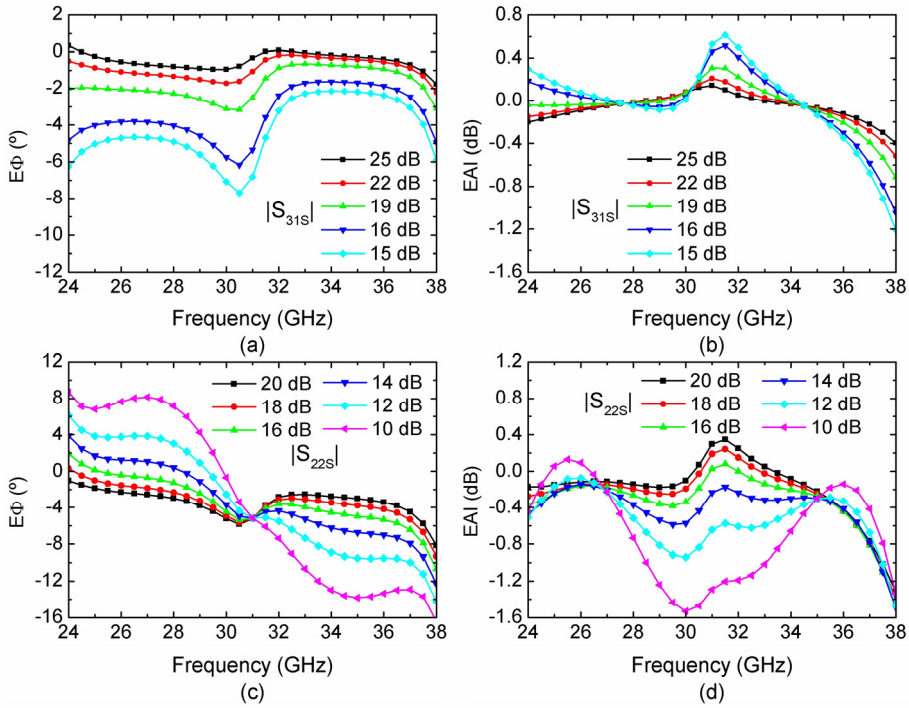

Fig. 5. 23. Errors in phase (EΦ) and amplitude imbalance (EAI) of the phase switch relative to ideal ΔΦ and AI of the BPFs. (a) and (b) SPDT isolation sweep with perfect output return loss; (c) and (d) SPDT output return loss sweep with isolation |S31S|=16 dB.

As a conclusion, the impact of the SPDTs behaviour in the full phase switch performance is analyzed when the 254-µm alumina filters are used and becomes

significant in phase difference and amplitude imbalance deviation when isolation and output return loss are worse than 16 dB and 14 dB respectively.

5.3. Phase Switch Characterization

The characterization of the 90º phase switches in the different substrates is performed in two stages: first, the measurement at room temperature in the coplanar probe station, and, then, the cryogenic test of a specific circuit inside the cryostat. A vector network analyzer E8364A is used for both tests. At room temperature, the measurement set-up is composed of a pair of coplanar probes model 67A-GSG-150-C from PicoProbe by GGB Industries and 2.4-mm phase-stable flexible coaxial cables. A LRM calibration is performed with the CS-5 calibration substrate from PicoProbe by GGB Industries. For the cryogenic test, the circuit is assembled in a chassis and the measurement set-up is composed of semi-rigid and flexible 1.85-mm connector cables to connect the chassis with the outside of the cryostat. The cryostat walls are defined in 1.85-mm connector feedthroughs.

5.3.1 Room Temperature Measurements

The characterization at room temperature is divided in three stages, depending on the type of circuit under test. Initially, the measurement of the phase shifting filters is performed; then, the 90º phase switch circuits based on commercial SPDT MMICs; and, finally, the characterization of the 90º phase switch based on CPW-to-slotline-to microstrip SPDT in alumina substrate.

A Band Pass Filters Measurements

The band pass filters designed in each substrate are individually manufactured and tested in the coplanar probe station using commercial CPWG-to-microstrip transitions. The results of the filters for each substrate are shown in Fig. 5. 24, in which upper row shows the 127-μm CLTE-XT substrate filters, while lower row the results for the 254-μm alumina substrate filters. Considering the bandwidth of the radiometer (from 26 to 36 GHz), an average phase difference of 89.4º, a phase error lower than 4º, insertion loss of about 0.35 dB, amplitude imbalance of about 0.1 dB and return loss better than 14 dB are obtained for the CLTE-XT filters. The alumina filters provide an average phase shift of 88.9º, a phase error lower than 1.1º, insertion loss of about 0.5 dB, amplitude imbalance of 0.15 dB and return loss better than 13 dB.

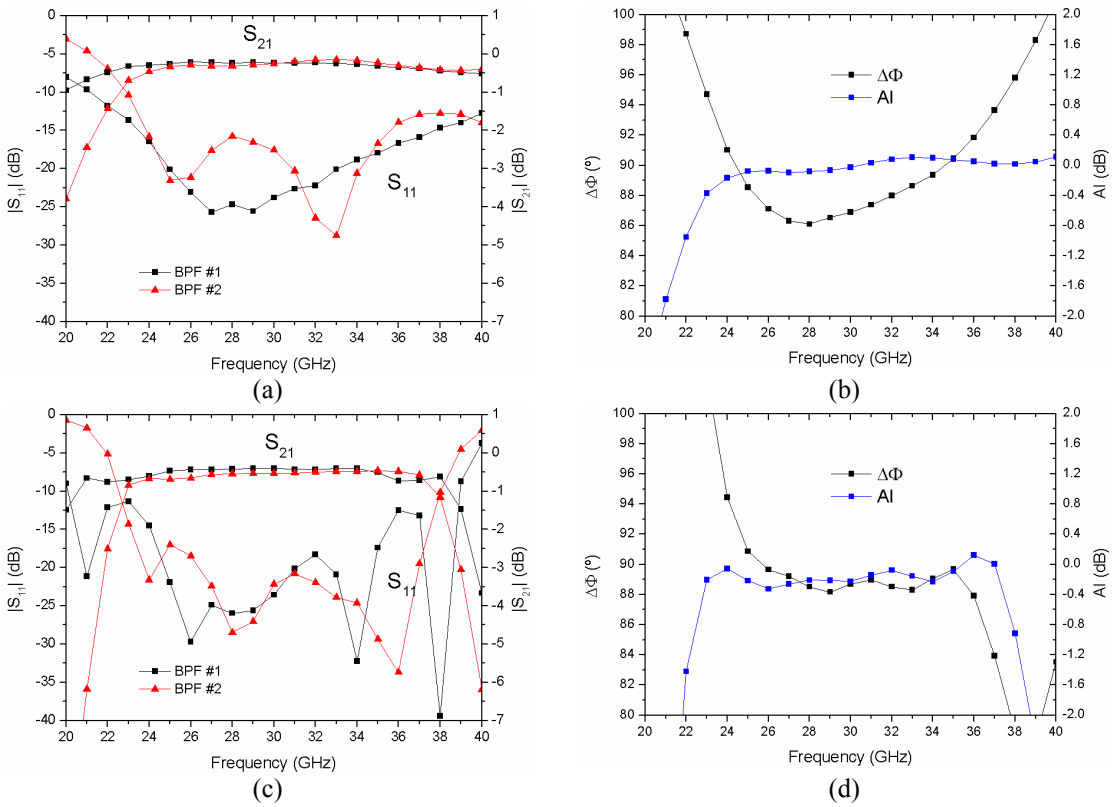

Fig. 5. 24. Measurements of the band pass filter in both substrates. (a) S-parameters in 127-µm CLTE-XT substrate. (b) Phase difference (ΔΦ) and amplitude imbalance (AI) in 127-µm CLTE-XT substrate. (c) S-parameters in 254-µm alumina substrate. (d) Phase difference (ΔΦ) and amplitude imbalance (AI) in 254-µm alumina substrate.

B Phase Switch Using MMIC SPDT Measurements

The assemblies of the two 90º phase switches with commercial SPDT MMICs and the 127-µm CLTE-XT substrate filters are shown in Fig. 5. 25.

The design based on PIN diode technology, using HMC975 devices, requires the use of bypass capacitors in order to bias the SPDTs. Hence, C = 0.3 pF capacitors are used at the outputs of the SPDTs and the inputs of the BPFs. Two different bias points are applied: V_1 = -10 V/I_1 = 10 mA and V_2 = 1.29 V/I_2 = 30 mA.

For the pHEMT AMMC-2008 devices, the transistors are biased using specific pads in the chip, and low-frequency capacitors (C = 100 pF) are used as recommended by the manufacturer. Two bias points are supplied with the following voltages V_1 = 0 V and V_2 = -3 V.

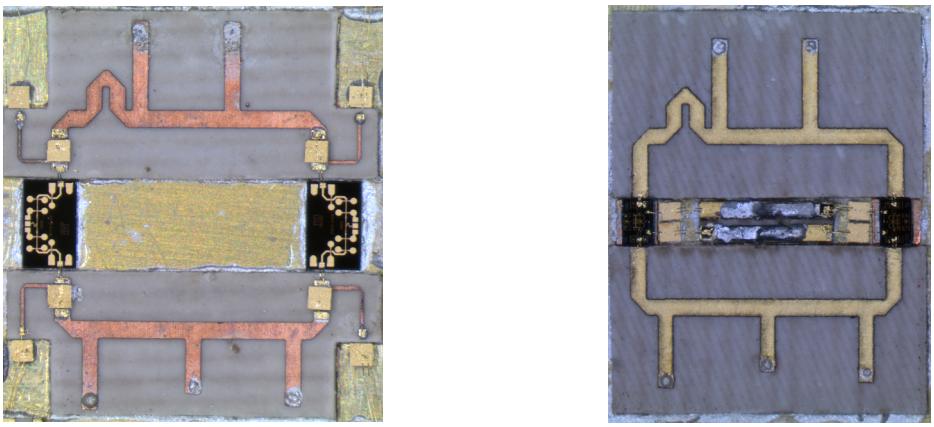

(a) (b)

Fig. 5. 25. Photograph of the 90º phase switch circuits with commercial SPDT MMICs. (a) HMC975. (b) AMMC-2008.

The results of the characterization of both circuits in the coplanar probe station are shown in Fig. 5. 26, in terms of return loss, insertion loss, phase difference and amplitude imbalance. The summary of the results measured are listed in Table 5. 3. In this table, the first row lists the results of the measurement of the CLTE-XT filters without the integration of the SPDTs. From these results, the 90º phase switch based on the AMMC-2008 SPDTs provides better results than design with HMC975 SPDTs. This is likely due to the need of less bond wire interconnections which increase the ripple in the measurements.

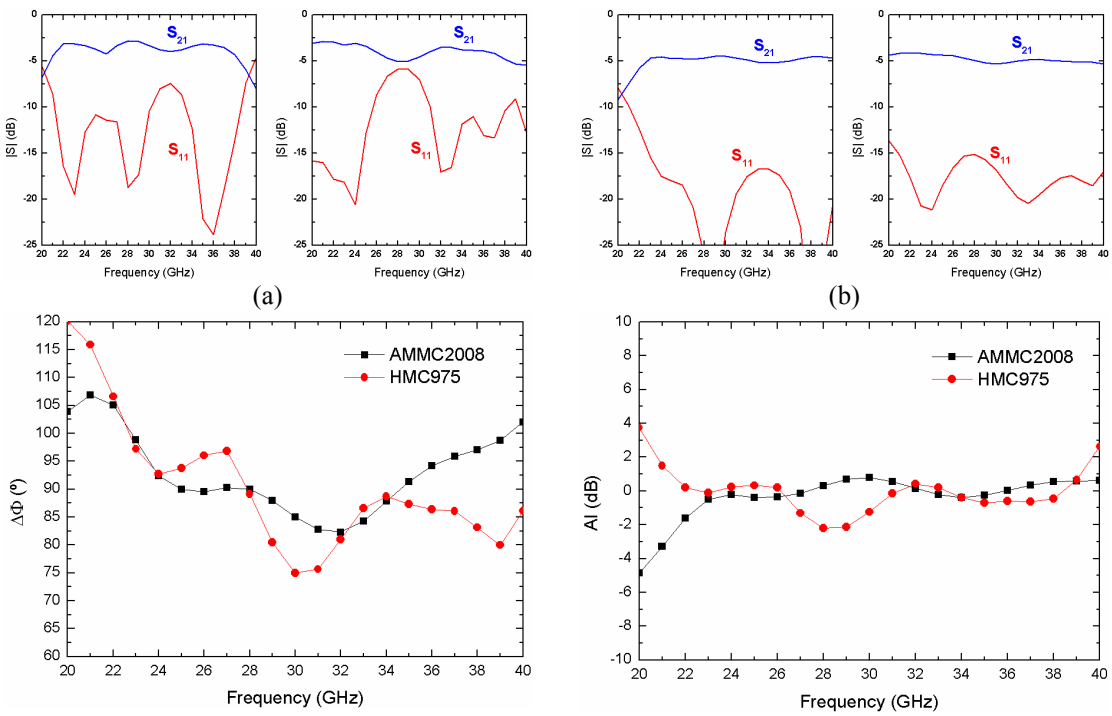

Fig. 5. 26. Phase switch circuit measurements for both switch states. (a) S-parameters with HMC975. (b) S-parameters with AMMC-2008. (c) Phase difference (ΔΦ). (d) Amplitude imbalance (AI).

Table 5. 3. Comparison of the results measured of the different phase switch assemblies in 127-µm CLTE-XT substrate in the frequency band from 26 to 36 GHz (IL=Insertion loss; RL=Return loss).

Phase Switch	ΔΦ (º)	IL (dB)	AI (dB)	RL (dB)	I_d/state (mA)
BPF #1/BPF #2	89.4º±4º	0.35	0.1	14	-
HMC975	85.3º±10º	3.9	2	6	80
AMMC-2008	88º±6º	4.7	0.5	15	0.04

C Hybrid Phase Switch on Alumina Substrate Measurements

The characterization of the circuit designed in 254-µm alumina substrate is performed in two stages: first, the measurement of the SPDT, and, then, the full phase switch circuit. In the particular case of the SPDT, the characterization is performed both with bond wires, in the location where the diodes are expected to be assembled acting as ideal short-circuit, and with PIN diodes as switching device. The full phase switch is tested under both conditions. The PIN diode HPND-4005 [3.3] is selected as switching device.

The SPDT switch on alumina substrate is shown in Fig. 5. 27, in which PIN diodes are used. The results of the electromagnetic simulation and measurement with bond wires and PIN diodes are shown in Fig. 5. 28. The electromagnetic simulation is performed using bond wires as short-circuits. Moreover, the CPW-to-microstrip transition in the SPDT is removed for measurement purposes. A good agreement between simulations and measurements is achieved, validating the design. The measurement of the SPDT with PIN diodes includes the DC bias network, which is composed of a quarter-wavelength bond wire at the centre frequency (freq=31 GHz), a capacitor C = 0.5 pF and a series resistor R = 10 Ω. The results with PIN diodes are performed for a total DC current consumption of 40 mA/state.

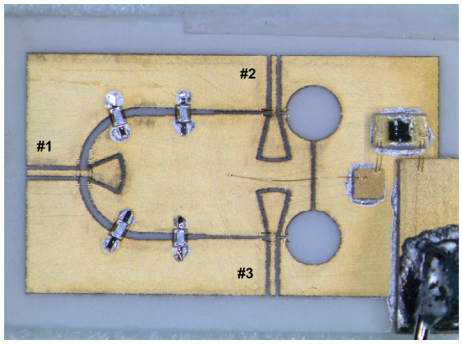

Fig. 5. 27. Photograph of the CPW-slotline SPDT on alumina substrate with four PIN diodes as switching devices and the bias network.

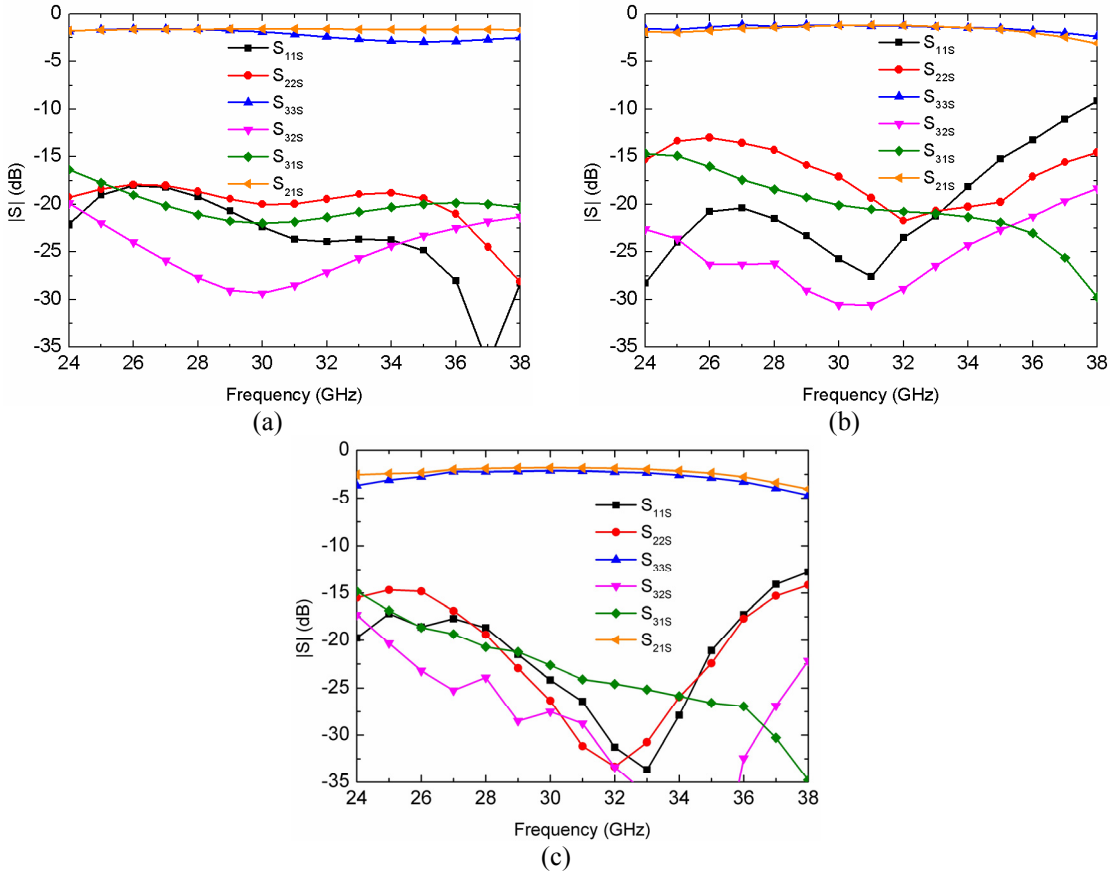

Fig. 5. 28. SPDT S-parameters results. (a) Electromagnetic simulation. (b) Measurement with bond wires. (c) Measurement with PIN diodes.

Considering the analysis described in section 5.2.6, it is performed with measured S-parameters of the SPDT (Fig. 5. 28) and 254-µm alumina BPFs (Fig. 5. 24(c) and (d)). The errors introduced in terms of phase difference and amplitude imbalance relative to the measurements of the BPFs are shown in Fig. 5. 29. Phase and amplitude imbalance errors better than 6.4º and 1.1 dB are expected for the integrated phase switch.

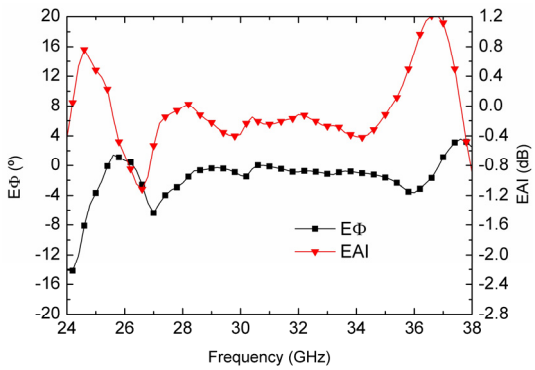

Fig. 5. 29. Errors in phase (EΦ) and amplitude imbalance (EAI) of the phase switch relative to measured BPFs.

The assembly of the integrated phase switch is shown in Fig. 5. 30, in which the bias network is doubled in order to bias both SPDT switches. The results of the measurement of the circuit with bond wires as perfect short-circuit are shown in Fig. 5. 31, and the test with PIN diodes in Fig. 5. 32.

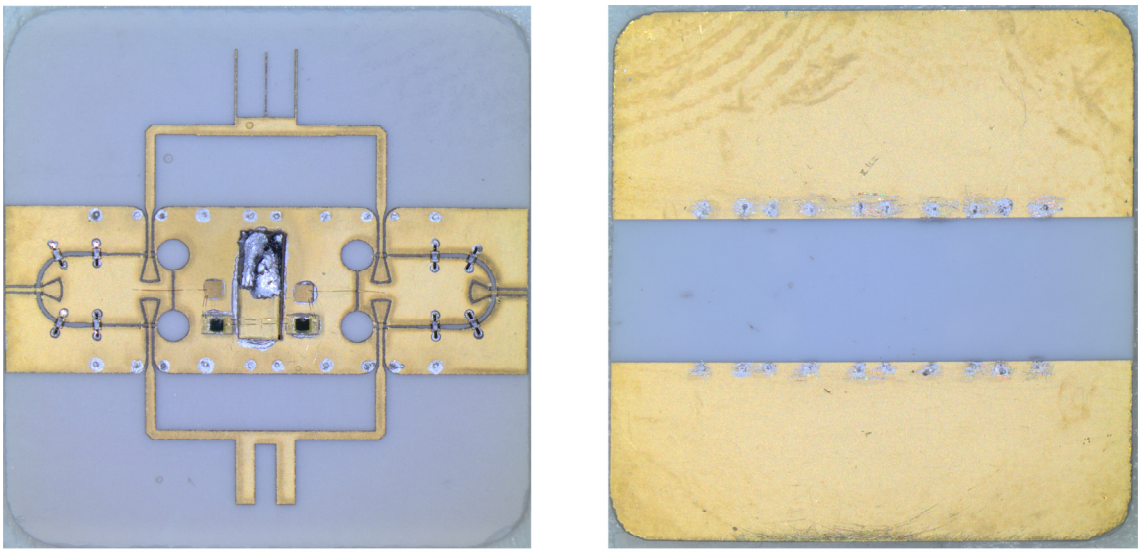

(a) (b)

Fig. 5. 30. Photograph of the full integrated 90º phase switch circuit in alumina substrate using PIN diodes. (a) Top view. (b) Bottom view.

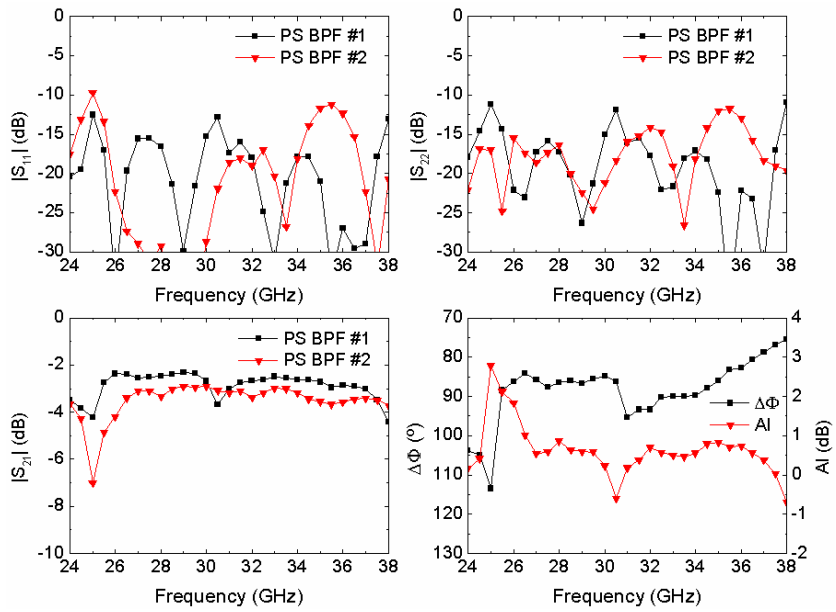

Fig. 5. 31. Alumina phase switch circuit measurements with bond wires as perfect short-circuit: S-parameters for both transmission branches, phase difference (ΔΦ) and amplitude imbalance (AI).

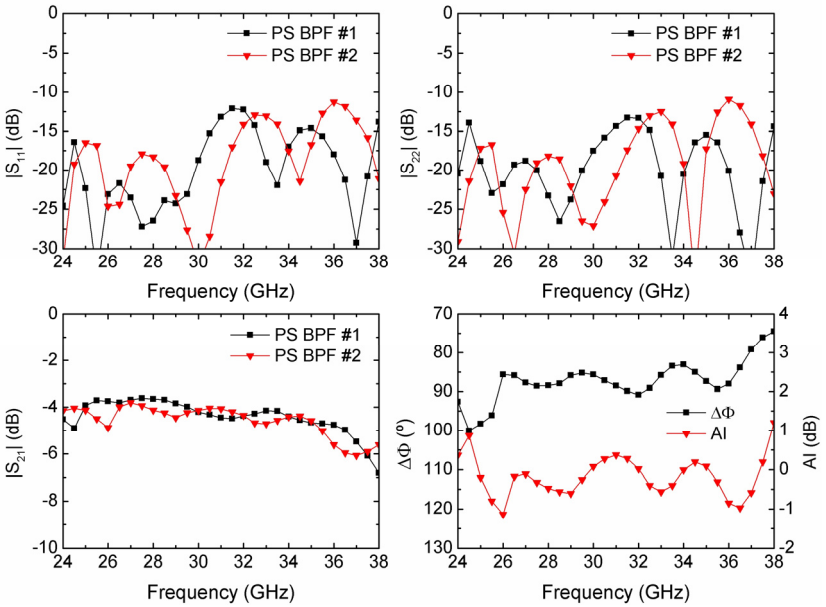

Fig. 5. 32. Alumina phase switch circuit measurements with PIN diodes: S-parameters for both transmission branches, phase difference (ΔΦ) and amplitude imbalance (AI).

Besides, the same circuit is assembled using Schottky diodes, model MA4E2037 from MACOM Technologies [3.1], in order to compare the results. The full assembly of the phase switch based on Schottky diodes is shown in Fig. 5. 33. The results of the measurement of the circuit are shown in Fig. 5. 34.

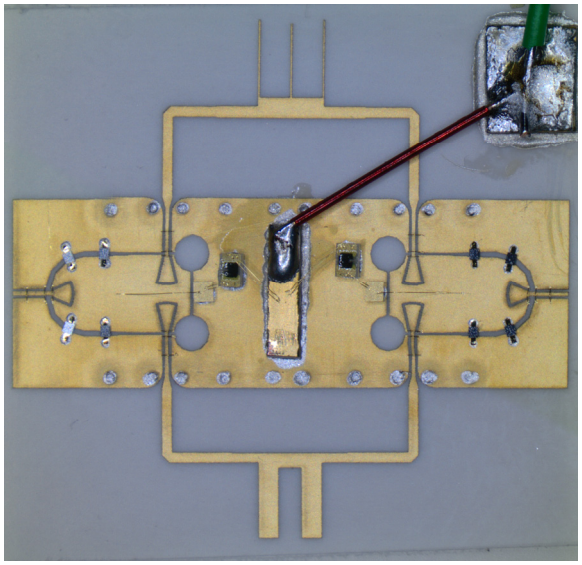

Fig. 5. 33. Top view of the full integrated 90º phase switch circuit in alumina substrate using Schottky diodes.

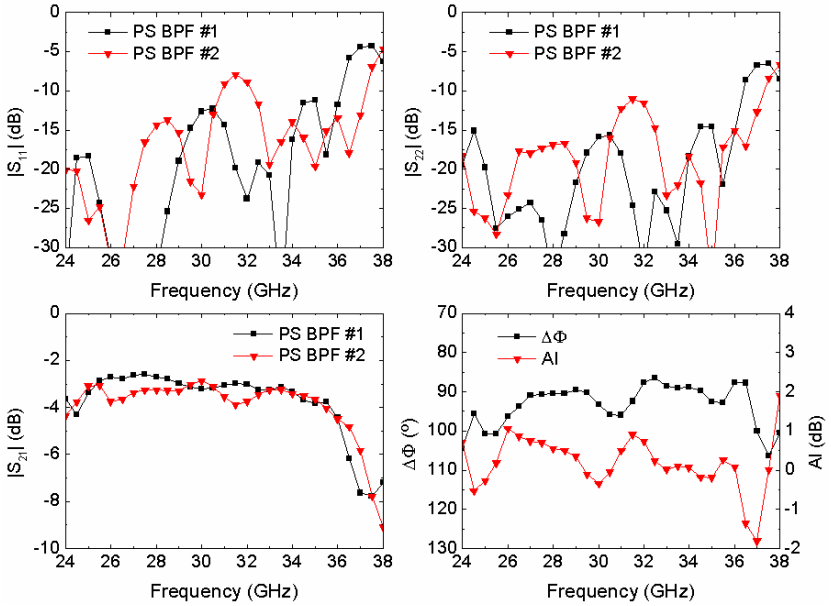

Fig. 5. 34. Alumina phase switch circuit measurements with Schottky diodes: S-parameters for both transmission branches, phase difference (ΔΦ) and amplitude imbalance (AI).

A summary of the results measured are listed in Table 5. 4, in terms of the mean values in the 26 to 36 GHz frequency band. The measurements are not compared to the circuit simulations with the diode model since the electromagnetic simulation of the circuit with the amount of required internal ports cannot be performed since memory allocation requirements are not feasible.

Table 5. 4. Comparison of the results measured of the 90º phase switch in 254-μm alumina substrate in the frequency band from 26 to 36 GHz (IL=Insertion loss; RL=Return loss).

Phase Switch	ΔΦ (º)	IL (dB)	AI (dB)	RL (dB)	I_d/state (mA)
BPF #1/BPF #2	88.9º±1.1º	0.5	0.15	13	-
Bond Wires	87.8º±5º	2.9	0.5	17	-
PIN Diodes	87.1º±4.5º	4	0.3	11	80
Schottky Diodes	91.05º±5º	3.5	0.31	9	80

5.3.2 Cryogenic Temperature Measurements

From the room temperature results, the 90º phase switch designed in alumina substrate is selected in order to perform cryogenic tests. Besides, from the previous results of the cryogenic measurements of diodes, as single units and as a part of a circuit

working at cryogenic temperatures, a circuit with MA4E2037 Schottky diodes from MACOM Technologies [3.1] as switching devices is assembled.

A Phase Switch Mechanical Design

In order to perform the cryogenic characterization, a mechanical chassis is designed to assemble the 90º phase switch circuit inside it.

A view of the chassis and the lid is shown in Fig. 5. 35. The chassis includes threaded holes in order to assure a good thermal link for the cooling down. Its mechanical drawings are included in Annex III.

The chassis is designed in brass and provides 2.4-mm connectors as radiofrequency interfaces. The 2.4-mm connectors [4.31] are from Southwest Microwave and are usually launched to microstrip, CPW or CPW with ground plane (CPWG) lines using 50 Ω seals [4.32]. The diameter of the centre contact of the seal (around 300 μm) is higher than the centre conductor of the CPW line (104 μm listed in Table 5. 2) in the 90º phase switch circuit. Therefore, the 90º phase switch is assembled with additional input and output CPWG lines in 254-μm CLTE-XT substrate in order to make easier the assembly. A detailed view of this assembly is shown in Fig. 5. 35(c).

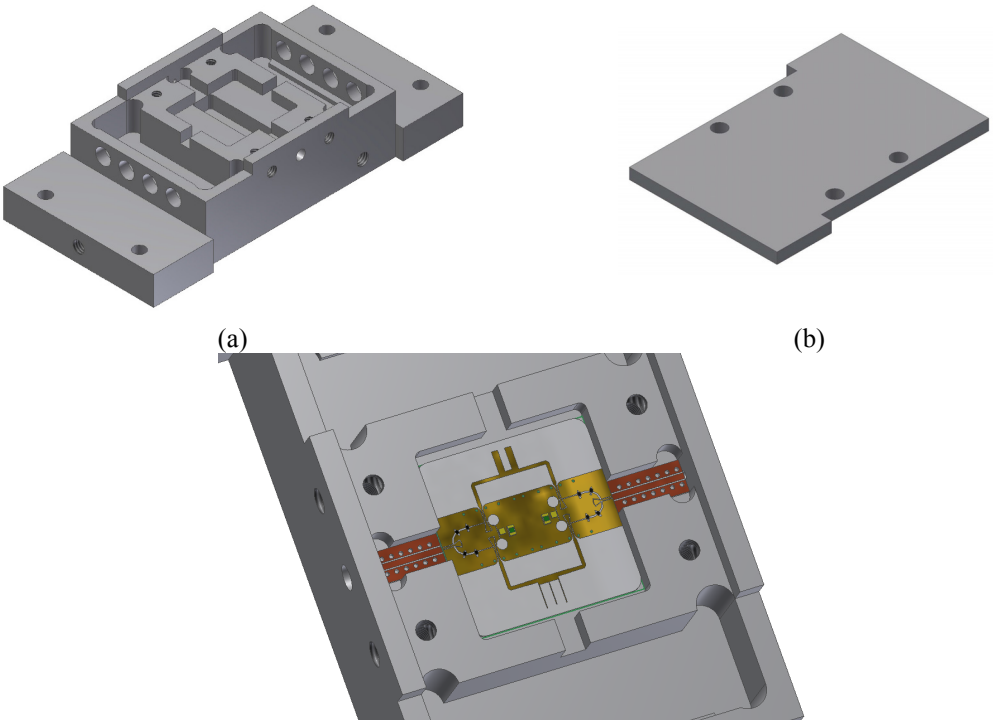

Fig. 5. 35. Artistic views of the chassis designed for the 90º phase switch in the cryogenic tests. Dimensions are 32x66x14 mm³. (a) Chassis. (b) Lid. (c) Detail of the assembly.

B Characterization

The assembly inside the cryostat requires thermal anchors between the cold base and the chassis in order to reach the lowest temperature. Detailed views of the phase switch assembly inside the chassis and the cryostat are shown in Fig. 5. 36.

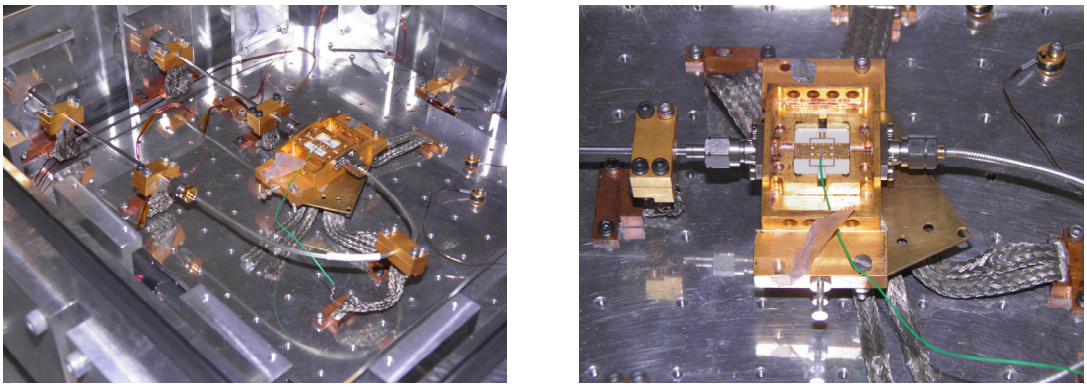

(a) (b)

Fig. 5. 36. Photograph of the cryogenic measurement set-up. (a) Assembly of the chassis inside the cryostat. (b) Detailed view of the circuit inside the chassis.

The characterization is performed using a calibration reference plane outside the cryostat. Therefore, a preliminary measurement of the cables directly connected is done at cryogenic temperature in order to correct to the phase switch insertion loss measurement. Once the cables are characterized, the phase switch chassis is assembled, cooled down and characterized for both switch states. This measurement returns the uncorrected insertion loss and real phase shift of the circuit, since it is a relative measurement.

The measurement of the 1.85-mm connector cables is performed with the cables anchored to the cold base. The physical temperature reached in the measurement is 15 K. The transmission losses of the different set of cables are given by

$$L_{1.85\_CONN}(dB) = 2.504 \cdot 10^{-6} \cdot freq(Hz)^{0.5346} + 2.108 \cdot 10^{-4} \cdot freq(Hz)^{0.3495} \quad (5.35)$$

Using (5.36), the losses of the cables are deducted and the corrected insertion loss at the chassis accesses of the 90º phase switch circuit is obtained.

The measurement results at 300 K and 15 K of the circuit are shown in Fig. 5. 37. Mean values of phase difference and insertion loss in the frequency band from 26 to 36 GHz are listed in Table 5. 5. At cryogenic temperature, a reduction in the insertion loss of the circuit is obtained, which depends on the bias current of the diodes. A limit between the reduction in losses and the power consumption can be achieved, since a very high current in the diodes makes the cryostat heat up. Therefore, suitable bias

points for the circuit are 10 mA or 20 mA, which correspond to 2.5 mA or 5 mA per diode respectively at 15 K, providing an insertion loss improvement of around 1.2 dB with respect to 300 K ambient temperature.

Table 5. 5. Mean values of the results measured of the 90º phase switch in the frequency band from 26 to 36 GHz at room (RT=300 K) and cryogenic temperature (CT=15 K).

Conditions	ΔΦ (º)	AI (dB)	State #1 IL (dB)	State #2 IL (dB)
RT I_d=80 mA	88º±9º	0.012	5.2	5.1
CT I_d=10 mA	88.5º±9º	0.004	3.9	3.9
CT I_d=20 mA	88.4º±9º	0.063	3.5	3.5
CT I_d=40 mA	88.3º±9º	0.064	3.3	3.3
CT I_d=60 mA	88.3º±9º	0.061	3.3	3.3
CT I_d=80 mA	88.4º±9º	0.059	3.2	3.2

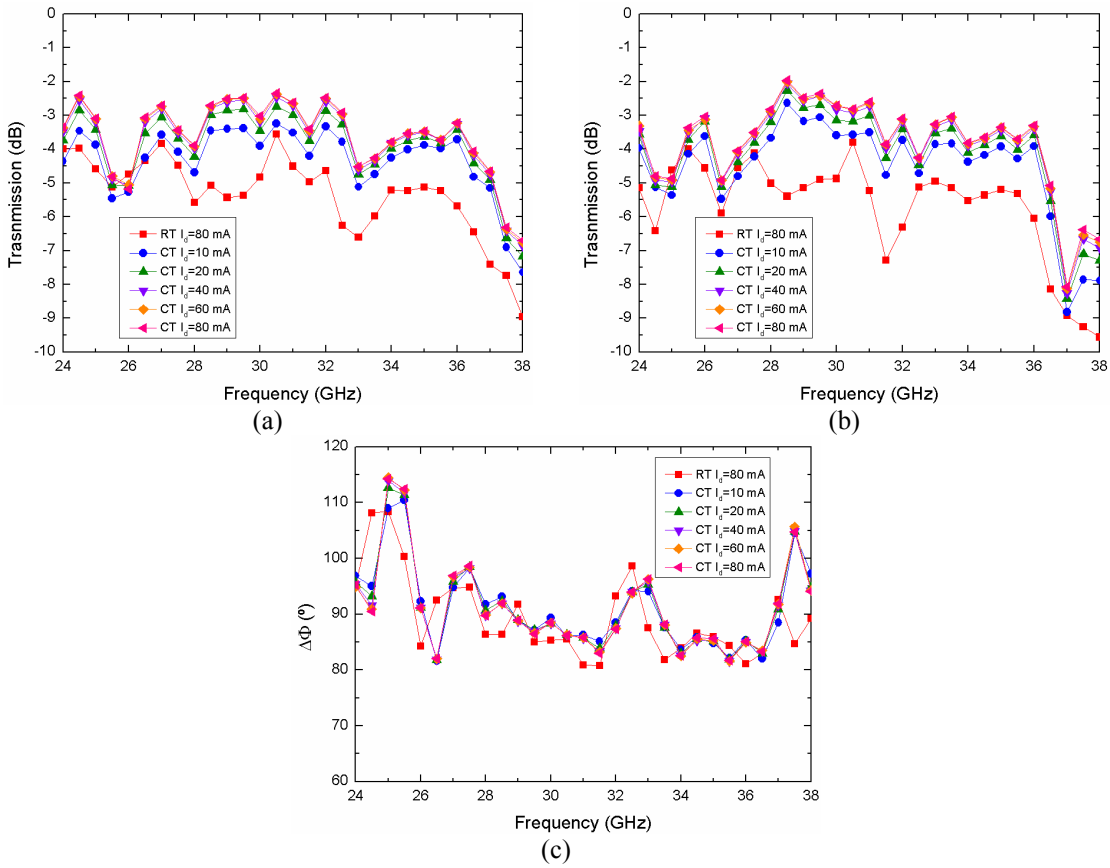

Fig. 5. 37. Results of the cryogenic measurements (RT = Room temperature; CT = Cryogenic temperature). (a) Transmission losses in state #1. (b) Transmission losses in state #2. (c) Phase difference for each bias point.

The comparison of the simulation results to the measurements at cryogenic temperatures, considering the substrate features and the diode model obtained in previous chapters, is not performed due to the simulation issues with internal ports.

5.4. Conclusions

This chapter has described the design and characterization of 90º phase switches at room and cryogenic temperatures for operating in the 26 to 36 GHz frequency band using different substrates and circuit topology.

The design of wideband band-pass filters as 90º phase shifters has been thoroughly analyzed from the use of a single π-network as basic cell of the filter. The analysis of short-circuited and open-circuited π-networks on soft and hard substrates, respectively, has been described considering phase shift and amplitude imbalance restrictions.

In the 26 to 36 GHz frequency band, an average phase difference of 89.4º, a phase error lower than 4º, insertion loss of about 0.35 dB, amplitude imbalance of about 0.1 dB and return loss better than 14 dB have been obtained for the CLTE-XT filters. For the same frequency range, the alumina filters have provided an average phase shift of 88.9º, a phase error lower than 1.1º, insertion loss of about 0.5 dB, amplitude imbalance of 0.15 dB and return loss better than 13 dB.

Hybrid phase switch solutions implemented using two different commercial SPDT MMICs have been presented with reasonable results, but with mismatching issues due to the interconnection between subsystems. The design based on PIN diode HMC975 SPDT has provided an average phase shift of 85.3º with an error of ±10º, while the design with pHEMT transistor-based AMMC-2008 has exhibited 88º as average phase shift with an error of ±6º. In these two circuits with SPDT MMICs, the repetitiveness issue of bond wires is critical. Therefore, a hybrid solution based on a CPW-to-slotline-to-microstrip SPDT with diodes as switching devices has been designed in order to minimize mismatching effects. A SPDT with isolation better than 15 dB in the 26 to 36 GHz band has been performed with HPND-4005 PIN diodes.

The characterization of the 90º phase switch based on CPW-to-slotline-to-microstrip SPDT has been performed at room (300 K) and cryogenic (15 K) temperatures. The full design has been developed in alumina substrate. The room temperature measurement in the coplanar probe station has demonstrated a good performance in the 26 to 36 GHz frequency band with an average phase shift of 87.1º

and a phase error lower than 4.5º using HPND-4005 PIN diodes. When the circuit has been assembled with MA4E2037 Schottky diodes, its performance has shown an average phase shift of 91º with a phase error of around 5º in the receiver band.

Finally, the characterization of the phase switch at cryogenic temperature has been performed with the Schottky diodes owing to the PIN diodes unsuitable cryogenic behaviour. The measurement has been made for different bias points of the diodes, obtaining a reduction of about 1.2 dB in the insertion losses of the phase switch, with a reduction of 80% of power consumption, compared to the room temperature results. Moreover, the cryogenic phase performance in the 26 to 36 GHz frequency band for the set of bias points has shown an average phase shift of around 88º with an error of 9º.

Chapter VI

Design of a Wideband Microstrip Detector Based on Schottky Diode

6.1. Introduction

The design of high sensitivity detectors in hybrid technology is a key aspect for many communication systems, especially in radio astronomy receivers, since the low power level of the incoming signal is needed to be transformed into a measurable signal in the order of millivolts. Therefore, the detector makes a non-linear transformation with the aim of obtaining a DC or low frequency voltage value proportional to the input power [6.1]. A typical solution implemented in radio astronomy receivers is based on square-law detectors which apply a non-linear conversion to obtain an output signal proportional to the variance of the input noise-like signal.

Microwave detectors are commonly performed using a metal-semiconductor device, such as Schottky diodes. These solutions are typically preferred since they are more efficient radiofrequency-to-DC converters than thermal device detectors [6.1]. Besides, Schottky diodes are used due to their lower reverse recovery time than p-n junctions and low equivalent capacitance and series resistance.

The device must be matched in order to maximize the power delivered to the diode avoiding mismatching effects, and different matching networks techniques could be used [6.2]. As starting solution, the LFI PLANCK mission detector, described in [6.2] and based on a low-loss transmission lines microstrip network followed by a discrete shunt resistor, is considered. This technique enables to reach good return loss with a reduction in the sensitivity of the detector considering ideal matching.

This chapter presents the development of a square-law detector in hybrid technology using a Schottky diode as discrete device. The design is based on the use of lossy transmission lines [6.3]-[6.4] as input matching network configured in a π-topology in order to achieve a flat sensitivity response versus frequency, improving the results reported in [6.2]. A thorough analysis is presented in order to obtain a highly efficient circuit in terms of sensitivity as well as input matching.

6.2. Detector Electrical Design

The detector is designed to transform the microwave signal into a voltage signal in the QUIJOTE phase II BEM, which works in the 26 – 36 GHz frequency band. The design considerations are listed in Table 6. 1. In order to accomplish a flat sensitivity response versus frequency, the analysis and design of the input matching network of the detector is very important since it enables the definition of trade-offs between the input return loss and sensitivity achieved.

Table 6. 1. Design specifications for the detector.

Frequency Range	26-36 GHz
Input Return Loss	>10 dB
Input Power Range	[-35,-25] dBm
Typical Output Voltage	<5 mV
Average Sensitivity	1000 mV/mW

The widespread bandwidth of the QUIJOTE radio astronomy receiver is expected to have a very low-power level input signal, so very sensitive radiometers are desired. Hence, the need of having a high sensitivity detector is analysed and described in order to achieve the maximum conversion ratio from the tiny radiofrequency power received. The typical radio astronomy receiver amplifies the incoming signal, at cryogenic and room temperatures stages, in order to adequate it to detectable power levels, usually around -30 dBm.

6.2.1 Principle of Operation

The operation of the detector is based on the rectification efficiency of the diode. The diode rectifies the input power of the incoming signal and it provides and output voltage signal which amplitude is proportional to the input power and its polarity depends on the connection of the diode contacts.

The conversion from radiofrequency to voltage signals is defined by a square-law ratio. This approximation is suitable for low enough input power levels, in which the voltage is proportional to the input power. For higher power levels, the conversion ratio is affected by compression effects in the diode response and the approximation is not valid. The equivalent sketch for the conversion in the diode is shown in Fig. 6. 1, where P_{avs} is the available power and V_{OUT} the output detected voltage. The typical current-voltage feature is shown in Fig. 6. 2, in which the operating regions dependent on the applied voltage are located and the square-law region is identified.

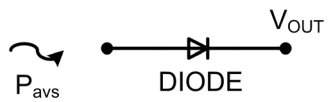

Fig. 6. 1. Diode sketch for the conversion analysis.

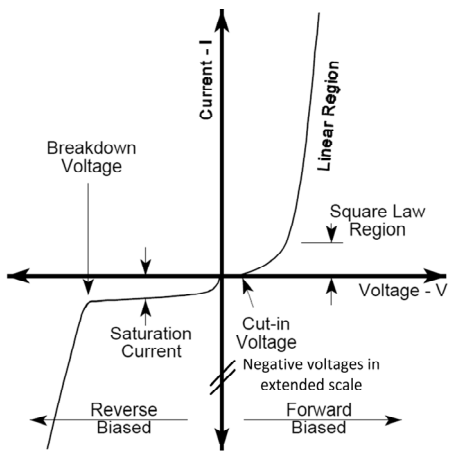

Fig. 6. 2. Typical current-voltage curve of a diode and the different operating regions.

From the previous information, when operating in the square-law region, the output voltage is proportional to the available input power, and given by

$$V_{OUT} \propto P_{avs} \tag{6.1}$$

where P_{avs} is the available power and V_{OUT} the output detected voltage.

Fig. 6. 3 shows a simplified detector schematic, which includes the input matching network and the low-frequency filter, usually composed of a capacitor and a resistor previously to the amplification of the detected voltage.

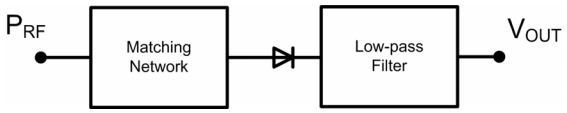

Fig. 6. 3. Simplified detector schematic.

A significant parameter of a detector is the sensitivity. It can be defined as voltage or current sensitivity depending on the considered output parameter. Hereinafter, voltage sensitivity, γ or S_{DET}, is assumed, and it is defined as the ratio of the open-circuit video or low-frequency/DC output voltage to the available input power. It is given by

$$S_{DET} = \frac{V_{OUT}}{P_{avs}} \tag{6.2}$$

usually characterized in mV/mW. The open-circuit condition in the output is considered when great load resistances are expected to be connected at the output of the circuit.

6.2.2 Discrete Device: Schottky Diode

The design of the detector is based on the use of a discrete Schottky diode. As described in Chapter III, different types of devices are available depending on their potential barrier. The choice of the type of device is based on several issues. Attending to low power level which enters to the diode, an external bias supply is needed to be applied in case of high-potential barrier devices to be able to detect [6.5]-[6.9]. Nevertheless, if high power levels are incoming to the diode, high-potential barrier diodes can detect without any external bias. When a low-potential barrier diode is selected, no bias supply is needed under any power level consideration, since it is able to detect due to the higher saturation current it usually exhibits which reduces the equivalent non-linear resistance of the diode. If the simplicity in the design of the circuit is considered, the use of low-potential barrier devices is a better option since no DC bias network is needed in the design. Additionally, if the operation temperature is considered, the potential barrier of the diode is modified when its physical temperature is lower, increasing the knee voltage compared to the one at room temperature. Therefore, in case of a low-potential barrier diode working at cryogenic temperature, its

knee voltage will be lower than the one in a high-barrier diode, so lower external bias supply will be needed.

According to the low power level of the expected input signal, a low-potential barrier diode is selected as the rectifier Schottky junction for the microwave detector. Besides, under room temperature operation, a low-potential barrier diode avoids the use of a bias network which makes the design more complicated. The zero-bias device available from Avago Technologies, and modelled in Chapter III, is the HSCH-9161 [3.2]. As obtained with the model presented in that chapter, the diode shows a knee voltage lower than 0.2 V at room temperature, which is increased up to around 0.3 V at 15 K. Besides considering the non-linear model performed, a room temperature sensitivity around S_{DIODE} = 3200 mV/mW is expected at the centre frequency of the operating band (31 GHz) without compression.

6.2.3 Input Matching Network

Once the rectifying device is selected, the detector needs a matching network in order to deliver the maximum power to the diode. The definition of the matching network is a key aspect of the design of a wideband zero-bias Schottky diode detector, since the impedance of the zero-bias diode is quite difficult to be matched in a wide frequency range.

Several techniques have been developed in order to properly match wideband microwave detectors [6.10]-[6.14], such as Chebyshev networks, resonant structures or coupled lines. Additionally, the use of microstrip transmission lines combined with a shunt resistor has been described as a feasible matching network for the detector [6.2].

Considering this combination of low-loss transmission lines and a discrete resistor, a new option is developed in this detector design based on full distributed transmission lines, combining low-loss and lossy lines [6.3]-[6.4] as an alternative solution to the design of a lossless transmission lines network in order to improve its results. The use of this distributed configuration is intended in order to improve the PLANCK designs, as the DICOM group was involved in their developments, in terms of the flatness of the voltage sensitivity response provided in that designs [6.2]. Besides, the use of this type of solution provides design procedures to achieve the intended flat sensitivity response as well as the minimum return loss listed in Table 6. 1. Moreover, models are available in commercial simulators such as ADS for the lossy transmission lines implemented as distributed thin film resistors. Additionally, the use of a

distributed lossy matching network enables a more accurate assembly of the detector, since the use of a discrete resistor adds uncertainty to the measurement due to the connections of the different components of the detector [6.2].

A Matching Network Analysis

The analysis of the suitable matching network must include the Schottky diode as specific load in its output access. The model obtained for the HSCH-9161 Schottky diode in Chapter III is used for the analysis developed in this chapter. The basic schematic shown in Fig. 6. 4 is considered as the equivalent one for the detector.

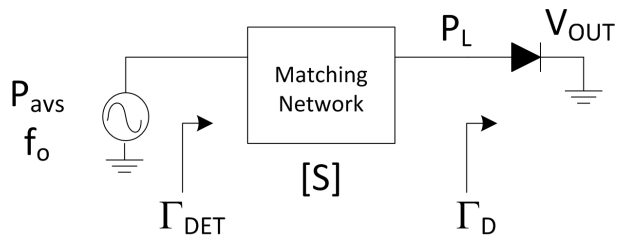

Fig. 6. 4. Basic detector schematic including the matching network.

Then, the input reflection coefficient of the detector can be approached as

$$\Gamma_{DET} = S_{11} + \frac{S_{21} \cdot S_{12} \cdot \Gamma_D}{1 - \Gamma_D \cdot S_{22}} \tag{6.3}$$

where the S_{11}, S_{21}, S_{12} and S_{22} are the corresponding Scattering parameters of the matching network and Γ_D is the input reflection coefficient of the small signal model of the diode; while, the sensitivity of the detector is given by

$$S_{DET} = G_T \cdot \frac{S_{DIODE}}{1 - |\Gamma_D|^2} \tag{6.4}$$

where S_{DIODE} is the sensitivity of the non-linear model of the diode and G_T is the transducer gain of the matching network given by

$$G_T = \frac{P_L}{P_{avs}} = |S_{21}|^2 \cdot \frac{1 - |\Gamma_D|^2}{|1 - \Gamma_D \cdot S_{22}|^2} \tag{6.5}$$

where P_{avs} is the available power and P_L is delivery power to the diode.

Generally, the matching network approaches the load impedance to 50 Ω in a frequency range. In the particular case of the detector, the matching network is focused on providing the available power to the diode within the frequency range from 26 to 36 GHz with significant return loss and, simultaneously, a flat sensitivity in that range.

Therefore, the matching network maximizes the delivery power to the diode, up to the limit when the available power is reached. When perfect match is achieved, the delivery power to the diode is equal to the available power.

If a lossless matching network is considered, it shows reciprocal behaviour and has a unitary matrix. In case of perfect match, the transducer gain of the matching network has unity value since the delivery power is equal to the available power. Then, the sensitivity of the detector has the same value than the sensitivity of the diode. Therefore, the sensitivity of the detector is given by

$$S_{DET} = \frac{V_{OUT}}{P_L} = \frac{V_{OUT}}{\frac{1}{2} \cdot real\left(v_D \cdot conj\left(i_D\right)\right)} \tag{6.6}$$

where V_{OUT} is the output voltage (V), v_D is the AC voltage in the diode (V) and i_D is the AC current (A) which flows through the diode.

The sensitivity of the detector is calculated using the non-linear model described in Chapter III of the HSCH-9161. The simulation of the sensitivity, using (6.6), of the Schottky diode is shown in Fig. 6. 5. It shows an appreciable slope versus the frequency, which means that a flat sensitivity cannot be reached in that case.

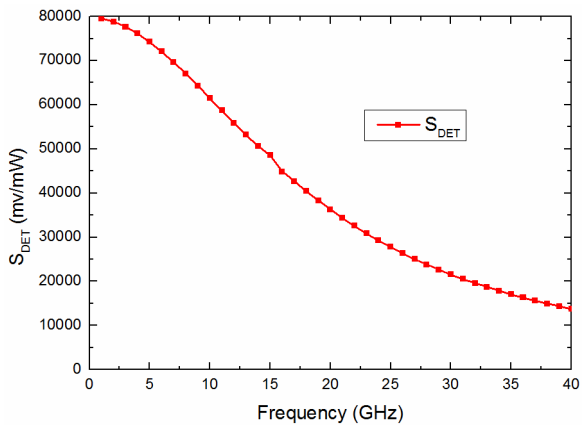

Fig. 6. 5. Sensitivity of the diode at room temperature (300 K) calculated with (6.6) for a frequency sweep of the input signal with constant available power P_{RF}=-30 dBm.

Therefore, a lossless matching network does not satisfy the flat sensitivity requirement in a wideband frequency range. On the other hand, if a poor input return loss level in wideband operation is considered using lossless matching network, a flat sensitivity could be achieved, but the matching results makes it unsuitable. Hence, the matching network has to compensate the slope in the sensitivity of the diode by adding losses, which are frequency dependent. The proposed matching network is designed

combining microstrip low-loss and lossy transmission lines. The lossy transmission lines, implemented with thin-film resistors, replace the shunt SMD resistor in [6.2]. The network is performed using distributed elements directly etched over the substrate, so a multi-layer one must be selected.

The network is configured in a π-topology in which the shunt transmission lines are lossy lines emulating distributed resistors. The basic network is shown in Fig. 6. 6.

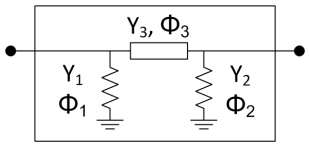

Fig. 6. 6. π–network transformation from full transmission line topology to shunt lossy transmission lines.

The basic detector schematic is shown in Fig. 6. 7, in which the Schottky diode is connected at the output of the matching network with an additional transmission line to ease its connection, and a signal generator applies the P_{avs} input power to the circuit.

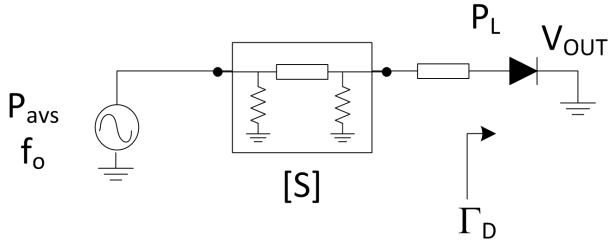

Fig. 6. 7. Detector schematic including the lossy transmission line matching network.

Therefore, the whole matching network under analysis is shown in Fig. 6. 8. The impedance of the series transmission lines are set to the same impedance $Z_3=1/Y_3$ and electrical length Φ_3 values to simplify the initial analysis.

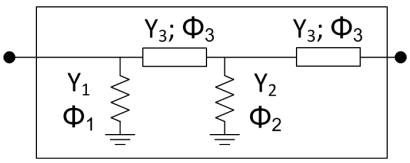

Fig. 6. 8. Matching network under analysis to obtain the detector design.

The equivalent admittance matrix of a short-circuited π-network such as the one depicted in Fig. 6. 6 is given by

$$[Y]_{LOSSY} = \begin{bmatrix} Y_1 \cdot \coth(\theta_1) - j \cdot Y_3 \cdot \cot(\theta_3) & -j \cdot Y_3 \cdot \csc(\Phi_3) \\ -j \cdot Y_3 \cdot \csc(\Phi_3) & Y_2 \cdot \coth(\theta_2) - j \cdot Y_3 \cdot \cot(\theta_3) \end{bmatrix} \quad (6.7)$$

where $Y_1 = 1/Z_1$, $Y_2 = 1/Z_2$ and $Y_3 = 1/Z_3$ are the admittances of the transmission lines and Φ_i their electrical lengths.

From a lossy transmission line, its basic equivalent model per unit length is considered and it is shown in Fig. 6. 9.

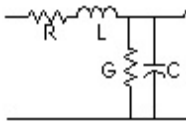

Fig. 6. 9. Lossy transmission line model per unit length.

In order to obtain a model of the lossy transmission line, the basic *RLCG* parameters per unit length must be defined, taking special interest on the equivalent resistance-conductance *RG* per unit length. These parameters define the losses in the conductor and in the dielectric of the transmission line respectively. As general approach, the losses in the conductor are much higher than the losses in the dielectric [6.15]. Therefore, the conductance element in the model is negligible, and $G = 0$ is assumed. Besides, when low-loss approximation is considered, so $R << \omega \cdot L$ and $G << \omega \cdot C$ are assumed, with ω the angular frequency [6.16].

From a lossless transmission [6.17], the basic inductance-capacitance *LC* per unit length parameters in the model are obtained. In this case, the characteristic impedance of a lossless transmission line can be used. Hence, both parameters *L* and *C* can be calculated using the propagation constant β_0 and the impedance Z_0 of a transmission line when its width W is known for a substrate with height H. They are obtained using

$$\left.\begin{aligned} \beta_o &= \frac{2\pi}{\lambda} = \frac{2\pi\cdot\left(f\cdot\sqrt{\varepsilon_{eff}}\right)}{c} = \omega\cdot L\cdot C \\ Z_o &= \sqrt{\frac{L}{C}} \end{aligned}\right\} \Rightarrow \left\{\begin{aligned} C &= \frac{\sqrt{\varepsilon_{eff}}}{Z_o\cdot c} \\ L &= Z_o^2\cdot C \end{aligned}\right. \tag{6.8}$$

where $\omega = 2\cdot\pi\cdot f$, f is the frequency, *c* the speed of the light in vacuum and ε_{eff} the effective dielectric constant.

The impedance Z_0 of a lossless microstrip transmission line [2.27] is given by

$$Z_o = \frac{377}{2\pi\sqrt{0.5(\varepsilon_r+1)}}\left(\ln\left(\frac{8}{u}\right)+\frac{1}{8}\left(\frac{u}{2}\right)^2-\frac{1}{2}\frac{\varepsilon_r-1}{\varepsilon_r+1}\left(\ln\left(\frac{\pi}{2}\right)+\frac{1}{\varepsilon_r}\ln\left(\frac{4}{\pi}\right)\right)\right) \tag{6.9}$$

where u = W/H.

Once the *LC* parameters are known, the calculus of the *R* parameter is analysed since *G* is negligible. The equivalent resistance per unit length *R* of a lossy line [6.16]-[6.17] can be calculated as

$$R = \frac{\rho}{Wt} \tag{6.10}$$

where ρ (Ω·mm) is the bulk resistivity, W (mm) the width and *t* (mm) the thickness of the conductor.

The characteristic impedance of the transmission line is expressed as

$$Z_{o\_loss} = \sqrt{\frac{R + j\omega L}{G + j\omega C}} \tag{6.11}$$

while the propagation constant in a lossy line is given by

$$\gamma = \sqrt{(R + j\omega L)(G + j\omega C)} = \alpha_C + j\beta_1 \tag{6.12}$$

where α_C is conductor losses and β_1 the phase constant.

Thus, using (6.12), considering $G = 0$ and squaring both sides of the equation, the following expression is obtained

$$-\omega^2 LC + j\omega RC = \alpha_c^2 - \beta_1^2 + j2\alpha_c\beta_1 \tag{6.13}$$

The attenuation constant α_C can be approached by a simple expression which includes the conductor losses, since the dielectric losses are negligible related to the conductor ones. Then, the conductor losses α_C can be approached by

$$\alpha_C = \frac{1}{2}\frac{R}{Z_0} \tag{6.14}$$

Then, once the conductor losses are known, the phase constant β_1 can be calculated from (6.13) as

$$\beta_1 = \sqrt{\alpha_C^2 + \omega^2 LC} \tag{6.15}$$

Once the parameters of the lossy transmission line are obtained, the analysis of the matching network shown in Fig. 6. 8 is fulfilled.

B Simplified Detector Performance with Lossy Lines

As described in equation (6.7), the admittance matrix of a π-network based on lossy transmission lines in their shunt elements combines hyperbolic and ordinary trigonometric functions.

A complete analysis of cascaded matrixes is performed and the ABCD matrix is obtained as the product of the ABCD matrix of the lossy transmission line π-network

and the ABCD matrix of the series transmission line (see Fig. 6. 8). The basic lossy transmission line π-network is shown in Fig. 6. 6 and the electrical length and impedance of each line are described from (6.16) to (6.18). These equations include the parameters calculated in the previous section for the case of lossy and lossless transmission lines.

$$\Phi_1 = \gamma \cdot long_1 = (\alpha_c + j\beta_1) \cdot long_1;\ Y_1 = \frac{1}{Z_{o\_loss}} \tag{6.16}$$

$$\Phi_2 = \gamma \cdot long_2 = (\alpha_c + j\beta_1) \cdot long_1;\ Y_2 = \frac{1}{Z_{o\_loss}} \tag{6.17}$$

$$\Phi_3 = \beta_o \cdot long_3;\ Y_3 = \frac{1}{Z_o} \tag{6.18}$$

where $long_1$, $long_2$ and $long_3$ are the physical lengths of each transmission line.

Besides, the series transmission line has an ABCD matrix given by

$$\begin{bmatrix} A & B \\ C & D \end{bmatrix}_{SERIES\_LINE} = \begin{bmatrix} \cos(\Phi_3) & j\frac{1}{Y_3}\sin(\Phi_3) \\ jY_3\sin(\Phi_3) & \cos(\Phi_3) \end{bmatrix} \tag{6.19}$$

Therefore, the equivalent ABCD matrix of the matching network up to the diode contact is given by

$$\begin{bmatrix} A & B \\ C & D \end{bmatrix} = \begin{bmatrix} -\frac{Y_{22}}{Y_{21}} & -\frac{1}{Y_{21}} \\ -\frac{Y_{11}Y_{22} - Y_{21}Y_{12}}{Y_{21}} & -\frac{Y_{11}}{Y_{21}} \end{bmatrix} \cdot \begin{bmatrix} A & B \\ C & D \end{bmatrix}_{SERIES\_LINE} \tag{6.20}$$

where Y_{11}, Y_{12}, Y_{21} and Y_{22} are the corresponding parameters of the admittance matrix described in (6.7).

From the ABCD matrix of the full network, the Scattering matrix is obtained and, then, the analysis of the input reflection coefficient and the sensitivity of the detector, using (6.3) and (6.4), in order to obtain initial design parameters is performed. These equations will consider $|\Gamma_{DET}|<0.1$ in a wide frequency range (-10 dB over 26-36 GHz) and a flat sensitivity in the whole frequency band ($S_{DET}(f_{start}) = S_{DET}(f_{stop})$).

The analysis is based on a sweep of the width W and physical lengths $long_1$ and $long_2$ of the lossy transmission lines with 20 Ω per square of sheet resistance in the frequency band from 26 to 36 GHz, while the series lossless transmission lines are set to a fixed impedance and electrical length values Z = 50 Ω, in order to avoid discontinuities in the microstrip lines, and $\Phi_3 = 90^o$ respectively. The width is swept in

the range from 130 to 350 µm, while the physical lengths are swept between 300 and 2500 µm. The analysis is focused on finding sets of values for W, *long1* and *long2* which make the detector have a sensitivity value around 1000 mV/mW and an input return loss higher than 10 dB. Besides, an additional requirement is considered for the sensitivity in order to achieve a flat response versus frequency. Therefore, the condition that the difference between the maximum and the minimum values of the sensitivity in the frequency range from 26 to 36 GHz must be less than 100 mV/mW is used. The results obtained with the analysis are shown in Fig. 6. 10, in which four different widths for the same combination of the physical lengths (*long1* = 500 µm and *long2* = 1900 µm) are obtained. These values are considered as the initial design parameters in the electrical circuit model.

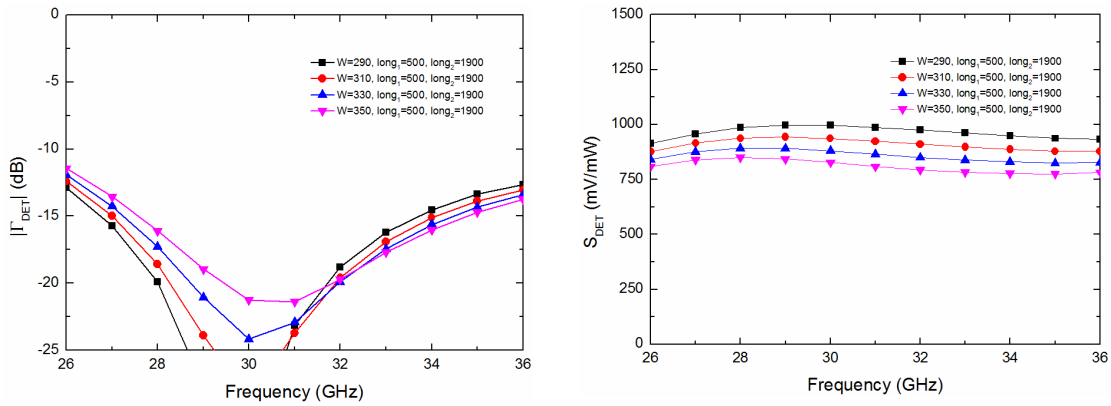

(a) (b)

Fig. 6. 10. Results of the detector for the frequency sweep of the π-network lossy transmission lines design. (a) Input reflection coefficient. (b) Sensitivity.

6.2.4 DC Output Network

Once the design parameters for the input matching network have been obtained, the design of the output network is analysed. This network must provide a good radiofrequency short-circuit to the cathode of the diode and, at the same time, the DC output contact in which the detected voltage is measured.

The design of the input matching network using short-circuited lossy microstrip lines, through via holes to ground, as thin film resistors provides DC current return paths for the diode. Therefore, the output network is not needed to have a physical ground return which enables the use of this point as a possible DC bias point.

The radiofrequency short-circuit is approached using a radial stub at the cathode of the diode, which forms a radiofrequency ground providing what is known as the video capacitance of the detector. The use of this type of virtual ground enables the

measurement of the DC voltage. The virtual ground is composed of two radial stubs in order to assure a good radiofrequency ground in the whole band of interest, and between them a high impedance quarter-wavelength (Z_4, Φ_4) microstrip line is used. Both radial stubs are tuned in slightly different frequencies to assure their effect in different sub-bands. An extra high impedance (Z_4, Φ_5) microstrip line is placed at the output of the second radial stub to connect a low-pass filter.

Then, the low-pass filter is added at the output of the network in order to determine the upper frequency limit of the DC bandwidth signal. The filter is implemented with surface mount devices. The schematic of the output network used for the detector is shown in Fig. 6. 11.

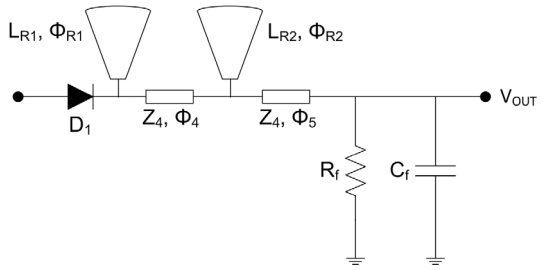

Fig. 6. 11. Output network schematic for the detector.

The detector also includes a specific pad in order to apply a DC bias to the diode, in case the detector must work at cryogenic temperature. It is placed in the output of the circuit, after the detected voltage is measured. A high value resistor, about Rb = 1 MΩ, is connected to the output to apply the DC bias.

6.2.5 Detector Design, Layout and Performance

The design of the detector has been divided into three different stages: the election of the diode, the input matching network and the DC output network. Once the described issues in previous sections are taken into account in order to have an initial design point, a full circuit schematic is implemented. The schematic of the detector used in ADS simulator is shown in Fig. 6. 12, in which the microstrip T-junctions and the resistor to bias the diode are not depicted. The lossy microstrip are implemented with thin-film resistors (TFRs) [6.18] which includes the conductor losses. The TFRs take into account the sheet resistance of the selected substrate; in the case of the alumina substrate [2.9] used for the design, a value of 20 Ω per square of sheet resistance is defined.

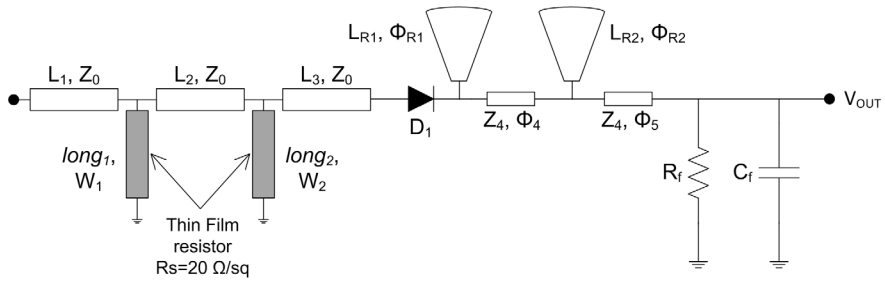

Fig. 6. 12. Complete detector schematic.

The optimization of the circuit is performed taken into account the radiofrequency-to-DC conversion and the input return loss simultaneously. Therefore, a combined simulation of harmonic balance and small signal Scattering parameters are performed in order to obtain a sensitivity S_{DET} around 1000 mV/mW and return loss better than 10 dB. Besides, the low-pass filter is configured with a resistor R_f = 100 kΩ and a capacitor C_f = 100 pF, which defines a cut-off frequency of around 16 kHz. The final dimensions obtained in the optimization process are listed in Table 6. 2, in which the length of the TFRs are not included.

Table 6. 2. Physical dimensions of the detector.

Variable	Value	Variable	Value
Z_0	50 Ω	L_1	100 μm
Z_4	85 Ω	L_2	800 μm
W_1=W_2	170 μm	L_3	1200 μm
Φ_{R1}	90º	L_{R1}	550 μm
Φ_{R2}	90º	L_{R2}	550 μm
Φ_4	93º	Φ_5	93º

The TFRs are divided into small sections in order to have a better solution in terms of the layout, since a too long line, as predicted for the initial value of the second lossy line, makes difficult to perform a suitable layout with a feasible area. Therefore, the TFRs are designed as shown in Fig. 6. 13(a), in which the final configuration is depicted. The equivalent length, joining the different sections, for $long_1$ and $long_2$ are, respectively, 520 μm and 1665 μm.

Additionally, due to the dimensions obtained after the optimization process and in order to have the access to the circuit in the middle of the substrate width, 50 Ω microstrip bends and a longer 50 Ω input line are included. This is shown in Fig. 6.

13(b). These microstrip lines add an extra 555 µm length straight line and a 600 µm length 45º line.

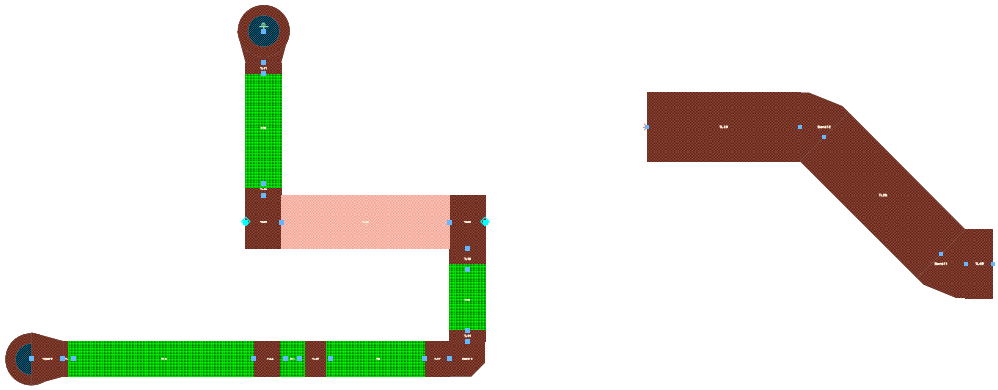

(a) (b)

Fig. 6. 13. Different parts of the detector layout. (a) Input matching network with the TFRs in green colour. (b) Additional structure at the input of the detector.

The electromagnetic simulation of the input microstrip network is done after the circuit is optimized. The simulations of the detector include a frequency sweep in order to analyse its performance in terms of the input return loss and sensitivity versus frequency with a fixed input power, and, on the other hand, a power sweep to describe its response versus the input power at a fixed frequency. The model of the HSCH-9161 diode developed in Chapter III is used in the simulations. The results of the detector simulation are shown in Fig. 6. 14. Mean values of the input return loss and sensitivity in the frequency band from 26 to 36 GHz are 15.4 dB and 1032 ± 40 mV/mW for an input power of -30 dBm. When the input power is swept, a fixed frequency of 31 GHz is used, and the detector starts compressing for high values of the input power.

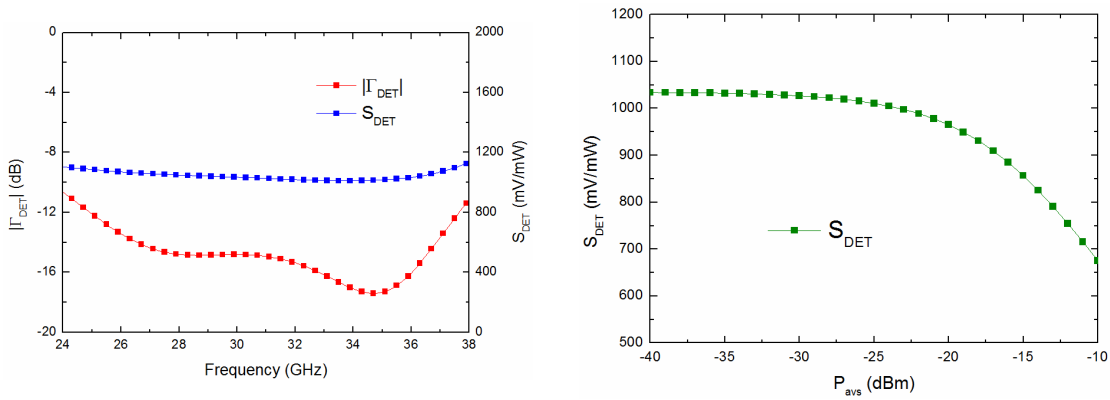

(a) (b)

Fig. 6. 14. Results of the detector simulation. (a) Input return loss and sensitivity versus frequency for an input power -30 dBm. (b) Sensitivity versus input power for a frequency of 31 GHz.

For measurement purposes in a coplanar probe station, the detector includes a 50 Ω CPWG-to-microstrip transition. The transition is not included in the optimization process since its effect is negligible and it is going to be removed in calibration process. A view of the detector is shown in Fig. 6. 15, in which the components are not included. The bias resistor (Rb in the figure) is expected to be placed between Vo and Vcc pads.

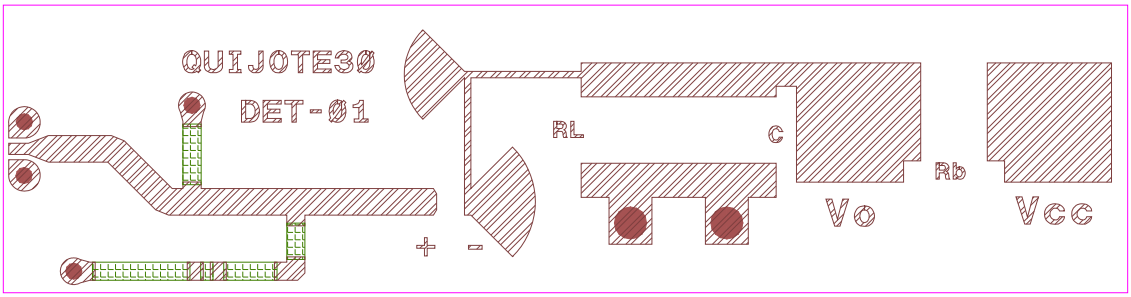

Fig. 6. 15. Layout of the detector.

6.3. Assembly of the detector

The assembly of the detector circuit is shown in Fig. 6. 16. In the photograph, the Schottky diode HSCH-9161 is placed at the end of the microstrip line before the radial stubs, the R_fC_f low-pass filter is included and the grey transmission lines are the TFRs as lossy lines.

The alumina substrate [2.9], presented and used in the previous designs described in this thesis, is composed of a gold conductive layer with a 20 Ω per square nickel-chromium resistive layer underneath. This layer enables the implementation of the lossy lines. The nickel-chromium layer shows a stable resistivity with the temperature, and it has around 0.075 μm thickness. The alumina has a ε_r=9.9 with a 254-μm thickness and a loss factor of 0.0001.

The elements of the low-pass filter are surface mount devices, with a stable dielectric material with the temperature, otherwise their performances at cryogenic temperature could be unforeseen. For instance, the NP0/C0G dielectric for capacitors shows a negligible temperature coefficient which means that under cryogenic temperature the value of the component is almost invariant from the nominal value at room temperature.

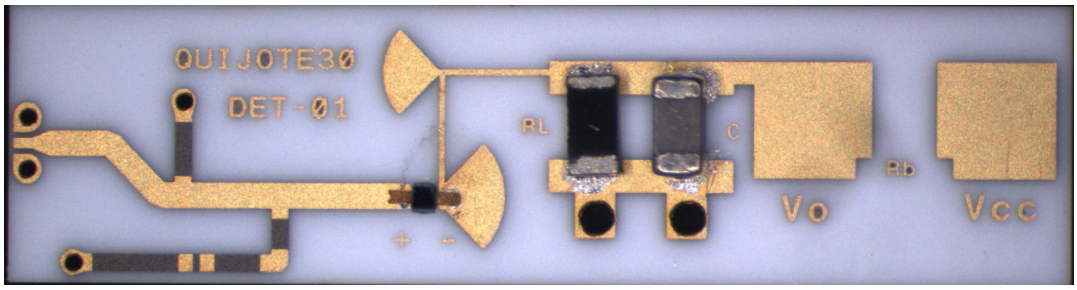

Fig. 6. 16. Photograph of the detector with components assembled (expect bias resistor not needed at room temperature).

6.4. Detector Characterization

The characterization of the detector is performed at room temperature in the coplanar probe station, and, then, at cryogenic temperature inside the cryostat. A vector network analyzer E8364A is used for the measurement of the input return loss, while a signal generator model 83650B from Agilent Technologies is used for the sensitivity characterization. At room temperature, the measurement set-up, which includes the probe station, is composed of a coplanar probe model 67A-GSG-150-C from PicoProbe by GGB Industries and a 2.4-mm flexible coaxial cable. For the cryogenic test, the circuit is assembled in a chassis and the measurement set-up is composed of semi-rigid and flexible 1.85-mm connector cables to connect the chassis with the outside of the cryostat through a 1.85-mm connector feedthrough and a 2.4-mm flexible coaxial cable outside the cryostat. In both measurements, the losses of the cables added to perform the characterization are corrected in the power signal generator.

6.4.1 Room Temperature Measurements

The detector in 254-µm alumina substrate is characterized at room temperature in the coplanar probe station. It is done in two steps: initially, the S-parameters are measured, and, then, the detected voltage is characterized through the frequency and power sweeps. The frequency sweep is done for a fixed available power to the detector of -31 dBm, while the power sweep is performed at the start, mid and stop frequencies of the band of interest (26 – 36 GHz). Besides, once the power sweeps are performed, the compression of the detector is obtained. Therefore, the figure of 1-dB compression point is defined as the point in which the detected voltage drops 1 dB when a logarithmic scale is considered, and it is given by

$$Compression(dB) = V_{OUT}(dBmV) - P_{avs}(dBm) \tag{6.21}$$

where the detected voltage in dBmV is calculated as

$$V_{OUT}(dBmV) = 10 \cdot \log_{10}(V_{OUT}(mV)) \tag{6.22}$$

The results obtained in the measurement process in the probe station are shown in Fig. 6. 17, in which the input return loss, the sensitivity versus frequency for an input power of -31 dBm, the sensitivity versus input power at three frequency points and the compression figure are depicted. The tests are performed using the zero-bias condition of the diode.

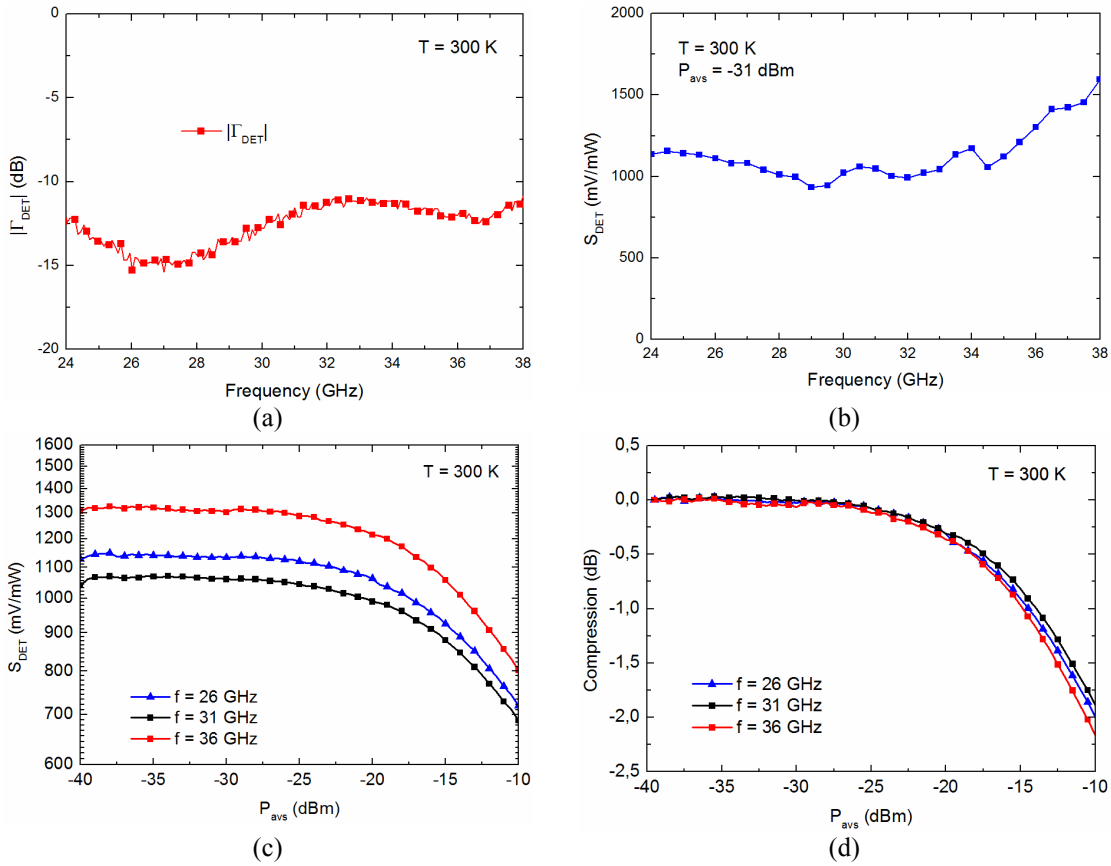

Fig. 6. 17. Results of the detector characterization at room temperature (300 K). (a) Input return loss. (b) Sensitivity versus frequency for an input power of -31 dBm. (c) Sensitivity versus input power for the frequencies of 26, 31 and 36 GHz. (d) Gain compression versus input power for the frequencies of 26, 31 and 36 GHz.

An additional measurement performed for the detector is the tangential sensitivity. It is defined as the lowest input signal power level which provides a detectable output signal. For this purpose, a low-frequency modulation microwave signal is applied to the input of the detector and the detected output is measured in an oscilloscope. Then, the power level of the microwave signal is decreased until the modulated output voltage cannot be measured. The measurement is performed using a square modulating signal of 1 kHz with an amplitude of 1 V peak to peak. Initially, the power signal is fixed to a

value of -20 dBm at a frequency of 31 GHz. The connection between the signal generator and the detector is made using a 2.4-mm coaxial cable, whose insertion loss at 31 GHz is 2.2 dB. The results are shown in Fig. 6. 18 and a minimum input power level for which a measurable output voltage is obtained is -40.2 dBm.

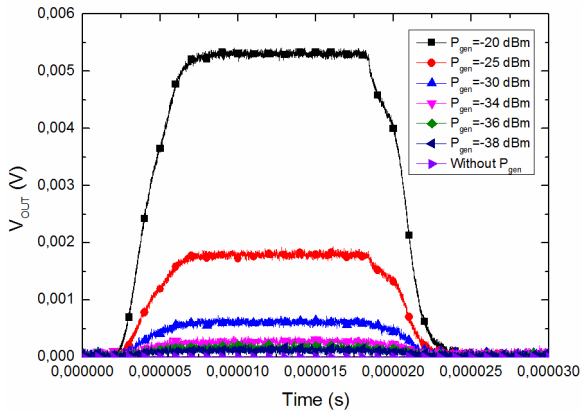

Fig. 6. 18. Tangential sensitivity of the detector at room temperature (300 K) for a frequency of 31 GHz.

From these results, a flat sensitivity is measured with a mean value of the sensitivity in the frequency band from 26 to 36 GHz of 1066 ± 120 mV/mW for an input power of -31 dBm, return loss better than 12 dB and a 1-dB compression point of around -15 dBm is achieved. A maximum input power of about -23 dBm is desired in order to disregard compression effects in the detected voltages.

6.4.2 Cryogenic Temperature Measurements

Once the room temperature tests are performed, the detector is characterized at cryogenic temperatures (15 K). The tests are done inside the cryostat at DICOM facilities. The assembly of the detector includes for this measurement the bias resistance, named Rb in the layout, since the performance of the diode at cryogenic conditions requires it. The value of the bias resistor is selected Rb = 1 MΩ.

A Detector Mechanical Design

In order to perform the cryogenic characterization, a mechanical chassis is designed to assemble the detector circuit inside it. The chassis is based on the design used for the 90º phase switch cryogenic characterization described in section 5.3.2.A in Chapter V with slight modifications. The main channel is only modified to add an open section to provide the DC output and input voltages. Besides, the detector is a

microstrip design, instead of a slot based circuit as in the case of the 90º phase switch, so the open cavity in the bottom of the channel is not mechanised.

A view of the chassis and the lid is shown in Fig. 6. 19. The chassis includes threaded holes in order to assure a good thermal link for the cooling down. The chassis uses thin wires to provide the DC output voltage and the DC bias supply.

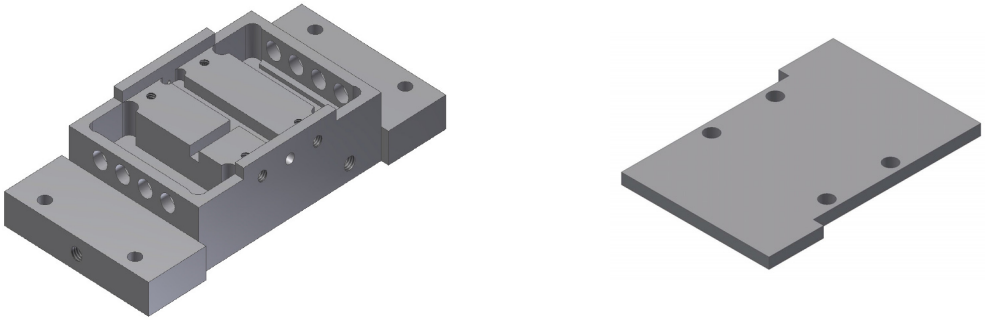

(a) (b)

Fig. 6. 19. Artistic views of the chassis designed for testing the detector at cryogenic temperature. Dimensions: 32x66x14 mm^3.

B Characterization

The chassis is thermally anchored inside the cryostat to the cold base of the cryostat to be cooled down. Detailed views of the detector inside the cryostat and the chassis are shown in Fig. 6. 20.

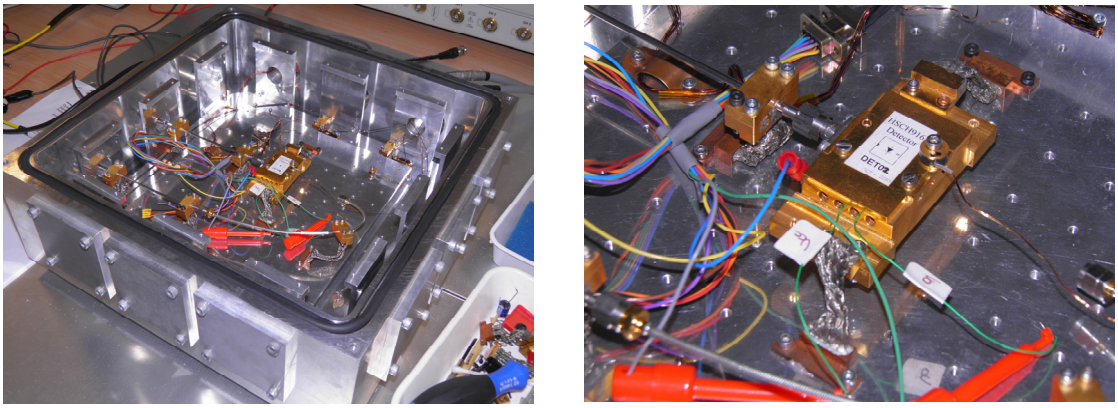

(a) (b)

Fig. 6. 20. Photograph of the cryogenic measurement set-up. (a) Assembly of the chassis inside the cryostat. (b) Detailed view of the chassis.

The characterization is performed using a 1.85-mm feedthrough connector which connects the outside of the cryostat to the chassis inside it through a 1.85-mm connector coaxial cable. They are thermally attached with heat sinks, to the different cold stages of the cryostat. The losses of this cable and the feedthrough are corrected in order to have a

constant input available power in the detector of around -31 dBm. These losses at cryogenic temperature (15 K) are approached by

$$L_{1.85\_CONN}(dB) = 4.817E-5f^{0.4064} \tag{6.23}$$

The losses of the external cable are corrected using a power sensor once connected to the signal generator in order to achieve a constant available power.

As described in Chapter III, the Schottky diode modifies its behaviour when working at cryogenic temperatures. The knee voltage of the HSCH-9161 diode is higher than at room temperature, and the zero-bias condition is not applicable at cryogenic temperatures. Therefore, the measurements at 15 K of the circuit are done for different bias points and the results are shown in Fig. 6. 21. The input return loss at cryogenic temperatures is not measured, since the results would be masked by the connection cables needed for the measurement set-up. The frequency sweep is performed for an input power of -32 dBm for different bias points of the diode. The power sweeps are done in the same way with a fixed frequency of 31 GHz.

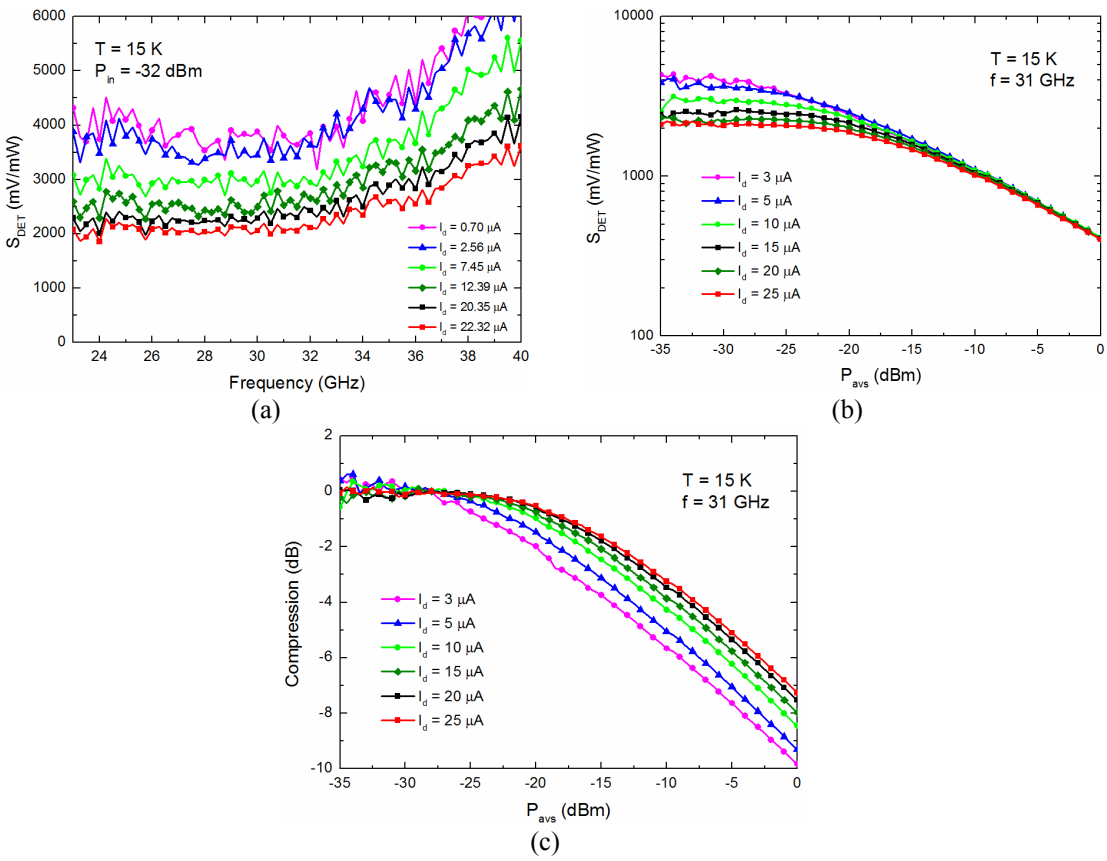

Fig. 6. 21. Results of the detector characterization at cryogenic temperature (15 K). (a) Sensitivity versus frequency for an input power of -32 dBm for different bias points. (b) Sensitivity versus input power for a frequency of 31 GHz for different bias points. (c) Gain compression versus input power for a frequency of 31 GHz for different bias points.

As summary, Table 6. 3 lists the mean values of the sensitivity and the 1-dB compression points achieved for the different bias points at 15 K.

Table 6. 3. Mean values of the sensitivity in the frequency band from 26 to 36 GHz for an input power of -32 dBm and the 1-dB compression point of the detector for a frequency of 31 GHz at 15 K.

Bias Conditions	**S (mV/mW)**	**P_{1dB} (dBm)**
I_d=3 μA	3960	-26
I_d=5 μA	3777	-23.5
I_d=10 μA	3144	-21.5
I_d=15 μA	2715	-21
I_d=20 μA	2440	-20
I_d=25 μA	2217	-19.5

At cryogenic temperature, an increase in the sensitivity of the detector is obtained related to the room temperature measurement, which depends on the bias current of the diode. Moreover, the higher the bias point, the lower the sensitivity of the detector. Besides, the compression of the detector also depends on the applied bias point, and the higher the diode current, the better the compression level.

6.5. Conclusions

This chapter has described the design and characterization of a wideband detector at both room and cryogenic temperatures for operating in the 26 to 36 GHz frequency band using microstrip technology and the HSCH-9161 Schottky diode.

A new detector in alumina substrate has been described, based on the use a π–network as matching solution. The matching network uses lossy transmission lines as distributed resistors in order to achieve a detector with good matching and flat sensitivity results. The analysis of short-circuited π-networks on hard substrate has been thoroughly described considering the input matching and sensitivity as design goals. The analysis of lossy transmission lines, implemented with thin-film resistors, has been demonstrated as a suitable solution in order to achieve significant results in the detector.

The design of the detector has been aided with electromagnetic simulators and the model of the zero-bias Schottky diode described in chapter 3 has been used.

The characterization of the detector at room temperature has been performed in a coplanar probe station in zero-bias conditions. The detector has shown an average sensitivity of 1066 ± 120 mV/mW in the 26 to 36 GHz band and a 1-dB input compression point of around -15 dBm, but input power lower than -23 dBm would be desired in order to avoid compression effects. The input return loss better than 12 dB has been measured in the same frequency range.

The characterization of the detector at cryogenic temperature (15 K) has been also performed. The modification in the performance of the HSCH-9161 Schottky diode at cryogenic temperatures involves the use of an external bias supply for the detector in order to work properly. Therefore, the detector has been tested under different DC bias currents for the diode, obtaining a variable sensitivity and 1-dB compression point depending on the bias point. A reduction in the sensitivity at cryogenic temperature is measured when the DC bias current is increased. This effect is due to the fact that the output equivalent resistance of the diode decreases with the increasing of the DC current. On the other hand, an increase in the 1-dB compression point is achieved when increasing the bias current in the diode. Besides, the sensitivity measured at cryogenic conditions is higher than at room temperature; for a DC bias current of 10 μA in the diode at 15 K, a mean sensitivity in the frequency band from 26 to 36 GHz higher than 3100 mV/mW is obtained facing the 1066 mV/mW as the mean value at room temperature for zero bias condition.

Chapter VII

Implementation of a Radio Astronomy Receiver: QUIJOTE Polarimeter

7.1. Introduction

The subsystems described in former chapters are aimed for their use in a receiver intended for radio astronomy applications working in the Ka-band (26 to 36 GHz). This type of receivers is one of the specific fields in which the cryogenic technology is particularly significant, since a reduction of their noise temperature and an increase of their sensitivity are achieved. Besides, the reduction of the physical temperature of the circuits involves a reduction in the losses or an improvement in the gains of the circuits, which is particularly important when working with so low-power level incoming signals as those radiated from the sky.

Consequently, all the circuits previously presented, 180º- and 90º-phase switches and the detector, have been designed concerning the physical temperature they could be

operating in the receiver, so the verification of their performance at cryogenic temperature has been described.

As final goal faced in this thesis, the analysis, description and characterization of the full Ka-band receiver are done. A short foreword of typical sketches used in radio astronomy receivers is outlined as introduction to the receiver configuration developed in the Thirty-GHz QUIJOTE instrument. Then, a brief analysis of the different subsystems which compose the receiver is described, and, finally, the full characterization of the receiver is presented.

7.2. Radio Astronomy Receivers

Radiometry is defined as the field of science and engineering in charge of the measurement of incoherent electromagnetic emission [7.1]. The thermal electromagnetic radiations are measured using highly sensitive receivers called radiometers. The requirement of high sensitivity in the designs is due to the signal power level expected at the input of the receiver is quite low, almost indistinguishable from the noise generated in the own receiver.

The goal of a radiometer is to measure the power of signals [7.2], which is commonly expressed in terms of an equivalent temperature. This measurement is needed to be performed in an accurate and high resolution way due to the low power level of the incoming signal.

The radiometric sensitivity is the parameter which characterizes the accuracy of a radiometer and it is defined as the signal which produces a DC output voltage equal to the effective value of the output fluctuations due to the system noise [7.3]. The receiver topology is one of the parameters that defines its sensitivity. The most common configurations used for radio astronomy receivers are described in the following sections.

7.2.1 The Total Power Radiometer

The total power radiometer is considered as the basic configuration and it measures the total noise power from the antenna and from the receiver itself. The block diagram of this kind of radiometer is shown in Fig. 7. 1.

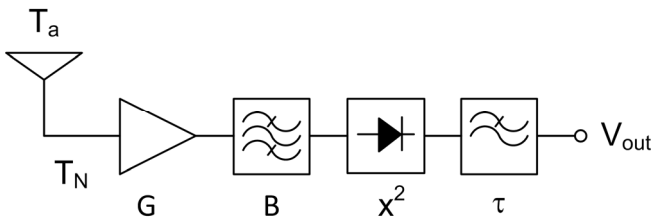

Fig. 7. 1. Total Power Radiometer sketch.

This type of radiometer calculates the average value of the detected voltage in a defined period of time, after being amplified a gain value *G*, filtered with a *B* frequency range band-pass filter and detected with a the square-law detector which provides a DC output voltage directly proportional to the receiver input noise power. Finally, a simple resistance-capacitor RC low-pass filter is used as an integrator at the output of the detector. The receiver noise T_N is mainly defined by the noise of the *G* amplifying stage. Therefore, it is commonly cooled down to cryogenic temperatures in order to reduce the equivalent noise temperature and to improve the sensitivity of the receiver.

The sensitivity of this type of radiometer [7.1]-[7.4], with an integrating time τ, is given by

$$\Delta T = \frac{T_a + T_N}{\sqrt{B \cdot \tau}} = \frac{T_{sys}}{\sqrt{B \cdot \tau}} \tag{7.1}$$

where T_a is the effective antenna noise temperature, *B* is the effective noise bandwidth of the receiver before the detector and $\tau=(1/2 \cdot B_{RC})$ with B_{RC} the equivalent bandwidth of the low-pass filter. The effective bandwidth [7.1]-[7.4], considering the power gain of the full chain before the detector, is defined as

$$B = \frac{\left[\int_0^\infty G(f)df\right]^2}{\int_0^\infty G(f)^2 df} \tag{7.2}$$

The above expression (7.1) for the receiver sensitivity takes only into account the noise fluctuations, but the receiver is also affected by gain fluctuations in the amplification stages, which are a key aspect in radio astronomy receivers [7.5], since they can be blended the noise incoming signal together. In this case, a 1/f noise output spectrum is generated [7.6]-[7.7]. These gain fluctuations are mainly due to physical temperature fluctuations or instabilities of the semiconductor devices. The noise uncertainty and the gain uncertainty are treated as independent variables since they are

caused by uncorrelated mechanisms, so their effects in the sensitivity are added, which is given by

$$\Delta T = T_{sys}\sqrt{\frac{1}{B\cdot\tau}+\left(\frac{\Delta G}{G_0}\right)^2} \tag{7.3}$$

where ΔG is the effective value of the receiver power gain variation and G_0 is the average predetection power gain.

7.2.2 The Dicke Radiometer

An advanced configuration for radiometers minimizing the fluctuation issues was first proposed by Dicke [7.8] with the idea of using modulation techniques, which avoids the reduction in the sensitivity due to the gain fluctuations. The block diagram of Dicke radiometer is shown in Fig. 7. 2.

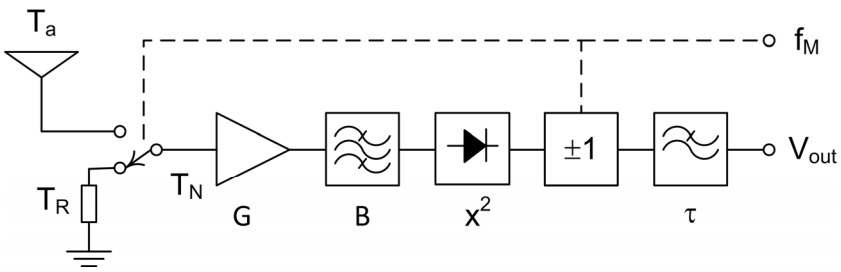

Fig. 7. 2. Dicke Radiometer sketch.

The receiver is based on the use of a switch which enables the measurement of the input signal from the sky or a reference load during equal periods of time modulated by a signal at frequency rate f_M. This f_M is needed to be higher than the gain fluctuation frequency to enable free-of-fluctuations measurements. At the ±1 multiplication stage, the output voltage is independent of the receiver noise while the gain variations are still present [7.1].

Hence, the sensitivity of the radiometer can be expressed as (7.4). When a balanced Dicke radiometer (T_a=T_R, with T_R the noise temperature of the reference load) is achieved, the effects of the gain fluctuations are removed, and therefore, the sensitivity can be rewritten as (7.5).

$$\Delta T = \left[\frac{2\cdot(T_a+T_N)^2+2\cdot(T_R+T_N)^2}{B\cdot\tau}+\left(\frac{\Delta G}{G_0}\right)\cdot(T_a-T_N)^2\right]^{1/2} \tag{7.4}$$

$$\Delta T = \frac{2\cdot(T_a+T_N)}{\sqrt{B\cdot\tau}} = \frac{2\cdot T_{sys}}{\sqrt{B\cdot\tau}} \tag{7.5}$$

7.2.3 The Correlation Radiometer

A correlation radiometer is composed of two or more identical receivers which are connected in parallel configuration and the incoming signal is divided into each one. The block diagram of this radiometer is shown in Fig. 7. 3, in which the orthogonal components of the input signal are the incoming signals to each receiver. Other configurations of the correlation radiometer are based on the connection of different antennas resulting in an interferometer with correlation receiver [7.4].

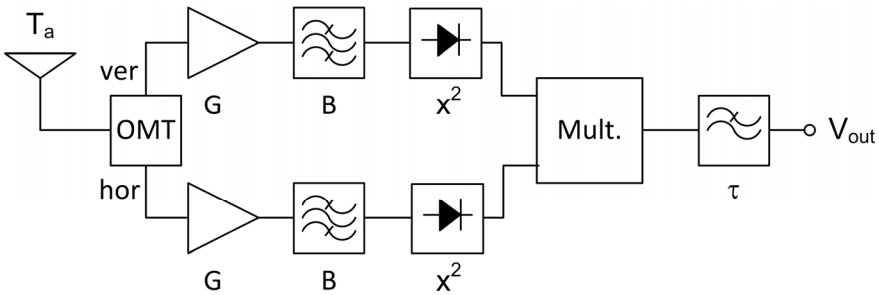

Fig. 7. 3. Correlation Radiometer sketch.

The signals from each receiver chain are correlated in order to improve the sensitivity of the radiometer. Since the noise signals introduced by each receiver are uncorrelated, after the multiplier module they will not add any contribution to the output signal. Therefore, the multiplier output contains a correlation signal proportional to the incoming antenna noise power which is the same for both receivers. The sensitivity of the correlation receiver is given by

$$\Delta T = \sqrt{2} \cdot \frac{T_{sys}}{\sqrt{B \cdot \tau}} \cdot \sqrt{1 + \left(\frac{0.5 \cdot T_a}{T_{sys}} \right)^2} \tag{7.6}$$

where T_{sys}=0.5·T_a+T_{REC}, with T_{REC} the receiver noise temperature.

7.2.4 The Pseudo-Correlation Radiometer

The pseudo correlation radiometer is an evolution of the previous receiver and combines the comparison with a reference load from the Dicke radiometer with the combination of signals from the correlation radiometer. The block diagram of this radiometer is shown in Fig. 7. 4. This topology was used in the Low-Frequency Instrument for the PLANCK mission [7.9]-[7.10].

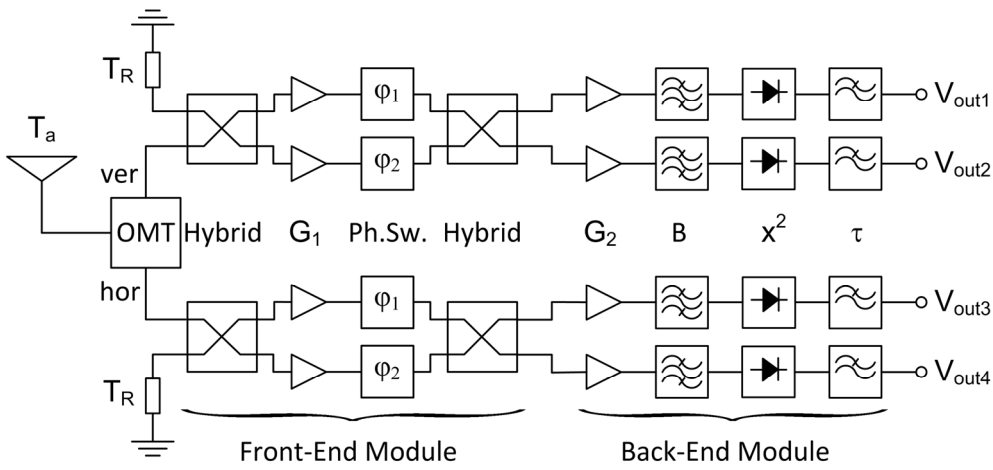

Fig. 7. 4. PLANCK Low-Frequency Instrument Pseudo-correlation Radiometer sketch.

This configuration compares the antenna temperature with the reference load to reduce the instabilities in the G_1 amplification stage and the use of phase switches minimizes the impact of the fluctuations of the final part of the receiver chains (called *Back-End Module* in Fig. 7. 4).

The sensitivity of the pseudo-correlation radiometer is given by (7.7), where T_{sys} is the addition of the antenna noise temperature and the noise temperature of one receiver branch.

$$\Delta T = \sqrt{2} \cdot \frac{T_{sys}}{\sqrt{B \cdot \tau}} \tag{7.7}$$

7.2.5 The Polarimetric Radiometer

The polarimetric radiometer is another variation of the correlation radiometer and is intended to obtain the Stokes parameters [7.11] which enable to determine the polarization state of an electromagnetic wave. An example of this type of receiver is used in the radiometers for QUIJOTE project [7.12], which is composed of two different topology receivers: the Multi-Frequency and the Thirty-GHz/Forty-GHz Instruments. The block diagram of the radiometer for the Multi-Frequency Instrument of the QUIJOTE polarimeter is shown in Fig. 7. 5, which is based on the rotation of a polar modulator at a frequency rate f_M placed before an orthomode transducer (OMT). The system provides a rotating reference system for the vertical and horizontal components in the OMT. For a high enough f_M, the polar cycle is faster than the low-frequency gain fluctuations and their effect is removed from the output signal. The configuration of the high frequency receivers (Thirty-GHz and Forty-GHz polarimeters)

is slightly different and they are based on electrical phase switching. The design of the receiver working in the Ka-band is the seed of this thesis and it will be explained in more details in the next section. The instantaneous sensitivity of each individual Stokes parameter is also calculated using (7.7).

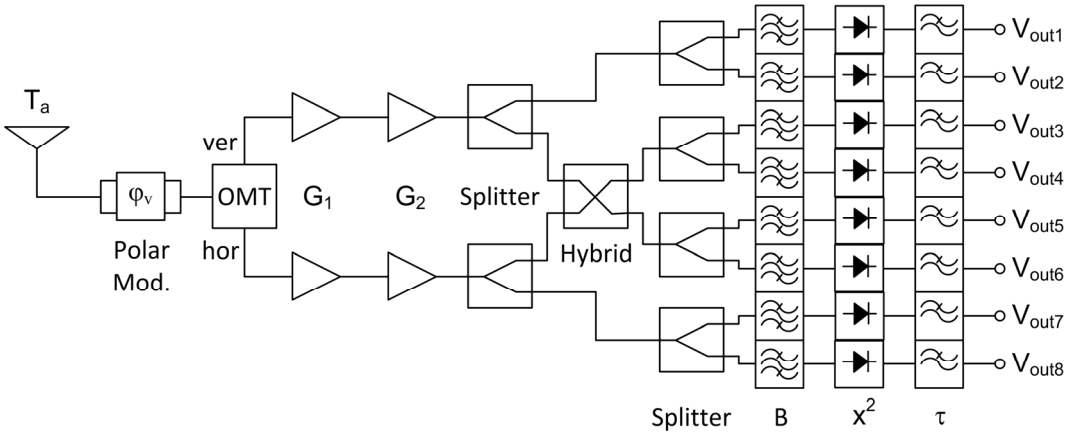

Fig. 7. 5. Multi-Frequency Receiver QUIJOTE Polarimeter Radiometer sketch.

7.3. The QUIJOTE Phase II Project

The QUIJOTE (Q-U-I JOint TEnerife) project is a ground-based experiment installed and being operated at Teide Observatory (Canary Islands, Spain) aimed for characterizing the polarization of the CMB and other galactic and extragalactic emissions in the frequency range 10 – 47 GHz and at large angular scales.

The experiment is divided into two stages. In the first one, called Phase I, a multi-frequency instrument (MFI), consisting on 4 pixels with 2 channels per horn, characterizes the CMB covering different bands within the frequency range from 10 to 20 GHz. The block diagram of this receiver is the one shown in Fig. 7. 5. In the Phase II, two instruments are under development for a second telescope, a 30-GHz (TGI – Thirty-GHz Instrument) and a 40-GHz (FGI – Forty-GHz Instrument). Both instruments are composed of 31 pixels working all of them in the 26 – 36 GHz and 35 – 47 GHz frequency band respectively. The temperature sensitivity per beam [7.12] for these radiometers is calculated as

$$\Delta T = \sqrt{2} \cdot \frac{T_{sys}}{\sqrt{B \cdot \tau \cdot N_{ch}}} \tag{7.8}$$

where N_{ch} is the number of channels in the receiver.

This experiment is intended as a valuable complement for the low-frequencies receivers of the PLANCK mission [7.10] and aimed for detecting primordial

gravitational-wave components (B-modes) and characterizing the polarization of the synchrotron and other anomalous emissions in our Galaxy [7.13].

From previous experiments [7.14], most CMB information has been obtained from intensity measurements. Therefore, the analysis of its polarization signal provides helpful data in order to completely characterize the CMB radiation.

As stated before, the standard theory assumes that the CMB is linearly polarized, so its polarization state can be described using Q and U Stokes parameters, defined by complex spin spherical harmonics. However, scientific polarization maps are usually defined in terms of E- and B- field components, which correspond to a combination of Q and U coefficients. These parameters enable the calculation of the angular power spectra in terms of temperature, E- and B- modes, which define the way in which the CMB anisotropies are originated from scalar or gravitational waves perturbations respectively.

The QUIJOTE experiment is defined with two polarization surveys. This strategy enables the receiver to scan sky areas and to obtain significant information of inflationary state of the CMB. The first one is a deep survey intended to analyse a sky area of around 3000 square degrees, whereas the second one is a shallow survey scanning around 18000 square degrees. Both surveys will reach low sensitivities in order to obtain sky maps and synchrotron information.

7.3.1 Receiver Description and Analysis

The receiver presented in this thesis is focused on the TGI instrument, which is under its last assembly stage and integration. The QUIJOTE TGI radiometer is intended to measure the polarization of the CMB measuring three of the Stokes parameters (Q, U and I) simultaneously. They are related to the amplitude of the two orthogonal electrical field components, providing the intensity of the signal through the I parameter and the linear polarization from the Q and U parameters.

The calculation of the Stokes parameters is achieved from the combination of measurable signals in the receiver. A polarizer, placed in front of an OMT, provides left- and right-hand circular polarization output signals, which detected and properly combined enable to obtain the parameters.

The TGI polarimeter block diagram is shown in Fig. 7. 6. Each pixel of the TGI is composed of a cold stage module (20 K) and a room temperature (298 K) module. The cryogenic part is made up of a feedhorn, a polarizer, an OMT and two low-noise

amplifiers. Outside the cryostat, two Gain and Filtering Modules, the Phase Switches Module and the Correlation and Detection Module operate at room temperature, in which the microwave signal is amplified, filtered, correlated by 180º microstrip hybrids and, finally, converted into DC voltages using square-law detectors. These signals are collected by a data acquisition system (DAS). The Phase Switches Modules comprise 0/180º and 0/90º phase switches generating four polarization states and their performance is crucial in order to obtain the Stokes parameters, minimizing the leakage among them and, at the same time, overcoming the 1/f noise and different systematic errors in the receiver.

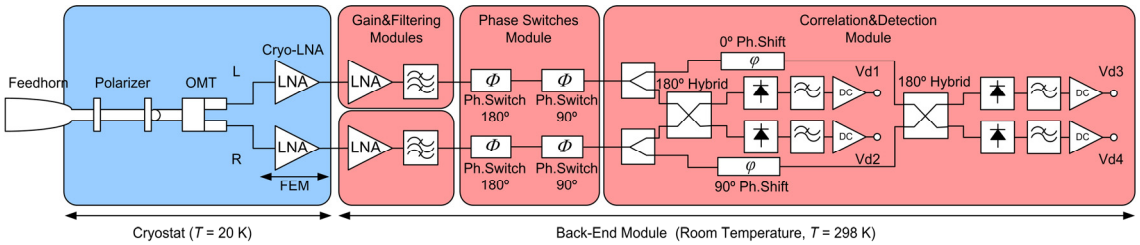

Fig. 7. 6. Sketch of the 31 GHz QUIJOTE receiver.

The sketch in Fig. 7. 6 shows four outputs (V_{d1} to V_{d4}) providing the detected DC voltages, which are combined in the DAS.

Considering a circular coordinate system, the Stokes parameters are defined by

$$I = |E_l|^2 + |E_r|^2 \tag{7.9}$$

$$Q = 2 \cdot \mathrm{Re}\left(E_l^* \cdot E_r\right) \tag{7.10}$$

$$U = -2 \cdot \mathrm{Im}\left(E_l^* \cdot E_r\right) \tag{7.11}$$

$$V = |E_l|^2 - |E_r|^2 \tag{7.12}$$

where E_l and E_r are the electrical field components in a circular coordinate system [7.11]. The parameter V is assumed to be $V = 0$ and therefore it is not measured.

A simplified schematic of the TGI receiver shown in Fig. 7. 7 is assumed in order to analyse the operation of the polarimeter. According to the scheme, the combination of the 90º- and 180º-phase switches provides four phase states per branch. Hence, sixteen phase states are achieved between both branches of the pixel. Since different combinations of phase states cause redundant states, the analysis of the phase state of the pixel is easier analysed in terms of the difference between branches of the pixel Φ_T, given by

$$\Phi_T = \Phi_{B2} - \Phi_{B1} = (\Phi_3 + \Phi_4) - (\Phi_1 + \Phi_2) \tag{7.13}$$

where Φ_{B2} corresponds to the phase state of the lower branch of the Phase Switch Module and Φ_{B1} to the phase state of the upper branch of the Phase Switch Module in Fig. 7. 7.

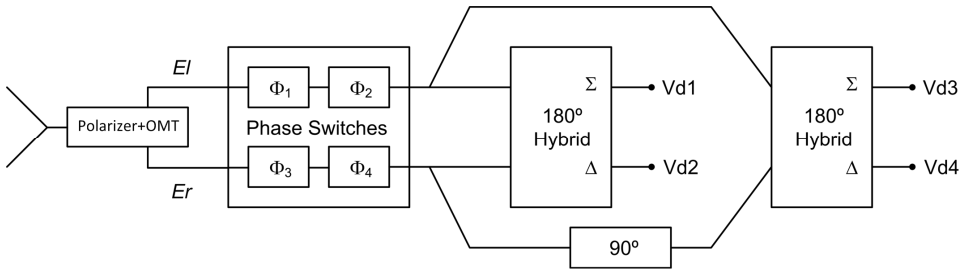

Fig. 7. 7. Simplified sketch of the TGI polarimeter.

The input signals to the phase switch module, E_l and E_r, are the outputs of the OMT, which are the components of the incoming electromagnetic radiation to a circular polarization receiver. These signals are defined by

$$E_l \propto \frac{1}{\sqrt{2}} \cdot (E_X + j \cdot E_Y) \tag{7.14}$$

$$E_r \propto \frac{1}{\sqrt{2}} \cdot (E_X - j \cdot E_Y) \tag{7.15}$$

where E_X and E_Y are the orthogonal electrical field components in a Cartesian coordinate system incoming to the feedhorn. Then, considering the phase state $\Phi_T = 0º$ which corresponds to the reference state in each phase switch, the detected output voltages are obtained as

$$V_{d1} \propto |E_l + E_r|^2 \tag{7.16}$$

$$V_{d2} \propto |E_l - E_r|^2 \tag{7.17}$$

$$V_{d3} \propto |E_l + j \cdot E_r|^2 \tag{7.18}$$

$$V_{d4} \propto |E_l - j \cdot E_r|^2 \tag{7.19}$$

Therefore, performing the linear combination between outputs, the following values are achieved:

$$V_{d1} + V_{d2} \propto |E_l + E_r|^2 + |E_l - E_r|^2 \tag{7.20}$$

$$V_{d3} + V_{d4} \propto |E_l + j \cdot E_r|^2 + |E_l - j \cdot E_r|^2 \tag{7.21}$$

$$V_{d1} - V_{d2} \propto |E_l + E_r|^2 - |E_l - E_r|^2 = 4 \cdot \mathrm{Re}\left(E_l \cdot E_r^*\right) \tag{7.22}$$

$$V_{d3} - V_{d4} \propto |E_l + j \cdot E_r|^2 - |E_l - j \cdot E_r|^2 = 4 \cdot \mathrm{Im}\left(E_l \cdot E_r^*\right) \tag{7.23}$$

These values correspond to the Stokes parameters defined in a circular coordinate system, equations (7.9) to (7.12). In an analogous way, the Stokes parameters are calculated for the other phase states and they are listed in Table 7. 1.

Table 7. 1. Stokes parameters from output detected voltages.

Φ_T	I	Q	U
0º	$V_{d1}+V_{d2}=V_{d3}+V_{d4}$	$V_{d1}-V_{d2}$	$V_{d3}-V_{d4}$
90º	$V_{d1}+V_{d2}=V_{d3}+V_{d4}$	$V_{d3}-V_{d4}$	$V_{d1}-V_{d2}$
180º	$V_{d1}+V_{d2}=V_{d3}+V_{d4}$	$V_{d2}-V_{d1}$	$V_{d4}-V_{d3}$
270º	$V_{d1}+V_{d2}=V_{d3}+V_{d4}$	$V_{d4}-V_{d3}$	$V_{d2}-V_{d1}$

As the CMB is expected to be weakly linearly polarized, the previous analysis is focused on a linear polarization as input signal to the polarimeter. The translation from linear polarization signal to circular polarized wave is performed with the square quad-ridge waveguide polarizer combined with the OMT, which splits left-hand and right-hand circular components. The reference plane of the polarizer is rotated 45º regarding the reference system of the input signal and the OMT in order to accomplish the behaviour of a septum polarizer [7.15]. The combination of the polarizer plus OMT enables to overcome the septum polarizer bandwidth limitation with a simple arrangement.

Considering the input signal with an amplitude level A in the sketch shown in Fig. 7. 7, the detected outputs for the phase state $\Phi_T = 0º$ are given by

$$V_{d1} = K \cdot A^2 \tag{7.24}$$

$$V_{d2} = 0 \tag{7.25}$$

$$V_{d3} = (K/2) \cdot A^2 \tag{7.26}$$

$$V_{d4} = (K/2) \cdot A^2 \tag{7.27}$$

where K is a constant related to the amplification in the receiver chain.

By changing the phase state of the phase switches module, the values for the different polarization states are listed in Table 7. 2.

Table 7. 2. Detected voltages for an x-axis polarized signal with amplitude A.

Φ_T	V_{d1}	V_{d2}	V_{d3}	V_{d4}
0º	$K \cdot A^2$	0	$(K/2) \cdot A^2$	$(K/2) \cdot A^2$
90º	$(K/2) \cdot A^2$	$(K/2) \cdot A^2$	$K \cdot A^2$	0
180º	0	$K \cdot A^2$	$(K/2) \cdot A^2$	$(K/2) \cdot A^2$
270º	$(K/2) \cdot A^2$	$(K/2) \cdot A^2$	0	$K \cdot A^2$

In the particular case of a y-axis linear polarization input signal, the analysis of the receiver response is analogous and the four detected voltages of the polarimeter are listed in Table 7. 3.

Table 7. 3. Detected voltages for a y-axis polarized signal.

Φ_T	V_{d1}	V_{d2}	V_{d3}	V_{d4}
0º	0	$K{\cdot}A^2$	$(K/2){\cdot}A^2$	$(K/2){\cdot}A^2$
90º	$(K/2){\cdot}A^2$	$(K/2){\cdot}A^2$	0	$K{\cdot}A^2$
180º	$K{\cdot}A^2$	0	$(K/2){\cdot}A^2$	$(K/2){\cdot}A^2$
270º	$(K/2){\cdot}A^2$	$(K/2){\cdot}A^2$	$K{\cdot}A^2$	0

In the following sections, the subsystems of the QUIJOTE TGI radiometer are described: the feedhorn antenna, the OMT, the polarizer, the cryogenic low-noise amplifiers and, finally, the complete Back-End Module. All these subsystems have been designed and assembled at the DICOM.

7.3.2 QUIJOTE Switching Strategy

As mentioned in previous section, the performance of the phase switches is significant for the receiver operation in order to minimize noise and systematics errors interaction in the output signals which enable the calculation of the Stokes parameters. Therefore, the way to switch the state of the Phase Switches Module could derive in better results.

As shown in Fig. 7. 6, each pixel of the receiver is composed of a Correlation and Detection Module. At their inputs, the noise contribution, especially the 1/f spectrum, is different in each branch of the receiver due to the signals are not correlated. Then, the fluctuations in the amplifying stages, not only cryogenic ones but also room temperature LNAs, are propagated in the receiver. Once the microwave signals go into the Module, the 180º hybrid correlates both of them. Therefore, the signals are affected with the contribution of both amplifying chains and the 1/f gain fluctuations are the same in the output channels (V_{d1} to V_{d4}).

The phase switches are used to remove the 1/f noise of the system. The switching frequency of the phase switches is fixed above the knee frequency of the 1/f noise. The sixteen phase states, combining the 90º and the 180º phase switches, are needed to be performed in a period of time lower than the period of the 1/f noise. In this case, the cancellation of the 1/f noise is achieved.

Moreover, the phase switches are designed using PIN diodes in the receiver configuration, since the Phase Switches Module works at room temperature. Then, the switching capability of the diodes must ensure a good performance for high modulation frequencies (in the order of kilohertz). The switching response of the HPND-4005 PIN diode has been tested [7.16], enabling the use of switching frequencies up to 5 MHz.

In the TGI receiver, a knee frequency lower than f_{knee} = 500 Hz for the 1/f noise is expected and a sampling strategy of 1000 samples/s will be used in the acquisition unit to properly avoid 1/f noise. Then, the switching frequency is f_s = 4 kHz since four phase states are configured in the receiver (Φ_T = 0º, 90º, 180º and 270º) and, as in the Phase Switches Module, with two branches, sixteen commutations are defined, a switching frequency of f_s = 16 kHz will be used in the system.

Moreover, the use of the phase switches enable the cancellation of the systematic errors in the hardware of the receiver, since the state of the phase switches modify the calculation of the Stokes parameters using different outputs (Table 7. 1)

7.3.3 QUIJOTE TGI Feedhorn

The antenna designed for the receiver is based on a corrugated feedhorn, in which the matching and the cross-polarization are defined by the throat of the horn. This design is done in our researching group at DICOM.

The circular input waveguide diameter is 8 mm, which enables a good performance at the lower end of the bandwidth, especially in the input matching.

After the constant section of circular waveguide, a few corrugations with increasing diameters, modifying theirs depths and thickness, are designed in order to define the cross-polarization value, critical for radio astronomy. The remaining set of corrugations is optimized in diameter, but keeping fix their depth and thickness, to achieve high gain and matching. Due to mechanical constraints, the antenna is divided into three parts: the initial critical set of corrugation together the circular waveguide is manufactured individually, while the second part of fixed depth and thickness corrugations are divided into two parts due to its full length. A cross-section view of the antenna and the internal corrugations are shown in Fig. 7. 8, while a photograph of the manufactured antenna is shown in Fig. 7. 9.

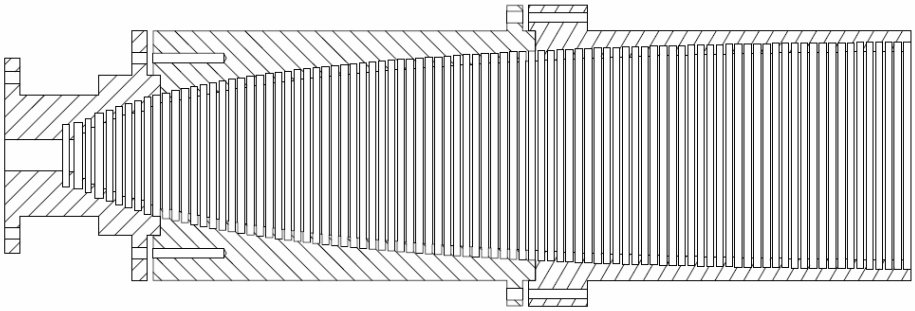

Fig. 7. 8. Cross-section of the feedhorn antenna. Length 235.4 mm. Outer diameter 77 mm.

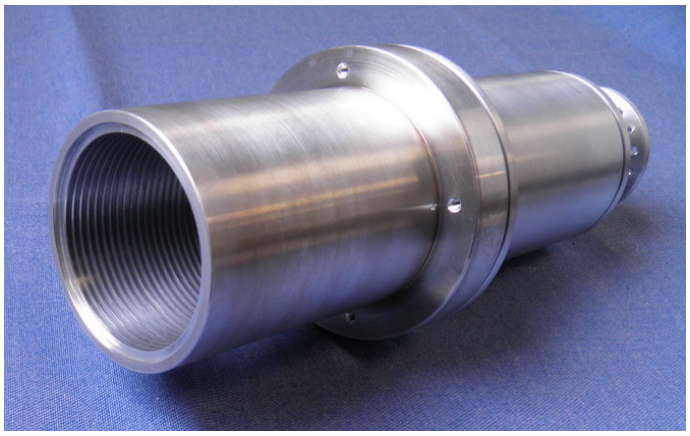

Fig. 7. 9. Photograph of the feedhorn antenna.

The antenna has been characterized in an anechoic chamber and its performance is shown in Fig. 7. 10. Return loss better than 20 dB and directivity of about 20 dB are measured. A cross-polarization value of around -40 dB is obtained and its measurement is limited by the noise floor of the measurement setup.

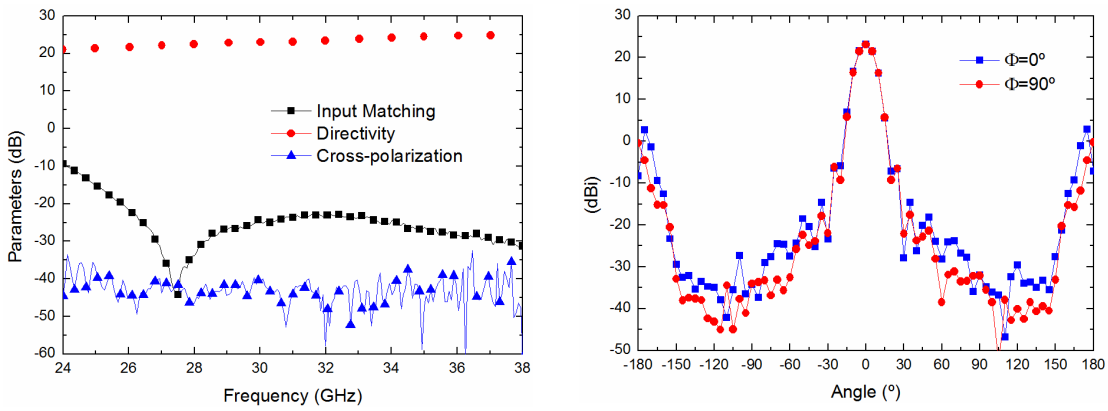

(a) (b)

Fig. 7. 10. Measurement results of the feedhorn antenna. (a) Input matching, directivity (in dBi) and cross-polarization. (d) Radiation pattern at 31 GHz.

7.3.4 QUIJOTE TGI Polarizer

A polarizer is a subsystem that provides orthogonal circular components (RHCP – Right Hand Circular Polarization and LHCP – Left Hand Circular Polarization) of a linear polarization incoming signal when the polarizer is rotated 45º regarding the input reference axis.

The TGI polarizer is designed using square waveguide with a ridge in each internal wall and it was designed by our researching group. The ridges enable the mode matching as well as they produce a 90º phase shift between the two propagated modes in each physical port, TE_{11s} and TE_{11c}, which means a four electrical port device. It is based on [7.17].

As described in section 7.3.1, the polarizer is placed in front of the OMT and is rotated 45º regarding the reference axis of the OMT. Then, both devices together work as a septum polarizer [7.15]. The combination of both subsystems enables to achieve wider bandwidths than with a typical septum polarizer structures. It provides a relative bandwidth wider than 30%, which is difficult to be obtained using a septum. The internal views of the polarizer considering x- and y-axis sections are shown in Fig. 7. 11. Besides, it shows a front view of the square waveguide (a=7.54 mm) with the ridges in the four walls.

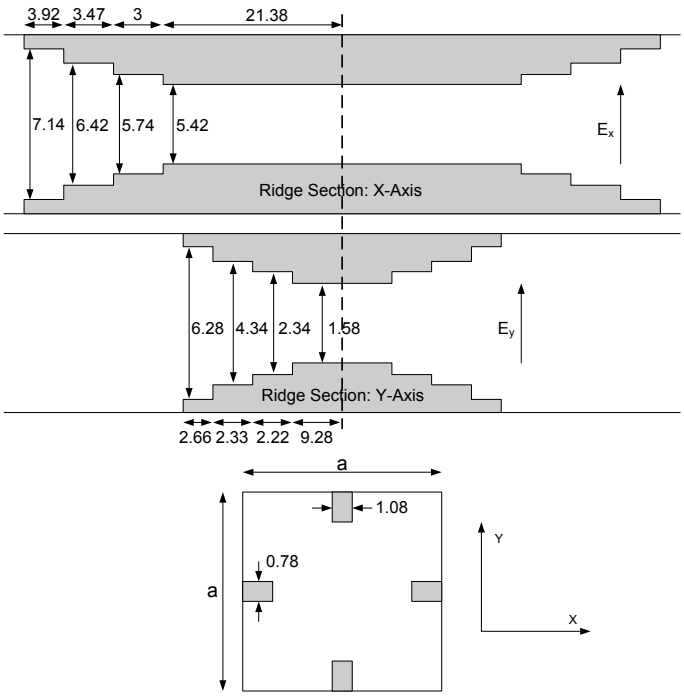

Fig. 7. 11. Cross-sections and front view of the polarizer (dimensions in mm).

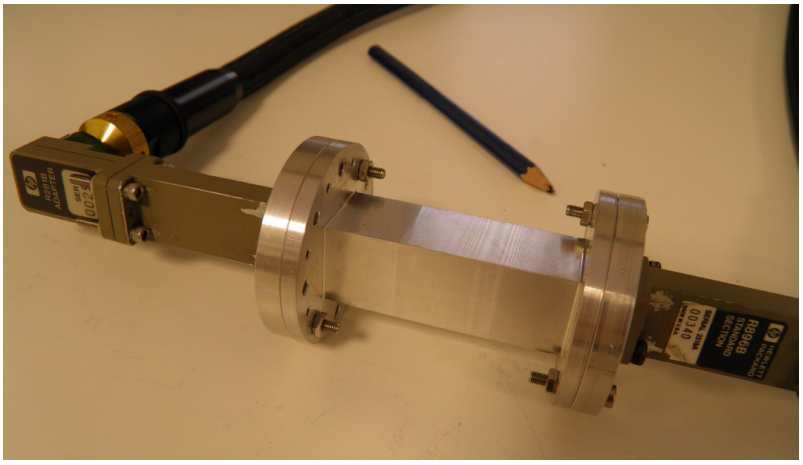

Fig. 7. 12. Photograph of the polarizer during its characterization.

Since the polarizer is a square waveguide design, a transformer from circular waveguide is designed in order to interconnect it to the feedhorn and the OMT. The transformers are based on octagonal shape pieces [7.18]. A manufactured circular to square waveguide octagonal transformer is shown in Fig. 7. 13.

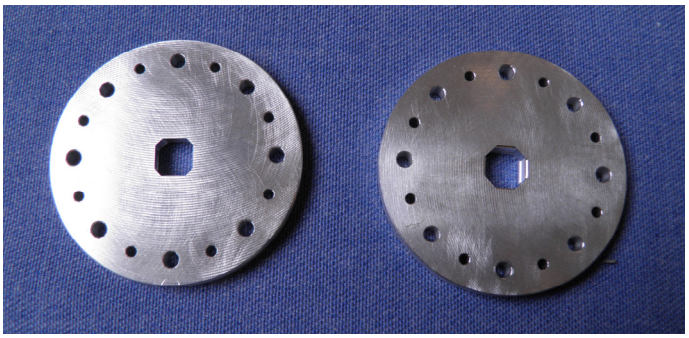

Fig. 7. 13. Photograph of the octagonal transformer from circular to square waveguide.

The measurement of the polarizer is performed in two steps, since the device must be spun related to the reference plane of the rectangular input waveguide used in the calibration of the measurement setup. Besides, octagonal-shaped waveguide transformers are used in order to match rectangular waveguide to the square one in the polarizer accesses. Measured results are presented in Fig. 7. 14, with an average phase difference between outputs of 89.7º ± 1º and insertion loss lower than 0.2 dB in both measurements.

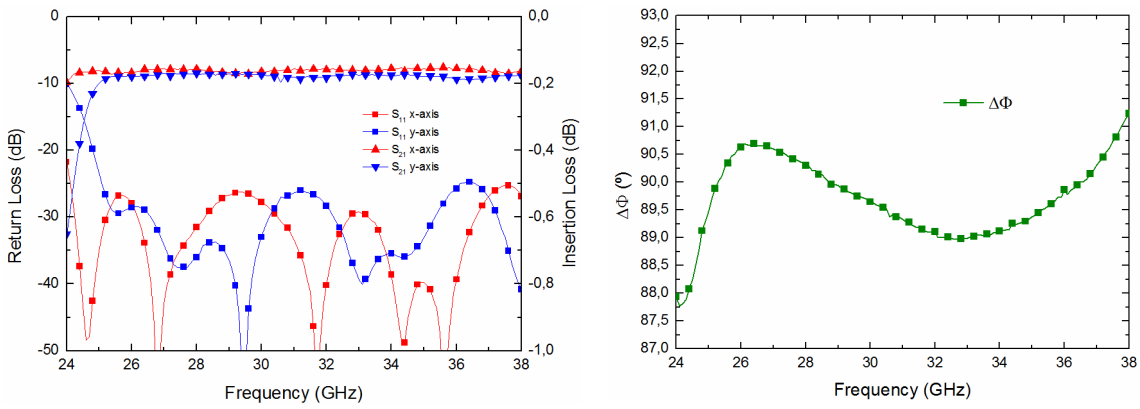

(a) (b)

Fig. 7. 14. Measured results of the TGI polarizer. (a) Return and insertion loss along x- and y-axis of the device. (b) Phase difference between outputs.

7.3.5 QUIJOTE TGI Orthomode Transducer

The QUIJOTE polarimeter is based on the use of linear orthogonal polar components of the incoming signal. The action of separating the components is achieved by an OMT, whose design is based on a turnstile junction with an inserted scatterer. Further details about its design are described in [7.19]. Some views of the OMT are shown in Fig. 7. 15, with details of the internal waveguide paths and the scatterer piece, while two manufactured units of the OMT are depicted in Fig. 7. 16.

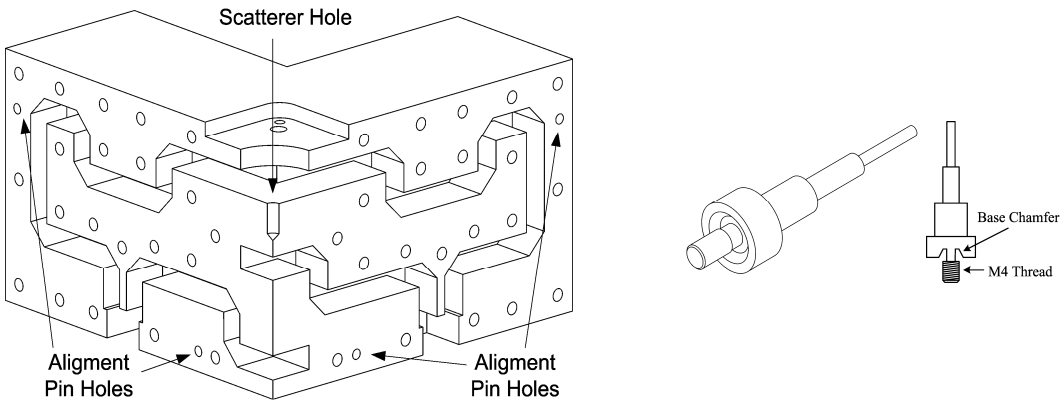

(a) (b)

Fig. 7. 15. Views of the OMT. (a) Internal faces of one OMT quarter. (b) Scatterer.

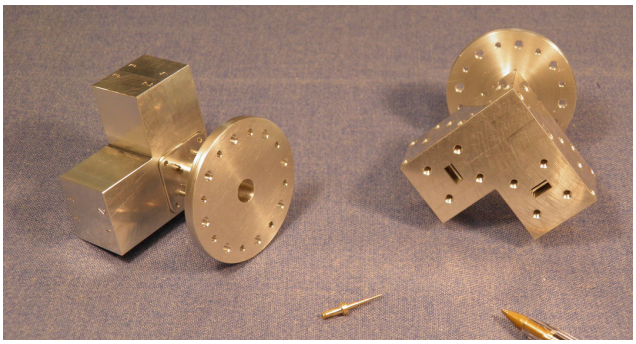

Fig. 7. 16. Photograph of the OMT, showing the circular waveguide input (left part) and the rectangular WR28 waveguide outputs (right part).

The measurement of the OMT is performed using a WR28 calibration kit, so the rectangular output ports are characterized. The results of the characterization are shown in Fig. 7. 17. The reflection in both WR28 outputs, traces *WR28* S_{11} and *WR28* S_{22} in the figure, is measured connecting the waveguides of the setup and placing a radiation load at the circular access. The isolation between WR28 outputs is measured as the transmission between accesses when a radiation load is placed at the circular port. The insertion loss between the circular port and one of the rectangular ports, *Transmission* in the figure, is estimated as the one half of the reflection coefficient at the rectangular port when a short-circuit is placed in the circular port. Finally, the phase difference between branches is calculated as the difference between the phases of the reflection measurements at each rectangular port divided by two also with a short-circuit in the circular port. Return loss better than 25 dB, insertion loss of around 0.15 dB, isolation between output ports better than 50 dB and a phase difference lower than 2º are obtained.

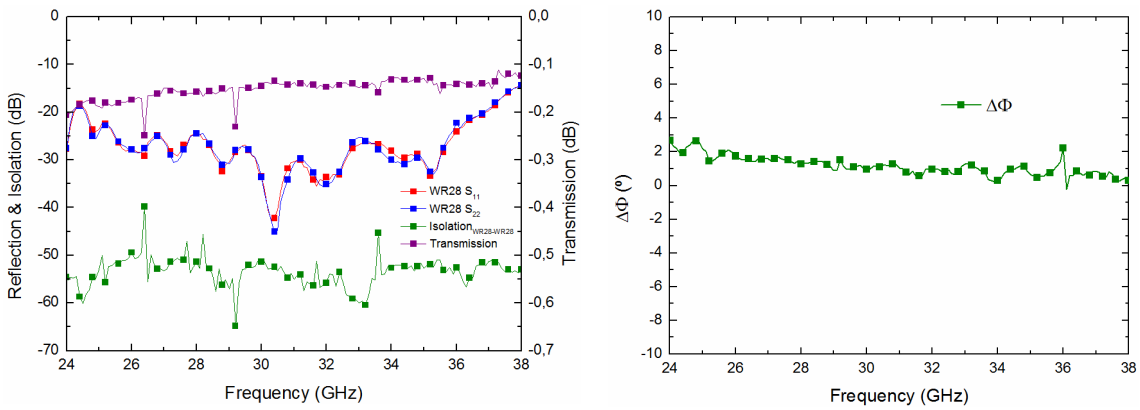

(a) (b)

Fig. 7. 17. Measured results of the TGI OMT. (a) Isolation between rectangular waveguide outputs, return loss at rectangular ports and insertion loss from circular to rectangular waveguides. (b) Phase difference between outputs.

7.3.6 QUIJOTE TGI Cryogenic Low-Noise Amplifiers

An important subsystem in the receiver is the cryogenic low-noise amplifier (LNA), since its equivalent noise temperature partially defines the noise temperature of the receiver. It is part of the Front-End Module (FEM) together with the optomechanic components.

The cryogenic LNA is composed of two cascaded monolithic microwave integrated circuit (MMIC) low-noise amplifiers. The first MMIC is based on 100 nm metamorphic high-electron-mobility-transistor (mHEMT) technology from the Fraunhofer IAF (Freiburg – Germany) [7.20] and the second one is designed on 130 nm mHEMT technology from OMMIC foundry [7.19]. Photographs of both LNAs are shown in Fig. 7. 18 and Fig. 7. 19 respectively. Additionally, a 5 dB microstrip attenuator is designed to be allocated between both LNAs. The attenuator isolates both LNAs, reducing the mismatching between them and providing a way of adjusting the total gain of the module while the bias point is focused on noise performance. A picture of the attenuator is shown in Fig. 7. 20.

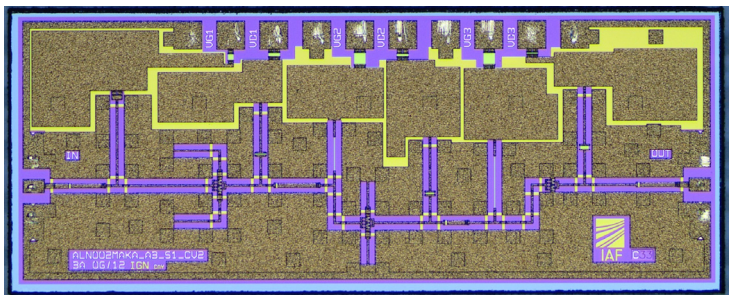

Fig. 7. 18. Photograph of the IAF MMIC chip. Dimensions 2.5x1 mm².

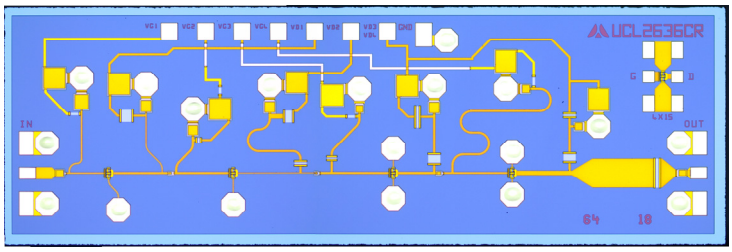

Fig. 7. 19. Photograph of the OMMIC MMIC chip. Dimensions 3x1 mm².

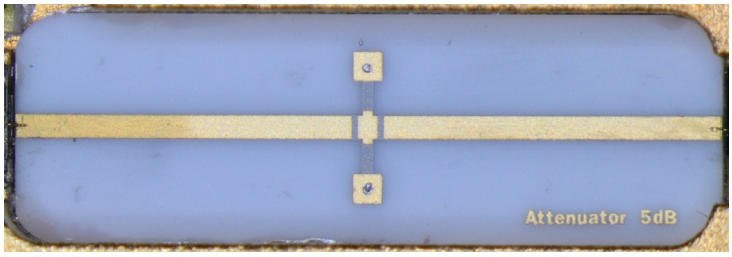

Fig. 7. 20. Photograph of the 5 dB microstrip attenuator on Alumina substrate. Dimensions 7.5x2.5 mm².

The full assembly of the cryogenic LNA is shown in Fig. 7. 21, together with a view of the assembly inside the cryostat, to measure the performance of the amplifier in terms of noise and gain at cryogenic temperature (13 K).

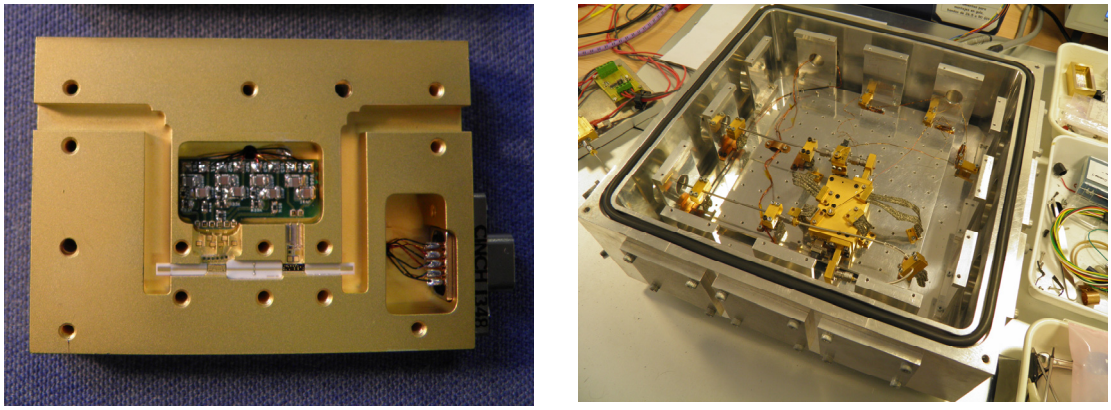

(a) (b)

Fig. 7. 21. Photographs of the cryogenic LNA. (a) View of the assembly in the gold-plated chassis. (b) Assembly inside the cryostat.

The measurement of the LNA at 13 K is shown in Fig. 7. 22. An average noise temperature of 23.1 K is achieved for an average insertion gain of 40.9 dB for total power consumption of 7.8 mW in the 26 to 36 GHz frequency band using the cold-attenuator method, the noise figure analyzer (NFA) N8975A from Agilent Technologies, the 346CK01 noise source from Agilent Technologies and an external frequency down converter with input signal up to 50 GHz.

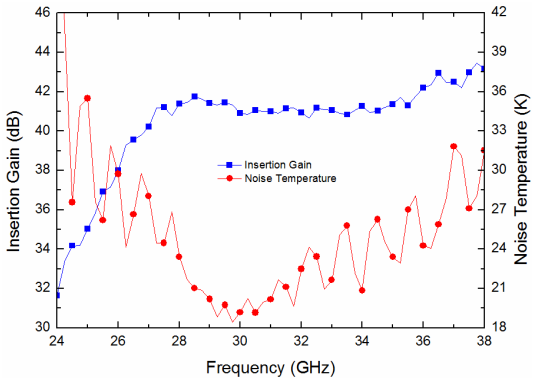

Fig. 7. 22. Performance of the low-noise amplifier at 13 K.

7.3.7 QUIJOTE TGI Back-End Module

The BEM of the TGI receiver is composed of several subsystems which are cascaded. The block diagram of the unit is shown in Fig. 7. 23. Two Gain and Filtering Modules, followed by a Phase Switches Module and, finally, a Correlation and Detection Module are part of the BEM.

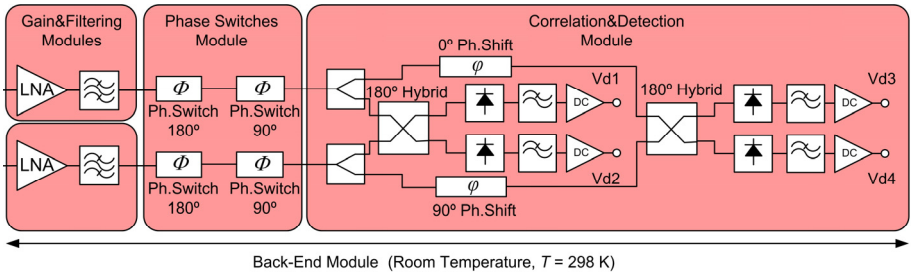

Fig. 7. 23. Complete Back-End Module schematic.

The Gain and Filtering Module is composed of two low-noise amplifiers, an attenuator and a band-pass filter. Some views of the mechanical chassis manufactured are shown in Fig. 7. 25.

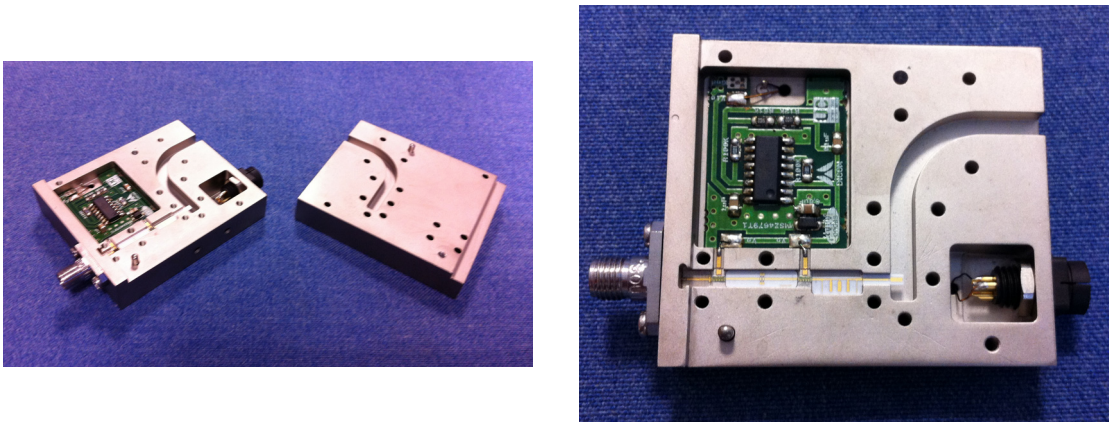

(a) (b)

Fig. 7. 24. Photographs of the module. (a) General view of the opened chassis. (b) Internal view.

The assembly of a radiofrequency chain inside the chassis of the Gains and Filtering Modules is shown in Fig. 7. 25. The LNAs used in the module is a commercial solution from Avago Technologies model AMMC-6241 [7.21], and two units are included in order to provide a further amplification of around 45 dB. A 10 dB attenuator is included to achieve the required power level and to avoid the compression of the detector. Besides, the module includes a band-pass filter which defines the operation bandwidth. The S-parameters of a representative unit are shown in Fig. 7. 26, obtaining average values for gain of 33.8 dB, input insertion loss of 17 dB, output return loss of 13.6 dB and noise figure of 3.3 dB are achieved in the frequency band from 26 to 36 GHz. The bias point of the unit is fixed at +5 V, and a voltage regulator accommodates the voltage to +2 V (a current around 140 mA) applied to the LNAs.

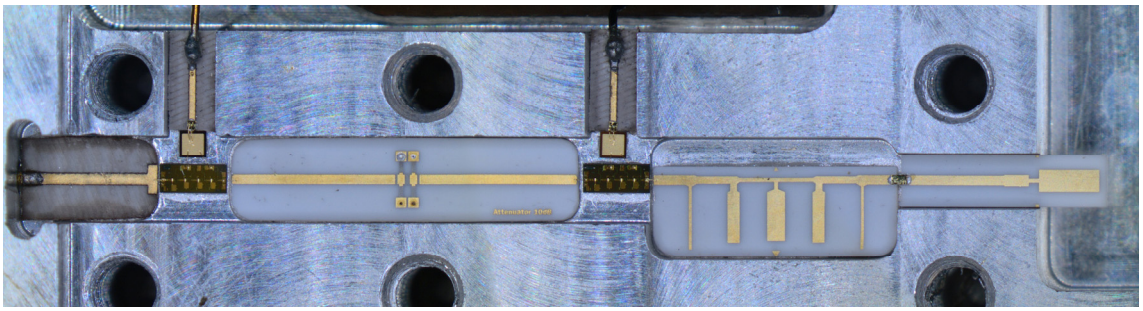

Fig. 7. 25. Detail of the assembly of the radiofrequency circuits of the Gain and Filtering Module.

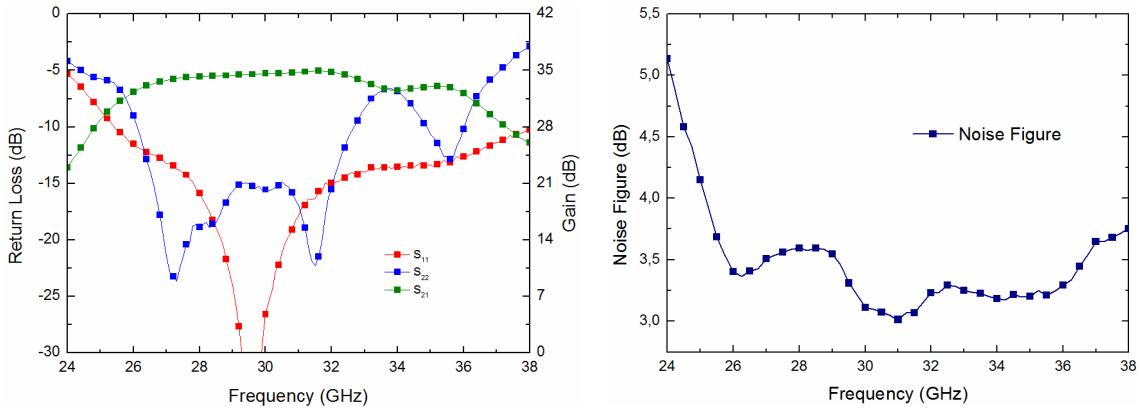

(a) (b)

Fig. 7. 26. Measurement results of the Gain and Filtering Module. (a) S-parameters. (b) Noise figure.

After the Gain and Filtering Module, the Phase Switches Module is directly connected to its waveguide output. This module is composed of two radiofrequency branches which uses the 180º- and 90º-phase switches, described in chapters IV and V of this thesis, assembled together in order to generate a four state sequence per branch and it is designed with WR-28 waveguide ports. The phase switches are assembled with PIN diodes since they operate at room temperature. The assembly inside the chassis is shown in Fig. 7. 27, in which general, backside and detailed views are presented. The new chassis drawings are shown in Annex IV. The Phase Switches Module has the functionality of providing the sixteen phase states by the combination of its two branches. Then, the module is provided with TTL drivers, model DR65-0109 from MACOM Technology Solutions [7.22] adding the full-switching capability to the module. The phase switches are biased with I_d=20 mA per diode, so the driver has a circuitry which accommodates the output values of the square signals to the corresponding one to each phase switch. The measurement results of the Phase Switches Module are shown in Fig. 7. 28, in terms of the phase difference between states in each branch and the insertion loss for each state and branch. Both branches of the Module are

labelled R1 and R2 in Fig. 7. 28, which corresponds to the upper and lower chains of the receiver shown in Fig. 7. 23. The average values for each branch of the phase difference, in the 26 - 36 GHz frequency band, obtained in each state are listed in Table 7. 4.

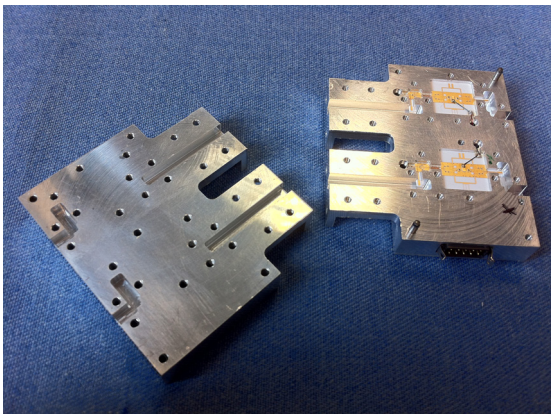

(a)

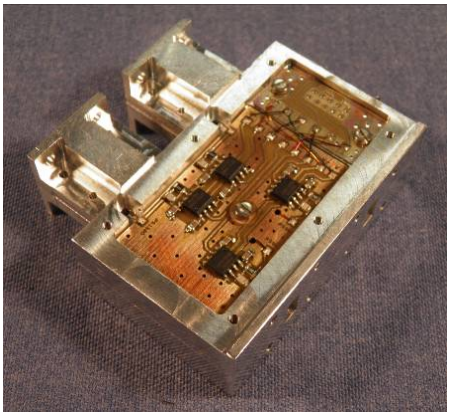

(b)

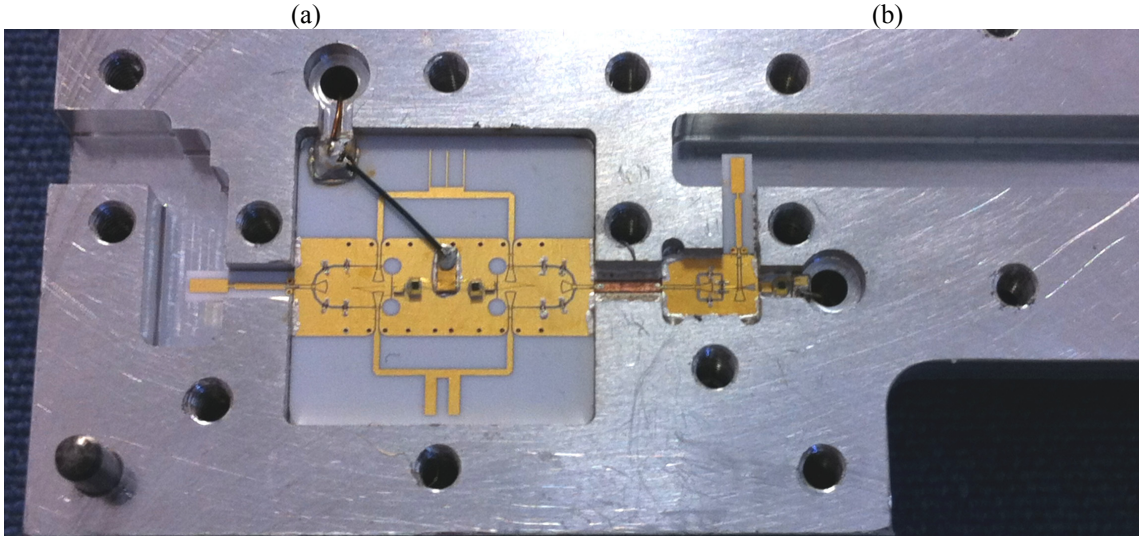

(c)

Fig. 7. 27. Photographs of the TGI Phase Switches Module. (a) General view. (b) Backside of the chassis with the driver board. (c) Detail of one branch with phase switches.

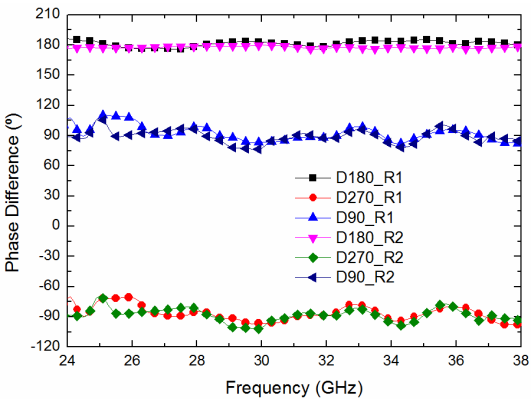

(a)

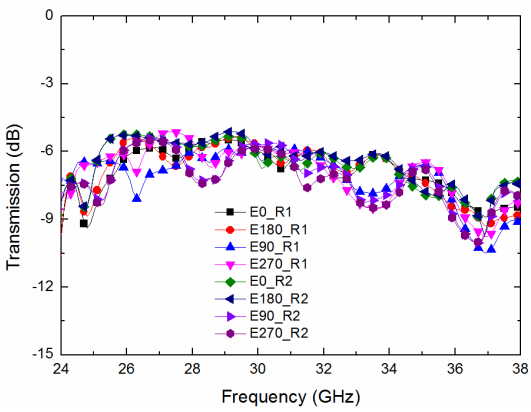

(b)

Fig. 7. 28. Phase Switches Module results. (a) Phase difference between states for each branch. (b) Transmission coefficient for state and branch.

Table 7. 4. Average values of the phase difference in each phase state of the module in the frequency band from 26 to 36 GHz.

State	Phase Diff. (º)	State	Phase Diff. (º)
D180_R1	181.06	D180_R2	177.73
D270_R1	-87.73	D270_R2	-88.88
D90_R1	90.74	D90_R2	88.71

Finally, the BEM chain ends with the Detection and Correlation Module, which is in charge of performing the modulation of the microwave signals and converting them into DC voltages using the detector described in chapter VI. The block diagram of the module is shown in Fig. 7. 29. It is designed with WR-28 interfaces and it is composed of waveguide in-phase power splitters, waveguide corrugation-based shape 90º-phase shifter, 180º microstrip hybrids couplers and the detectors also in microstrip technology. In the last part of the module, a video amplifier is included, amplifying the detected signal to higher values which are processed in the Data Acquisition Unit (DAE), external to the receiver.

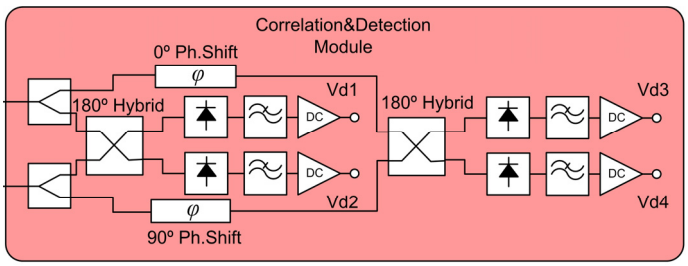

Fig. 7. 29. TGI Correlation and Detection Module scheme.

The designs of the waveguide components were aided with electromagnetics simulators and they were individually tested. Both designs have been developed in our researching group at DICOM. The 90º-phase shifter shows an in-band phase error lower than 3º with return loss better than 25 dB. The 180º microstrip hybrids are designed on alumina substrate [7.23], as an optimized design based on [4.9], [7.24], and they were also individually characterized to verify its performance, showing a phase error lower than 5º within the 26-36 GHz band with a good amplitude balance.

The video amplifier is included in each detected voltages and it provides a differential output of these voltages, using a variable-gain differential amplifier configuration as first stage and then, an inverting and a non-inverting amplifier topologies are used as second stages to obtain the differential voltage. More detailed information about it is described in Annex V.

The Correlation and Detection Module is shown in Fig. 7. 30. The chassis is equipped with two different connectors. A 9-way micro-D female connector is used to extract the detected and amplified signals from the module, while a 15-way micro-D male connector connects the bias signals and the potentiometers for perform the variable gain in the video amplifier.

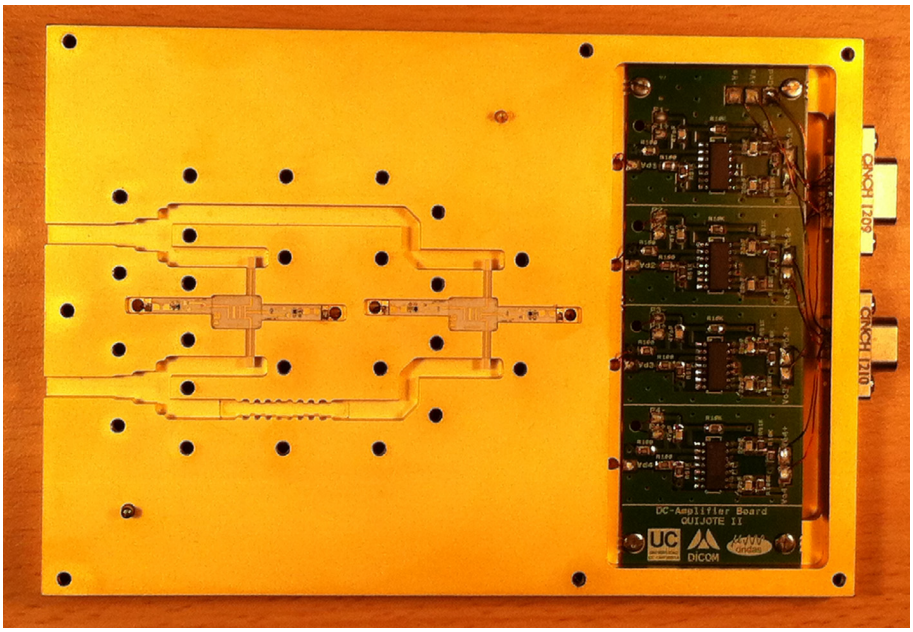

(a)

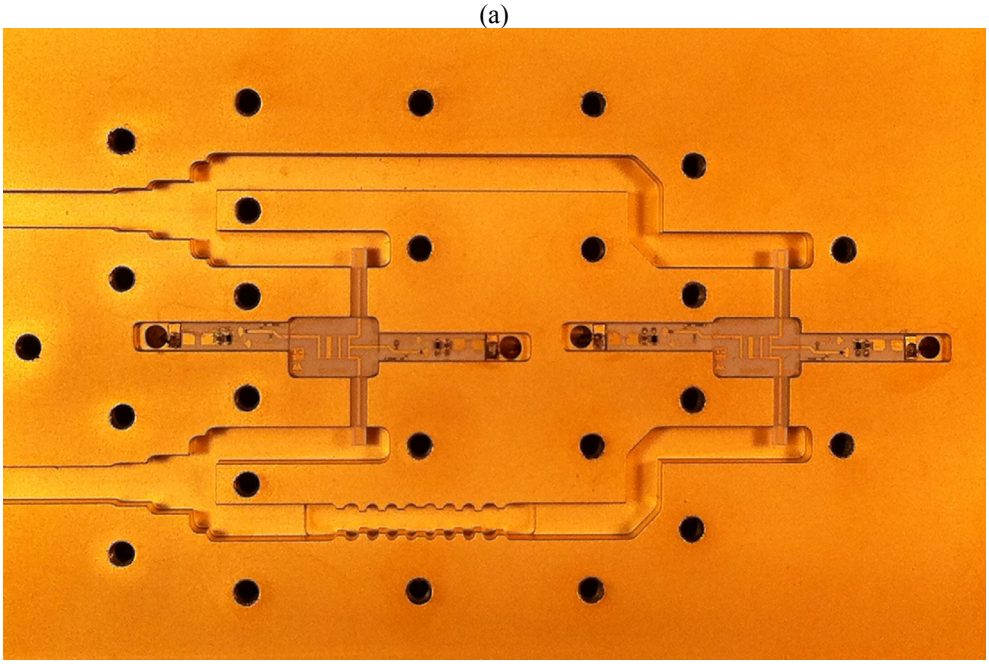

(b)

Fig. 7. 30. Photograph of the TGI Correlation and Detection Module. (a) General view of the chassis without lid. (b) Detail of the microwave circuitry.

The measurements of the module are performed in two stages. First of all, the S-parameters of the module are tested. Both WR-28 accesses show return loss better than

10 dB within the 26 – 36 GHz band, with an isolation between accesses better than 10 dB.

Afterwards, frequency and input power sweeps are done to characterize the response of the four detected voltages. The potentiometers of the video amplifier are set to 2.5 kΩ, which enables to measure detected voltages lower than 10 V. The frequency sweep is performed for an input power to the module in which the detector operates in its linear region. An input power of around -25 dBm to the detector assures a good performance in the linear region. Therefore, an input power of -15 dBm to the correlation module is configured in the signal generator taking into account the losses of the different subsystems. For the variable input power sweep, a fixed frequency value is used. Hence, the centre frequency (31 GHz) of the receiver band is selected. The results obtained for the module are shown in Fig. 7. 31. It is observed that for high power levels in the signal generator, there is compression since the detector is working in a non-linear region.

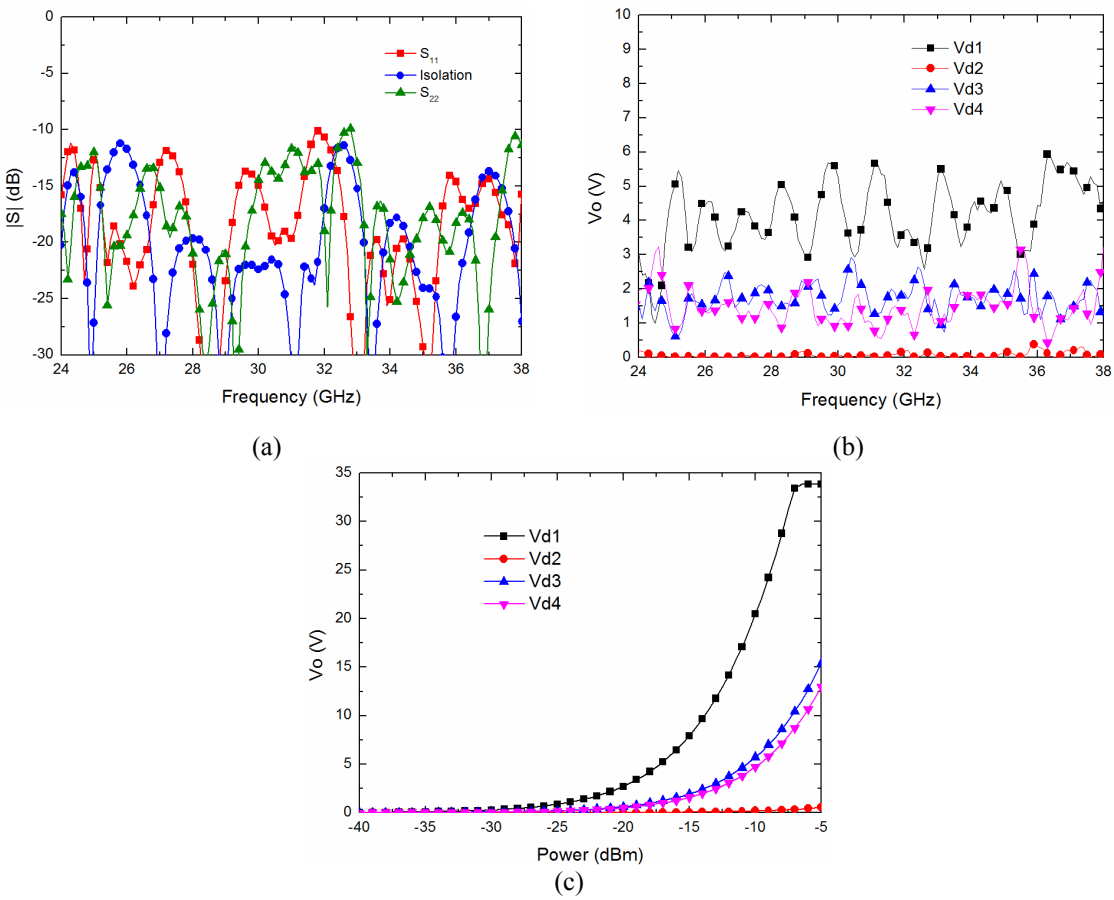

Fig. 7. 31. Correlation and Detection Module measurements. (a) WR-28 port matching and isolation. (b) Detected voltages versus frequency for an input power in the detector of -25 dBm. (c) Detected voltage versus generator power at frequency of 31 GHz.

7.4. Radiometer Integration

As described in the previous section, the TGI receiver is composed of 31 pixels, which must be integrated in the TGI telescope at Teide Observatory. A photograph of the telescope is shown in Fig. 7. 32, which has been designed and manufactured by the company IDOM (Bilbao, Spain). During July 2014 it will be installed at the observatory. The telescope is installed inside a building, able to host two telescopes simultaneously. It is provided with a dome, which will be opened and closed depending on the climate conditions to perform the observations. A photograph of the telescope inside the building with the opened dome is shown in Fig. 7. 33.

Fig. 7. 32. QUIJOTE TGI telescope.

Fig. 7. 33. Building for the QUIJOTE instrument which includes the telescope with opened dome.

The cryogenic part of the receiver, which includes the optomechanics and the cryogenic LNAs described in section 7.3 of this chapter, is assembled inside a cryostat which is designed by the Instituto de Astrofísica de Canarias (IAC). Some views of the cryostat are shown in Fig. 7. 34, in which the left picture shows the internal part where each pixel will be assembled, while the right picture shows the enclosure of the cryostat.

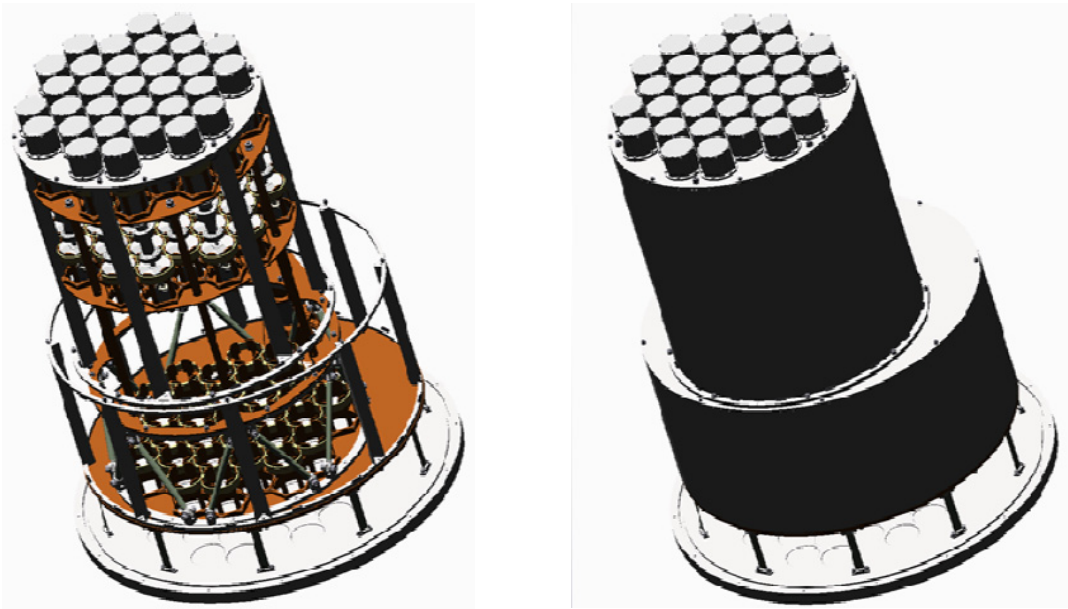

(a) (b)

Fig. 7. 34. TGI cryostat design. (a) Internal view of the cryostat where each pixel is assembled. (b) View of the enclosure cryostat.

The 31 units of the feedhorn, polarizer and OMT together with the 62 units needed for the cryogenic LNAs will be individually attached pixel by pixel and assembled inside the cryostat. A complex and carefully step-by-step procedure is defined in order to thermally anchor the subsystems to the cold plates. This process is critical in order to reach the lowest physical temperature, which is estimated to be 20 K.

The cryogenic LNAs need DC bias sources, which are designed and assembled at the DICOM facilities. These bias cards are assembled in a 19” standard rack of 4U (177 mm) of height and 280 mm of depth. They have been divided into three racks with 22 cards each one. A photograph of the racks including the bias cards is shown in Fig. 7. 35.

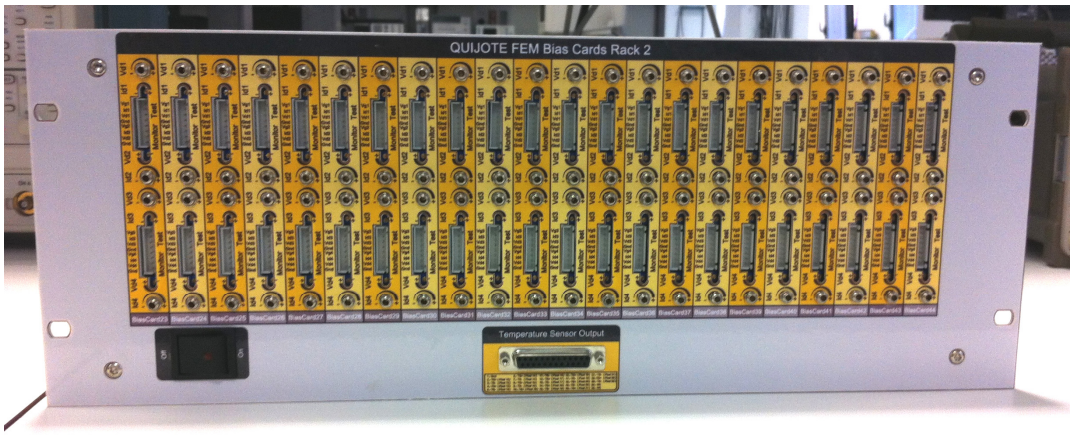

Fig. 7. 35. Photograph of one the bias cards rack for the TGI receiver. 19" rack of 4U (177 mm) of height and 280 mm of depth.

The integration of the room temperature components of the receiver is performed in 19" standard aluminium racks of 3U (133 mm) of height and 450 mm of depth properly mechanised to include all the subsystems. The 62 units of the Gain and Filtering Module together with the 31 units of the Phase Switches Module and Detection and Correlation Module are assembled inside two racks, with the capacity to 16 complete chains each one. An artistic view of the assembly of the complete chains inside the rack is shown in Fig. 7. 36.

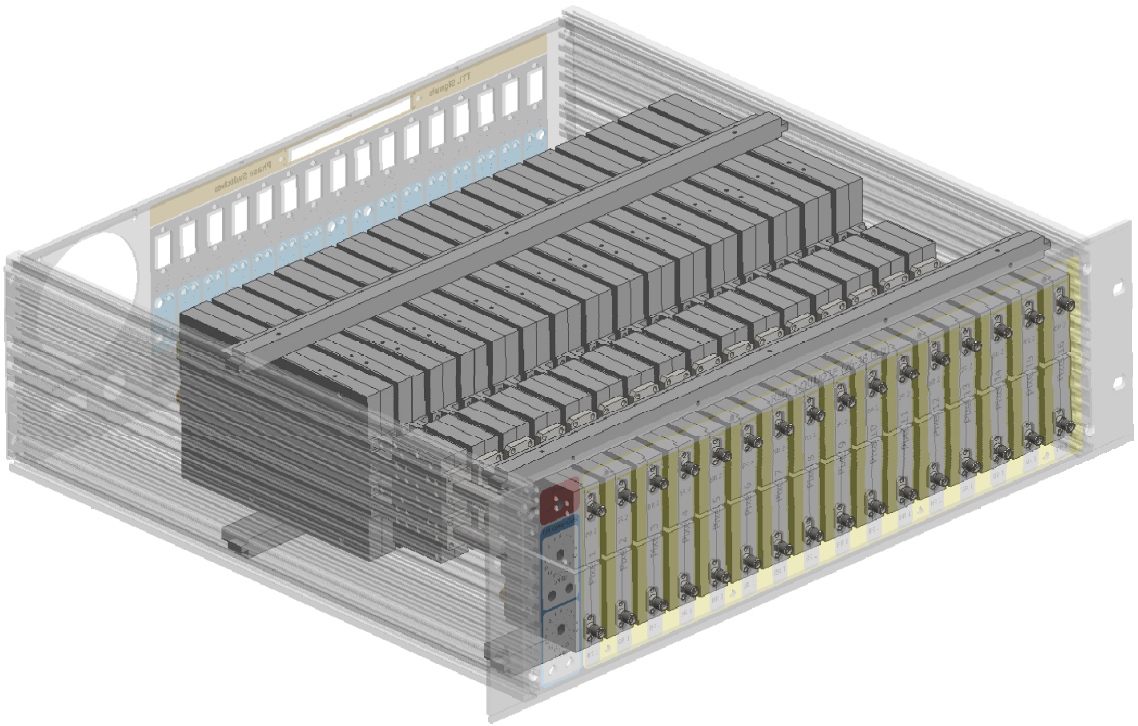

Fig. 7. 36. Artistic view of the assembly of the Gain and Filtering Module together with the Phase Switches Module and Detection and Correlation Module inside the rack. 19" rack of 3U (133 mm) of height and 450 mm of depth.

After the integration of the individual modules which composes the BEM, each resulting chain is assembled inside the BEM rack. This rack is provided with bias cards for the Gain and Filtering, Phase Switches and Correlation and Detection Modules. It is also provided with a fan to keep cool the unit. Fig. 7. 37 shows final views of the BEM rack integration. The centre picture (Fig. 7. 37 (c)) shows the upper view of the rack, which includes a 64-way ribbon cable to control the phase switches states by commanding TTL signals. The rear panel of the rack is provided with 9-pin female D-type connector to obtain the detected voltages. Besides, it also is equipped with the screws of the video amplifier potentiometers to control the DC gain.

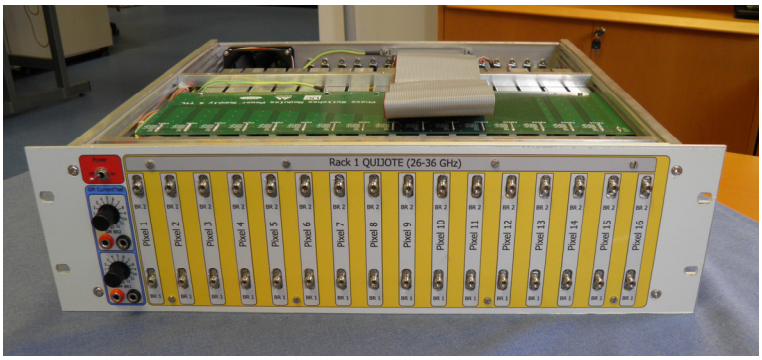

(a)

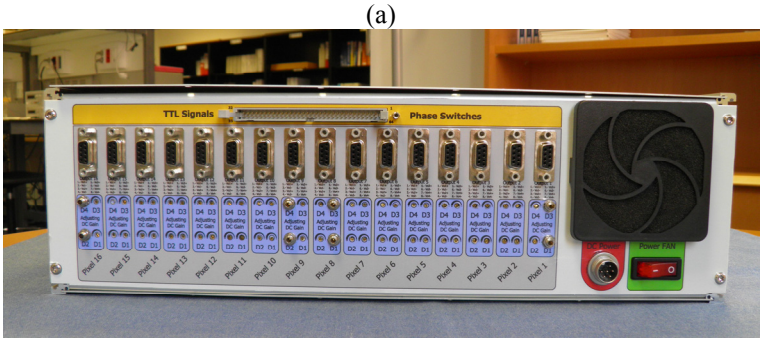

(b)

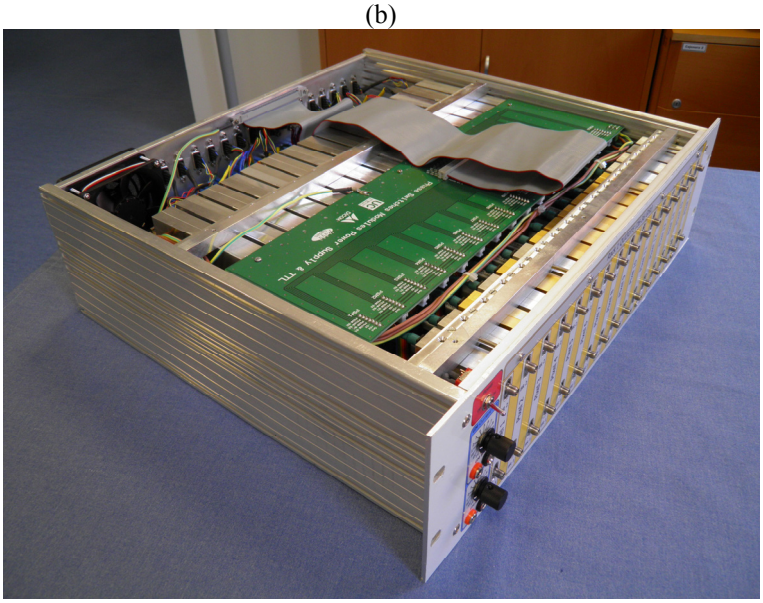

(c)

Fig. 7. 37. Photographs of the BEM rack. (a) Front view. (b) Rear view. (c) Side and upper view.

7.5. Radiometer Characterization

The functionality test carried out with a representative pixel of the QUIJOTE TGI consists of providing a broadband linearly polarized signal at the receiver input and recording the detected voltages at the BEM outputs, expecting Stokes parameters according to the input signal polarization. The receiver chain does not include the cryogenic LNAs due to the excess of signal power at room temperature. Besides, the functionality of the receiver is not committed by the absence of the cryogenic LNAs since the optomechanics, phase switches and detection and correlation modules assure the proper usefulness of the receiver. As main consideration, the absence of the cryogenic LNAs only implies an analysis of the power budget of the receiver.

The test is carried out exciting the receiver with a broadband x-axis linearly polarized signal. A sketch of the functionality test is shown in Fig. 7. 38. Unlike the final application, in the functionality test it is required a relatively high power polarized signal, much greater than the unpolarized receiver contributions, since the use of a large integration time for data post-processing is beyond the scope of this test.

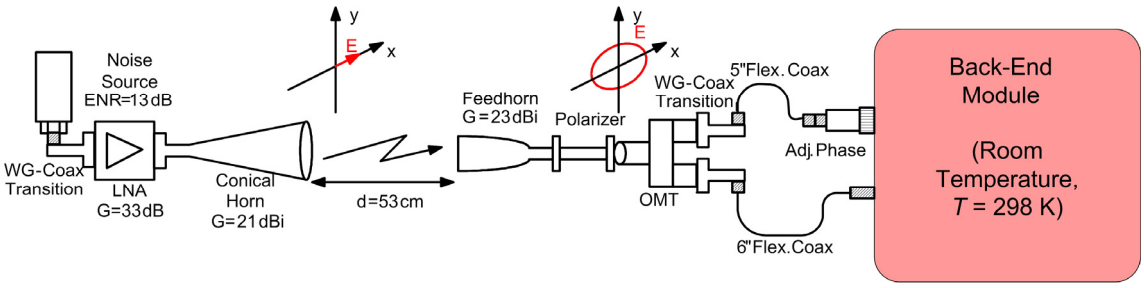

Fig. 7. 38. Receiver functionality test bench.

The broadband linearly polarized signal is accomplished using a noise source model 346CK01 from Agilent Technologies with an excess noise ratio of 13 dB in the Ka-band, which is further amplified (33 dB) and transmitted by a conical horn (21 dBi of gain). The rectangular waveguide input of the conical horn provides the required linear polarization. The distance between transmitting antenna and the receiver feedhorn is adjusted to avoid compression in the detector devices, which assure their linear operation up to an incoming power level of about -25 dBm. The detectors have a sensitivity around 1000 mV/mW and the gain of the video amplifiers is adjusted to provide output voltages lower than 10 V, according with the DAS and resolution requirements for a 24-bits system PXI-4495 from National Instruments in the telescope. The power budget of the functionality test is listed in Table 7. 5.

The two signals split up in the OMT outputs are correlated in the last module of the chain, so the electrical paths of each branch must be identical. Since the individual subsystem in a branch of the receiver could show slight differences in their phase response related to the one assembled in the other branch of the receiver, both signals are affected for a phase imbalance. Therefore, one of the branches of the receiver is provided with an adjusting phase element, which enables the minimization of the phase difference between branches. Thus, the extra electrical length added by the adjusting phase element is compensated by using different lengths in the connection cables from the OMT outputs to the amplifying modules inputs. Hence, the lengths of the flexible coaxial cables are one inch different.

Table 7. 5. Power Budget for the functionality test.

Parameter	Units	Value	Description
ENR	dB	13.00	Noise source mean value in the band
T_{NS}	K	6076.26	Noise temperature at noise source output
k	J/K	1.38E-23	Boltzmann constant
G_{LNA}	dB	33.00	Gain of the LNA in the signal source
B_{EFF}	GHz	16.00	Effective bandwidth of the LNA in the signal source
$G_{TX\text{-}HORN}$	$G_{TX\text{-}HORN}$ (dB)	21.00	Gain of the transmitting antenna
P_{RAD}	dBm	-4.72	Radiated power
d	cm	53.00	Radio-link distance (between horns)
f	GHz	31.00	Frequency of the radio-link
L_{TX}	dB	56.71	Propagation losses: L(dB)=20·log(d[km])+20·log(f(MHz)+32.4
P_{REC}	dBm	-61.44	Power level at receiver input
$G_{RX\text{-}HORN}$	dB	23.00	Gain of the receiving antenna
L_{OPT}	dB	4.50	Losses of the optomechanics and coaxial cables
$G_{LNA\text{-}BEM}$	dB	33.50	Mean gain of the BEM LNAs (26-36 GHz band)
L_{PS}	dB	8.7	Mean losses of one branch in the Phase Switches Module with $\Phi_1=\Phi_2=0$ state (26-36 GHz band)
$P_{DET\text{-}MOD}$	dBm	-18.14	Power level at the Correlation and Detection Module input
L_{HYB}	dB	1.50	Mean losses of the 180º hybrid in the Correlation and Detection Module (26-36 GHz band)
S_{DET}	mV/mW	1000	Detector sensitivity
G_{VIDEO}		522	Gain of the DC amplifiers with all the potentiometers set at R=2.5 kΩ
V_{OUT}	V	5.6	Detected voltage at the hybrid sum output

The detected values are measured covering all the phase switches states, so four TTL signals are implemented to bias each phase switch circuit and change the state of the receiver. The frequencies of each TTL signal and the phase switch which is activated using each one are listed in Table 7. 6.

Table 7. 6. Actuation TTL control signals for the phase switches

Branch	Active Phase Switch	Freq. (Hz)
R1	180º	1
R1	90º	2
R2	180º	4
R2	90º	8

The tests at DICOM facilities are made using a PXI-1031DC module from National Instruments as DAS in the setup, implementing the measurements under LabVIEW software with a 24-bits NI PCI/PXI-4462 card. The tests consist of measuring the detected voltages of the receiver in a defined period of time and the Stokes parameters are calculated after processing the values. A sampling rate of 1 kHz is configured in the system and the number of points is equal to 1000, which corresponds to 1 second of acquisition time and real data. This period is the minimum needed time to cover a complete period of all the states of the phase switches with the configuration of the TTL signals shown in

Table 7. *6*. The calculation method is based on the analysis of the values obtained from each detected voltage in each state and the comparison among them. Therefore, the adjusting phase is configured to minimize the difference between the two mid-voltage outputs, corresponding to the values $(K/2)\cdot A^2$ in Table 7. 2, in a specific state. Then, the full sequence of states is analysed calculating the parameters in each phase state.

Once the Stokes parameters are obtained, two figures of merit are defined as the isolation between the Q and I parameters and between the U and Q parameters. The ratios are given by

$$Q/I\big|_{dB} = 10\cdot\log_{10}(Q/I) \tag{7.28}$$

$$U/Q\big|_{dB} = 10\cdot\log_{10}(U/Q) \tag{7.29}$$

Ideally, they should be 0 and -∞ values, but in a real scenario they denote the leakage signal due to the imperfections of the subsystems which are part of the receivers.

Since the phase adjust is only made for one state, a certain phase imbalance will affect to the others states. Therefore, from the analysis of the isolation ratios, a combination of four individual phase states (Φ_T =0º, 90º, 180º and 270º) achieving significant isolation performances defines a sequence of four states for each pixel of the receiver in which outstanding results are expected. This is possible since the

combination of the sixteen individual states of the Phase Switch Module branches originates redundant phase states. This set of phase states is defined as the operation sequence for the analysed receiver chain. The TTL signals commanding the Phase Switches Module states must be well known to determine the operation of the pixel. This procedure must be carried out for each pixel to define individual state sequences.

The test bench used for the test is shown in Fig. 7. 39, in which the optomechanics are connected with 2.92-mm coaxial cables to the BEM inputs.

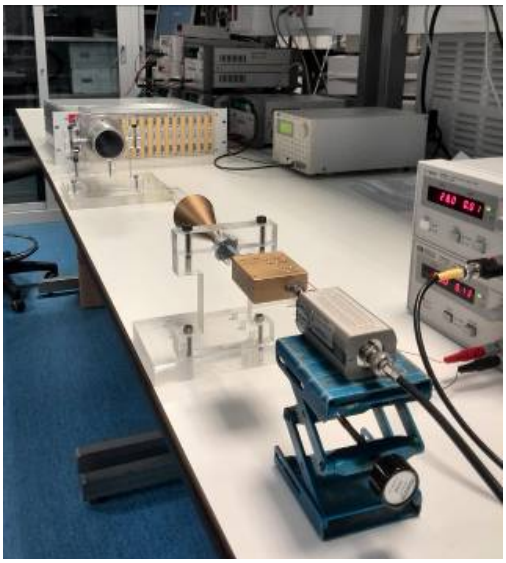

(a)

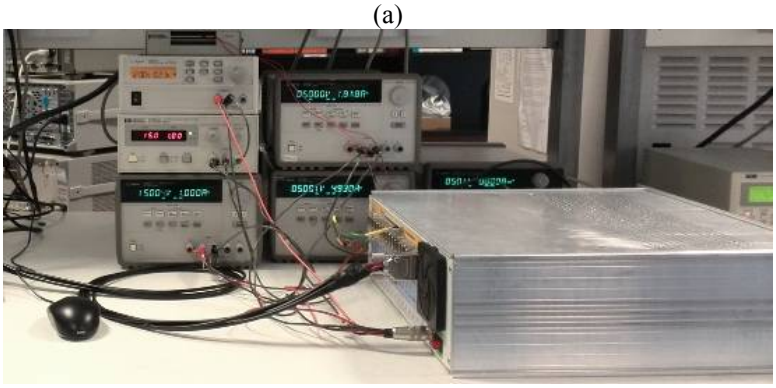

(b)

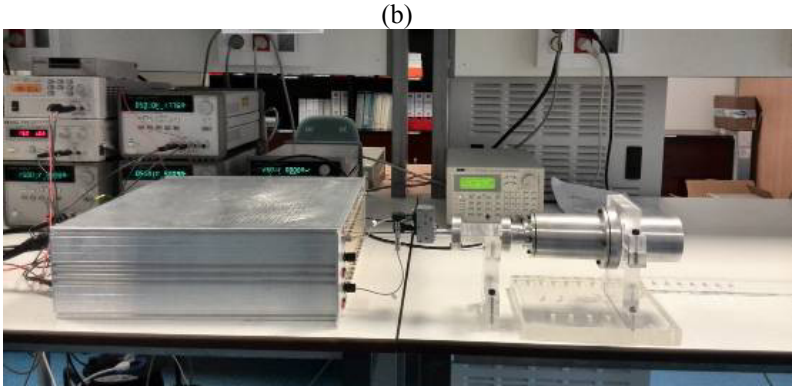

(c)

Fig. 7. 39. Photograph of the polarimeter test bench. (a) View of the x-axis linearly polarized signal generator and the input feedhorn. (b). Rear view with the connection to the acquisition system. (c) Optomechanics and connection to Back-End Module input.

The detected voltages at the output of the pixel are measured in the PXI system and are shown in Fig. 7. 40. Each detected voltage (V_{d1} to V_{d4}) is measured in the 16 phase states during a complete switching period time, and the average values for each phase state and detected voltage are listed in Table 7. 7.

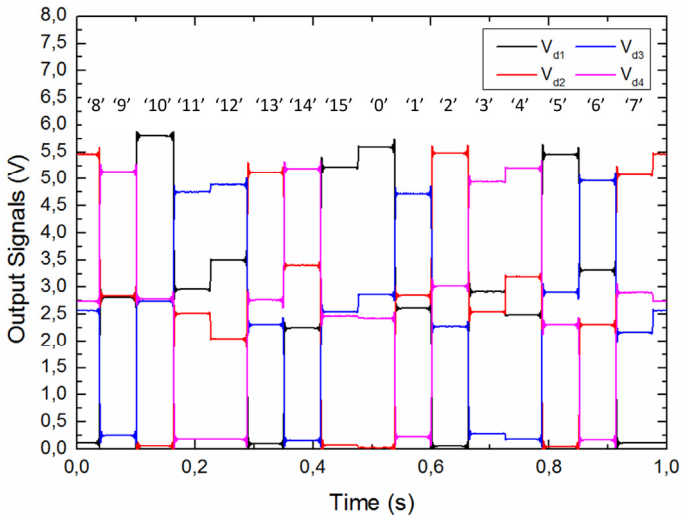

Fig. 7. 40. Output signals of the receiver for an x-axis linear polarization input signal for the sixteen individual states of the Phase Switch Module.

Table 7. 7. Detected voltages in each output and each phase state.

State	Φ_T (º)	Φ_{B2} (º)	Φ_{B1} (º)	V_{d1}	V_{d2}	V_{d3}	V_{d4}
0	0	0	0	5.58923	0.019719	2.86146	2.42446
1	90	90	0	2.61324	2.84884	4.72056	0.226836
2	180	180	0	0.049983	5.48491	2.27414	3.01733
3	270	270	0	2.91712	2.54655	0.286344	4.94478
4	270	0	90	2.48787	3.19384	0.179587	5.20477
5	0	90	90	5.45768	0.046415	2.90879	2.30805
6	90	180	90	3.31255	2.30506	4.96672	0.167264
7	180	270	90	0.107236	5.07609	2.16204	2.90036
8	180	0	180	0.11356	5.45632	2.56659	2.74299
9	270	90	180	2.81116	2.83811	0.251629	5.13035
10	0	180	180	5.80072	0.131732	2.74594	2.78675
11	90	270	180	2.95782	2.51029	4.74652	0.182773
12	90	0	270	3.49686	2.04445	4.88716	0.175395
13	180	90	270	0.096804	5.11774	2.30738	2.76165
14	270	180	270	2.24513	3.40142	0.15916	5.18756
15	0	270	270	5.21551	0.067717	2.54831	2.46514

The detected voltages are listed in the phase order expected in the receiver according to the TTL control signals. Thus, the so-called state '0' corresponds to the eighth phase change in Fig. 7. 40 in which the detected voltage V_{d1} gives the maximum

value according to Table 7. 2. Then, a 90º-phase change in the receiver state makes that V_{d1} goes to medium voltage value while V_{d4} takes the minimum one, which corresponds to change state '0' to state '1' in Table 7. 7.

From these values, the Stokes parameters are calculated for each state, but as stated before, a combination of phase states provides the best sequence for the pixel. The best phase states for the representative tested pixel are listed in Table 7. 8, in which the intensity Stokes parameter *I* is obtained as the mean value between the two possible ways of calculation (see Table 7. 1). The selection of these states defines the sequence for this concrete measured pixel. The rest of the states show worse isolation values due to the phase and amplitude imbalances in the receiver, which are not removable, especially the amplitude differences. The correction performed by the adjusting phase produces phase imbalances since it corrects the equivalent electrical phase for some states, but others are not possible to correct due to the imperfections of the microwave circuits.

Table 7. 8. Stokes parameters and isolation ratios in each phase state.

Φ_T (º)	*I*	*Q*	*U*	*Q*/*I* (dB)	*U*/*Q* (dB)
0 (state #10)	5,732	5,669	0,041	-0,049	-21,427
90 (state #1)	5,205	4,494	0,236	-0,638	-12,804
180 (state #8)	5,439	5,343	0,175	-0,078	-14,813
270 (state #9)	5,516	4,879	0,027	-0,533	-22,577

Ideally, the *I* and *Q* Stokes parameters for a horizontal linearly polarized incoming signal are identical, while the *U* parameter takes null value. The discrepancies between these ideal values and the measured ones in Table 7. 8 are due to the errors in the microwave circuits which are part of the receiver.

7.6. Conclusions

This chapter has described the design, assembly and characterization of a radio astronomy receiver as the final application of the circuits discussed in the previous chapters.

The chapter has been introduced with a short outline of some receiver configurations, focusing in the topology selected for the QUIJOTE project in its Phase II. The analysis of the Thirty-GHz Instrument (TGI) has been performed, which is aimed for characterizing the CMB and other emissions. The DICOM researching group

has been involved in the design of the subsystems of the full chain of the receiver, which has been described in this chapter.

The TGI receiver block diagram has been presented, based on a circular coordinate system to calculate the Stokes parameters of the incoming signal to the receiver, which is divided into its orthogonal components. The operation of the feedhorn antenna, polarizer and OMT have been analysed along this chapter, with outstanding results in terms of S-parameters in the 26 – 36 GHz frequency band. Then, the cryogenic low-noise amplifiers have been detailed, composed of two cascaded MMICs from the IAF and OMMIC mHEMT technologies respectively. The integration of both LNAs has been performed together with a 5 dB microstrip attenuator. The cryogenic chassis has achieved an average noise temperature of 23.1 K and an average insertion gain of 40.9 dB in the TGI band. Lastly, the description of the BEM module has been presented, which is composed of three individual chassis: the amplifying and filtering stage, the modulation of the operation using phases switches and the correlation and detection of the microwave signals. The BEM module will operate at room temperature, but the circuits which are part of it are able to operate under cryogenic conditions, as described in the previous chapters, if needed.

Finally, the characterization of the receiver functionality has been described by introducing an x-axis linear polarization signal. The Stokes parameters and the isolation between them have been calculated for the sixteen states in the pixel and a sequence of four states have been defined for it considering the states which have shown the best isolation results. This characterization process has demonstrated the right operation of the receiver. Moreover, the functionality test has demonstrated that the 180º- and 90º-phase switches designed are adequate to the receiver operation. Their phase difference errors and amplitude imbalances between states in the operation bandwidth have enabled a proper output voltages in the different states.

Chapter VIII

Conclusions and Future Lines

8.1. Conclusions

This thesis has presented the analysis and development of different circuits and subsystems in order to be part of very sensitive receivers intended for radio astronomy applications. Besides, it has included the investigation of the cryogenic performance of discrete devices and full circuits as an evidence that a drastic modification in the physical temperature of operation in a system involves significant variations in their behaviour.

The dissertation has been organised from basic to more complex issues dealing with the modification of the physical temperature of operation. The mentioned issues have described from the characterization of dielectric substrates or measurement techniques, in order to measure and model the performance of devices, such as diodes, or circuits with the temperature, up to the design and characterization of subsystems that are parts of a very sensitive receiver for radio astronomy, describing and defining also its performance. All these issues have been split into different sections, considering the room temperature operation and the cryogenic one. Therefore, as a temperature

dependent analysis of devices or circuits has been desired, a cryogenic environment has been used along the different chapters to characterize the circuit responses.

It is clear that the initial step for the characterization of devices or circuits requires a well-defined measurement technique which enables their characterization at room and cryogenic temperatures. Therefore, the definition of two measurement procedures has been described and tested at both physical temperatures in order to define their features. The kits designed enable the measurement of discrete diodes in order to obtain accurate models of them. Different discrete diodes have been characterized considering their DC and small-signal S-parameters performances at both room temperature and cryogenic temperature, which has allowed to develop a small-signal model for each one at both physical temperatures. Three diodes are considered to be used: two Schottky diodes with different barrier height (MA4E2037 and HSCH-9161) and a PIN diode (HPND-4005). The performance of the diodes is quite different when their physical temperature is extremely modified. A reduction in their saturation current and an increase in their ideality factor under cryogenic temperature compared to room temperature performance are observed. Besides, an increase in the knee voltage of the diodes is measured at cryogenic temperature compared to room temperature. The model for the HSCH-9161 Schottky diode is achieved considering the small signal S-parameters and the non-linear behaviour, for its use as detector diode. Special performance is observed for the PIN diode at cryogenic temperature. Hysteresis effects are measured when a static bias supply is used, which are removed for pulsed measurements.

Besides, another significant issue is the knowledge of how a dielectric substrate changes its parameters with the temperature. Hence, an evaluation of the characteristics of three commonly used microwave substrates, at room and cryogenic temperatures, have been reported for their consideration in further circuit designs. At cryogenic temperature, a reduction in the total losses with a slight variation in the dielectric permittivity (ε_r) of each substrate have been described.

Once the features of the dielectric substrate are estimated and the diodes are modelled, the design of the circuits is ready to be started. In this work the design of three new and different circuits have been outlined: a 180º phase switch, a 90º phase switch and a detector. All of them have been thoroughly analysed and discussed, and finally, characterized at room and cryogenic temperature. The circuits have been designed in the Ka-band, covering the frequency band from 26 to 36 GHz, and they

have used the modelled diodes as key component. The circuits have been designed in planar technologies, using microstrip, CPW and slotline as transmission lines.

The design of the 180º phase switch has been described. It is based on the use of transitions from CPW to slotline transmission lines. Moreover, a slotline T-junction enables two symmetric transmission paths which excite a CPW line. Depending on the transmission path after the T-junction in the slotline, a 180º phase shift is achieved at the output CPW line. The selection of the transmission path is performed by a set of diodes, properly placed in the circuit layout. The phase switch is analysed at room and cryogenic temperature using both MA4E2037 and HPND-4005 diodes. The 180º phase switch provides outstanding flat phase difference with a very small phase error lower than 2º with both type of diodes at both physical temperatures (300 and 15 K). The insertion loss of the circuit is reduced around a 30% at cryogenic temperature from its original value at room temperature when the Schottky diodes are used and a reduction of a 50% in the power consumption. The performance of the circuit with PIN diodes at cryogenic temperature is not as good as with Schottky, since the individual behaviour of the PIN diode at cryogenic temperatures needs a huge DC power consumption which is undesired under cryogenic temperature.

Several designs of a 90º phase switch have been discussed. They are based on hybrid technology, employing available MMIC SPDTs or novel home-made design, based on CPW-to-slotline-microstrip SPDTs with diodes, as switching devices. The differential 90º phase shift is achieved with broadband microstrip band-pass filters. The 90º phase switch circuit with CPW-to-slotline-microstrip SPDTs provides a flat phase response with a small phase error lower than 5º at room temperature with both type of diodes, which improves the results obtained with commercial MMIC solutions as SPDTs. On the other hand, its operation at cryogenic temperatures with Schottky diodes shows a reduction in the insertion loss of the circuit with a reduction of about 80% of the power consumption while the phase difference keeps approximately constant.

A microwave detector has been analysed and designed using the zero-bias Schottky diode HSCH-9161. The novelty on the design is the use of lossy transmission lines, defined as distributed thin-film resistors, in the matching network of the circuit in order to fulfil the requirements of the circuit. A thorough analysis of the lossy transmission lines is developed in order to achieve sensitivity values of around 1000 mV/mW with return loss better than 10 dB at room temperature in the 26 – 36 GHz frequency band. When cryogenic temperature is applied to the detector, an increase in

the sensitivity is measured which is bias-dependent, and a reduction of the sensitivity is observed when the DC bias current is increased, but being always higher than the zero-bias room temperature performance. Moreover, the 1-dB compression point is reduced from the room temperature value, but its value increases for higher bias points.

Finally, this thesis has described the application in which the design of the different circuit is aimed to: a radio astronomy receiver, called radiometer. The QUIJOTE project has been detailed, which is focused on the characterization of the polarization of the Cosmic Microwave Background and other galactic and extragalactic emissions in a wide frequency range. The receiver of the Thirty-GHz Instrument (TGI – from 26 to 36 GHz frequency band) is inside the development of the Phase II of the project and it has been described including the different subsystems which are part of it. It is intended to provide four DC output signals which enable the calculation of the Stokes parameters, which defines the polarization of an electromagnetic wave. The design of the circuits of the TGI receiver has been almost totally carried out by the DICOM group.

8.2. Future Lines

All the information described in this thesis can be continued with different aspects to improve this work.

First of all, the models obtained for the diodes have been performed at room temperature (300 K) and at cryogenic temperature (15 K). The development of an electro-thermal model from 300 K to 15 K including the full range of temperatures would be very interesting in order to predict their performance at any physical temperature and the feasibility of their insertion in any circuit.

The development of circuits in hybrid technologies involves a detailed assembly of the elements in order not to introduce additional effects which could modify the desired result. The interconnections between parts, usually performed by bonding wires, are critical for the phase response since it is quite difficult to control the length of these connections. Therefore, using MMIC technologies enable a high accuracy level since all these interconnections are part of the monolithic process, and only external connections are required. The design of the 180º and 90º phase switches in MMIC technology could improve the phase difference response, particularly for the 90º phase switch case.

The use of 180º and 90º phase switches with phase errors causes differences in the output signals of the system which includes them. Therefore, an analysis of the impact

of the phase errors in the phase switches would derive in a deep knowledge of the performance of the receiver.

Besides, the implementation of a single circuit which performs the four phase states (0º, 90º, 180º and 270º) will improve the results obtained using the interconnection of two cascaded circuits.

The microwave detector shows a narrow dynamic range. The analysis of the increase of this dynamic range working in the square-law region of the detector is a significant task, in order to improve the detector.

The final application of the circuits of this thesis is a radio astronomy receiver in the 26 to 36 GHz frequency band for sky observation. The characterization of the complete radiometer including the cryogenic LNAs will conclude the measurement include in this thesis. Besides, the analysis and definition of a calibration process for the receiver in order to remove the hardware errors would define a complete procedure for the characterization of a radiometric system.

Additionally, the DICOM group is involved in the design of new radiometers in the Q- and W-band. Therefore, the frequency extension of the diode models and the scaling of the circuits up to these bands are challenging issues.

Capítulo VIII

Conclusiones y Líneas Futuras

8.1. Conclusiones

En esta tesis se ha presentado el análisis y desarrollo de varios circuitos y subsistemas que formarán parte de receptores de muy alta sensibilidad para aplicaciones de radioastronomía. Se ha incluido el análisis del comportamiento a temperaturas criogénicas de dispositivos discretos y circuitos como evidencia de que una drástica modificación en su temperatura de funcionamiento puede provocar variaciones en el sistema en el que están integrados.

La tesis se ha organizado desde aspectos básicos hasta algunos más complejos de acuerdo a la temperatura de operación que presente el dispositivo bajo prueba. Se ha descrito la caracterización de sustratos y diferentes técnicas de medida, para la medida y modelado de dispositivos tales como diodos, así como la caracterización de circuitos completos, hasta la descripción del diseño y medida de subsistemas que forman parte de un receptor de alta sensibilidad para radio astronomía. Estas tareas se han dividido en distintas secciones atendiendo a la temperatura de funcionamiento. Por lo tanto, un sistema criogénico se ha utilizado a lo largo de las tareas desarrolladas como medio para la caracterización con la temperatura de los distintos circuitos y dispositivos.

En este sentido, y para la caracterización de dispositivos o circuitos, se requiere la definición de una técnica de medida que permita llevar a cabo su medida a temperatura ambiente y criogénica. De esta manera, se han definido dos procedimientos de medida, que se han caracterizado a ambas temperaturas físicas, para definir sus características. Los kits diseñados permiten la medida de diodos para la obtención de modelos precisos. Concretamente, varios diodos se han caracterizado en términos de su respuesta en DC y parámetros S pequeña señal a temperatura ambiente y criogénica, lo que he permitido desarrollar los modelos pequeña señal para cada uno a ambas temperaturas. Se han considera tres diodos: dos diodos Schottky con diferente potencial de barrera (MA4E2037 y HSCH-9161) y un diodo PIN (HPND-4005). La respuesta de los mismos es distinta con el cambio de su temperatura de funcionamiento, obteniendo una reducción en la corriente de saturación y un incremento en el factor de idealidad cuando se trabaja a temperatura criogénica frente a temperatura ambiente. Además, se ha observado un incremento en la tensión de codo de los diodos cuando se trabaja en criogenia frente a temperatura ambiente. De manera adicional, para el diodo Schottky HSCH-9161 se ha implementado el modelo no lineal para su uso como detector. Se ha observado un comportamiento atípico en el caso del diodo PIN a temperatura criogénica, ya que se produce efectos de histéresis cuando se polariza el dispositivo de manera estática, mientras que opera de manera normal al ser polarizado a través de una fuente pulsada.

Adicionalmente, el conocimiento del cambio que se produce en los sustratos dieléctricos con la temperatura es bastante importante. Se ha presentado una técnica basada en el diseño de resonadores microstrip para la estimación de las características de tres sustratos de microondas a temperatura ambiente y criogénica y se han reportado las modificaciones encontradas. A temperatura criogénica, se reduce las pérdidas totales y se produce una muy ligera modificación en el valor de la permitividad relativa del dieléctrico.

Una vez que las características de los sustratos han sido estimadas y los diodos modelados, se ha presentado el diseño de tres nuevos circuitos: un conmutador de fase de 180º, un conmutador de fase de 90º y un detector. Se ha realizado un análisis detallado de su diseñado y han sido caracterizados tanto a temperatura ambiente como criogénica. Estos circuitos han sido diseñados para operar en la banda Ka, cubriendo desde 26 a 36 GHz, y han utilizado los modelos desarrollados para los diodos. Los

circuitos se han diseñado en tecnología planar, utilizando líneas de transmisión microstrip, CPW y slotline.

Se ha descrito el diseño de un conmutador de fase de 180º. Está basado en la utilización de transiciones de banda ancha de líneas CPW a slotline. Además, el uso de uniones en T en slotlin permite tener dos caminos de transmisión que pueden excitar a una línea CPW de salida. Dependiendo del camino por el que haya transmisión después de la unión en T, se obtiene una diferencia de fase de 180º en la línea CPW de salida. La selección del camino de propagación se lleva a cabo por un conjunto de diodos. Se ha caracterizado la respuesta del circuito tanto a temperatura ambiente como criogénica utilizando los diodos MA4E2037 y HPND-4005. El circuito proporciona una respuesta de fase plana con un error de fase inferior a 2º para ambos tipos de diodos y ambas temperaturas (300 K y 15 K). En cuanto a las pérdidas de inserción del circuito, se ha obtenido una reducción en las mismas de aproximadamente del 30% respecto al valor a temperatura ambiente con una reducción del 50% en el consumo de potencia cuando se ha medido el circuito con diodos Schottky. Sin embargo, cuando el circuito se ha caracterizado con los diodos PIN, la respuesta del circuito se ve alterada por el funcionamiento de los diodos PIN en criogenia, que necesita un consumo de potencia muy alto.

Se han presentado varios diseños de conmutadores de fase de 90º. Están basados en tecnología híbrida utilizando SPDTs como conmutador, utilizando dispositivos comerciales o un nuevo diseño implementado en líneas CPW-slotline-microstrip con diodos. La diferencia de fase se obtiene utilizando filtros paso banda. El circuito basado en la solución del conmutador SPDT en líneas CPW-slotline-microstrip ha proporcionado una diferencia de fase plana con un error inferior a 5º a temperatura ambiente para diodos MA4E2037 y HPND-4005. Estos resultados mejoran la respuesta ofrecida por los diseños basados en SPDTs MMICs comerciales. Por otro lado, la respuesta a temperatura criogénica ha sido implementada únicamente con los diodos Schottky y se ha obtenido una reducción de las pérdidas de inserción del circuito con una reducción aproximadamente del 80% en el consumo de potencia, mientras que la respuesta en fase se mantiene constante.

Se ha analizado y diseñado un detector basado en el diodo ‘zero-bias’ HSCH-9161. Como aspecto novedoso en el diseño, se ha presentado el uso de líneas de transmisión con pérdidas en la red de adaptación del diodo, implementadas como resistencias distribuidas tipo ‘thin-film’. Se ha desarrollado un análisis detallado de las

líneas de transmisión con pérdidas para alcanzar una sensibilidad plana de aproximadamente 1000 mV/mW con pérdidas de retorno mejores de 10 dB a temperatura ambiente en el rango de 26 a 36 GHz. Cuando el detector es enfriado, se ha obtenido un incremento de la sensibilidad que es dependiente de la corriente de polarización del diodo. A su vez, se ha observado que la sensibilidad del detector se reduce cuando se incremente el valor de la corriente continua, aunque siempre se obtienen valores superiores al de temperatura ambiente. Además, el punto de compresión 1-dB en criogenia es inferior al valor a temperatura ambiente, aunque su valor se incrementa cuando se incrementa el valor de la corriente.

Finalmente, en esta tesis se ha descrito el receptor de radio astronomía, radiómetro, en el que los diferentes diseños van a ser integrados. Se ha detallado el proyecto QUIJOTE que está concebido para la caracterización de la polarización del Fondo Cósmico de Microondas y otras emisiones galácticas y extragalácticas. Dentro de la segunda fase del proyecto se lleva a cabo el desarrollo e integración del instrumento en la banda de 30 GHz, llamado TGI. Se ha descrito el funcionamiento del TGI, que proporciona a cuatro tensiones de salida que permitan calcular los parámetros de Stokes, que definen la polarización de una onda electromagnética. Prácticamente la totalidad de los diseños del TGI se ha desarrollado por el DICOM.

8.2. Líneas Futuras

El trabajo desarrollado en esta tesis puede ser ampliado teniendo en cuenta diferentes aspectos de los diferentes capítulos presentados.

Primero, los modelos obtenidos para los diferentes diodos se han desarrollado únicamente a dos temperaturas físicas, 300 K y 15 K. El desarrollo de un modelo electro-térmico desde 300 K a 15 K que incluya el rango completo de temperaturas sería muy interesante para predecir el funcionamiento de los dispositivos a cualquier temperatura de operación y analizar su inserción en cualquier circuito.

El desarrollo de circuitos en tecnología híbrida conlleva un cuidadoso montaje de los diferentes componentes para no añadir efectos no deseados que pueden modificar el funcionamiento esperado. La interconexión a través de hilos de bonding es crítica para la respuesta en fase del circuito, ya que es difícil controlar la longitud de dichas conexiones. De esta manera, el uso de tecnologías monolíticas permitiría un mayor nivel de precisión ya que estas interconexiones son parte de la propia tecnología, y únicamente se necesitarían las interconexiones hacia el exterior del circuito. El diseño

de conmutadores de fase de 180º y 90º en tecnología monolítica resultaría en mejores resultados de fase.

El uso de conmutadores de fase de 180º y de 90º que presentan ciertos errores de fase provoca diferencias en las tensiones de salida del sistema que los contiene. El análisis del impacto de estos errores de fase en los conmutadores de fase conllevaría un mejor conocimiento del funcionamiento del receptor.

Además, el diseño de un circuito que incluyese los cuatro estados de fase (0º, 90º, 180º y 270º) mejoraría los resultados obtenidos frente a la opción del montaje en cascada de los circuitos individuales.

El detector presenta un rango dinámico estrecho. El análisis de cómo se podría ampliar dicho margen cuando trabaja en régimen cuadrático sería de mucho interés para mejorar el diseño.

La aplicación final de los circuitos presentados en esta tesis es su integración en un receptor para radioastronomía que opera en la banda de 26 a 36 GHz para la observación del cielo. La caracterización completa del receptor incluyendo los amplificadores bajo ruido criogénicos completaría el análisis aquí descrito. Además, la definición de un sistema de calibración del receptor para eliminar errores completaría el procedimiento de caracterización del sistema.

Por último, el grupo del DICOM está involucrado en el diseño de nuevos radiómetros en las bandas Q y W, así que la extensión en frecuencia de los modelos de los diodos y el escalado de los circuitos están siendo desarrollados como nuevas tareas.

Annex I

Resonator Module Drawings

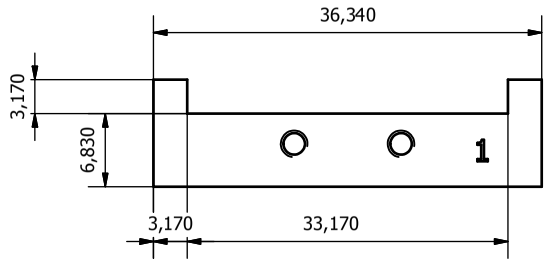

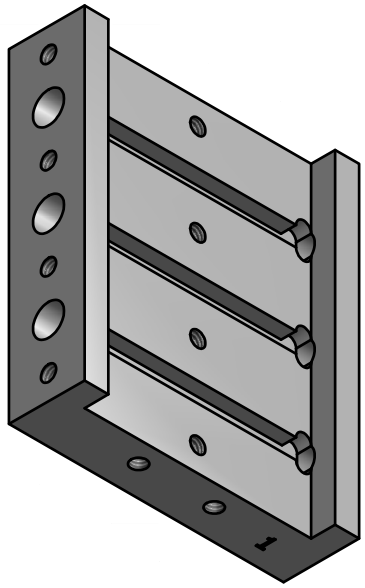

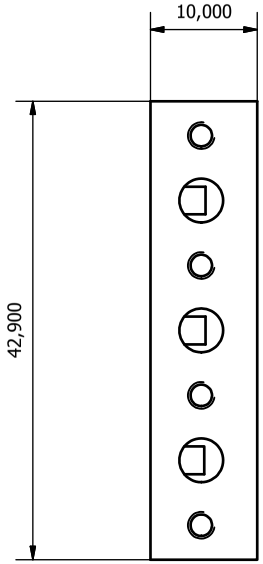

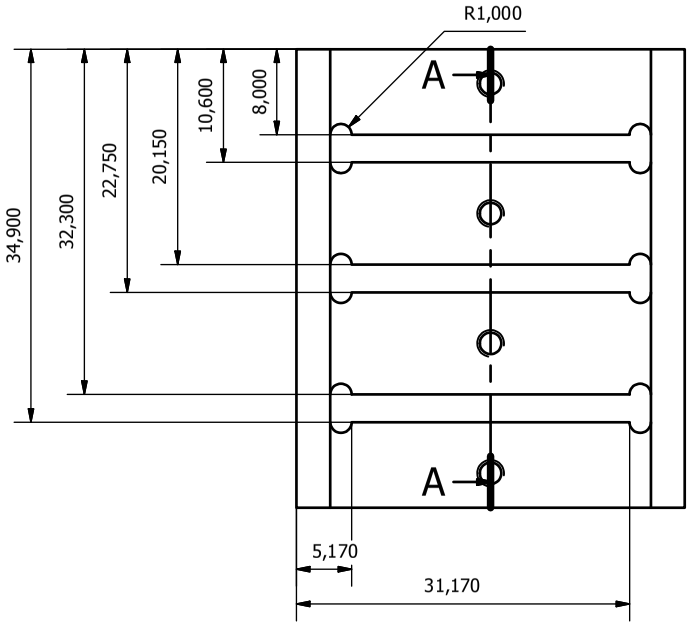

A-A (2 : 1)

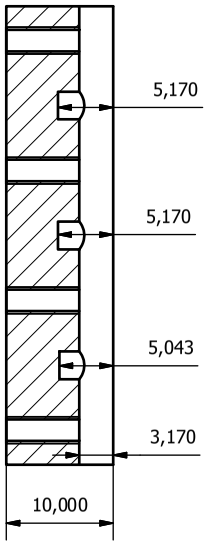

Diseño de	Revisado por	Aprobado por	Fecha		Fecha	
Enrique						
UC - DICOM		Units: mm		Aluminium		
		plano_caja			Edición	Hoja 1 / 1

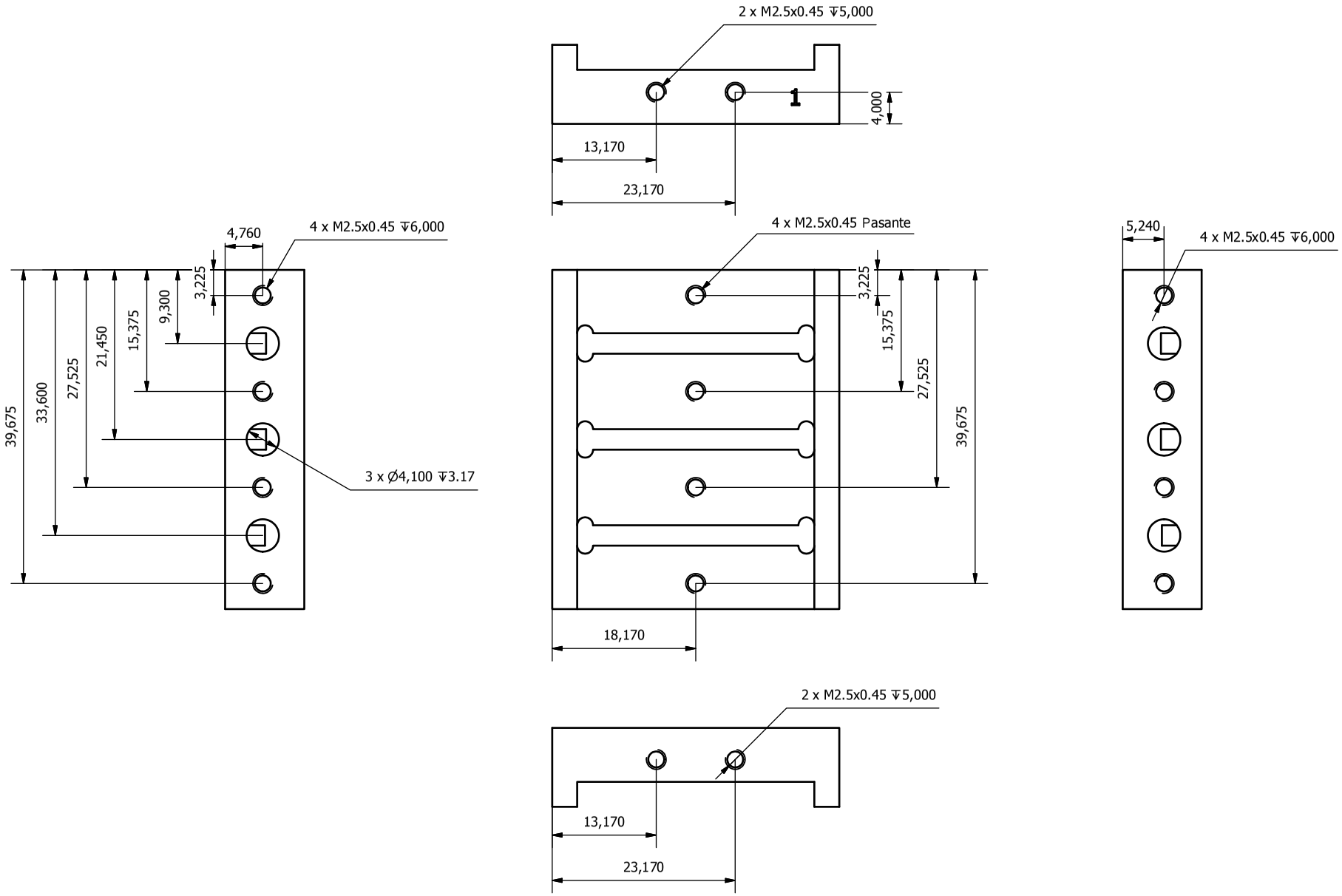

Diseño de	Revisado por	Aprobado por	Fecha		Fecha	
Enrique						
UC - DICOM		Units: mm		Aluminium		
		plano_caja			Edición	Hoja 2 / 2

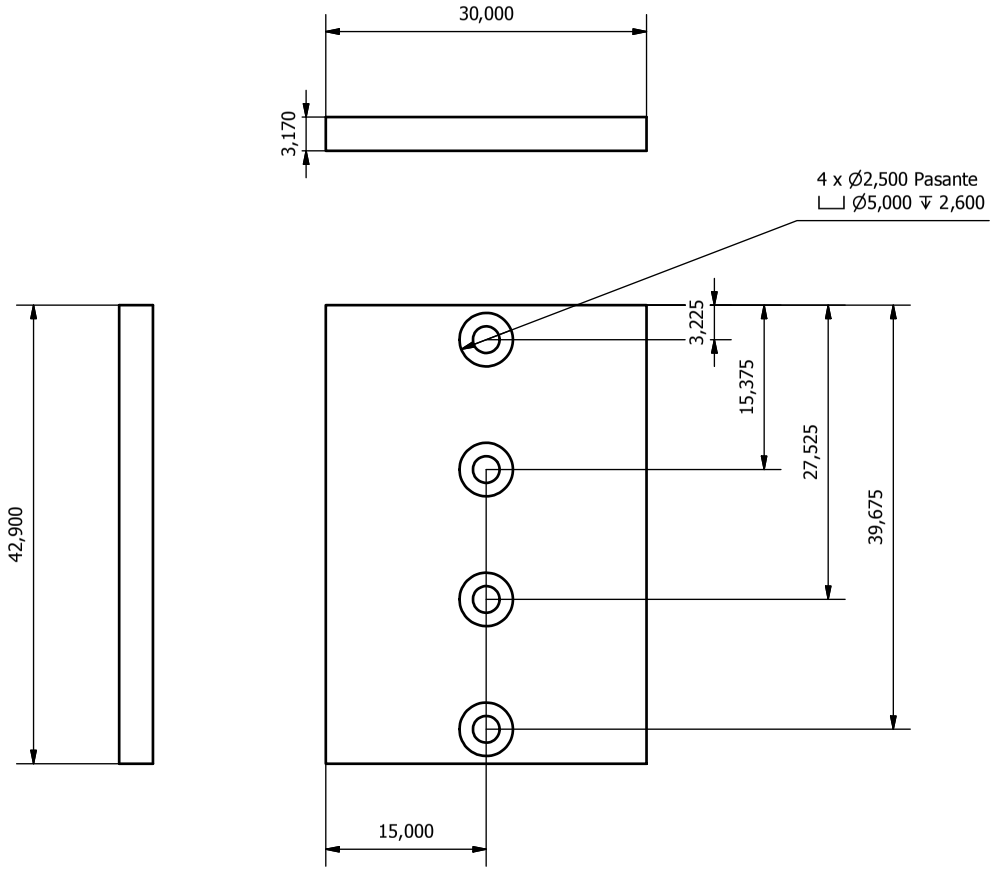

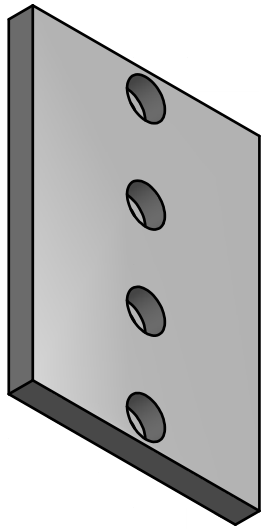

Diseño de	Revisado por	Aprobado por	Fecha		Fecha	
Enrique						

UC - DICOM	Units: mm Aluminium		
	plano_tapa_caja	Edición	Hoja 1 / 1

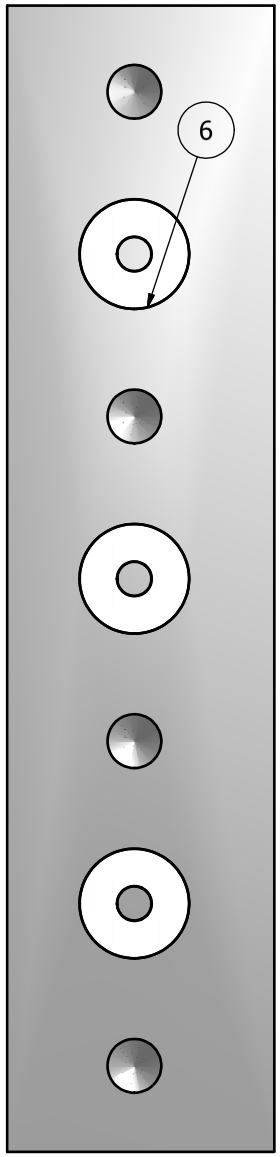

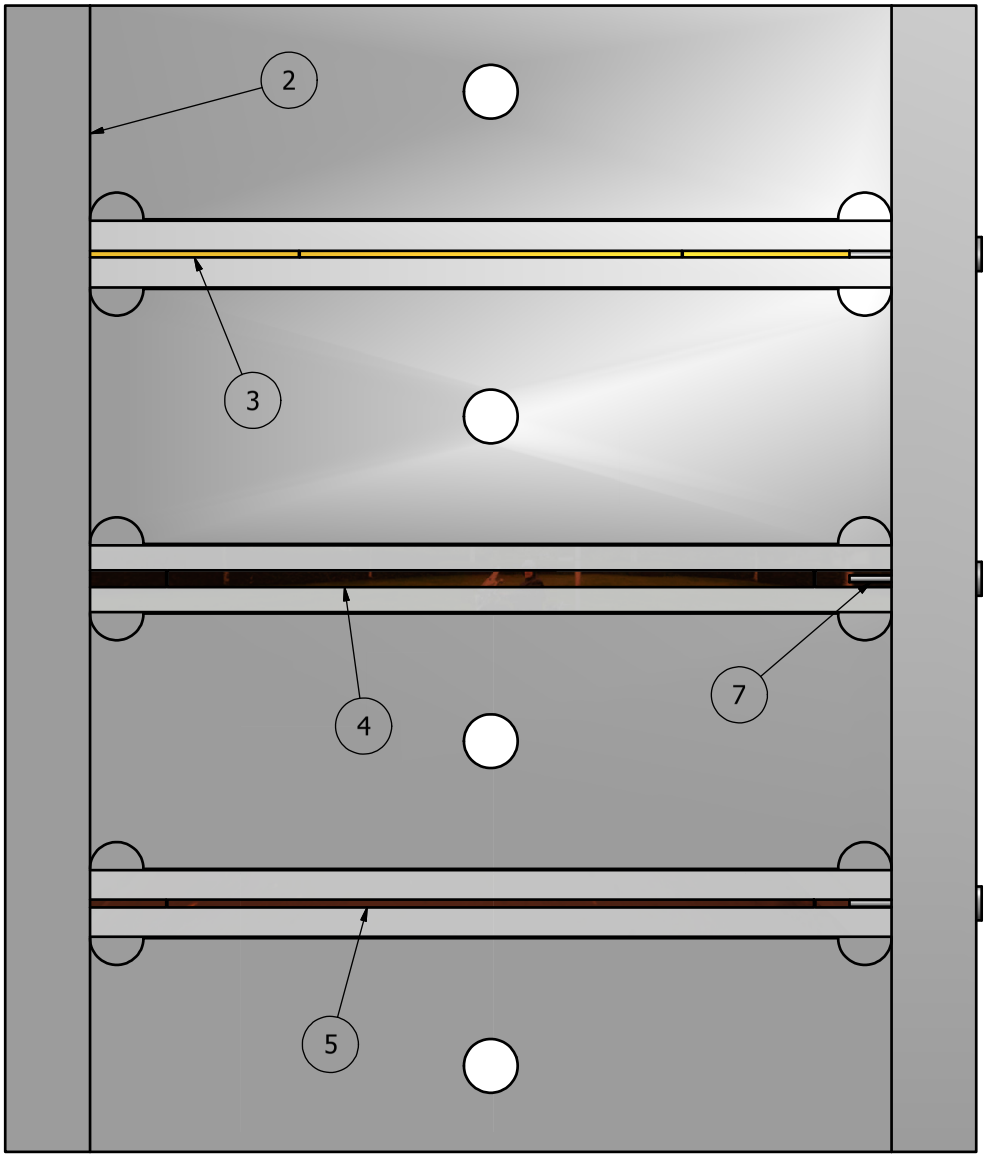

LISTA DE PIEZAS			
ELEMENTO	CTDAD	Nº DE PIEZA	DESCRIPCIÓN
1	1	tapa_caja	
2	1	caja	
3	1	resonador_alumina	
4	1	resonador_clte10	
5	1	resonador_clte5	
6	6	teflon	R280 468 000
7	6	pin	R280 463 000

- Montaje para temperatura ambiente y criogénica
- Pegado a la caja de los sustratos con pasta
- Pegado del pin a las líneas con indio

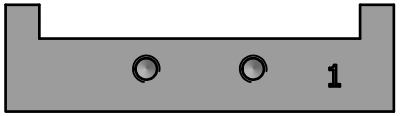

Diseño de	Revisado por	Aprobado por	Fecha		Fecha	
Enrique						
UC - DICOM		Assembly - Components				
		montaje		Edición	Hoja 1 / 1	

Annex II

180º Phase Switch Module Drawings

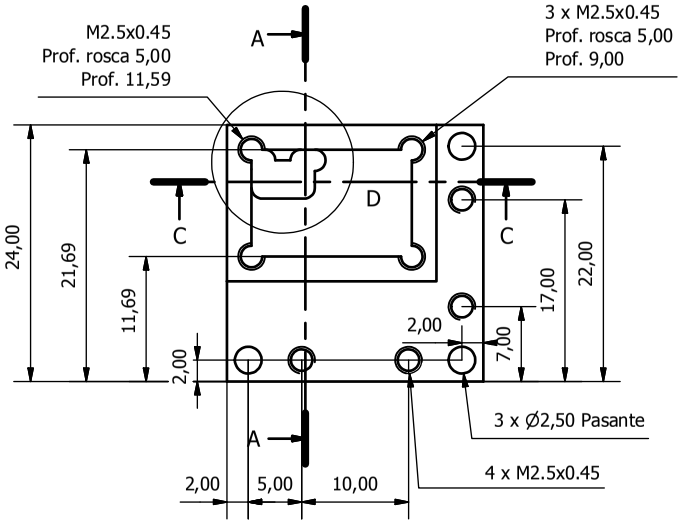

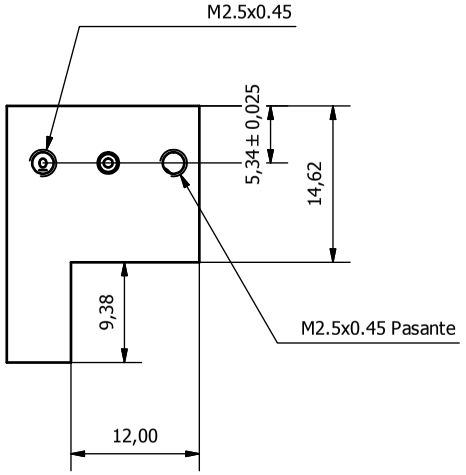

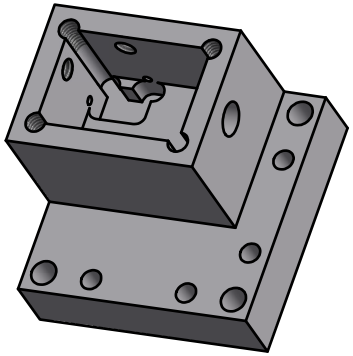

B (6 : 1)

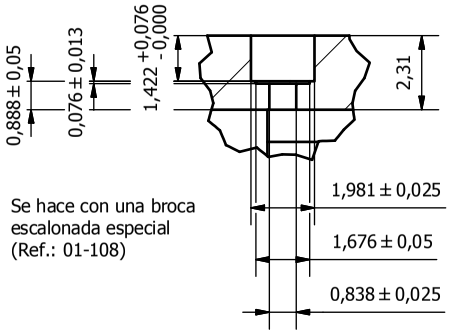

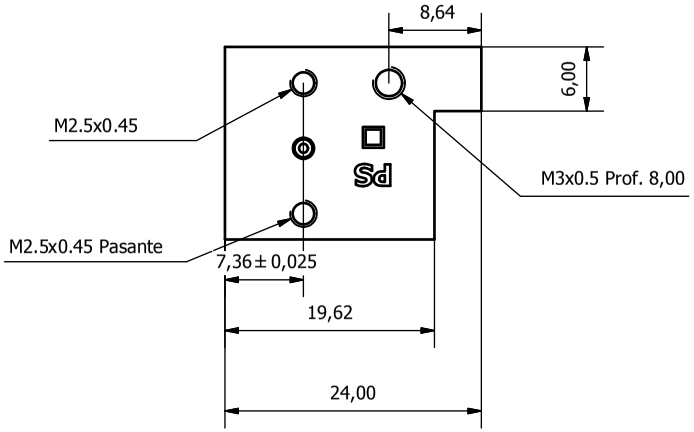

A-A (2 : 1)

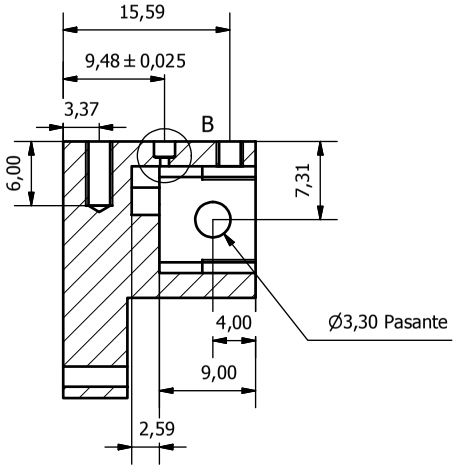

D (4 : 1)

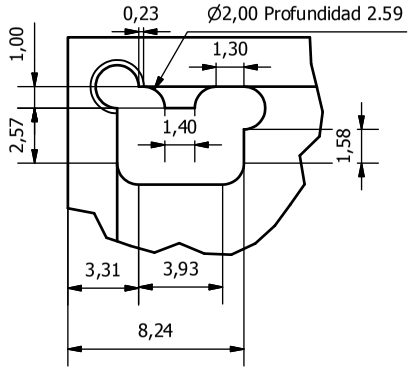

C-C (2 : 1)

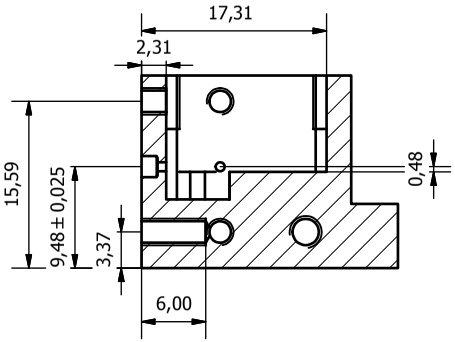

Diseño de	Material	Unidades	Escala	Fecha
Enrique Villa	Brass	mm	2:1	

UC - DICOM	Caja PS Cuadrado		
	QUIJOTE	Edición	Hoja 1 / 1

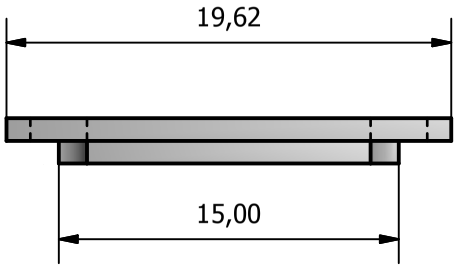

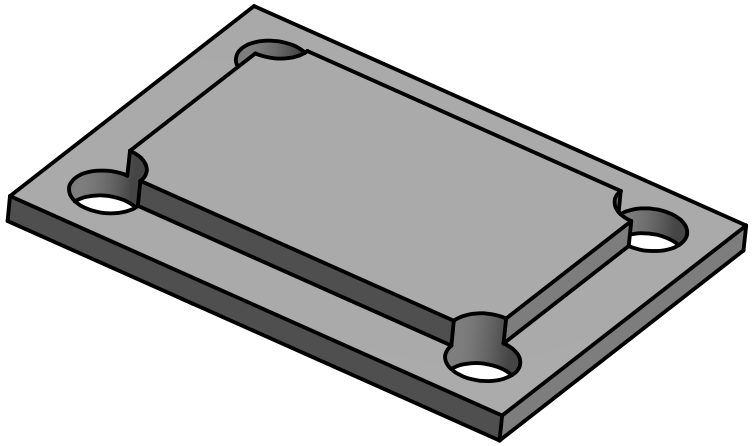

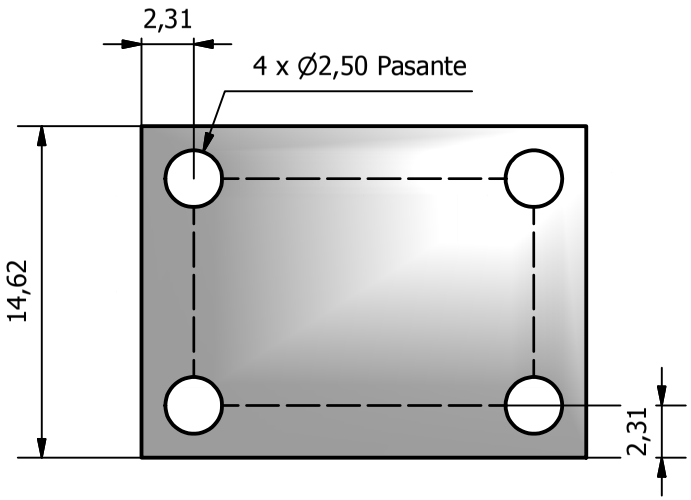

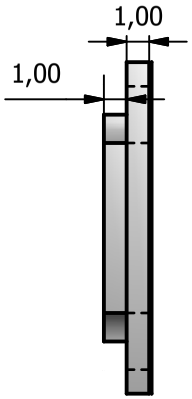

Diseño de	Material	Unidades	Escala	Fecha	
Enrique Villa	Brass	mm	3:1		

UC - DICOM	Tapa caja PS		
	QUIJOTE	Edición	Hoja 1 / 1

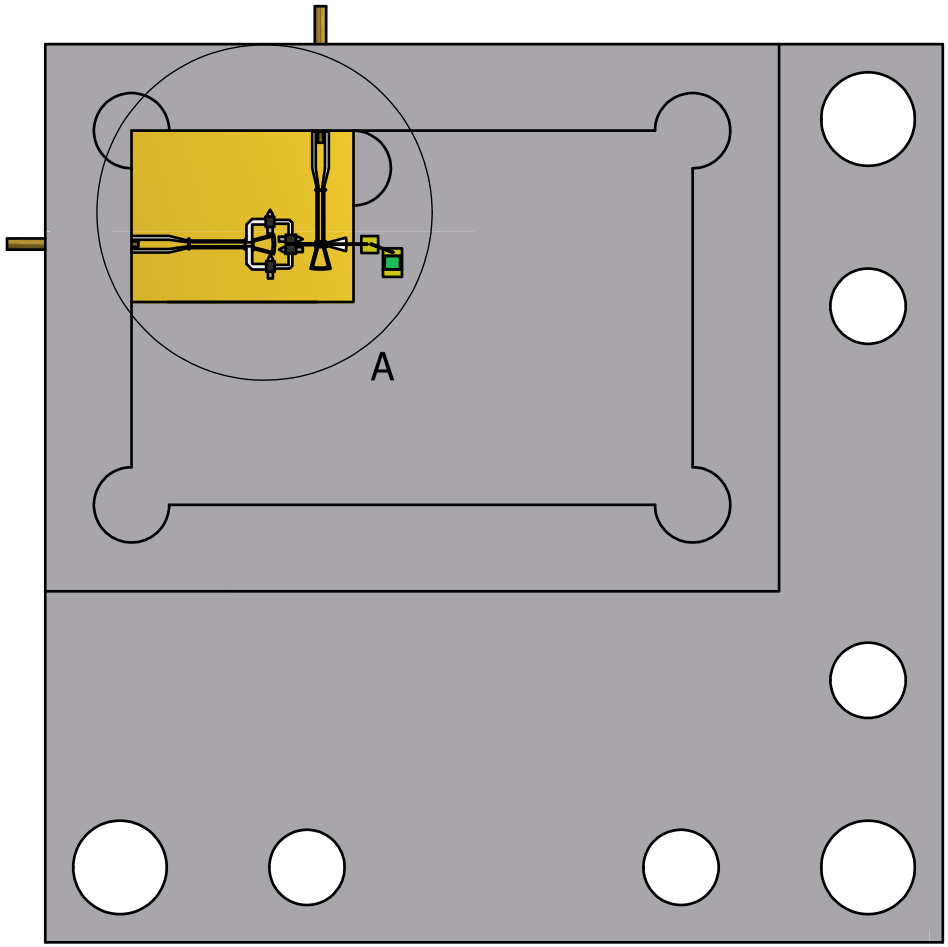

LISTA DE PIEZAS			
ELEMENTO	CTDAD	Nº DE PIEZA	DESCRIPCIÓN
1	1	caja_circular	
2	1	alumina	
3	2	Glass_Bead_Anritsu	
4	2	Sliding contact2	
5	4	Diodos PIN HPND-4005/Schottky MA4E2037	
6	1	Condensador ATC 0.5 pF 116SCA0R5A100TT	
7	1	Resistencia SOTA 10 Ohm S0302APG100J20	

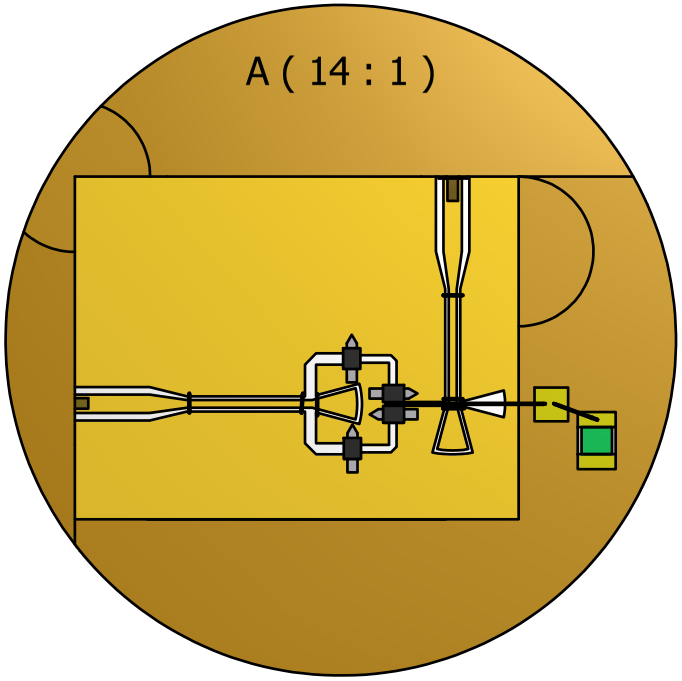

· Montaje PS180º:
Bondings en las uniones T de línea coplanar
Bondings equipotencialidad cada 1mm en línea coplanar
Bonding Lhilo aprox. 2.4mm (Lrecto 2mm, loop 0.8mm) desde centro de la isla al condensador
Unión bordes alúmina a la caja con pasta

Diseño de	Revisado por	Aprobado por	Fecha		Fecha	
Enrique						
UC - DICOM		Assembly - Components				
				Edición	Hoja	
					1 / 1	

Annex III

90º Phase Switch Module Drawings

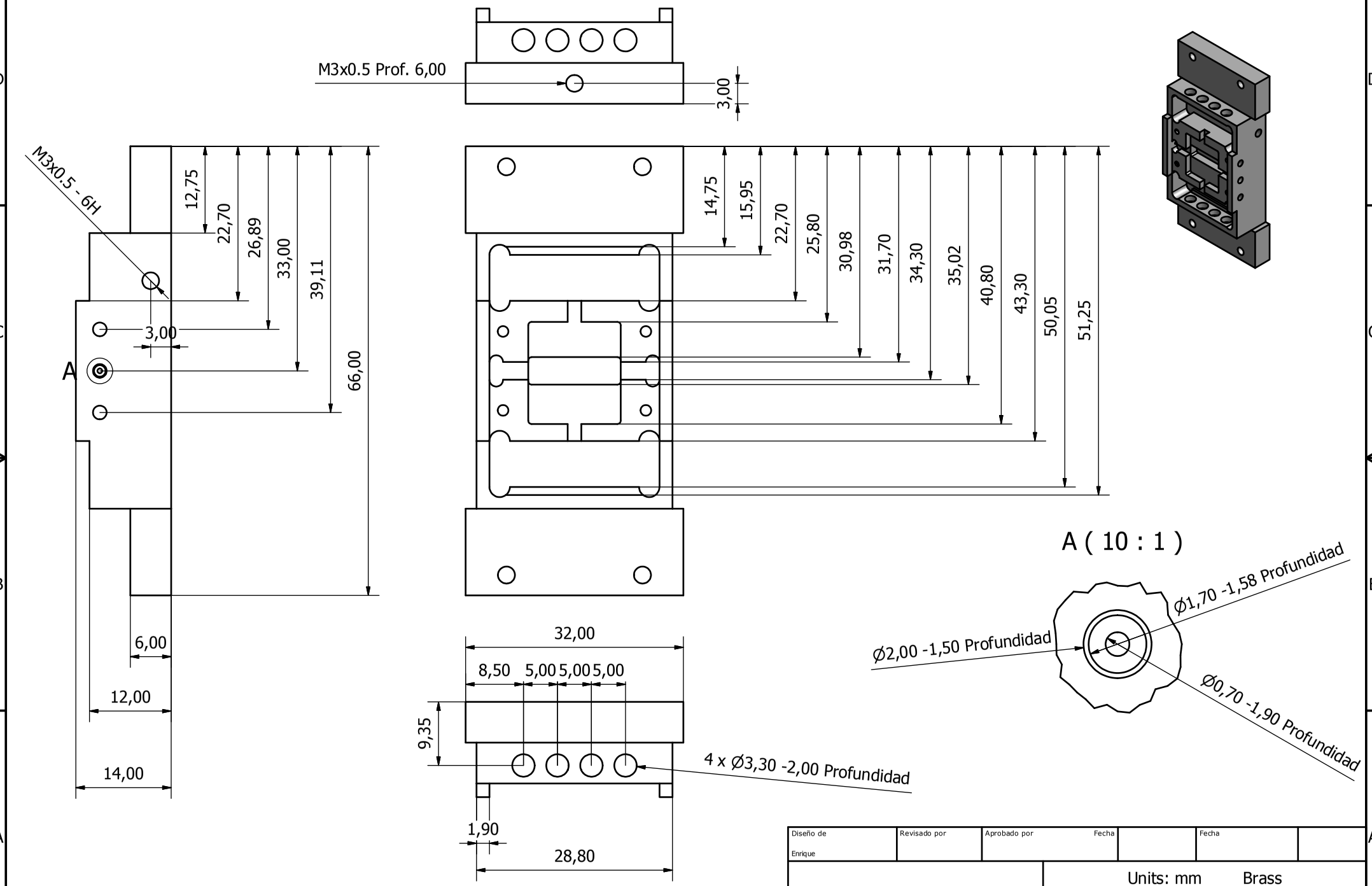
M3x0.5 Prof. 6,00
3,00
M3x0.5 - 6H
12,75
22,70
26,89
33,00
39,11
66,00
3,00
A
6,00
12,00
14,00
14,75
15,95
22,70
25,80
30,98
31,70
34,30
35,02
40,80
43,30
50,05
51,25
A (10 : 1)
Ø1,70 -1,58 Profundidad
Ø2,00 -1,50 Profundidad
Ø0,70 -1,90 Profundidad
32,00
8,50
5,00
5,00
5,00
9,35
4 x Ø3,30 -2,00 Profundidad
1,90
28,80
Diseño de
Enrique
Revisado por
Aprobado por
Fecha
Fecha
UC - DICOM
Units: mm
Brass
Pieza1
Edición
Hoja
1 / 2

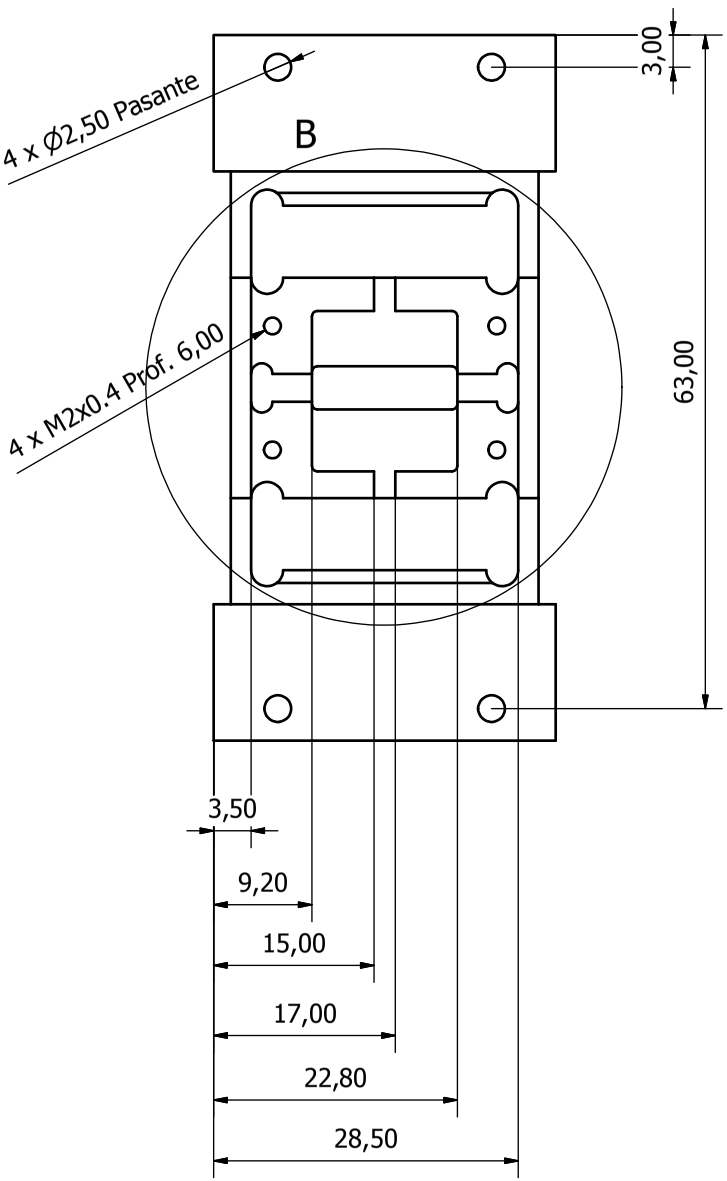

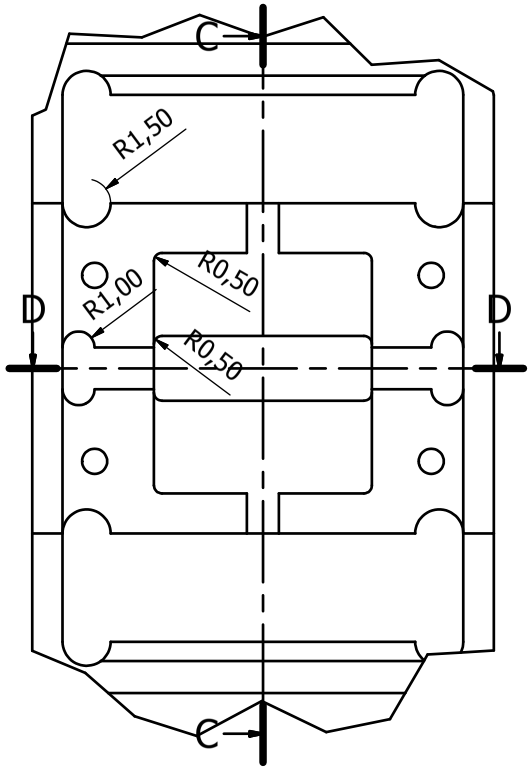

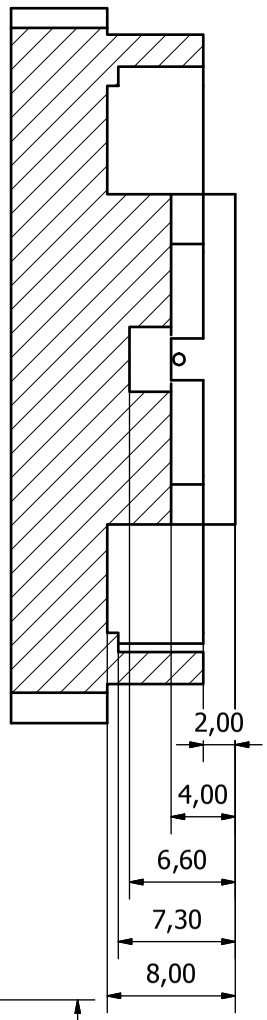

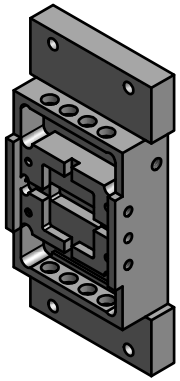

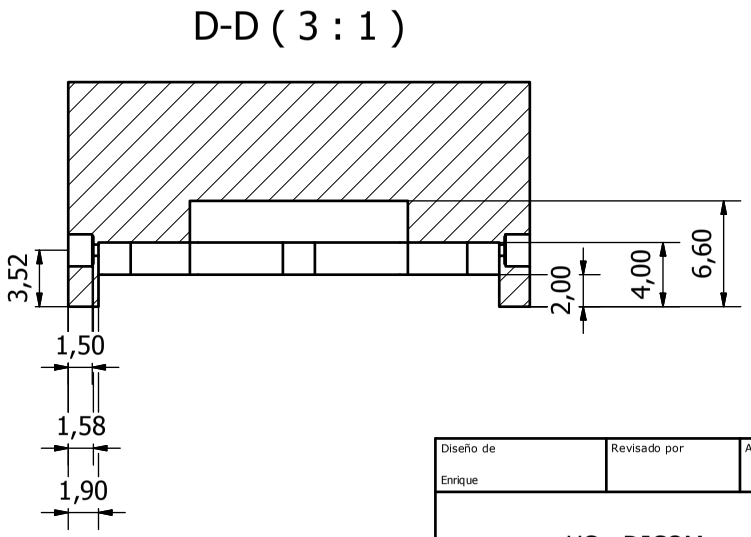

Diseño de	Revisado por	Aprobado por	Fecha		Fecha	
Enrique						
UC - DICOM		Units: mm		Brass		
		Pieza1			Edición	Hoja 2 / 2

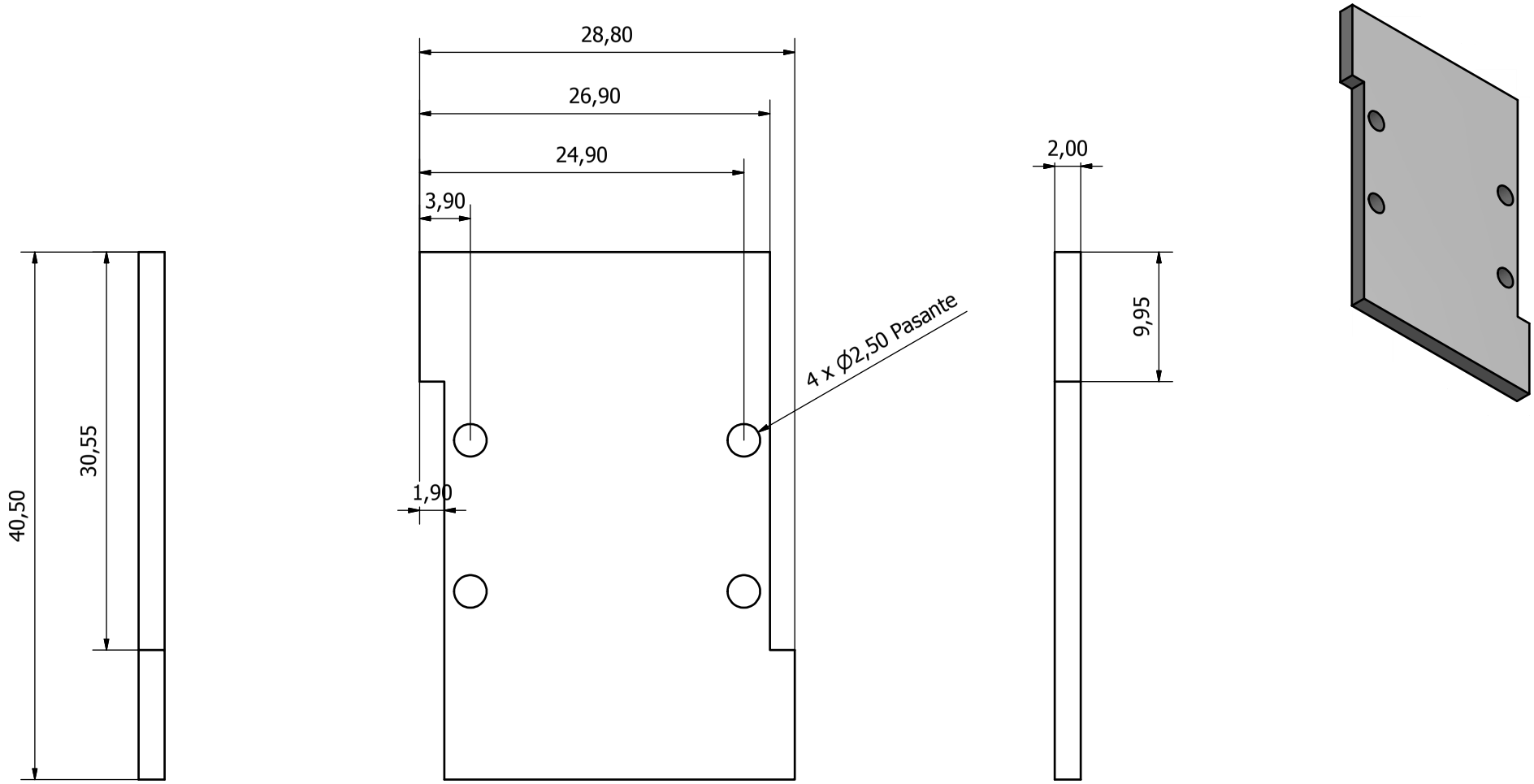

Diseño de	Revisado por	Aprobado por	Fecha		Fecha	
Enrique						
UC - DICOM		Units: mm		Brass		
		tapa			Edición	Hoja 1 / 1

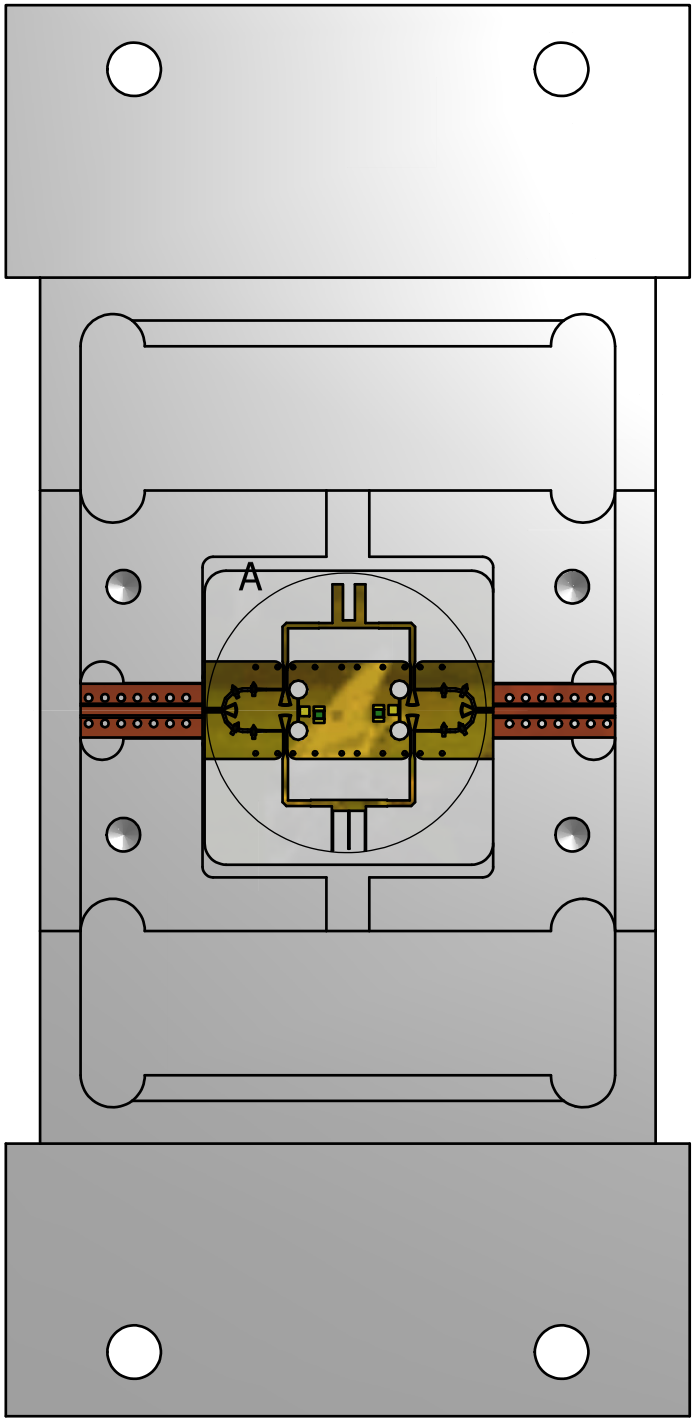

LISTA DE PIEZAS			
ELEMENTO	CTDAD	Nº DE PIEZA	DESCRIPCIÓN
1	1	Pieza1	
2	2	linea_CPWG	
3	1	Ensamblaje_PS90	
3.1	4	Diodos	
3.2	1	PS90 alumina	
3.3	4	Diodos	
3.4	2	Condensador_05pF	
3.5	2	Resistencia_SOTA	

· Montaje PS90º:
Bondings en las uniones T de línea coplanar
Bondings equipotencialidad a la mitad de líneas coplanares
Bonding Lhilo aprox. 2.4mm (Lrecto 2mm, loop 0.8mm) desde la isla al condensador
Unión bordes alúmina a la caja con pasta

A (8 : 1)

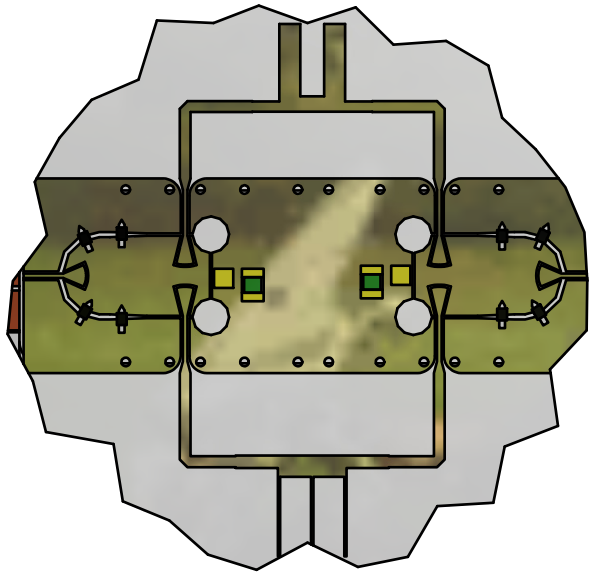

Diseño de	Revisado por	Aprobado por	Fecha		Fecha	
Enrique					28/08/2014	

UC - DICOM	Assembly - Components		
	Ensamblaje2	Edición	Hoja 1 / 1

Annex IV

TGI Phase Switches Module Drawings

Roscas y agujeros

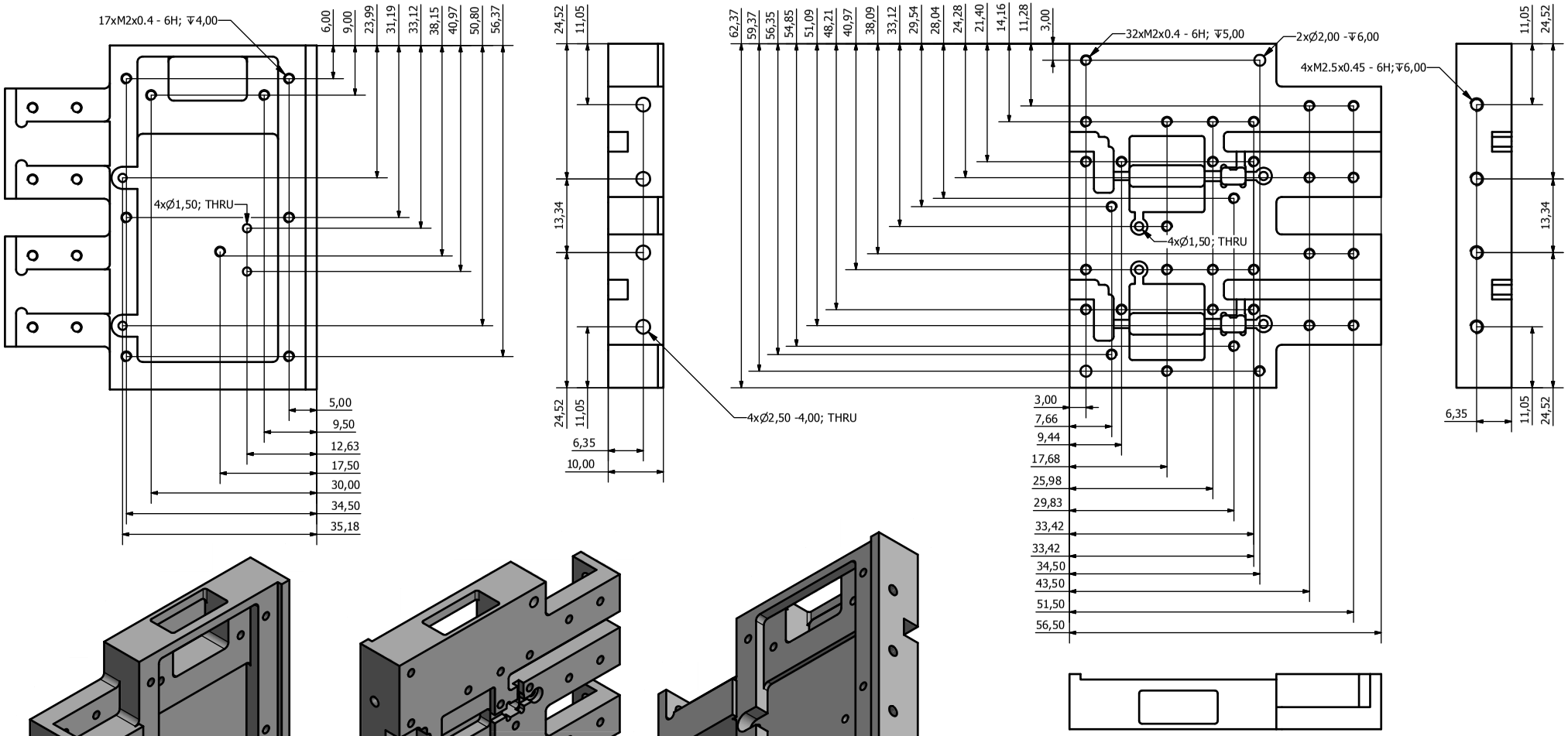

Diseño de:	Material:	Aprobado por:	A Fecha:	Escala:	Fecha	Tamaño Hoja:
Enrique	Aluminio			4:3		A3

UC - DICOM	Parte Inferior Caja Phase Switch QUIJOTE		
	Dpto. Ingeniería de Comunicaciones	Edición	Hoja 1 / 3

Cara superior

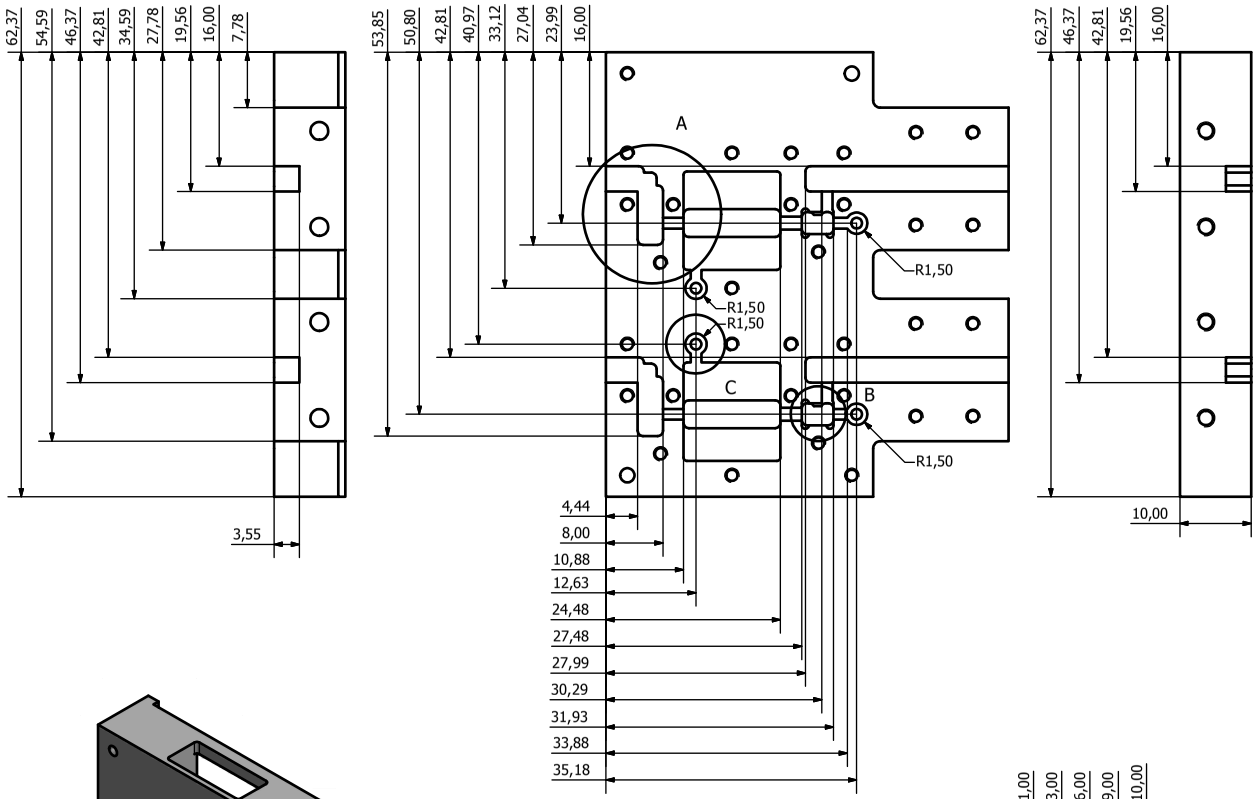

Detalle A (5 : 1)

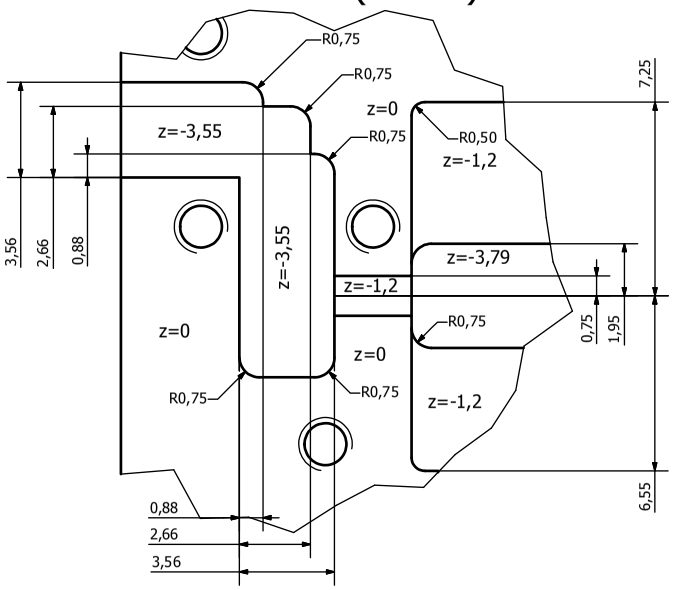

Detalle B (10 : 1)

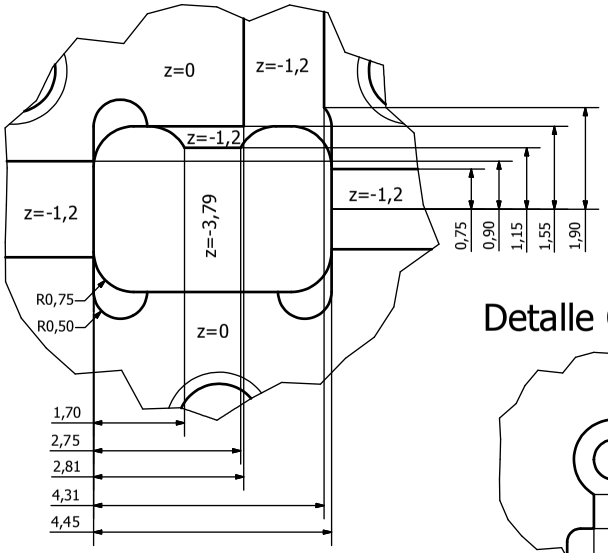

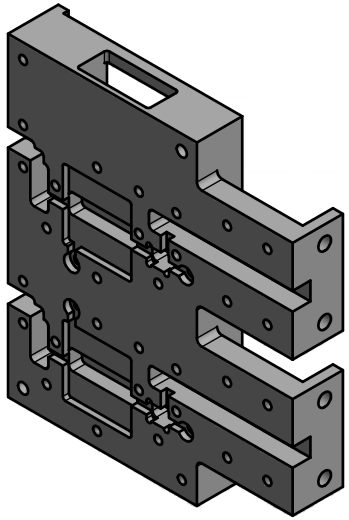

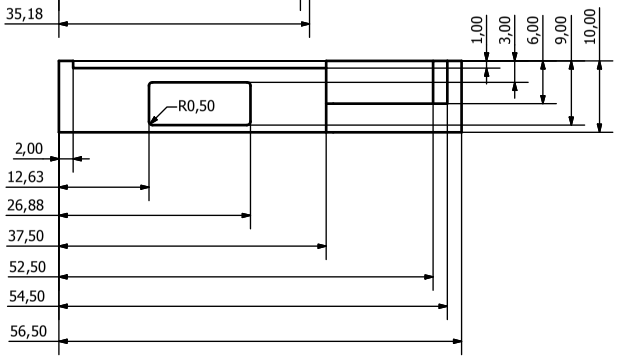

Detalle C (5 : 1)

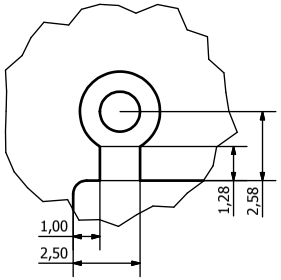

Diseño de:	Material:	Aprobado por:	A Fecha:	Escala:	Fecha	Tamaño Hoja:
Enrique	Aluminio			4:3		A3

UC - DICOM	Parte Inferior Caja Phase Switch QUIJOTE		
	Dpto. Ingeniería de Comunicaciones	Edición	Hoja 2 / 3

Cara inferior

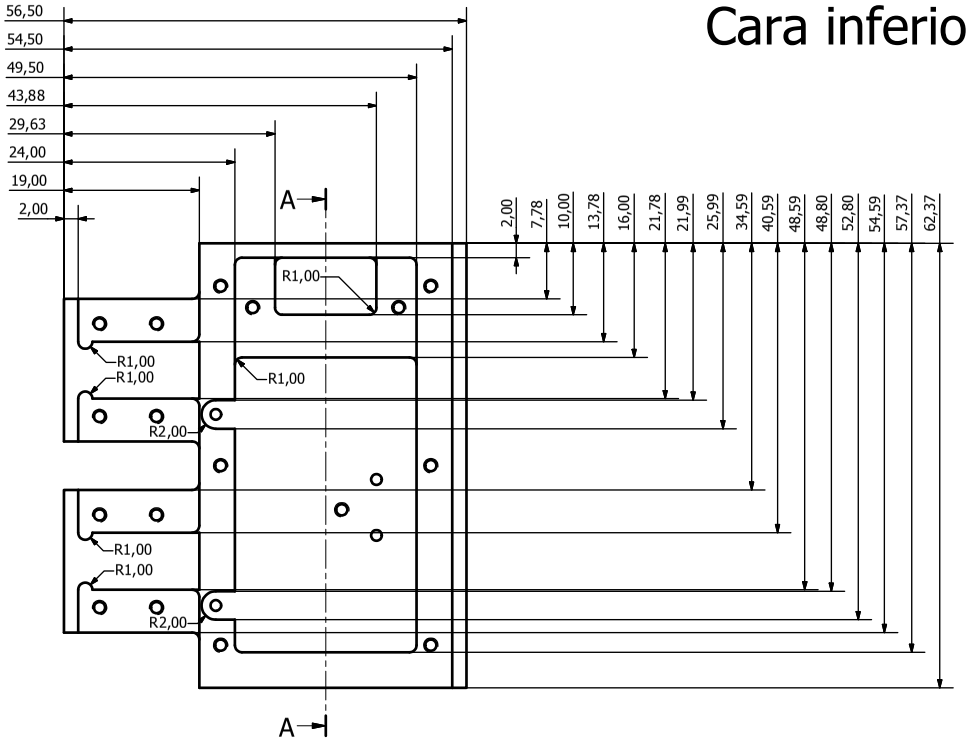

Corte A-A (4 : 3)

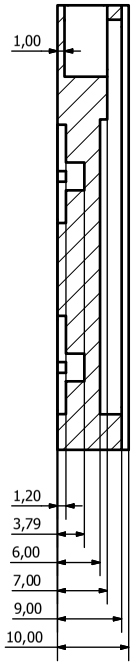

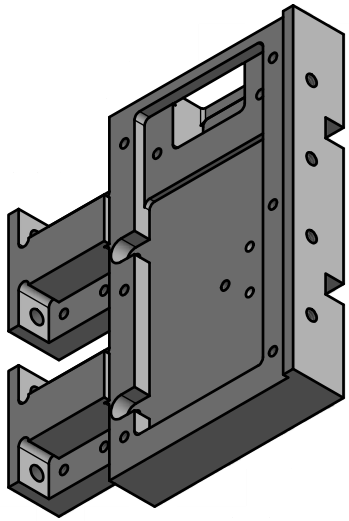

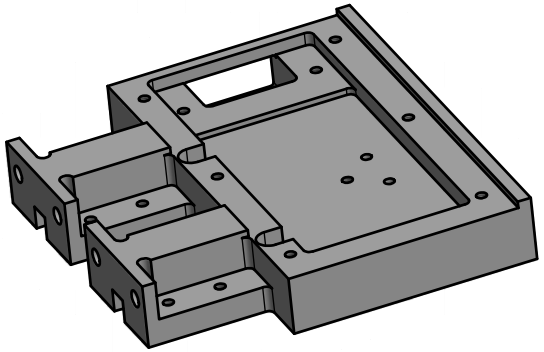

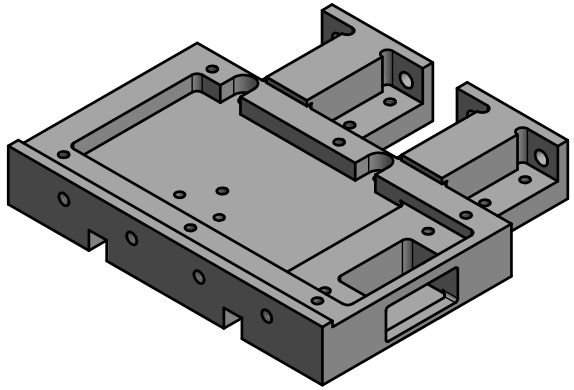

Tapa 1 mm

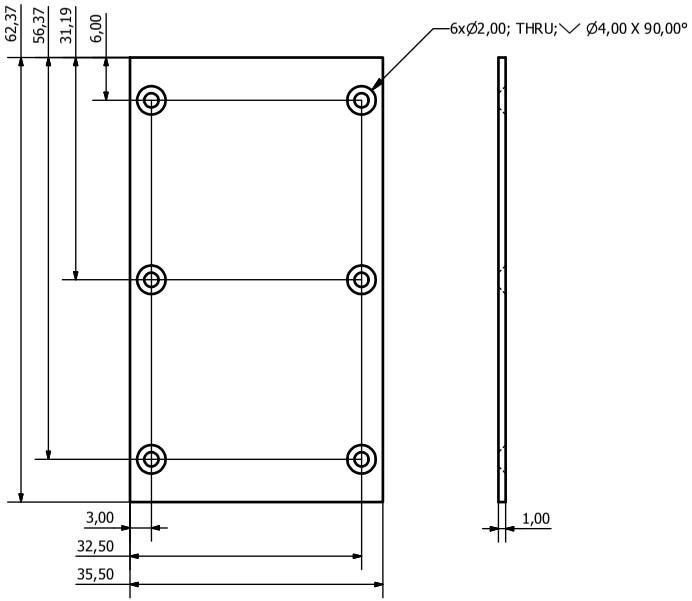

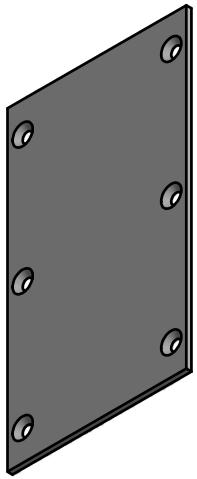

Diseño de:	Material:	Aprobado por:	A Fecha:	Escala:	Fecha	Tamaño Hoja:
Enrique	Aluminio			4:3		A3

UC - DICOM	Parte Inferior Caja Phase Switch QUIJOTE		
	Dpto. Ingeniería de Comunicaciones	Edición	Hoja 3 / 3

Roscas y agujeros

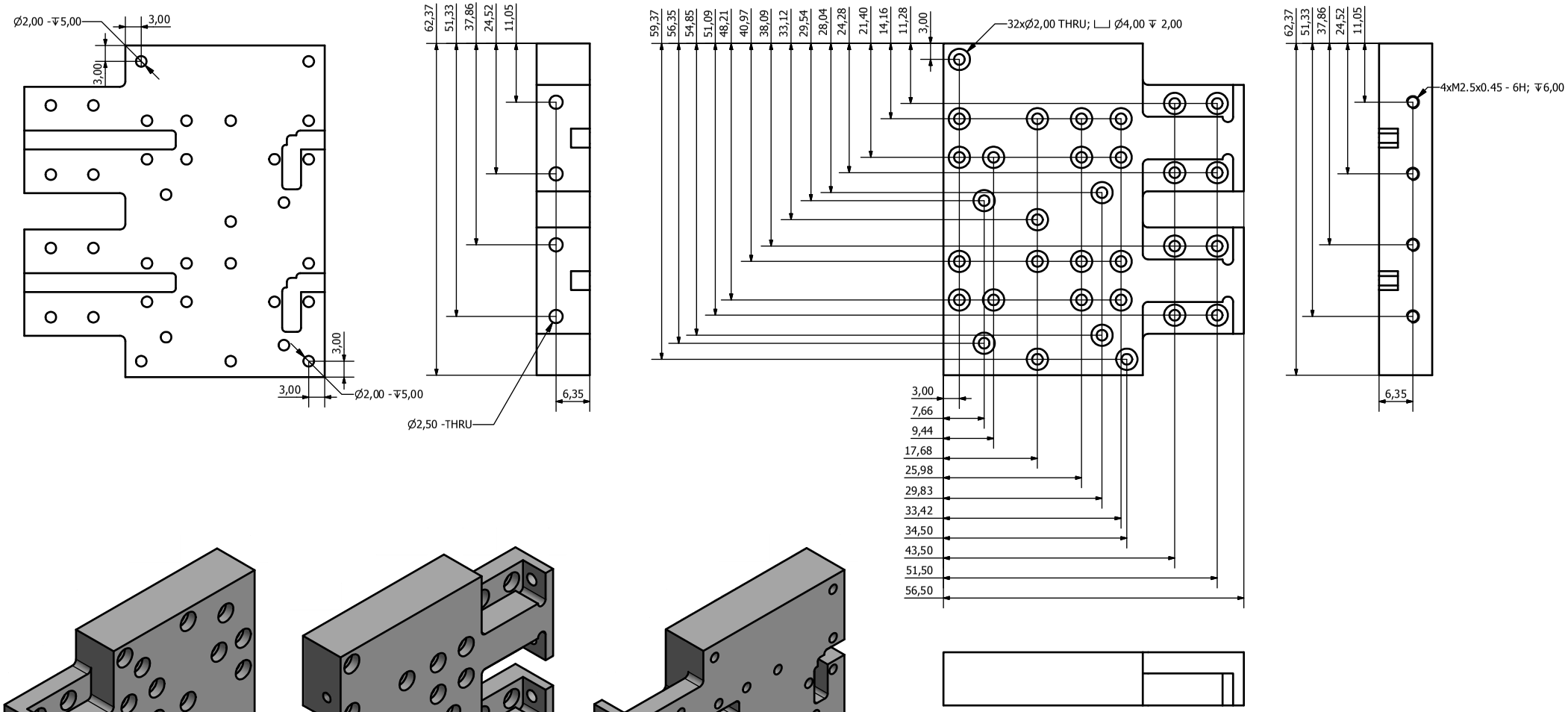

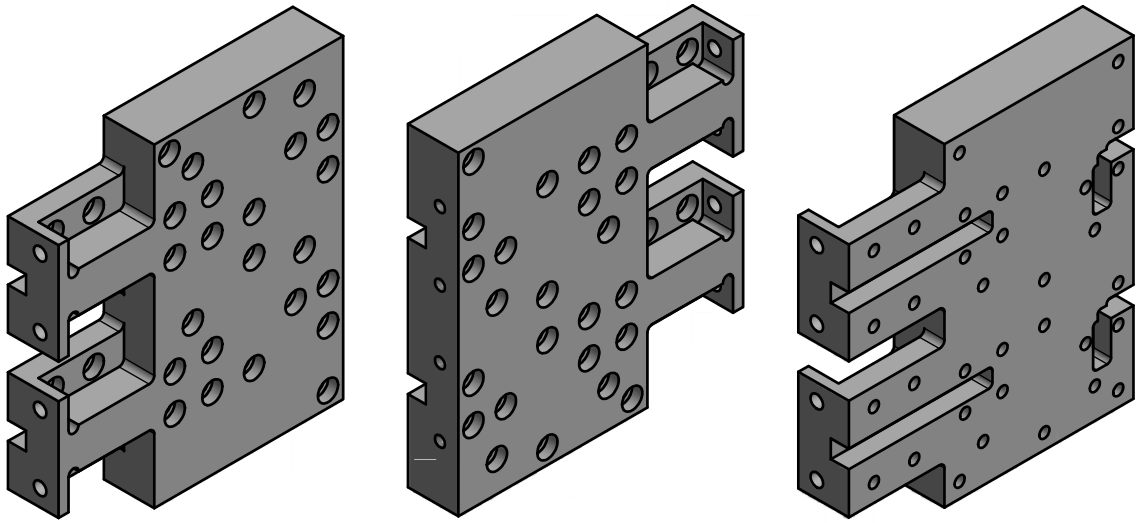

Diseño de:	Material:	Aprobado por:	A Fecha:	Escala:	Fecha	Tamaño Hoja:
Enrique	Aluminio			4:3		A3

UC - DICOM	Parte Superior Caja Phase Switch QUIJOTE		
	Dpto. Ingeniería de Comunicaciones	Edición	Hoja 1 / 2

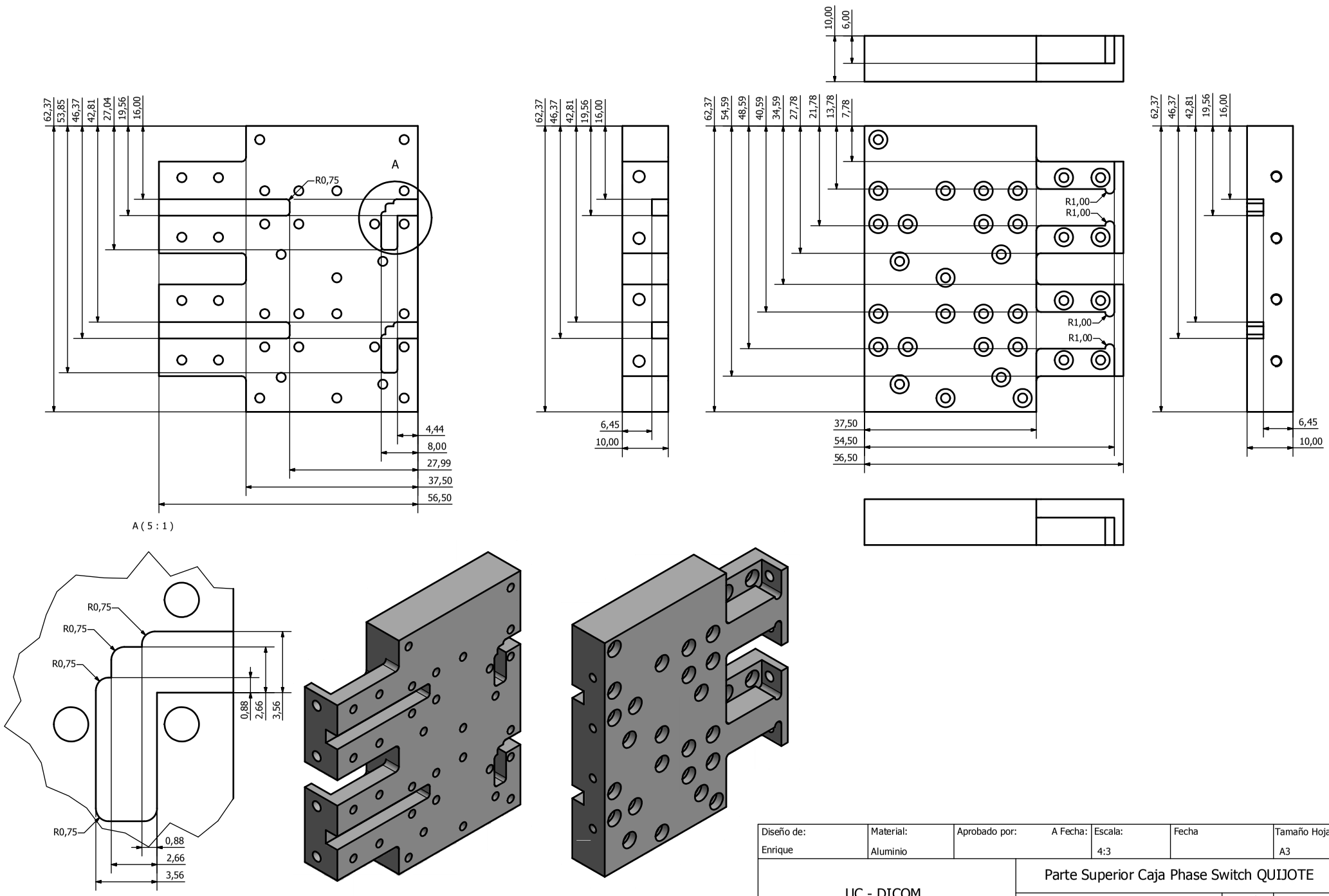

Diseño de:	Material:	Aprobado por:	A Fecha:	Escala:	Fecha	Tamaño Hoja:
Enrique	Aluminio			4:3		A3

UC - DICOM	Parte Superior Caja Phase Switch QUIJOTE		
	Dpto. Ingeniería de Comunicaciones	Edición	Hoja 2 / 2

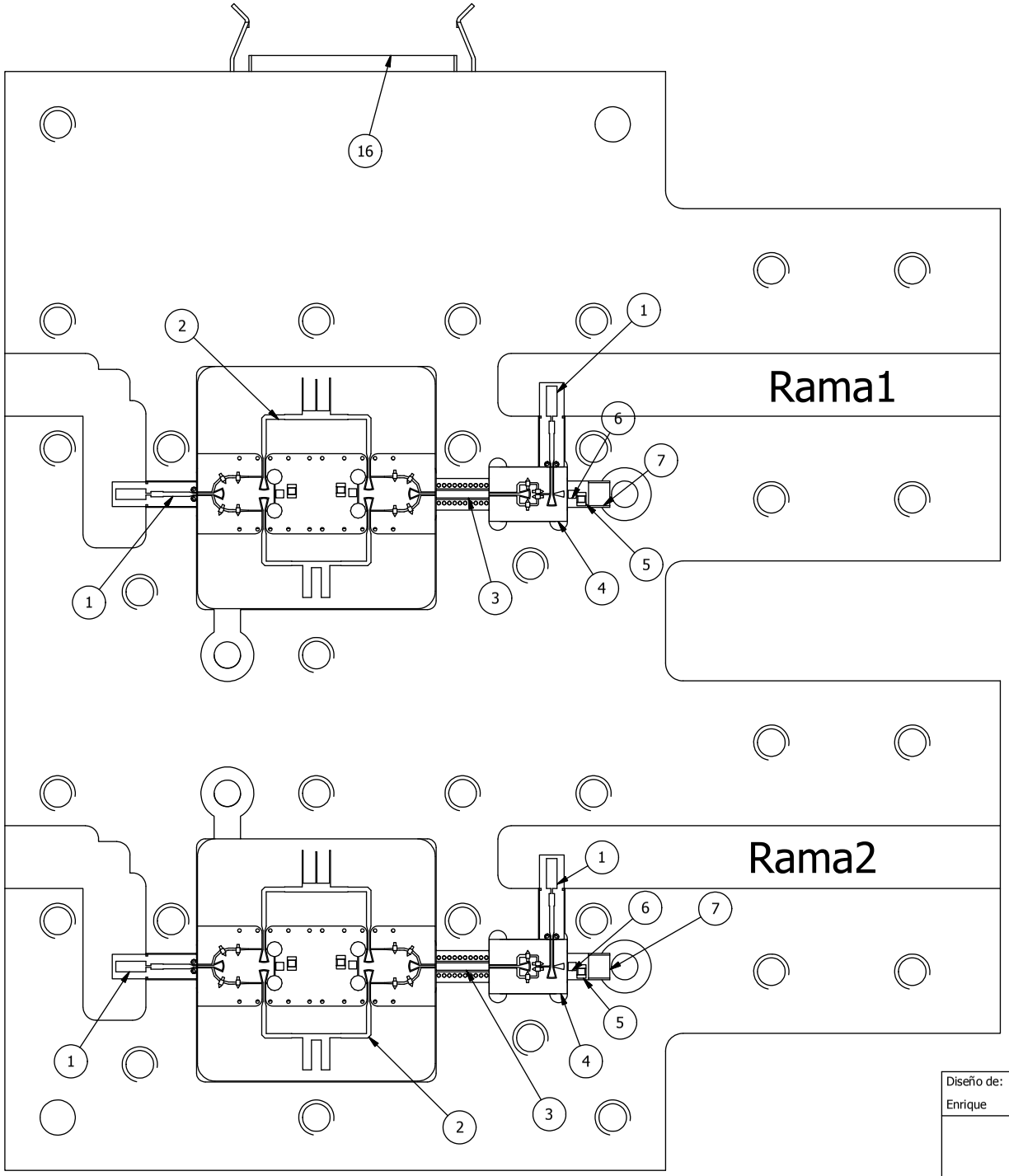

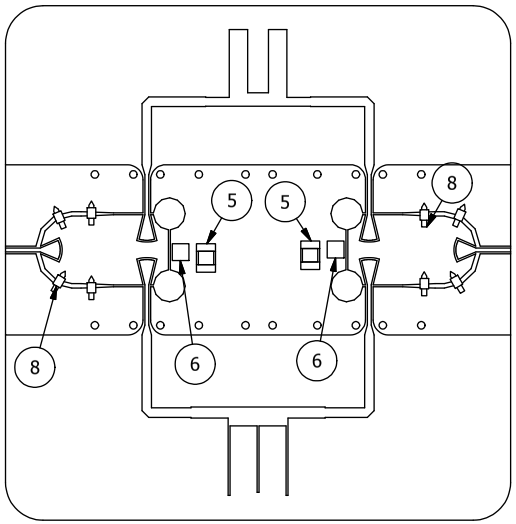

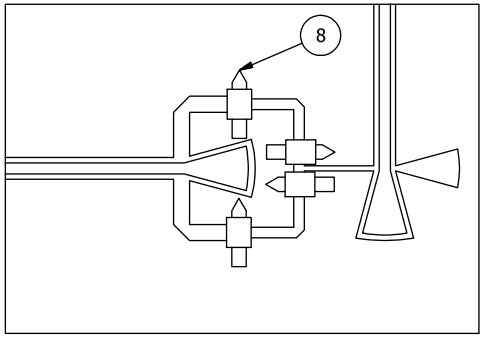

Diseño de:	Material:	Aprobado por:	A Fecha:	Escala:	Fecha	Tamaño Hoja:
Enrique	Aluminio					A3

UC - DICOM	Montaje PS Module		
	DICOM	Edición	Hoja 1 / 1

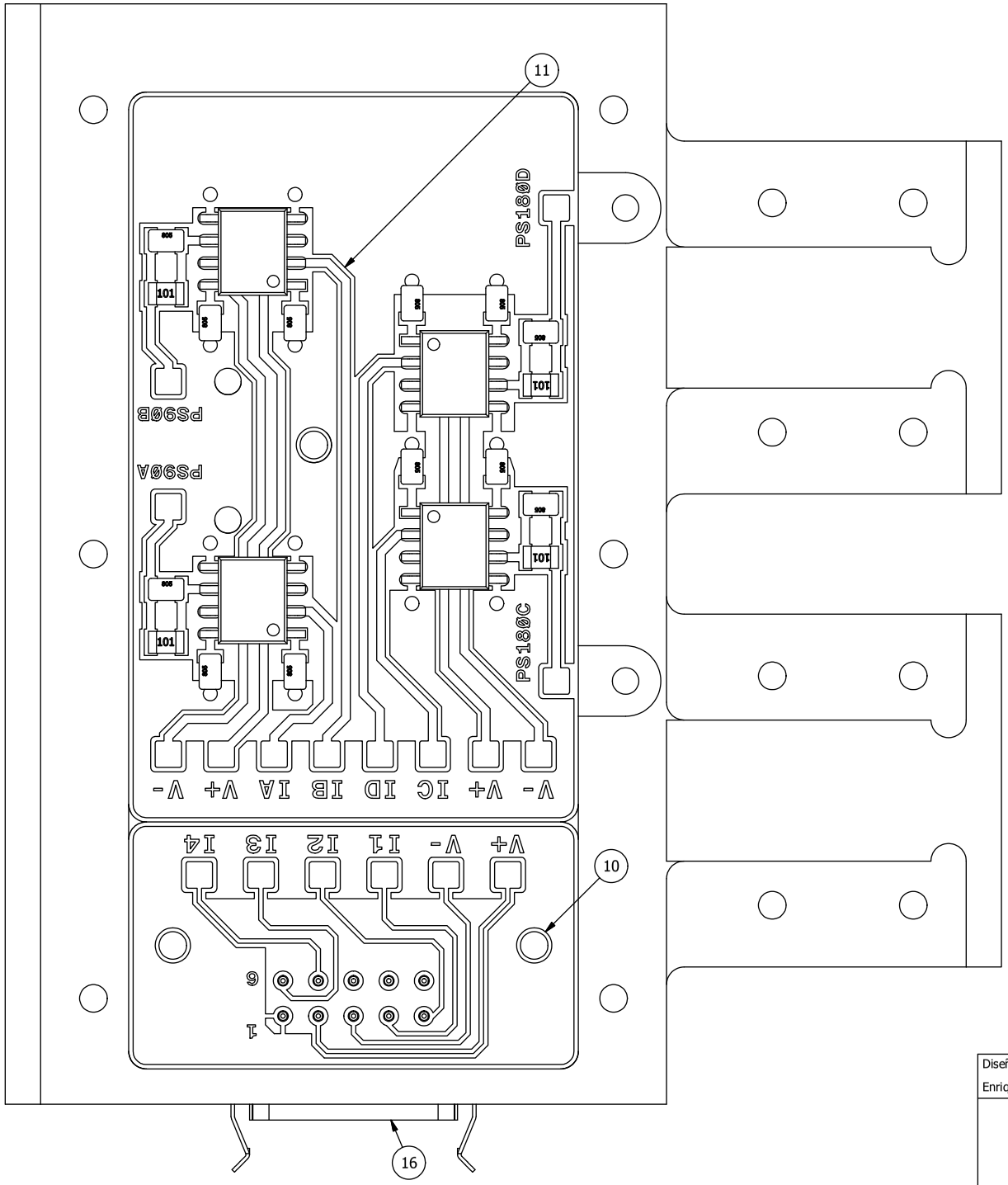

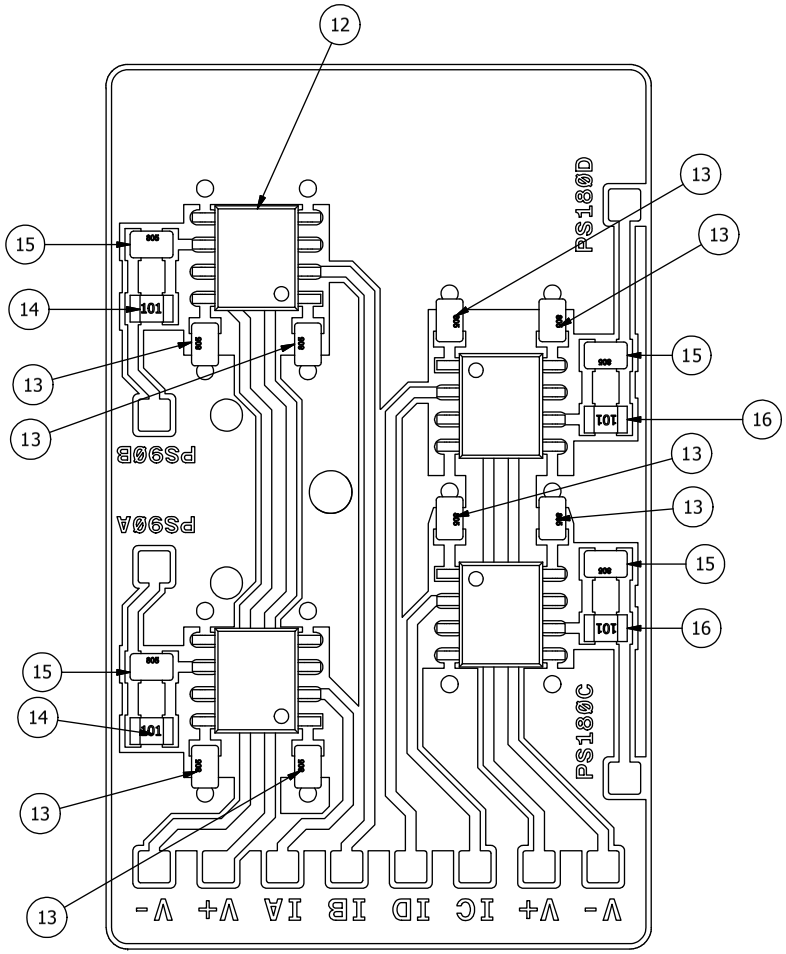

Diseño de:	Material:	Aprobado por:	A Fecha:	Escala:	Fecha	Tamaño Hoja:
Enrique	Aluminio					A3

UC - DICOM

Montaje PS Module

DICOM

Edición

Hoja 2 / 2

Lista de Piezas Caja			
ITEM	QTY	PART NUMBER	DESCRIPTION
0	1	Caja	
1	4	Transición CPWG-uStrip-WR28 CLTE-XT 10mils	
2	2	Phase Switch 90º	
3	2	Linea CPWG CLTE-XT 10mils	
4	2	Phase Switch 180º	
5	6	Resistencia Sota	10 Ohm S0302APG100J20
6	6	Condensador Dicap	0,5 pF ATC 116SCA0R5A100TT
7	2	Linea Auxiliar Polarización	
8	24	Diodo PIN	HPND-4005
10	1	Placa Conector	
11	1	Placa Drivers	
16	1	m80-8511042_asm	

Lista de Componentes Placa de los Drivers			
ITEM	QTY	PART NUMBER	DESCRIPTION
12	4	Chip Driver	DR65-0109
13	8	Condensador	10nF SMD 0805
14	2	Resistencia	24 Ohm SMD 0805
15	4	Condensador	560pF SMD 0805
16	2	Resistencias	66,5 Ohm SMD 0805

Interconexión Placas			
Pin	ID Placa Conec	ID Placa Driver	Info
1	Gnd	nc	Ground
2	+V	+V	+5V
3	-V	-V	-5V
4	I1	IC	PS180-B1
5	I2	IA	PS90-B1
6	I3	ID	PS180-B2
7	I4	IB	PS90-B2
8	nc		
9	nc		
10	nc		

Asignación Pines Conector		
Pin	Bias	Info
1	Gnd	Ground
2	V+	+5V
3	V-	-5V
4	PS180-B1	Rama1
5	PS90-B1	Rama1
6	PS180-B2	Rama2
7	PS90-B2	Rama2
8	nc	
9	nc	
10	nc	

· Montaje
Unión con cinta de oro de línea CPWG en CLTE-XT a alúmina, entre línea central y planos laterales
· Montaje PS180º:
Bondings en las uniones T de línea coplanar
Bondings equipotencialidad cada 1mm en línea coplanar
Bonding Lhilo aprox. 2.4mm (Lrecto 2mm, loop 0.8mm) desde centro de la isla al condensador
Unión bordes alúmina a la caja con pasta
· Montaje PS90º:
Bondings en las uniones T de línea coplanar
Bondings equipotencialidad a la mitad de líneas coplanares
Bonding Lhilo aprox. 2.4mm (Lrecto 2mm, loop 0.8mm) desde la isla al condensador
Unión bordes alúmina a la caja con pasta

Diseño de:	Material:	Aprobado por:	A Fecha:	Escala:	Fecha	Tamaño Hoja:
Enrique	Aluminio					A3

UC - DICOM	Montaje PS Module		
	DICOM	Edición	Hoja 3 / 3

Annex V

Video Amplifier Configuration

The schematic of the video amplifier is shown in Fig. A.V. 1. The differential voltage is obtained combining a variable-gain differential amplifier configuration as first stage and then, an inverting and a non-inverting amplifier topologies as second stages. The variable gain of the differential amplifier is achieved by the use of external potentiometers, labelled as R_4 in the figure, which enable the fitting of the input signal to the DAE.

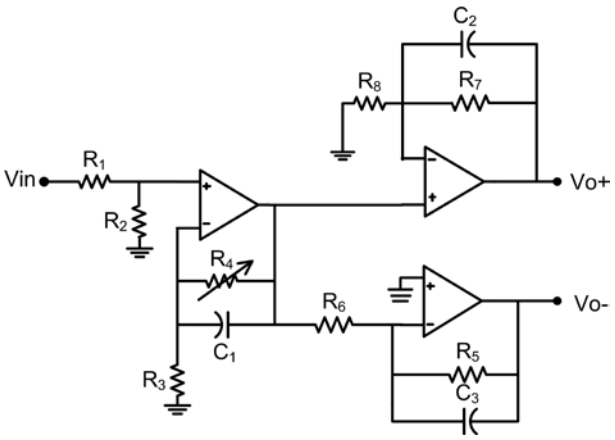

Fig. A.V. 1. Schematic of the video amplifier.

Using the above circuit configuration, the output voltages V_{0+} and V_{0-} are given by

$$V_{0+} = V_{in} \cdot \left(\frac{R_2 \cdot (R_4 + R_3)}{R_3 \cdot (R_1 + R_2)} \right) \cdot \left(1 + \frac{R_7}{R_8} \right) \qquad \text{(A.V.1)}$$

$$V_{0-} = -V_{in} \cdot \left(\frac{R_2 \cdot (R_4 + R_3)}{R_3 \cdot (R_1 + R_2)} \right) \cdot \left(\frac{R_9}{R_6} \right) \qquad \text{(A.V.2)}$$

The components and their selected values which are part of the video amplifier are listed in Table A.V. 1.

Table A.V. 1.Component values of the video amplifier.

Component	Value
Operational Amplifier	OPA4227
R_1	100 Ω
R_2	51 kΩ
R_3	100 Ω
R_4	0 - 10 kΩ
R_5	100 kΩ
R_6	10 kΩ
R_7	91 kΩ
R_8	10 kΩ
C_1	47 pF
C_2, C_3	22 pF

The potentiometer R_4 enables the variation of the gain in the range from 20 to 2000 in linear scale. It is placed outside the module and it is connected by a short cable. The initial value of the potentiometer is set to R_4=2.7 kΩ in order to provide a voltage gain of about 560.

$$V_{0+} = V_{in} \cdot \left(\frac{R_2 \cdot (R_4 + R_3)}{R_3 \cdot (R_1 + R_2)} \right) \cdot \left(1 + \frac{R_7}{R_8} \right) = 282.24 \cdot V_{in} \qquad \text{(A.V.3)}$$

$$V_{0-} = -V_{in} \cdot \left(\frac{R_2 \cdot (R_4 + R_3)}{R_3 \cdot (R_1 + R_2)} \right) \cdot \left(\frac{R_9}{R_6} \right) = -279.52 \cdot V_{in} \qquad \text{(A.V.4)}$$

$$G = \frac{V_{0+} - V_{0-}}{V_{in}} = 561.7 \qquad \text{(A.V.5)}$$

Publications

Articles

1 E. Villa, B. Aja, J. Cagigas, L. de la Fuente and E. Artal, "Design methodology and performance analysis of a wideband 90º phase switch for radiometer applications", *Review of Scientific Instruments*, vol. 84, 124704, Dec. 2013.

2 E. Villa, L. de la Fuente, J. Cagigas, B. Aja and E. Artal, "Broadband Ka-band 90º phase switch for radio astronomy", *Electronics Letters*, vol. 49, no. 5, pp. 349-351, Feb. 2013.

3 B. Aja, M. Seelmann-Eggebert, D. Bruch, A. Leuther, H. Massler, B. Baldischweiler, M. Schlechtweg, J. D. Gallego-Puyol, I. López-Fernández, C. Díez-González, I. Malo-Gómez, E. Villa and E. Artal, "4-12 and 25-34-GHz Cryogenic mHEMT MMIC Low-Noise Amplfiers", *IEEE Trans. Microwave and Tech.*, vol. 60, no. 12, pp. 4080-4088, Dec. 2012.

4 E. Villa, B. Aja, J. L. Cano, L. de la Fuente and E. Artal, "Cryogenic Ka-Band 180º Phase Switch Based on Schottky Diodes", *IEEE Microwave and Wireless Components Letters*, vol. 22, no. 2, pp. 52-54, Feb. 2012.

5 A. Colin, D. Ortiz, E. Villa, E. Artal and E. Martínez-González, "An array of lens-coupled antennas for cosmic microwave background measurements in the 30 GHz band", *Experimental Astronomy*, vol. 33, pp. 27-37, Dec. 2011.

6 A. Colin, D. Ortiz, E. Villa, E. Artal and E. Martínez-González, "A 30-GHz Planar Array Antenna Using Dipole-coupled-lens", *Progress in Electromagnetics Research Letters*, vol. 25, pp. 31-36, Jul. 2011.

7 A. Colin, E. Artal, E. Villa, D. Ortiz and E. Martínez-González, "Bow-tie Slot Antenna for 29 to 45 GHz Band", *Far East Journal of Electronics and Communications*, vol. 4, no. 1, pp. 69-76, Mar. 2010.

8 E. Villa, B. Aja, L. de la Fuente and E. Artal, "Wideband uniplanar 180º phase switch", *Electronics Letters*, vol. 45, no. 11, pp. 556-557, May 2009.

International Conference Papers

1 A. R. Pérez de Taoro et al., "QUIJOTE-CMB Experiment: a Technical Overview", *Proc. SPIE 9145, Ground-based and Airborne Telescopes V, 91454T*, Montreal, Canada, Jul. 2014.

2 R. J. Hoyland et al., "The QUIJOTE TGI", *Proc. SPIE 9153, Millimeter, Submillimeter, and Far-Infrared Detectors and Instrumentation for Astronomy VII, 915332*, Montreal, Canada, Jul. 2014.

3 M. López-Caniego et al., "The QUIJOTE CMB Experiment: status and first results with the multi-frequency instrument", *Conference Proceedings Rencontres du Vietnam 2013: Cosmology in the Planck Era, Instrumentation and Methods for Astrophysics,* Feb. 2014.

4 E. Artal, J. L. Cano, A. Mediavilla, B. Aja, L. de la Fuente and J. Cagigas, "EM Developments for a Radio Astronomy Polarimeter: The QUIJOTE Experiment", *International Conference on Electromagnetics in Advanced Applications,* Torino, Italy, 9-13 Sep. 2013, pp. 250-253.

5 R. Rebolo et al., "QUIJOTE: a CMB polarizatrion experiment", *47th ESLAB: The Universe as seen by PLANCK, Experimental Aspects*, Noordwijk, The Netherlands, 2-5 Apr. 2013.

6 J. L. Cano, E. Villa, J. Cagigas, B. Aja, J. V. Terán, A. R. Pérez, L. de la Fuente, E. Artal, A. Mediavilla and R. Hoyland, "Multi-Pixel Ka-Band Radiometer for

the QUIJOTE Experiment (Phase II)", *42nd European Microwave Conference,* Amsterdam, The Netherlands, 29 Oct.-1 Nov. 2012, pp. 37-40.

7 J. A. Rubiño et al., "The QUIJOTE-CMB Experiment: studying the polarization of the Galactic and Cosmological microwave emissions", *Proc. SPIE 8444, Ground-based and Airborne Telescopes IV, 84442Y,* Amsterdam, The Netherlands, Sep. 2012.

8 R. J. Hoyland et al., "The status of the QUIJOTE I Multi-Frequency Instrument", *Proc. SPIE 8452, Millimeter, Submillimeter, and Far-Infrared Detectors and Instrumentation for Astronomy VI, 845233*, Amsterdam, The Netherlands, Oct. 2012.

9 B. Aja, M. Seelmann-Eggebert, A. Leuther, H. Massler, M. Schlechtweg, J. D. Gallego, I. López-Fernández, C. Díez, I. Malo, E. Villa and E. Artal, "4-12 and 25-34-GHz Cryogenic mHEMT MMIC Low-Noise Amplfiers for Radio Astronomy", *IEEE MTT-S International Microwave Symposium Digest*, Montreal, Canada, 17-22 Jun. 2012, pp. 1-3.

10 J. L. Cano, E. Villa, B. Aja, L. de la Fuente, E. Artal, R. Watson, E. Blackhurst, J. Edgley and C. Baines, "The Ka-Band Receiver for the QUIJOTE Experiment", *41st European Microwave Conference,* Manchester, United Kingdom, 10-13 Oct. 2011, pp. 1181-1184.

11 E. Artal, B. Aja, J. Cagigas, J. L. Cano, L. de la Fuente, A. Pérez and E. Villa, "Low frequency noise measurements in direct detection radiometers", *RadioNET-FP7 Engineering Forum Workshop, Receiver Gain Stability,* Cagliari, Italy, 12-13 May 2011.

12 E. Artal, L. de la Fuente, B. Aja, J. L. Cano, E. Villa, R. Hoyland, J. A. Rubiño-Martín and R. Génova, "Cosmic Microwave Background Polarization Receivers: QUIJOTE Experiment", *40th European Microwave Conference,* Paris, France, 28-30 Sep. 2010, pp. 497-500.

13 E. Artal, L. de la Fuente, B. Aja, J. L. Cano, E. Villa, R. Hoyland, J. A. Rubiño and R. Génova, "Cosmic Microwave Background Polarisation Receivers: QUIJOTE Experiment", *RadioNET-FP7 2nd Engineering Forum Workshop, Multi Pixel Camera Receivers,* Bonn, Germany, 16-17 Nov. 2009.

14 J. L. Cano, B. Aja, E. Villa, L. de la Fuente and E. Artal, "Broadband Back-End Module for Radio-Astronomy Applications in the Ka-Band", *38th European*

Microwave Conference, Amsterdam, The Netherlands, 27-31 Oct. 2008, pp. 1113-1116.

15 E. Villa, B. Aja, L. de la Fuente and E. Artal, "mm-wave device testing using wideban coplanar transitions", *Gigahertz Symposium 2008,* Gothenburg, Sweden, 5-6 Mar. 2008.

16 J. L. Cano, B. Aja, E. Villa, L. de la Fuente and E. Artal, "Back-end demonstrator for radio-astronomy applications", *Gigahertz Symposium 2008,* Gothenburg, Sweden, 5-6 Mar. 2008.

17 A. Casanueva, E. Zubizarreta, O. González, A. Grande and E. Villa, "Analysis and Design of a Miniaturized Low Pass Filter in Suspended Microstrip Substrate", *1st Symposium of the Portuguese Committee of URSI, Radiocommunications – New Paradigms and Health Impact,* Lisbon, Portugal, 28 Nov. 2007.

National Conference Papers

1 E. Villa, B. Aja, J. Cagigas, L. de la Fuente and E. Artal, "Modelado con la temperature de diodo Schottky para conmutador de fase 90º", *XXIX Simposium Nacional de la Unión Científica Internacional de Radio,* Valencia, Spain, 3-5 Sep. 2014.

2 A. R. Pérez, J. L. Cano, E. Villa, A. Mediavilla and E. Artal, "Módulo de Correlación y Detección de Banda Ancha y Banda Q en Guía de Onda", *XXIX Simposium Nacional de la Unión Científica Internacional de Radio,* Valencia, Spain, 3-5 Sep. 2014.

3 E. Artal, B. Aja, L. de la Fuente, J. L. Cano, E. Villa, J. Cagigas, J. V. Terán, E. Martínez-González, F. Casas and D. Ortiz, "Receptores de 30 GHz para el experimento QUIJOTE", *Encuentro RIA-AstroMadrid, Desarrollo de instrumentación astronómica en España,* Madrid, Spain, 25-27 Sep. 2013.

4 E. Villa, L. de la Fuente, B. Aja, J. Cagigas and E. Artal, "Conmutador de fase 90º en tecnología híbrida microstrip", *XXVIII Simposium Nacional de la Unión Científica Internacional de Radio,* Santiago de Compostela, Spain, 11-13 Sep. 2013.

5 D. Ortiz, F. J. Casas, E. Villa, J. L. Cano and E. Artal, "Correladores en Banda Base para un Interférometro de Gran Formato a 30 GHz", *XXVIII Simposium*

Nacional de la Unión Científica Internacional de Radio, Santiago de Compostela, Spain, 11-13 Sep. 2013.

6 E. Villa, B. Aja, L. de la Fuente and E. Artal, "Detector basado en diodo Schottky en la banda de 35 a 47 GHz", *XXVII Simposium Nacional de la Unión Científica Internacional de Radio,* Elche, Spain, 12-14 Sep. 2012.

7 E. Artal, B. Aja, J. Cagigas, J. L. Cano, L. de la Fuente, A. Mediavilla, J. V. Terán, E. Villa, R. Hoyland, F. J. Casas and D. Ortiz, "Receptor de polarización a 31 GHz para radioastronomía", *XXVII Simposium Nacional de la Unión Científica Internacional de Radio,* Elche, Spain, 12-14 Sep. 2012.

8 J. V. Terán, E. Villa, J. L. Cano, L. de la Fuente and E. Artal, "Análisis de los efectos dispersivos en baja frecuencia de transistores HEMT a través de medidas de capacidad y conductancia", *XXVII Simposium Nacional de la Unión Científica Internacional de Radio,* Elche, Spain, 12-14 Sep. 2012.

9 J. Cagigas, E. Villa, E. Artal and R. Hoyland, "Híbrido de 180º de Banda Ancha en Tecnología Microstrip a 41 GHz", *XXVII Simposium Nacional de la Unión Científica Internacional de Radio,* Elche, Spain, 12-14 Sep. 2012.

10 E. Villa, B. Aja, L. de la Fuente and E. Artal, "Dispositivos de Conmutación en Criogenia para Conmutadores de Fase de 180º", *XXVI Simposio de la URSI,* Leganés, Spain, 7-9 Sep. 2011.

11 J. L. Cano, E. Villa, J. Cagigas, L. de la Fuente, B. Aja, E. Artal and A. Mediavilla, "Diseño de un Nuevo Módulo Posterior para el Experimento QUIJOTE (Fase II)", *XXVI Simposio de la URSI,* Leganés, Spain, 7-9 Sep. 2011.

12 E. Artal, B. Aja, L. de la Fuente, J. L. Cano, E. Villa, J. Cagigas, E. Martínez-González, F. Casas and D. Ortiz, "Low noise millimeter wave receivers for Cosmic Microwave Background radiometers", *Encuentro RIA-AstroMadrid, Desarrollo de instrumentación espacial,* Madrid, Spain, 29-30 Jun. 2011.

13 E. Artal, B. Aja, L. de la Fuente, J. L. Cano, E. Villa, J. Cagigas, E. Martínez, F. J. Casas and D. Ortiz, "Broadband Components for the Millimeter-Wave Radiometers: The QUIJOTE Experiment", *Encuentro RIA-AstroMadrid, Desarrollo de instrumentación espacial,* Madrid, Spain, 29-30 Jun. 2011.

14 E. Artal, B. Aja, L. de la Fuente, J. L. Cano, E. Villa, J. Cagigas, E. Martínez, F. J. Casas and D. Ortiz, "IFCA/DICOM Technical Developments with Application to Space Scientific Missions", *Encuentro RIA-AstroMadrid, Desarrollo de instrumentación espacial,* Madrid, Spain, 29-30 Jun. 2011.

15 E. Artal, B. Aja, L. de la Fuente, E. Villa and E. Martínez, "Radiometers at 30 GHz and 44 GHz for the PLANCK mission", *Encuentro RIA-AstroMadrid, Desarrollo de instrumentación espacial,* Madrid, Spain, 29-30 Jun. 2011.

16 E. Villa, J. Cagigas and E. Artal, "Híbrido 180º de banda ancha en tecnología uniplanar para ondas milimétricas", *XXV Simposium Nacional Unión Científica Internacional de Radio,* Bilbao, Spain, 15-17 Sep. 2010.

17 B. Aja, E. Villa, L. de la Fuente and E. Artal, "Detector cuadrático con diodo Schottky de 26 a 36 GHz", *XXV Simposium Nacional Unión Científica Internacional de Radio,* Bilbao, Spain, 15-17 Sep. 2010.

18 J. Cagigas, E. Villa, E. Artal and R. J. Hoyland, "Híbrido 180º de Banda Ancha en Tecnología microstrip a 31 GHz", *XXV Simposium Nacional Unión Científica Internacional de Radio,* Bilbao, Spain, 15-17 Sep. 2010.

19 E. Villa, B. Aja, L. de la Fuente and E. Artal, "Conmutador de fase 180º en banda milimétrica basado en diodo PIN", *XXIV Simposium Nacional de la Unión Científica Internacional de Radio,* Santander, Spain, 16-18 Sep. 2009.

20 J. L. Cano, E. Villa, D. Ortiz and E. Artal, "Transición en guía WR-28 de acceso al criostato para la medida de sistemas enfriados", *XXIV Simposium Nacional de la Unión Científica Internacional de Radio,* Santander, Spain, 16-18 Sep. 2009.

21 D. Ortiz, E. Villa, J. L. Cano, L. de la Fuente and E. Artal, "Medidas de componentes pasivos en criogenia", *XXIV Simposium Nacional de la Unión Científica Internacional de Radio,* Santander, Spain, 16-18 Sep. 2009.

22 E. Villa, B. Aja, L. de la Fuente and E. Artal, "Conmutadores de fase 180º de banda ancha con transiciones coplanares", *XXIII Simposium Nacional de la Unión Científica Internacional de Radio,* Madrid, Spain, 22-24 Sep. 2008.

23 E. Villa, B. Aja, L. de la Fuente and E. Artal, "Método de medida de dispositivos para banda milimétrica usando transiciones coplanares de banda ancha", *XXIII Simposium Nacional de la Unión Científica Internacional de Radio,* Madrid, Spain, 22-24 Sep. 2008.

24 J. L. Cano, B. Aja, E. Villa, L. de la Fuente and E. Artal, "Módulo posterior de un receptor en banda Ka para aplicaciones de radioastronomía", *XXIII Simposium Nacional de la Unión Científica Internacional de Radio,* Madrid, Spain, 22-24 Sep. 2008.

25 J. A. Rubiño-Martín et al., "The QUIJOTE CMB Experiment", *VIII Reunión Científica de la Sociedad Española de Astronomía,* Santander, Spain, 7-11 Jul. 2008.

26 J. L. Cano, B. Aja, E. Artal, L. de la Fuente, J. P. Pascual and E. Villa, "Amplificador de bajo ruido MMIC en la banda Ka a temperatura criogénica", *XXII Simposium Nacional de la Unión Científica Internacional de Radio,* Madrid, Spain, 19-21 Sep. 2007.

Chapters in Books

1 J.A. Rubiño-Martin et al., "The QUIJOTE CMB Experiment", *Highlights of Spanish Astrophysics V, Astrophysics and Space Science Proceedings*, Part 3, Ed. Springer, 2010, pp. 127-135.

References

Chapter I

[1.1] D. Christian, *Maps of Time: An Introduction to Big History*, University of California Press, LA, USA, 2004.

[1.2] http://www.astromia.com/astronomia/teoriabigbang.htm.

[1.3] http://en.wikipedia.org/wiki/Chronology_of_the_universe.

[1.4] http://en.wikipedia.org/wiki/Cosmic_microwave_background.

[1.5] E. L. Wright, "Theoretical Overview of Cosmic Microwave Background Anisotropy", in *Carnegie Observatories Astrophysics Series, Vol. 2: Measuring and Modeling the Universe*, Ed. W. L. Freeman (Cambridge Univ. Press), pp. 291, May 2003.

[1.6] R. A. Alpher, H. Bethe and G. Gamow, "The Origin of Chemical Elements", *Physical Review*, vol. 73, no. 7, pp. 803-804, Apr. 1948.

[1.7] A. A. Pentizias and R. W. Wilson, "A Measurement of Excess Antenna Temperature at 4080 Mc/s", *Astrophysical Journal*, vol. 142, pp. 419-421, 1965.

[1.8] P. L. Richards, "Cosmic Microwave Background Experiments – Past, Present and Future", in *32nd International Conference on Infrared and Millimeter*

Waves and 15th International Conference on Terahertz Electronics, Cardiff, Wales, Sep. 2007, pp. 12-15.

[1.9] B. Aja, E. Artal, L. de la Fuente, J. P. Pascual, A. Mediavilla, N. Roddis, D. Kettle, W. F. Winder, L. Pradell and P. de Paco, "Very Low-Noise Differential Radiometer at 30 GHz for the PLANCK LFI", *IEEE Trans. Microwave and Tech.*, vol. 53, no. 6, pp. 2050-2062, Jun. 2005.

[1.10] P. Kangaslahti, T. Gaier, M. Seiffert, S. Weinreb, D. Harding, D. Dawson, M. Soria, C. Lawrence, B. Hooberman and A. Miller, "Planar Polarimetry Receivers for Large Imaging Arrays at Q-band", in *IEEE MMT-S Int. Microwave Symp. Dig.*, San Francisco, CA, Jun. 2006, pp. 89-92.

[1.11] D. Kettle and N. Roddis, "A Ten-Beam Ka-Band Radiometric Receiver Using Custom Designed InP MMICs at Cryogenic Temperatures", *IEEE Trans. Microwave and Tech.*, vol. 55, no. 12, pp. 2700-2708, Dec. 2007.

[1.12] http://map.gsfc.nasa.gov/.

[1.13] http://sci.esa.int/planck/.

Chapter II

[2.1] S. A. Wartenberg, *RF Measurements of Die and Packages*, Artech House, Inc., Norwood, 2002.

[2.2] "Specifying Calibration Standards for the Agilent 8510 Network Analyzer", Product Note 8510-5B, Agilent Technologies, Inc., 2001.

[2.3] "Applying Error Correction to Network Analyzer Measurements", Application Note 1287-3, Agilent Technologies, Inc., 2002.

[2.4] G. F. Engen and C. A. Hoer, "Thru-Reflect-Line: An Improved Technique for Calibrating the Dual Six-Port Automatic Network Analyzer", *IEEE Trans. Microwave and Tech.*, vol. MMT-27, no. 12, pp. 987-993, Dec. 1979.

[2.5] R. B. Marks, "A Multiline Method of Network Analyzer Calibration", *IEEE Trans. Microwave and Tech.*, vol. 39, no. 7, pp. 1205-1215, Jul. 1991.

[2.6] A. Davidson, E. W. Strid and K. E. Jones, "Achieving Greater On-Wafer S-Parameter Accuracy with the LRM Calibration Technique", Cascade Microtech Application, Cascade Microtech, Inc., 1995.

[2.7] Cascade Microtech Analytical Probe Station Summit 9000 Instruction Manual, Cascade Microtech, Inc.

[2.8] "Network Analysis Applying the 8510 TRL Calibration for Non-Coaxial Measurements", Agilent PN 8510-8A, Agilent Technologies, 2001.

[2.9] Alumina substrate data sheet. Reinhardt Microtech. Available http://www.cicor.com/fileadmin/cicorcom/downloads/TechSpecVer12.pdf

[2.10] G. Gauthier, L. P. Katehi, and G. M. Rebeiz, "W-band Finite Ground Coplanar Waveguide (CPWPW) to Microstrip Line Transition", in *IEEE MMT-S Int. Microwave Symp. Dig.*, vol. 1, Baltimore, MD, Jun. 1998, pp. 107-109.

[2.11] G. Zheng, J. Papapolymerou, and M. M. Tentzeris, "Wideband Coplanar Waveguide RF Probe Pad to Microstrip Transitions Without Via Holes", *IEEE Microwave and Wireless Components Letters*, vol. 13, no. 12, pp. 544-546, Dec. 2003.

[2.12] D. F. Williams and T. H. Miers, "A Coplanar Probe to Microstrip Transition", *IEEE Trans. Microwave and Tech.*, vol. 36, no. 7, pp. 1219-1223, Jul. 1988.

[2.13] L. Zhu, K. L. Melde, and J. L. Prince, "A broadband CPW-to-microstrip Via-less Transition for on Wafer Package Probing Applications", in *Electrical Performance of Electronic Packaging*, Princeton, NJ, Oct. 2003, pp. 75-78.

[2.14] K. Schmidt von Behren, D. Pienkowski, and G. Boeck, "77 GHz Si-Schottky Diode Harmonic Mixer", in *32nd European Microwave Conference*, Milan, Italy, Sep. 2002, pp. 1-4.

[2.15] A. M. E. Safwat, K. A. Zaki, W. Johnson, and C. H. Lee, "Novel Design for Coplanar Waveguide to Microstrip Transition", in *IEEE MMT-S Int. Microwave Symp. Dig.*, vol. 2, Phoenix, AZ, May 2001, pp. 607-610.

[2.16] Probepoint adapter substrate data sheet. Jmicro Technology. Available http://www.jmicrotechnology.com/PP10.pdf

[2.17] HSCH-9161 Zero Bias Beamlead Detector Diode data sheet. Avago Technologies. Available http://www.avagotech.com/pages/en/rf_microwave/diodes/schottky/hsch-9161/

[2.18] S. N. Demurie and D. de Mey, "Parasitic Capacitance Effects of Planar Resistors", *IEEE Trans. On Components, Hybrids, and Manufacturing Tech.*, vol. 12, no. 3, pp. 348-351, Sep. 1989.

[2.19] Z. Wang, M. J. Deen and A. H. Rahal, "Accurate Modelling of Thin-Film Resistor up to 40 GHz", in *Proceeding of the 32nd European Solid-State Device Research Conference*, Firenze, Italy, Sep. 2002, pp. 307-310.

[2.20] E. Artal, B. Aja, R. García, M. Detratti, and L. A. Rodríguez, "Measurement of Active and Passive Millimetre Wave Devices using Microstrip to Coplanar Line Transitions". Available http://www.jmicrotechnology.com/info.html

[2.21] R. Finger and A. R. Kerr, "Microwave loss reduction in cryogenically cooled conductors", *International of Infrared and Millimeter Waves*, vol. 29, no. 10, pp. 924-932, Oct. 2008.

[2.22] S. W. Van Sciver, *Helium Cryogenics: Low-Temperature Material Properties*, 2nd Edition, Springer, 2002.

[2.23] R. G. Geyer and J. Krupka, "Dielectric properties of materials at cryogenic temperatures and microwave frequencies", in *Conference of Precision Electromagnetic Measurements,* NIST, Boulder, CO, Jun. 1994, pp. 350-351.

[2.24] N. J. Simon, "Cryogenic Properties of Inorganic Insulation Materials for ITER Magnets; A Review", NIST, Boulder, CO, Tech. Rep. 5030, Dec. 1994.

[2.25] J. M. Miranda, J. L. Sebastián, M. Sierra, J. Margineda, *Ingeniería de Microondas: Técnicas Experimentales*, Prentice Hall, 2002.

[2.26] CLTE-XT substrate data sheet. Arlon Materials for Electronics (MED). Available http://www.arlon-med.com/CLTE-Series-:-Advanced-Temperature-Dieletric/

[2.27] K. C. Gupta, R. Garg, I. Bahl, P. Barthia, *Microstrip Lines and Slotlines*, 2nd Edition, Artech House, Inc., 1996.

[2.28] T. C. Edwards, M. B. Steer, *Foundations of Interconnections and Microstrip Design*, 3rd Edition, Wiley, 2000.

[2.29] G. Kompa, *Practical Microstrip Design and Applications*, Artech House, 2005.

[2.30] SMA connector data sheet. Radiall. Available http://www.radiall.com/sma-universal-2-holes-flange-jack-receptacle.html

[2.31] Insulator data sheet. Radiall. Available http://www.radiall.com/accessory-sma-n-removable-insulator-1.html

[2.32] Contact data sheet. Radiall. Available http://www.radiall.com/accessory-sma-n-removable-male-center-contact-3.html

[2.33] I. J. Bahl and D. K. Trivedi, "A Designer's Guide to Microstrip Line", *Microwaves*, pp. 174-182, May 1977.

[2.34] K. D. Timmerhaus, T. M. Flynn, *Cryogenic Process Engineering*, International Cryogenics Monograph Series, Springer, 1989.

[2.35] T. M. Flynn, *Cryogenic Engineering*, 2nd Edition, Revised and Expanded, Marcel Dekker, 2005.

Chapter III

[3.1] MA4E2037 GaAs Beamlead Schottky Barrier Diodes data sheet. M/A-COM Technology Solutions. Available https://www.macomtech.com/schottky-mixer-and-detector-diodes

[3.2] HSCH-9161/HSCH-9162 GaAs Detector Diode data sheet. Agilent Technologies. Available http://www.home.agilent.com/en/pd-1066301-pn-HSCH-9161/millimeter-wave-zero-bias-gaas-schottky-diode?&cc=ES&lc=eng

[3.3] HPND-4005 Beam Lead PIN Diode data sheet. Avago Technologies. Available http://www.avagotech.com/pages/en/rf_microwave/diodes/pin/hpnd-4005/

[3.4] S. M. Sze, *Semiconductor Devices: Physics and Technology*, Wiley, 1985.

[3.5] E. H. Roderick, *Metal-Semiconductor Contacts*, Oxford, 1978.

[3.6] I. A. Glover, S. R. Pennock and P. R. Shepherd, *Microwave Devices, Circuits and Subsystems for Communications Engineering*, Wiley, 2005.

[3.7] "The PIN Diode Circuit Designers' Handbook", Microsemi Corp.-Watertown, 1998.

[3.8] "PIN Diode Basics", Application Note, Skyworks Solutions, Inc., 2008.

[3.9] D. M. Kim, D. H. Kim and S. Y. Lee, "Characterization and Modeling of temperature-dependent Barrier Heights and Ideality Factors in GaAs Schottky Diodes", *Solid-State Electronics*, vol. 51, no. 6, pp. 865-869, Jun. 2007.

[3.10] M. Missous, E. H. Rhoderick, D. A. Woolf and S. P. Wilkes, "On the Richardson Constant of Intimate metal-GaAs Schottky Barriers", *Semiconductor Science and Technology*, vol. 7, no. 2, pp. 218-221, Feb. 1992.

[3.11] H. Norde, "A Modified Forward IV Plot for Schottky Diodes with High Series Resistance", *Journal of Applied Physics*, vol. 50, no. 7, pp. 5052-5053, Jul. 1979.

[3.12] T. Göksu, N. Yildirim, H. Korkut, A. F. Özdemir, A. Turut and A. Kökçe, "Barrier Height Temperature Coefficient in Ideal Ti/n-GaAs Schottky Contacts", *Microelectronic Engineering*, vol. 87, no. 9, pp. 1781-1784, Nov. 2010.

[3.13] N. Brutscher and M. Hoheisel, "Schottky Diodes with high Series Resistance: A Simple Method of Determining the Barrier Heights", *Solid-State Electronics*, vol. 31, no. 1, pp. 87-89, Jan. 1988.

[3.14] A. Y. Tang, V. Drakinskiy, K. Yhland, J. Stenarson, T. Bryllert and J. Stake, "Analytical Extraction of a Schottky Diode Model From Broadband S-Parameters", *IEEE Trans. Microwave and Tech.*, vol. 61, no. 5, pp. 1870-1878, May 2013.

[3.15] T. Kiuru, J. Mallat, A. V. Räisänen and T. Närhi, "Schottky Diode Series Resistance and Thermal Resistance Extraction From Broadband S-Parameters and Temperature Controlled I-V Measurements", *IEEE Trans. Microwave and Tech.*, vol. 59, no. 8, pp. 2108-2116, Aug. 2011.

[3.16] L. F. Wagner, R. W. Young and A. Sugerman, "A Note on the Correlation Between the Schottky-Diode Barrier Height and the Ideality Factor as Determined from I-V Measurements", *IEEE Electron Device Letters*, vol. EDL-4, no. 9, pp. 320-322, Sep. 1983.

[3.17] J. Grajal, V. Krozer, E. González, F. Maldonado and J. Gismero, "Modeling and Design Aspects of Millimeter-Wave and Submillimeter-Wave Schottky Diode Varactor Frequency Multipliers", *IEEE Trans. Microwave and Tech.*, vol. 48, no. 4, pp. 700-711, Apr. 2000.

[3.18] M. Ravinandan, P. K. Rao and V. R. Reddy, "Temperature Dependence of Current-Voltage (I-V) Characteristics of Pt/Au Schottky Contacts on n-type GaN", *Journal of Optoelectronics and Advanced Materials*, vol. 10, no. 10, pp. 2787-2792, Oct. 2008.

[3.19] V. L. Borblik, Y. M. Shwarts and M. M. Shwarts, "A New Method of Extraction of a p-n Diode Series Resistance from I-V Characteristics and Its Application to Analysis of Low-Temperature Conduction of the Diode Base", *Semiconductor Physics, Quantum Electronics and Optoelectronics*, vol. 12, no. 4, pp. 339-342, Oct. 2009.

[3.20] R. R. Romanofski, "On the Relationship Between Schottky Barrier Capacitance and Mixer Performance at Cryogenic Temperatures", *IEEE Microwave and Guided Wave Letters*, vol. 6, no. 8, pp. 286-288, Aug. 1996.

[3.21] H. J. Lee, W. A. Anderson, H, Hardtdegen and H. Lüth, "Barrier Height Enhancement of Schottky Diodes on n-$In_{0.53}Ga_{0.47}As$ by Cryogenic Proccesing", *Applied Physics Letters*, vol. 63, no. 14, pp. 1939-1941, Oct. 1993.

[3.22] P. H. Siegel, I. Mehdi and J. East, "Improved Millimeter-Wave Mixer Performance Analysis at Cryogenic Temperatures", *IEEE Microwave and Guided Wave Letters*, vol. 1, no. 6, pp. 129-131, Jun. 1991.

[3.23] A. Jelenski, A. Grüb, V. Krozer and H. L. Hartnagel, "New Approach to the Design and the Fabrication of THz Schottky Barrier Diodes", *IEEE Trans. Microwave and Tech.*, vol. 41, no. 4, pp. 549-557, Apr. 1993.

[3.24] "The Zero Bias Schottky Diode Detector at Temperature Extremes – Problems and Solutions", Application Note AN 1090, Avago Technologies, 2010.

[3.25] D. R. Vizard, "Cryogenic Characteristic of Millimetre Wavelength Schottky Barrier Diodes", in *7th European Microwave Conference*, Copenhagen, Denmark, Sep. 1977, pp. 556-560.

[3.26] P. Antognetti and G. Massobrio, *Semiconductor device modeling with SPICE*, 2nd Edition, McGraw-Hill, 1993.

[3.27] R. Palomera-Arias, "PIN Diode Switch Circuit for Short Time High Current Pulse Signal", M. Sc. Dissertation, Massachusetts Institute of Technology, United States of America, 1998.

[3.28] "HMPP-3865 MiniPAK PIN Diode High Isolation SPDT Switch Design for 1.9 GHz and 2.45 GHz Applications", Application Note 1330, Avago Technologies, Inc., 2006.

[3.29] R. H. Caverly, "Microwave and RF p-i-n Diode Model for Time-Domain Simulation", *IEEE Transactions on Microwave Theory and Techniques*, vol. 60, no. 7, pp. 2158-2164, Jul. 2012.

[3.30] R. H. Caverly, "Modeling PIN Diodes for High Power RF and Microwave Applications", in *IEEE MTT-S International Microwave Symposium Digest*, Boston, MA, USA, Jun. 2009, pp. 897-900.

[3.31] D. Marcondes, W. A. Artuzi and M. J. C. Bonfim, "A PIN Diode Model for Finite Element Time Domain Simulations", *Journal of Microwaves, Optoelectronics and Electromagnetic Applications*, vol. 8, no. 1, pp. 38-48, Jun. 2009.

[3.32] A. G. M. Strollo and E. Napoli, "Improved PIN Diode Circuit Model with Automatic Parameter Extraction Technique", *IEE Proceedings-Circuits, Devices and Systems*, vol. 144, no. 6, pp. 329-334, Dec. 1997.

[3.33] K. K. Tantwai, "Microwave-frequency non-linear universal model for PIN diode", in *International Workshop on Physics of Semiconductor Devices*, Mumbai, India, Dec. 2007, pp. 119-122.

[3.34] P. M. Igic, P. A. Mawby, M. S. Towers and S. Batcup, "New physically-based PiN diode compact model for circuit modelling applications", *IEE Proceedings-Circuits, Devices and Systems*, vol. 149, no. 4, pp. 257-263, Aug. 2002.

[3.35] V. L. Borblik, Y. M. Shwarts, M. M. Shwarts and A. M. Fonkich, "Concerning the nature of relaxation oscillations in silicon diodes in the cryogenic temperature region", *Cryogenics*, vol. 50, no. 6-7, pp. 417-420, Jun.-Jul. 2010.

[3.36] D. J. Massey, J. P. R. David and G. J. Rees, "Temperature Dependence of Impact Ionization in Submicrometer Silicon Devices", *IEEE Transactions on Electron Devices*, vol. 53, no. 9, pp. 2328-2334, Sep. 2006.

[3.37] C. P. Baylis II and L. P. Dunleavy, "Understanding Pulsed IV Measurement Waveforms", in *The 11th IEEE International Symposium on Electron Devices for Microwave and Optoelectronic Applications*, Florida, USA, Nov. 2003, pp. 223-228.

[3.38] R. Singh and B. J. Baliga, "Cryogenic Operation of P-i-N Power Rectifiers", *Solid State Electronics*, vol. 37, no. 11, pp. 1833-1839, Nov. 1994.

Chapter IV

[4.1] V. E. Dunn, N. E. Hodges, O. A. Sy, W. Alyassini, M. Feng and Y. C. Chang, "MMIC Phase Shifters and Amplifiers for Millimeter-Wavelength Active Arrays", in *IEEE MTT-S Int. Microw. Symp. Dig.,* Long Beach, CA, USA, Jun. 1989, pp. 127-130.

[4.2] M. E. Goldfarb, "A Novel Design for a MMIC 180 Degree Phase Shifter", in *IEEE MTT-S Int. Microw. Symp. Dig.,* Albuquerque, NM, USA, Jun. 1992, pp. 175-177.

[4.3] A. E. Ashtiani, S. Nam, S. Lucyszyn, and I. D. Robertson, "MMIC Phase Shifters and Amplifiers for Millimeter-Wavelength Active Arrays", in *IEE Colloquium on Microwave and Millimetre-Wave Oscillators and Mixers (Ref. No. 1998/480),* Dec. 1998, pp. 7/1-7/6.

[4.4] R. J. Hoyland, "A new MMIC, Wideband 180º Phase Switch Design for Millimeter Wave Applications", in *Proceedings 3rd ESA Workshop on Millimetre Wave Technology and Applications*, Espoo, Finland, May 2003, pp. 305-310.

[4.5] D. Kettle, N. Roddis and R. Sloan, "A Ka-Band InP MMIC 180º Phase Switch", *IEEE Microw. Wireless Compon. Lett.,* vol. 15, no. 6, pp. 425-427, Jun. 2005.

[4.6] M. A. Llamas, D. Girbau, M. Ribó, L. Pradell, A. Lázaro, F. Giacomozzi and B. Margesin, "MEMS-Based 180º Phase Switch for Differential Radiometers", *IEEE Trans. Microw. Theory Tech.,* vol. 58, no. 5, pp. 1264-1272, May 2010.

[4.7] K. Tang, Y. M. Wu, Q. Wu, H. L. Wang, H. C. Zhu, and L. W. Li, "A Novel Dual-Frequency RF MEMS Phase Shifter", in *Asia-Pacific Symposium on Electromagnetic Compatibility and 19th International Zurich Symposium on Electromagnetic Compatibility,* Singapore, May 2008, pp. 750-753.

[4.8] P. Wu, Y. Zhang, Y. L. Dong and Q. Zhang, "A Novel Ka-Band Planar Balun using Microstrip-CPS-Microstrip Transition", *IEEE Microw. Wireless Compon. Lett.,* vol. 21, no. 3, pp. 136-138, Mar. 2011.

[4.9] A. Stark and A. F. Jacob, "Complex Loads for Millimetre-wave Digital Phase Shifter Design", in *Proceedings of the 6th European Microwave Integrated Circuits Conference*, Manchester, UK, Oct. 2011, pp. 462-465.

[4.10] Y. Cheng, W. Hong and K. Wu, "Novel Substrate Integrated Waveguide Fixed Phase Shifter for 180-degree Directional Coupler", in *IEEE MTT-S Int. Microw. Symp.,* Honolulu, HI, USA, Jun. 2007, pp. 189-192.

[4.11] Y. Ding and K. Wu, "Varactor-Tuned Substrate Integrated Waveguide Phase Shifter", in *IEEE MTT-S Int. Microw. Symp. Dig.,* Baltimore, MA, USA, Jun. 2011, pp. 1-4.

[4.12] I. Wolff, *Coplanar Microwave Integrated Circuits*, Wiley, 2006.

[4.13] K. C. Gupta, R. Garg, I. Bahl and P. Barthia, *Microstrip Lines and Slotlines*, 2nd Ed., Artech House, Inc., 1996.

[4.14] T. Q. Ho, and S. M. Hart, "A Broad-band Coplanar Waveguide to Slotline Transition", *IEEE Microwave Guided Wave Lett.,* vol. 2, no. 10, pp. 415-416, Oct. 1992.

[4.15] R. N. Simons, S. R. Taub, and P. G. Young, "Novel Coplanar to Slotline Transition on High Resistivity Silicon", *Electron. Lett.,* vol. 28, no. 24, pp. 2209-2210, Nov. 1992.

[4.16] K. P. Ma, Y. Qian, and T. Itoh, "Novel Coplanar to Slotline Transition on High Resistivity Silicon", *IEEE Trans. Microw. Theory Tech.,* vol. 47, no. 4, pp. 426-432, Apr. 1999.

[4.17] T. G. Lim, H. N. Ang, I. D. Robertson, and B. L. Weiss, "Ka-band CPW-to-slotline Transition in Photoimageable Thick Film Technology for Tapered Slot Antenna Applications", *Microwave Optical Technol. Lett.,* vol. 48, no. 10, pp. 2032-2034, Oct. 2006.

[4.18] K. Hettak, J. Ph. Coupez, T. Le Gouguec, S. Toutain, P. Legaud, and E. Penard, "Improved CPW to Slotline Transitions", in *IEEE MTT-S Int. Microw. Symp. Dig.,* vol. 3, pp. 1831-1834, Jun. 1996.

[4.19] K. Hettak, N. Dib, A. Sheta, A. A. Omar, G. Y. Delisle, M. Stubbs, and S. Toutain, "New Miniature Broad-Band CPW-to-Slotline Transitions", *IEEE Trans. Microw. Theory Tech.,* vol. 48, no. 1, pp. 138-146, Jan. 2000.

[4.20] C. H. Ho, L. Fan, and K. Chang, "Experimental Investigations of CPW-Slotline Transitions for Uniplanar Microwave Integrated Circuits", in *IEEE MTT-S Int. Microw. Symp. Dig.,* vol. 2, pp. 877-880, Jun. 1993.

[4.21] C. H. Ho, L. Fan, and K. Chang, "Transmission Line Modeling of CPW-Slotline Transitions and CPW Butterfly Filters", in *IEEE MTT-S Int. Microw. Symp. Dig.,* vol. 2, pp. 1305-1308, May 1994.

[4.22] Y. C. Zang, and B. Z. Wang, "Advances in Developing Transitions in Microwave Integrated Circuits", *Journal of Electronic Science and Technology of China,* vol. 3, no. 1, pp. 40-44, Mar. 2005.

[4.23] W. Grammer, and K. S. Yngvesson, "Coplanar Waveguide Transitions to Slotline: Design and Microprobe Characterization", *IEEE Trans. Microw. Theory Tech.,* vol. 41, no. 9, pp. 1653-1658, Sep. 1993.

[4.24] L. Fan, and K. Chang, "Slotline Components", chapter in *Wiley Encyclopaedia of Electrical and Electronics Engineering,* vol. 19, pp. 339-358, John Wiley and Sons Inc., 1999.

[4.25] M. K. Oldenburg, and T. M. Weller, "High Efficiency CPW-to-slotline Transitions on low ε_r Substrates", *Microwave Optical Technol. Lett.,* vol. 41, no. 2, pp. 91-93, Apr. 2004.

[4.26] T. H. Lin, and R. B. Wu, "CPW to Waveguide Transition with Tapered Slotline Probe", *IEEE Microw. Wireless Compon. Lett.,* vol. 11, no. 7, pp. 314-316, Jul. 2001.

[4.27] Y. S. Lin, and C. H. Chen, "Novel Lumped-Element Coplanar Waveguide-to-Slotline Transitions", in *IEEE MTT-S Int. Microw. Symp. Dig.,* vol. 4, pp. 1427-1430, Jun. 1999.

[4.28] M. H. Mao, R. B. Wu, C. H. Chen and C. H. Lin, "Characterization of Coplanar Waveguide Open End Capacitance – Theory and Experiment", *IEEE Trans. Microw. Theory Tech.,* vol. 44, no. 6, pp. 1016-1024, Jun. 1994.

[4.29] J. B. Knorr and J. Saenz, "End Effect in a Shorted Slot", *IEEE Trans. Microw. Theory Tech.,* vol. 21, no. 9, pp. 579-580, Sep. 1973.

[4.30] Foam-Clad 100 substrate data sheet. Arlon Materials for Electronics (MED). Available http://www.arlon-med.com/

[4.31] 2.4-mm connector model 1414-01SF data sheet. Southwest Microwave, Inc. Available http://mpd.southwestmicrowave.com/products/product.php?need=connectors&item=185

[4.32] 50 Ω hermetic seal model 290-07G data sheet. Southwest Microwave, Inc. Available http://mpd.southwestmicrowave.com/products/product.php?need=launchAccess&item=5

[4.33] Sliding Contacts for Microstrip K110-1 data sheet. Anritsu Ltd. Available http://www.anritsu.com/en-US/Products-Solutions/Products/K110-1-R.aspx

Chapter V

[5.1] B. M. Schiffman, "A new class of broad-band microwave 90-Degree phase shifters", *IRE Trans. Microw. Theory Tech.*, vol. 6, no 2, pp. 232-237, Apr. 1958.

[5.2] S. Zheng, W. Chan, and K. Man, "Broadband phase shifter using loaded transmission line", *IEEE Microw. Wireless Compon. Lett.,* vol. 20, no. 9, pp. 498-500, Sep. 2010.

[5.3] X. Tang and K. Mouthan, "Dual-band class III loaded-line phase shifters", in *Proc. Asia-Pacific Microw. Conf.,* Dec. 7-10, 2010, pp. 1731-1734.

[5.4] M. Sorn, R. Lech, and J. Mazur, "Simulation and experiment of a compact wideband 90º differential phase shifter", *IEEE Trans. Microw. Theory Tech.,* vol. 60, no. 3, pp. 494-501, Mar. 2012.

[5.5] Y. Wang, M. E. Bialkowski, and A. M. Abbosh, "Double microstrip-slot transitions for broadband ±90º microstrip phase shifters", *IEEE Microw. Wireless Compon. Lett.,* vol. 22, no. 2, pp. 58-60, Feb. 2012.

[5.6] A. Abbosh, "Broadband fixed phase shifters", *IEEE Microw. Wireless Compon. Lett.,* vol. 21, no. 1, pp. 22-24, Jan. 2011.

[5.7] Y. X. Guo, Z. Y. Zhang, and L. C. Ong, "Improved wide-band Schiffman phase shifter", *IEEE Trans. Microw. Theory Tech.,* vol. 54, no. 3, pp. 1196-1200, Mar. 2006.

[5.8] P. Sobis, J. Stake, and A. Emrich, "High/low-impedance transmission-line and coupled-line filter networks for differential phase shifters", *IET Microw., Antennas Propag.,* vol. 5, no. 4, pp. 386-392, Mar. 2011.

[5.9] S. Y. Eom, "Broadband 180º bit phase shifter using λ/2 coupled line and parallel λ/8 stubs", *IEEE Microw. Wireless Compon. Lett.,* vol. 14, no. 5, pp. 228-230, May 2004.

[5.10] X. Tang and K. Mouthan, "Phase-shifter design using phase-slope alignment with grounded shunt lambda/4 stubs", *IEEE Trans. Microw. Theory Tech.,* vol. 58, no. 6, pp. 1573-1583, Jun. 2010.

[5.11] X. Tang and K. Mouthan, "Design considerations for octave-band phase shifters using discrete components", *IEEE Trans. Microw. Theory Tech.,* vol. 58, no. 12, pp. 3459-3466, Dec. 2010.

[5.12] X. Tang and K. Mouthan, "180º and 90º phase shifting networks with an octave bandwidth and small phase errors", *IEEE Microw. Wireless Compon. Lett.,* vol. 19, no. 8, pp. 506-508, Aug. 2009.

[5.13] S. Y. Eom, and H. K. Park, "New switched-network phase shifter with broadband characteristics", *Microwave Optical Technol. Lett.,* vol. 38, no. 4, pp. 255-257, Aug. 2003.

[5.14] G. J. Sung, "Broadband 90º phase shifter using two short stubs", in *IEEE Radio and Wireless Symposium,* New Orleans, LA, 2010, pp. 464-467.

[5.15] S. H. Yeung, Q. Xue, and K. F. Man, "Broadband 90º phase shifter constructed using a pair of multisection radial line stubs", *IEEE Trans. Microw. Theory Tech.,* vol. 60, no. 9, pp. 3459-3466, Sep. 2012.

[5.16] H. R. Fang, X. Tang, K. Mouthaan, and R. Guinvarc'h, "180º and 90º Reflection-type phase shifters using over-coupled Lange couplers", *IEEE Trans. Microw. Theory Tech.,* vol. 60, no. 11, pp. 3440-3448, Nov. 2012.

[5.17] X. Tang and K. Mouthaan, "Large Bandwidth Digital Phase Shifters With All-Pass, High-Pass, and Low-Pass Networks", *IEEE Trans. Microw. Theory Tech.,* vol. 61, no. 6, pp. 2325-2331, Jun. 2013.

[5.18] M. Sieth et al., "Development of MMIC receivers for cosmic microwave background interferometry", in *Proc. SPIE 7741, 77412I,* Jun. 29, 2010.

[5.19] D. M. Pozar, *Microwave Engineering*, 3rd Ed., Wiley, 2005.

[5.20] HMC975 PIN MMIC High Isolation SPDT Switch data sheet. Hittite Microwave Corporation. Available http://www.hittite.com/products/view.html/view/HMC975

[5.21] AMMC-2008 DC-50 GHz SPDT Switch data sheet. Avago Technologies. Available http://www.avagotech.com/pages/en/rf_microwave/diodes/schottky/hsch-9161/

Chapter VI

[6.1] I. Bahl and P. Barthia, *Microwave Solid State Circuit Design*, 2nd Edition, Wiley-Interscience, 2003.

[6.2] P. de Paco Sánchez, *La Misión Planck. Diseño de Detectores de Banda Ancha y Alta Sensibilidad en Banda Milimétrica*, Ph. D. dissertation, Universidad Politécnica de Cataluña, Spain, May 2003.

[6.3] M. Thompson, "Transmission Lines", Physics 623, Department of Physics, University of Wisconsin-Madison, 1999. Available http://www.physics.wisc.edu/undergrads/courses/fall2011/623/sn/1-Transmission_Line_notes.pdf

[6.4] B. C. Wadell, *Transmission Line Design Handbook*, Artech House, 1991.

[6.5] "Is bias current necessary?", Application Note 987, Hewlett-Packard Co, 1982.

[6.6] "The Zero Bias Schottky Diode Detector at Temperature Extremes - Problems and Solutions", Application Note 1090, Agilent Technologies, Inc., 1999.

[6.7] "All Schottky Diodes are Zero Bias Detectors", Application Note 988, Hewlett-Packard Co, 1982.

[6.8] B. Siegal and E. Pendelton, "Zero Bias Schottky Barrier Diodes as Microwave Detectors", *Microwave Journal,* vol. 18, pp. 40-43, Sep. 1975.

[6.9] "The Zero Bias Schottky Detector Diode", Application Note 969, Avago Technologies, 1999.

[6.10] R. Levy, "Explicit Formulas for Chebyshev Impedance-Matching Networks, Filters and Interstages", in *Proc. IEE,* vol. 111, no. 6, pp. 1099-1106, Jun. 1964.

[6.11] "Impedance Matching Techniques for Mixers and Detectors", Application Note 963, Hewlett-Packard Co, 1980.

[6.12] A. Podcameni, "Symmetrical and Asymmetrical Edge-Coupled-Line Transformers with a Prescribed Insertion Loss Design", *IEEE Trans. Microw. Theory Tech.,* vol. MTT-34, no. 1, pp. 1-7, Jan. 1986.

[6.13] D. Kajfez and S. Vidula, "Design Equations for Symmetric Microstrip DC Blocks", *IEEE Trans. Microw. Theory Tech.,* vol. MTT-28, no. 9, pp. 974-981, Sep. 1980.

[6.14] S. R. Borgaonkar, "Analysis and Design of DC Blocks", *Electronics Letters,* vol. 17, no. 2, pp. 101-103, Jan. 1981.

[6.15] http://www.ece.uci.edu/docs/hspice/hspice_2001_2-269.html.

[6.16] "Practical Characterization and Analysis of Lossy Transmission Lines", Application Note, Agilent Technologies, Inc., 2002.

[6.17] G. González, *Microwave Transistor Amplifier Analysis and Design*, 2nd Edition, Prentice-Hall, Inc., 1984.

[6.18] E. Hammerstad and O. Jensen, "Accurate Models for Microstrip Computer-Aided Design", in *IEEE MTT-S Int. Microw. Symp. Dig.,* pp. 407-409, May 1980.

Chapter VII

[7.1] F. T. Ulaby, R. K. Moore, A. K. Fung, *Microwave Remote Sensing: Active and Passive*, Volume I Microwave Remote Sensing Fundamentals and Radiometry, Artech House, Inc., 1981.

[7.2] N. Skou, D. Le Vine, *Microwave Radiometer Systems: Design and Analysis*, 2nd Edition, Artech House, Inc., 2006.

[7.3] M. E. Tiuri, "Radio Astronomy Receivers", *IEEE Trans. on Antennas and Propagation,* vol. 12, no. 7, pp. 930-938, Dec. 1964.

[7.4] J. D. Kraus, *Radio Astronomy*, 2nd Edition, Cygnus-Quasar Books, 1986.

[7.5] M. S. Hersman and G. A. Poe, "Sensitivity of the Total Power Radiometer with Period Absolute Calibration", *IEEE Trans. Microw. Theory Tech.,* vol. 29, no. 1, pp. 32-40, Jan. 1981.

[7.6] N. C. Jarosik, "Measurements of Low-Frequency-Gain Fluctuations of a 30-GHz High-Electron-Mobility-Transistor Cryogenic Amplifier", *IEEE Trans. Microw. Theory Tech.,* vol. 44, no. 2, pp. 193-197, Feb. 1996.

[7.7] E. J. Wollack, "High-electron-mobility-transistor Gain Stability and its Design Implications for Wide Band Millimeter Wave Receivers", *Review of Scientific Instruments,* vol. 66, no. 8, pp. 4305-4312, Aug. 1995.

[7.8] R. H. Dicke, "The Measurement of Thermal Radiation at Microwave Frequencies", *Review of Scientific Instruments,* vol. 17, pp. 268-275, Jul. 1946.

[7.9] A. Mennella et al., "Advanced Pseudo-Correlation Radiometers for the Planck-LFI Instrument", in *Proc. of the 3rd ESA Workshop on Millimetre Wave Technology and Applications,* Espoo, Finland, May 2003, pp. 69-74.

[7.10] B. Aja, E. Artal, L. de la Fuente, J. P. Pascual, A. Mediavilla, N. Roddis, D. Kettle, W. F. Winder, Ll. Pradell and P. de Paco, "Very Low-Noise Differential Radiometer at 30 GHz for the Planck LFI", *IEEE Trans. Microw. Theory Tech.,* vol. 53, no. 6, pp. 2050-2062, Jun. 2005.

[7.11] E. Collet, *Field Guide to Polarization*, SPIE Press, Bellingham, 2005.

[7.12] J.A. Rubiño-Martin et al., "The QUIJOTE CMB Experiment", in *Highlights of Spanish Astrophysics V, Astrophysics and Space Science Proceedings*, Part 3, Ed. Springer, 2010, pp. 127-135.

[7.13] M. López-Caniego et al., "The QUIJOTE CMB Experiment: status and first results with the multi-frequency instrument", in *Conference Proceedings Rencontres du Vietnam 2013: Cosmology in the Planck Era, Instrumentation and Methods for Astrophysics,* Feb. 2014, pp. 1-6.

[7.14] J.A. Rubiño-Martin et al., "The QUIJOTE CMB Experiment: studying the polarisation of the galactic and cosmological microwave emissions", in *Proceedings SPIE 8444, Ground-based and Airbone Telescopes IV,* 84442Y, Sep. 2012.

[7.15] W. Zhong, B. Li, Q. Fan and Z. Shen, "X-band compact septum polarizer design", in *IEEE International Conference on Microwave Technology and Computational Electromagnetics (ICMTCE),* Beijing, May 2011, pp. 167-170.

[7.16] L. A. Rodríguez González, *Conmutadores de fase de banda ancha para ondas milimétricas*, Engineering Telecommunication degree dissertation, Universidad de Cantabria, Spain, Jul. 2004.

[7.17] A. Tribak, A. Mediavilla, J. L. Cano, M. Boussouis and K. Cepero, "Ultra-Broadband Low Axial Ratio Corrugated Quad-Ridge Polarizer", in *Proc. of the 39th European Microwave Conference,* Rome, Italy, Oct. 2009, pp. 73-76.

[7.18] A. Mediavilla, J. L. Cano and K. Cepero, "On the Octave Bandwidth Properties of Octagonal-Shaped Waveguide Mode Transformers", *IEEE Trans. Microw. Theory Tech.,* vol. 59, no. 10, pp. 2447-2451, Oct. 2011.

[7.19] J. L. Cano, *Cryogenic Technology in the Microwave Engineering: Application to MIC and MMIC Very Low Noise Amplifier Design*, Ph. D. dissertation, Universidad de Cantabria, Spain, May 2010, pp. 174-180.

[7.20] B. Aja, M. Seelman-Eggebert, D. Bruch, A. Leuther, H. Massler, B. Baldischweiler, M. Schlechtweg, J. D. Gallego-Puyol, I. López-Fernández, C. Díez-González, I. Malo-Gómez, E. Villa and E. Artal, "4-12 and 25-34-GHz Cryogenic mHEMT MMIC Low-Noise Amplifiers", *IEEE Trans. Microw. Theory Tech.,* vol. 60, no. 12, pp. 4080-4088, Dec. 2012.

[7.21] AMMC-6241 26-43 GHz Low Noise Amplifier data sheet. Avago Technologies. Available http://www.avagotech.com/pages/en/rf_microwave/amplifiers/low_noise_amplifiers/ammc-6241/

[7.22] DR65-0109 Single Driver for GaAs FET Switches and Attenuators. Macom Technology Solutions. Available http://api.macom.com/content/datasheets/DR65-0109.pdf

[7.23] J. Cagigas, E. Villa, E. Artal and R. J. Hoyland, "Híbrido 180º de Banda Ancha en Tecnología Microstrip a 31 GHz", in *Proc. of the XXV Simposium Nacional de la Unión Científica Internacional de Radio,* Bilbao, Spain, Sep. 2010.

[7.24] M. Muraguchi, T. Yukitake and Y. Naito, "Optimum Design of 3 dB Branch-Line Couplers Using Microstrip Lines", *IEEE Trans. Microw. Theory Tech.,* vol. 31, no. 8, pp. 674-678, Aug. 1983.